STUDYING CELLULOSE NANOSTRUCTURE THROUGH FLUORESCENCE LABELING AND ADVANCED MICROSCOPY TECHNIQUES

STUDYING CELLULOSE NANOSTRUCTURE THROUGH FLUORESCENCE LABELING AND ADVANCED MICROSCOPY TECHNIQUES

Mouhanad Babi, H.B.Sc.

A Thesis Submitted to the School of Graduate Studies in Partial Fulfilment of the Requirements for the Degree Doctor of Philosophy

McMaster University

DOCTOR OF PHILOSOPHY (2021) MCMASTER UNIVERSITY

(Chemical Biology) Hamilton, Ontario

TITLE: Studying cellulose nanostructure through fluorescence labeling and advanced microscopy techniques

AUTHOR: Mouhanad Babi
H.B.Sc.Chembio

SUPERVISOR: Professor Jose Moran-Mirabal

PAGES: xiii, 166

Abstract

As the major component of the plant cell wall, cellulose is produced by all plant species at an annual rate of over a hundred billion tonnes, making it the most abundant biopolymer on Earth. The hierarchical assembly of cellulose glucan chains into crystalline fibrils, bundles and higher-order networks endows cellulose with its high mechanical strength, but makes it challenging to breakdown and produce cellulose-based nanomaterials and renewable biofuels. In order to fully leverage the potential of cellulose as a sustainable resource, it is important to study the supramolecular structure and hydrolysis of this biomaterial from the nano- to the microscale.

In this thesis, we develop new chemical strategies for fluorescently labeling cellulose and employ advanced imaging techniques to study its supramolecular structure at the single-fibril level. The developed labeling method provides a simple and efficient route for fluorescently tagging cellulose nanomaterials with commercially available dyes, yielding high degrees of labeling without altering the native properties of the nanocelluloses. This allowed the preparation of samples that were optimal for super-resolution fluorescence microscopy (SRFM), which was used to provide for the first time, a direct visualization of periodic disorder along the crystalline structure of individual cellulose fibrils. The alternating disordered and crystalline structure observed in SFRM was corroborated with time-lapsed acid hydrolysis experiments to propose a mechanism for the acid hydrolysis of cellulose fibrils. To gain insight on the ultrastructural origin of these regions, we applied a correlative super-resolution light and electron microscopy (SR-CLEM) workflow and observed that the disordered regions were associated nanostructural defects present along cellulose fibrils. Overall, the findings presented in this work provide significant advancements in our understanding of the hierarchical structure and depolymerization of cellulose, which will be useful for the development of new and efficient ways of breaking down this polymer for the production of renewable nanomaterials and bio-based products like biofuels and bioplastics.

Lay Abstract

In this dissertation, we have studied in unprecedented detail the structure of cellulose – a polymer that is found in every plant. As the main structural component of the plant cell wall, cellulose endows trees with their strength and resilience while storing sunlight energy in its chemical bonds. Since plant biomass represents eighty percent of all living matter on Earth, cellulose is an abundant resource that can be used to produce sustainable and environmentally benign nanomaterials and bioproducts, like biofuels and bioplastics. Our ability to use cellulose as a renewable source of structural materials and energy is intimately linked to our capacity to break apart its tight structural packing. Deconstructing cellulose into various forms demands that we understand the multi-level organization of its structure and the susceptible regions within it. To gain this information, in this thesis we develop new labeling methods and apply state-of-the-art microscopy tools to directly visualize the arrangement of cellulose fibrils at the nanoscale (comparable to 1/10,000 the width of a human hair) and study their breakdown by acid treatment. The findings presented in this work furthers our fundamental understanding of the natural structure of cellulose, which has important implications on the development of industrial strategies to break down this abundant and renewable biomaterial.

Acknowledgements

Without doubt, the thesis you see in front of you could not have been made possible without the incredible support of my supervisor, lab mates, collaborators, friends and family.

First and foremost, I would like to sincerely thank Professor Jose Moran-Mirabal, who has been instrumental to my growth as a researcher since I took his undergraduate Analytical Chemistry course. Throughout my doctoral degree, I had the great pleasure of sharing my passion for my microscopy with Jose, who has taught me much of what I know today about this fascinating technique. I am deeply grateful for his continuous support, guidance, mentorship and scientific curiosity during this journey.

Being part of the MMG family, I shared many cherishable moments with my lab mates during collaborations, lab hangouts and random office shenanigans. I was fortunate for having Ayodele Fatona, Markus Rose and Kevin Saem as mentors who provided me with guidance on organic synthesis, microscopy, and my career. To the undergraduate students that I have worked with, Olivia (Xiang) Li, Christine Cerson and Jaclyn Winitsky: thank you so much for your hard work, patience and support, I could not have done this without you. I am also grateful for all the stimulating conversations I had around the office with Xiuping Ding, Urooj Gill, Taylor Stimpson, Sara Makaremi, Eduardo Gonzalez and Mabel Carpio.

During my Ph.D., I had the great pleasure of working with several collaborators at McMaster University, including Dr. Emily D. Cranston, Dr. Kevin de France, Dr. Todd Hoare, Dr. Trevor Gilbert, Victoria Jarvis, Dr. Kathryn Grandfield, Dr. Nabil Bassim, Alyssa Williams and Dr. Alex Adronov, who I would like to thank for playing a crucial role in the work presented in this thesis and for giving me the opportunity to expand my skills into new areas. I also thank my committee members, Dr. Cecile Fradin and Dr. Ray Truant, for their feedback and guidance during my degree. Across the globe in France and Netherlands, I would like to thank Dr. Aline Cerf, Dr. Laurent Malaquin and Dr. Angelo Accardo, who were incredibly supportive during my visit to LAAS-CNRS in Toulouse. During this time, I had the extreme pleasure of working with and befriending Roberto Riesco, who supported me in every step of the way, and with Marianne Elias, provided me with wonderful company and kept me fed.

Last but not least, I would like to give a big shoutout to my life-long friends, aka “The Boys”, “SMMAAQKS” and Jeffrey Leung, for always giving me a fun weekend to look forward to. To my coffee-buddy Rashik Ahmed: thank you for all the stimulating and uplifting conversations that made these pandemic PhD years more bearable. Finally, a huge thanks to my brother Mahmoud Babi, my sisters, mama and baba for their unwavering support and unconditional love that propelled me through to the finish line of this incredible journey.

Table of Contents

Chapter 3

Chapter 4

Chapter 5

Chapter 6

Appendix

List of Figures and Tables

Chapter 1

Chapter 2

Chapter 3

Chapter 4

Chapter 5

List of all Abbreviations and Symbols

ACF	Auto-correlation function
AFM	Atomic force microscopy
APAF	Azidopropyl aminofluorescein
BALM	Binding-activated localization microscopy
BC	Bacterial cellulose
BTA	Benzenetricarboxamide
CCF	Cross-correlation function
CESA	Cellulose synthase proteins
CM-CNFs	Carboxymethylated cellulose nanofibrils
CNCs	Cellulose nanocrystals
CNFs	Cellulose nanofibrils
CSC	Cellulose synthase complex
DCM	Dichloromethane
DNA	Deoxyribonucleic acid
DTAF	Dichlorotriazinyl aminofluorescein
DTAP	Dichlorotriaznyl propargylamine
DTPR	Dichlorotriazinyl piperazine Rhodamine 6G
ECM	Extracellular matrix
EELS	Electron energy loss spectroscopy
FAM	6-Carboxyfluorescein
FT-IR	Infrared spectroscopy
FWHM	Full width at half maximum
GFP	Fluorescent protein
GSD	Ground state depletion microscopy
HOMO	Highest occupied molecular orbital
LUMO	Lowest unoccupied molecular orbital
MD	Molecular dynamics
MPS	Membrane-associated periodic skeleton
MS	Mass spectrometry
NA	Numerical aperture
NDC	Nata de coco
NMR	Nuclear magnetic resonance
NSOM	Near-field scanning optical microscopy
PAH	Poly(allylamine hydrochloride)
PAINT	Accumulation for imaging in nanoscale topography
PALM	Photoactivated localization microscopy
PBS	Phosphate buffered saline
PSF	Point-spread function
RESOLFT	Reversible saturable optical linear fluorescence transitions
ROI	Regions of interest

RT	Room temperature
SANS	Small angle neutron scattering
SAXS	Small-angle X-ray scattering
SEM	Scanning electron microscopy
SIM	Structured illumination microscopy
SR-CLEM	Correlative super-resolution light and electron microscopy
SRFM	Super-resolution fluorescence microscopy
SRFM	Super-resolution
SSIM	Saturated structured illumination microscopy
STED	Stimulated emission depletion microscopy
STORM	Stochastic optical reconstruction microscopy
TC	Terminal complex
TEA	Triethylamine
TEM	Transmission electron microscopy
THF	Tetrahydrofuran
TLC	Thin-layer chromatography
UV	Ultraviolet
XRD	X-ray diffraction

Declaration of Academic Achievement

(1) Babi, M.; Palermo, A.; Abitbol, T.; Fatona, A.; Jarvis, V.; Nayak, A.; Cranston, E.; Moran-Mirabal, J. Visualization of Nanostructural Dislocations in Microcrystalline Cellulose Fibrils through Super-Resolution Fluorescence Microscopy. *Microscopy and Microanalysis* **2021**, *27* (S1), 854–857. https://doi.org/10.1017/S1431927621003354.

(2) Babi, M.; Williams, A.; Reid, M.; Grandfield, K.; Moran-Mirabal, J.; Bassim, N. Correlative Light and Electron Microscopy for the Study of the Structural Arrangement of Bacterial Microcrystalline Cellulose Microfibrils. *Microscopy and Microanalysis* **2021**, *27* (S1), 566–569. https://doi.org/10.1017/S1431927621002452.

(3) Babi, M.; Riesco, R.; Boyer, L.; Fatona, A.; Accardo, A.; Malaquin, L.; Moran-Mirabal, J. Tuning the Nanotopography and Chemical Functionality of 3D Printed Scaffolds through Cellulose Nanocrystal Coatings. *ACS Applied Bio Materials* **2021**. https://doi.org/10.1021/acsabm.1c00970.

(4) Babi, M.; Palermo, A.; Abitbol, T.; Fatona, A.; Jarvis, V. M.; Nayak, A.; Cranston, E. D.; Moran-Mirabal, J. Direct Super-Resolution Imaging of the Alternating Disordered and Crystalline Structure of Cellulose Fibrils. In submission.

(5) Babi, M.; Fatona, A.; Li, X.; Cerson, C.; Jarvis, V. M.; Abitbol, T.; Moran-Mirabal, J. Efficient Labelling of Nanocellulose for High-Resolution Fluorescence Microscopy Applications. *In submission*.

(6) Rose, M.; Babi, M.; Moran-Mirabal, J. The Study of Cellulose Structure and Depolymerization through Single-Molecule Methods. *Industrial Biotechnology* **2015**, *11* (1), 16–23.

Chapter 1

Super-resolution fluorescence microscopy and its application in studying the nanostructure of fibrillar systems

From a scientific point of view, our understanding of the world is driven through an interplay between observation, rational deduction, and hypothesis testing. Given that our most intuitive form of making observations is sight, to many individuals "seeing" is indeed believing. For centuries, we stared at the night sky and saw a blanket of bright spots revolve around us, leading to the belief that the Earth was at the center of the universe. This changed during the 16th century when Galileo Galilei and other astronomers looked through the lens of a telescope to see that we might be living in a heliocentric model instead, with the revolution of objects in our solar system being centered around the Sun.[1] During the same century, we went from staring at the infinitely faraway to the infinitely close, when Anton van Leeuwenhoek built a single-lens microscope and used it to visualize microorganisms and bacteria for the first time.[2]

The development of microscopy opened a door to the world beneath, compelling scientists to dig deeper and jump through different length scales to discover the fundamental components and processes of living things around them. This demand for higher magnification power and imaging resolution led to improvements in the quality of optical elements, allowing us to eventually observe cells and their organelles. Since then, microscopy became an indispensable tool for scientists to characterize cellular structures and their response to different environments, allowing us to understand the life of a cell.

1.1 Fluorescence Microscopy

Delving into the molecular components of cellular organelles requires high specificity, which is not offered by white light optical microscopy, as light interacts similarly with the different proteins, lipids and DNA molecules that the cell is comprised of. At the same time, illumination of some molecules by a specific wavelength of light can cause an electron in the highest occupied molecular orbital (HOMO, F_0) to absorb a photon and be excited to the lowest unoccupied molecular orbital (LUMO, F_1) (Figure 1.1a). This polarization causes the molecule to undergo vibrational relaxation almost instantaneously and places the electron at a lower energy within the LUMO for nanoseconds before returning to the HOMO, or ground state. If this relaxation occurs directly in one step, the electron emits a photon with energy equal to the difference between that of the HOMO and LUMO. Due to the vibrational relaxation that occurred at the LUMO, the emitted photon is of lower energy, or higher wavelength, than that of excitation. This process of rapid absorbance and remission of light is known as fluorescence (Figure 1.1a).

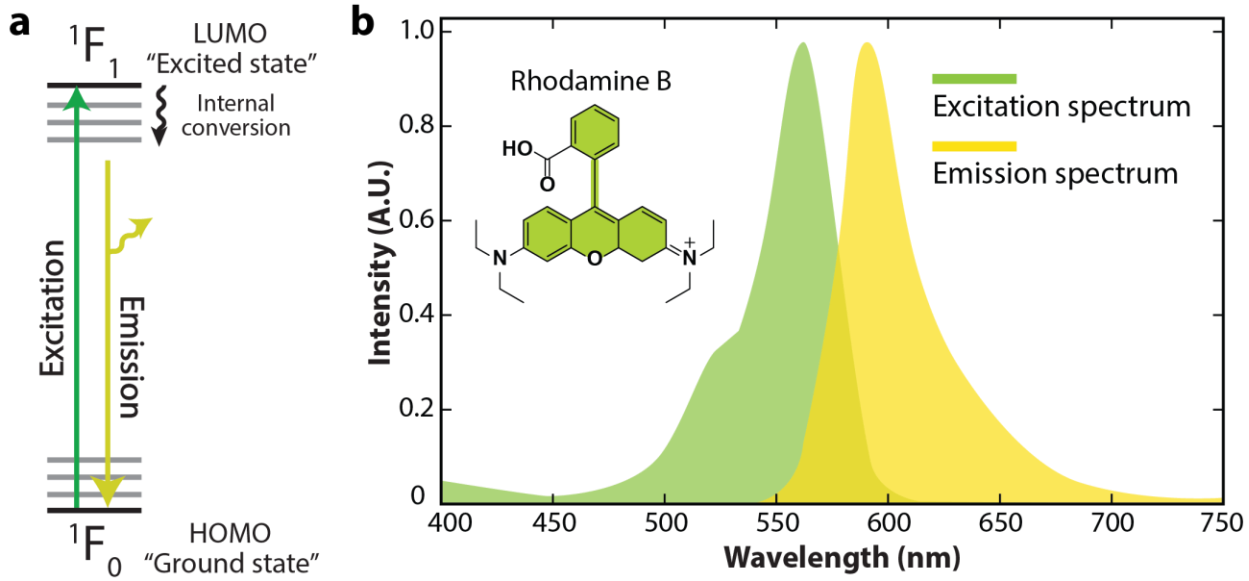

Figure 1.1. Principles of molecular fluorescence. a. Jablonski diagram describing the molecular electronic transitions involved in fluorescence. An electron in the HOMO, singlet ground state ($^1F_0$) absorbs a photon by an excitation source and transitions to the LUMO, excited state ($^1F_1$). Internal conversion by virtue of vibrational relaxation causes the electron to lose some energy, before directly returning to the ground state and emitting a photon. **b.** The energy loss by internal conversion causes the emission spectrum of fluorescent molecules to be red shifted (known as Stoke's shift) relative to the excitation spectrum. The excitation and emission spectra of Rhodamine B is used as an example.

The increase in light wavelength during fluorescence, known as Stoke's shift, allows the emitted light to be easily discriminated from the excitation source and is the foundation of the excellent signal-to-noise ratio and in turn the superior sensitivity of fluorescence microscopy (Figures 1.1b and 1.2a). Through selective labeling strategies, such as that of green fluorescent protein (GFP)-fusion constructs, specific molecular components can be visualized with minimal perturbation to their native state. Orthogonal labeling methods that utilize fluorescent dyes of different colours permit the simultaneous visualization of multiple molecular components, thus providing information on their interactions in a spatial and temporal manner.

Despite the versatility of this technique and the plethora of information scientists have gathered through it, the resolution of fluorescence microscopy remained limited by the natural diffraction of light. Given that optical microscopy relies on the interaction of photons with matter, the finite volume that light occupies at the focal plane of an objective due to diffraction prevents it from probing features smaller than itself. This limitation is described by Abbe's law, which states that the maximal theoretical resolution (d) of a microscope is defined by the ratio of the wavelength of light (λ) to twice the numerical aperture (NA) of the objective (**Equation 1**) in the transverse plane, and the ratio of twice λ to the square of NA in the axial direction (**Equation 2**). These limitations are tied to the dimensions of the point-spread function (PSF), a three-dimensional diffraction pattern that is formed when a point-source of light passes through the optical elements of a microscope (Figure 1.2b). Using high-NA objectives (e.g. NA 1.45) and visible light (e.g. 550 nm) would thus yield a resolution of approximately 200 nm and 525 nm in the lateral and axial directions, respectively.[3]

$$d_{x,y} = \frac{\lambda}{2NA} \qquad \textbf{Equation 1}$$

$$d_z = \frac{2\lambda}{NA^2} \qquad \textbf{Equation 2}$$

This led scientists to develop and use alternative, non-optical microscopy methods to image diffraction-limited structures, such as scanning or transmission electron microscopy (SEM or TEM) and atomic force microscopy (AFM). Although these techniques have been invaluable for studying the morphology of a variety of structures with nanometer resolution, their sample preparation requirements, low specificity and poor or non-existent temporal resolution often makes them incompatible for studying live, dynamic biological processes. This has placed pressure on the development of new optical microscopy methods that can break the diffraction limited resolution of light microscopy while maintaining the versatility and simplicity of conventional fluorescence microscopy. To meet this demand, over the past

two decades, fluorescence microscopy has seen significant advancements that overcame the diffraction-limit, leading to the development of super-resolution fluorescence microscopy (SRFM) that finally placed this commonly-used technique in the nanoworld.

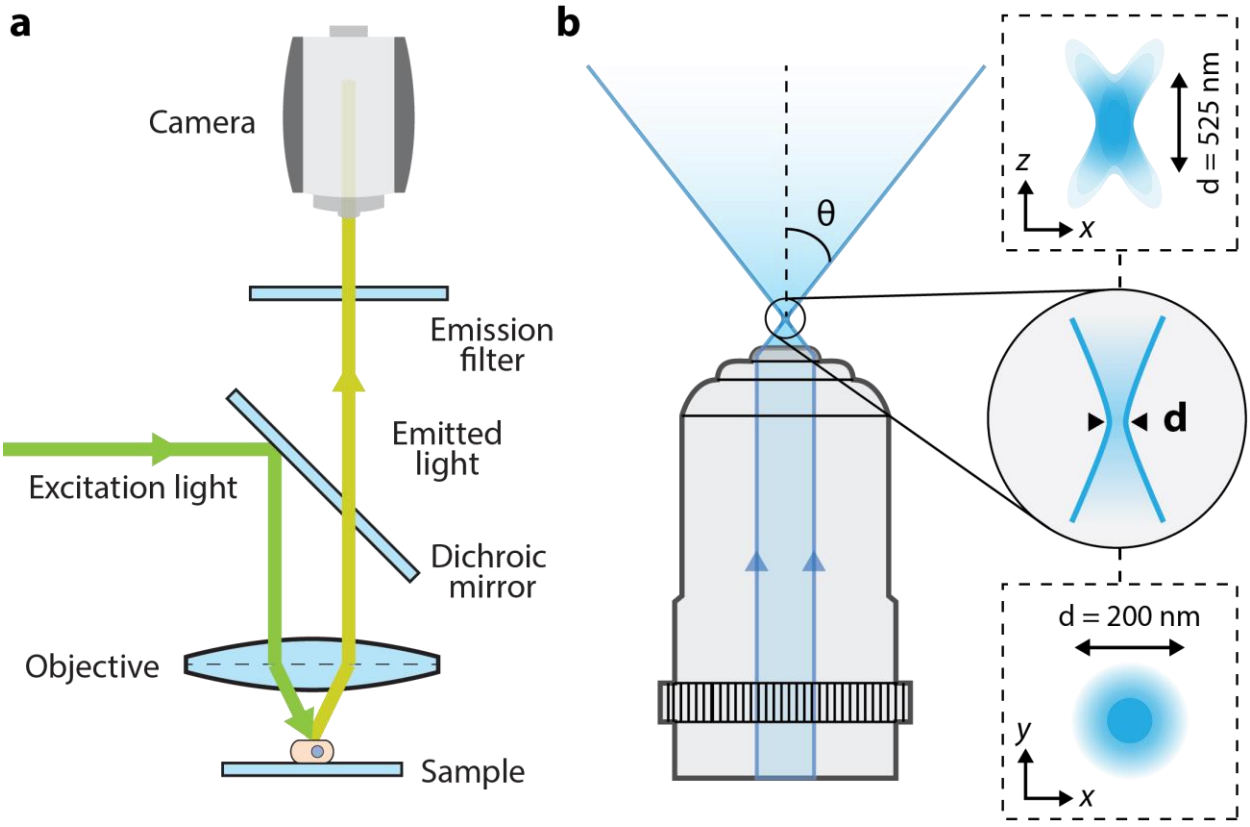

Figure 1.2. The working principles of a fluorescence microscope and the diffraction-limit of light. a. Fluorescently-labeled samples are excited with an illumination source of a colour that is specific to the dye being used. In an upright epifluorescence configuration, the light is reflected by a dichroic mirror and focused onto the sample by an objective from above, and emitted fluorescence light is collected by the objective through the same light path. Since the dichroic mirror only allows higher wavelength light through, the emission light can be separated from the excitation source, before undergoing further filtering and being detected by a camera. **b.** Due to diffraction, the light focused by an objective forms a three-dimensional diffraction pattern, with widths in the lateral and axial planes defined by Abbe's law. With a high numerical aperture objective (NA 1.45) and visible fluorescence light (e.g. 550 nm), the resolution of a conventional fluorescence microscope is limited by diffraction to 200 nm and 525 nm in the lateral and axial direction, respectively.

1.2 Super-Resolution Fluorescence Microscopy

1.2.1 True Super-Resolution Techniques

Early attempts at breaking the diffraction-limit used probes that pass light through an aperture smaller than the excitation wavelength, creating an evanescent field that only illuminates the sample surface. This technique, known as **Near-field Scanning Optical Microscopy (NSOM)**, utilizes a fine-tipped probe that is placed at a distance below than 10 nm above the sample, and scanned across to collect light and topographical information point-by-point.[4] The resolution of NSOM is limited by the size of the aperture used to collect light, which typically achieves a resolution of 20 – 50 nm in the transverse plane; however, it has a shallow penetration distance of only tens of nanometers, limiting it to the study of topographical features.

To extend SRFM into the far-field, the diffraction-limit can be reduced, as outlined in Abbe's law, by increasing the numerical aperture of the objective. Traditionally, microscopes collect light from only one side of the sample, leaving much of the spherical emitted light wasted. This reduces sensitivity and distorts the shape of the PSF in the axial direction, leading to poor z-resolution. To symmetrically focus light from nearly all directions, a second objective can be used to collect light from the opposite side of the sample, as done in **4Pi** and **I^{5}M** microscopy, which can reach lateral and axial resolutions of 140 and 100 nm, respectively.[5] However, the modest improvement in lateral resolution, the complex optics needed for the coherent alignment of two light paths and the severe restrictions on sample thickness and mounting has limited the use of 4Pi and I^{5}M microscopy.

1.2.2 Patterned Super-Resolution Techniques

The techniques mentioned so far have been "true" super-resolution microscopy, that utilize the fundamental properties of light and optics to reduce the diffraction-limit or bypass it. The second class of super-resolution techniques are considered to be "functional", as they intermix sub-diffraction-limited information in the illumination pattern and/or extract those features by exploiting the different photophysical states of fluorescent dyes. These techniques fall under the general category of **Reversible Saturable Optical Linear Fluorescence Transitions (RESOLFT)**, which in one way or another cause the selective suppression and detection of fluorescent molecules within a sub-diffraction-limited space to achieve super-resolution.

In principle, the simplest implementation of RESOLFT involves the overlay of a long-wavelength, doughnut-shaped illumination pattern over a focused, short-wavelength excitation beam. If the wavelength of the doughnut-shaped beam matches the energy gap

between vibrationally-relaxed LUMO and the highest-energy level of the HOMO, then a photon of this wavelength can stimulate the emission of an identical photon from an excited molecule and return it to the ground state (Figure 1.3a). Thus, if molecules are excited by the lower-wavelength, focused light beam, molecules that reside within the doughnut-shaped light will undergo stimulated emission at a wavelength longer than that of the conventional fluorescence process. With sufficient light intensity, the fluorescence emission of all the molecules within the doughnut will be suppressed due to saturated stimulated emission. This limits fluorescence to molecules residing within the center of the doughnut, effectively reducing the size of fluorescence emission to lengths below the diffraction-limit (Figure 1.3a). This is the working principle of **Stimulated Emission Depletion (STED) Microscopy**, which raster scans the illumination pattern over the sample to yield images with a lateral resolution of 30 nm.[6] If a pinhole is inserted, out-of-focus light can be blocked to achieve confocality and an axial resolution of 400 nm. Alternatively, STED can be combined with a 4Pi set-up to reach a z-resolution as low as 30 nm.[7]

Another patterned-illumination technique, **Structured Illumination Microscopy (SIM)**, uses two interfering, phase-shifted light sources to create a sinusoidal illumination pattern. Exciting a fluorescent structure with this pattern results in a moiré effect, bringing the high-frequency spatial information present in the sample to the low-frequency range that can detected by the microscope.[8] Acquiring a set of images where the pattern is shifted in one direction by changing the phase of the light source, and in another direction by a rotating mask, can allow the reconstruction of images with 100 nm resolution. This technique can also utilize the principles of RESOLFT, where high intensity lasers can close the diffraction-limited gap between the illumination bands by saturating the emission of dyes in areas where there is constructive interference. This method, known as **Saturated SIM (SSIM)**, can produce images with a resolution of 50 nm.[8] Unlike most super-resolution techniques, SIM has the advantage of being relatively independent of the dyes used, but requires additional components to be added to a widefield microscope and offers a modest two- to four-fold improvement in resolution.

1.2.3 Widefield Functional Super-Resolution Techniques

The RESOLFT imaging techniques mentioned so far require advanced modifications to the optical setup of a conventional fluorescence microscope to produce the illumination patterns needed for achieving super-resolution. These patterns suppress fluorescence in a sub-diffraction-limited manner through fluorescence saturation or stimulated emission, however, fluorescence molecules can reside in other “dark”, or non-emissive states even when illuminated. RESOLFT techniques that exploit these photophysical properties of dyes

fall within the category of **Ground State Depletion (GSD) Microscopy**. The working principle of GSD microscopy ultimately relies on achieving a sparse population of emitting fluorophores such that each emission is isolated within a diffraction-limited area. Recording single-molecule emission events on a sensitive camera, often an electron multiplying charge coupled device (EMCCD), would allow for the localization of each emitting molecule in a wide-field setup with nanometer precision. If the emitting molecules can enter a dark state, and a different subset of fluorophores is activated, then repeating the process of activation, localization, and deactivation for random fluorophore populations over thousands of recorded frames allows the localization of the fluorescent molecules comprising the labeled structure (Figure 1.3b). The localization precision is in principle dependent on the spread of the PSF (σ_{PSF}) and the number of detected photons (N) (**Equation 3**), with values typically between 10 and 20 nm. Thus, combining all the single-molecule localizations allows the reconstruction of an image with a lateral resolution of 20 – 50 nm.[9] This technique can be expanded to the axial dimension if the PSF is deformed in a z-dependent manner, as done with an astigmatic lens, which can elongate the PSF in the horizontal and vertical direction depending on whether the molecule lies below or above the focal plane. By calculating the extent and direction of the PSF ellipticity, the z-position of each molecule can be determined to a resolution of approximately 50 nm if it is within 1000 nm of the focal plane.[10]

$$\sigma_{loc} = \frac{\sigma_{PSF}}{\sqrt{N}} \qquad \textbf{Equation 3}$$

Photoblinking, where the fluorophores undergo rapid fluctuation between their emissive and dark states, can be accomplished in various ways. Upon excitation of an electron to the LUMO, there is a small probability that it may flip its spin and undergo intersystem crossing to the triplet state (T_1), where return to the ground state is quantum mechanically forbidden until the electron flips its spin again. This causes the lifetime of the triplet state to be micro- to milli-seconds long and results in a long-lived non-emissive, or "dark" state of the fluorophore (Figure 1.3c). The "pumping" of dyes into the triplet state can be accomplished with high intensity illumination, and the lifetime of the dark state can be prolonged by introducing reducing agents, commonly mercaptoethylamine or β-mercaptoethanol, that selectively react with excited molecules to create reduced dye adducts. This reaction can be randomly reversed by molecular oxygen present in the imaging medium, causing the molecule to return to the ground state and become reactivated. Thus, a population inversion from the "on" to the "off" state can be achieved by combining high intensity illumination with imaging buffers that contain reducing agents and an oxygen-scavenging system. The most popular super-resolution technique, **Stochastic Optical Reconstruction Microscopy (STORM)**, utilizes these principles to yield stochastically

blinking fluorophores that allow the localization of isolated, single-molecule emissions.[9] In the original implementation of STORM, photoblinking was achieved through the stochastic interaction of activator-reporter dye pairs. Other GSD techniques achieve photoblinking through different pathways, such as photoactive dyes and proteins that can activated or deactivated by specific wavelengths of light, as done in **Photoactivated Localization Microscopy (PALM or fPALM)**, or binding-activated fluorescence as done in **Points Accumulation for Imaging in Nanoscale Topography (PAINT)**, originally known as **Binding-Activated Localization Microscopy (BALM)**.[11–14] One way or another, these techniques all exploit the dark and emissive states of fluorophores to achieve photoblinking and utilize single-molecule localization algorithms to reconstruct super-resolution images with a 10-fold enhancement in resolution compared to the starting diffraction-limited image.

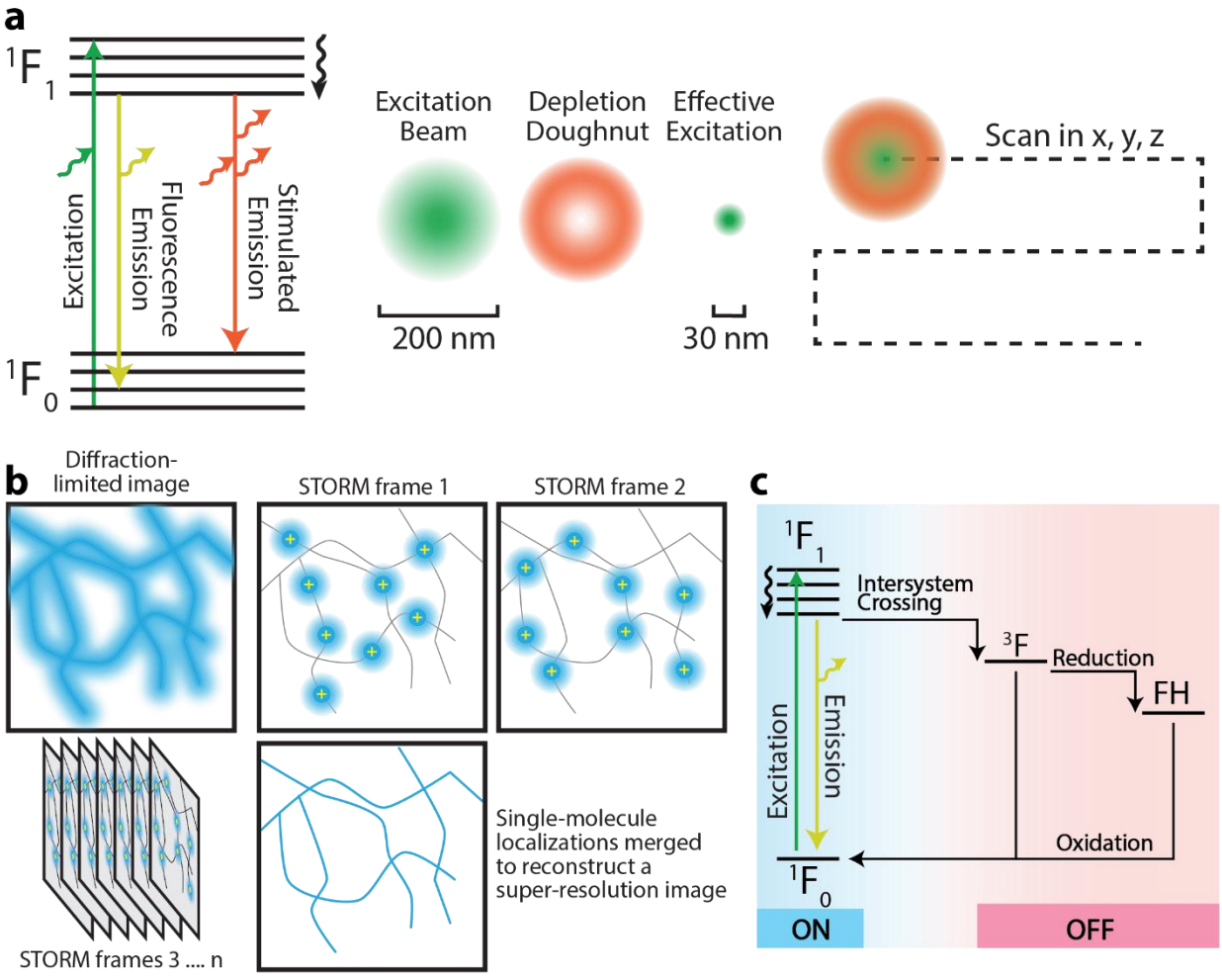

Figure 1.3. Working principles of STED and STORM super-resolution techniques. a. STED relies on the phenomenon of stimulated emission, where a photon matching the gap between highest energy level of the HOMO and lowest energy level of the LUMO would stimulate the emission of a

photon with the same energy when the electron is in the excited state. At high illumination powers, stimulated emission would predominate normal fluorescence, which also occurs in a slightly longer wavelength. Overlaying a stimulated emission doughnut-shaped beam on a conventional gaussian-shaped excitation beam would result in molecules only in the center of the doughnut to fluoresce, effectively breaking the diffraction-limited resolution to yield a 30 nm emission volume instead of the conventional 200 nm. The overlaid beams are raster scanned using a line-scanning confocal configuration to yield a super-resolution image. **b.** STORM exploits the photoblinking behaviour of fluorophores, where they undergo stochastic switching between dark and emissive states. When the dark state predominates, single-molecules that are discernable within a diffraction-limited area can be localized with nanometer precision. Since the blinking is reversible and stochastic, random populations of single molecules will emit light at different times. Acquiring a movie of thousands of images would allow the localization of most of the molecules comprising the structure of interest and recombining all the localizations at the end to yield a super-resolution image. **c.** Fluorophore photoblinking occurs when an excited electron undergoes intersystem crossing and flips its spin, resulting in a long-lived triplet state. The lifetime of this state can be prolonged by the addition of reducing agents, which would form dye adducts that are "dark" and can only return to their original emissive state following oxidation.

1.3 Application of SRFM in Studying Fibrillar Systems

Since their development, SRFM techniques have been extensively used to visualize diffraction-limited structures and their arrangement within various cellular organelles. Bringing the powers of specific, multicomponent labeling and visualization of fluorescence microscopy to the nanoworld makes SRFM suitable for revisiting topics that were previously only visualized at this scale using non-optical methods. Systems that can particularly benefit from this are those fibrillar in nature. Given the reduced dimensionality of fibrils, their substructures and supramolecular assembly predisposes them to be within the diffraction-limited regime. Here, I will review the application of SRFM in studying fibrillar systems in terms of their supramolecular structure, growth and association with other components.

1.3.1 Visualizing Cytoskeletal Fibrils

The information accessible by fluorescence microscopy is determined by the targets that are fluorescently-tagged, with the most basic and intuitive strategy being labelling a group that is abundantly present on the structure's surface. In a fibrillar system, this allows the measurements of the width of individual fibrils by determining the full width at half maximum (FWHM) of line-intensity profiles acquired from their cross-sections. This has been repeatedly done with microtubules *in vitro* to demonstrate the resolution capabilities of SRFM techniques as they were developed and tested. Initial imaging of microtubules with STORM yielded width measurements of 60 nm, however, established measurements by EM

report widths of 25 nm. This discrepancy is explained by the additional fluorophore displacement introduced by primary and secondary antibody labeling, which highlights the importance of good sample preparation and labeling techniques in achieving high quality SRFM images.[12] Artifacts produced through fluorophore displacement can be reduced by using fewer immunostaining components and smaller fluorescent probes to label the target of interest. Avoiding the use of secondary antibodies, and instead directly labeling primary antibodies with fluorescent dyes would reduce the observed microtubule width to 54 nm, and eventually to 40 nm when labelled fragmented antibody epitopes (nanobodies) or small molecules are used.[15,16]

Beyond accurate width measurements, high imaging resolution allows the discernment of individual fibrils that are densely packed in a small volume, which is critical for understanding the structural arrangement of cytoskeletal networks. Prominent examples of this include SRFM imaging of actin, a member of the cell cytoskeleton that is specifically involved in motor processes. Using a dual-objective 3D STORM microscope, a remarkable isometric resolution of 10 nm allowed the identification of two actin network layers that form sheet-like cellular protrusions, known as lamellipodia (Figure 1.4a).[17] Recognizing this multi-layer assembly would have been impossible with conventional fluorescence microscopy, as actin would have appeared to be a continuous sea of dye throughout this portion of the cytoplasm.

The cytoskeletal networks formed by actin also play an important role in the function of neuronal cells and their ability to transduce electrical signals. In instance, monitoring the dynamic rearrangement of actin in dendrites would provide insight on the processes that that are ultimately responsible for the plasticity of neural synaptic connections. Visualizing these dynamic processes was possible with PALM since it employs endogenously-expressed fluorescent proteins that are amenable for live-cell imaging. The enhanced imaging resolution of PALM allowed the live-monitoring of structural features of dendritic spines, including their neck length and width, and the size of the head and hole within it.[18]

The assembly of actin in neuronal cells was also studied with STORM, revealing a repeating pattern of actin rings present along the axon length. This discovery was unique to axons, as actin traveled continuously along the dendrites of neuron cells.[19] Multi-colour labelling of actin, the actin-capping protein adductin, the cytoskeletal protein spectrin and the sodium channel Na_v revealed a highly ordered distribution of these proteins along the axonal axis (Figure 1.4b). The labeling pattern imposed by this structure was analyzed using cross-correlation functions, an image analysis routine that is discussed in more detail later, to determine the periodicity and size of the observed domains. This analysis allowed the

formulation of a structural model that describes the role of different cytoskeletal components in regularly spacing sodium channels, which are responsible for the highly controlled signal transduction in neurons. This structure is now known as the actin/spectrin membrane-associated periodic skeleton (MPS), which has been characterized by a regular spacing of ~200 nm between adjacent actin rings.

1.3.2 Image Analysis of Periodic Structures using Correlation Methods

To monitor how the MPS develops and changes under different cellular conditions, a consistent and quantitative analysis method must be used. To this end, Barbas and colleagues developed an open-source program that can evaluate the presence, quality and structural characteristic of MPS from super-resolution neuronal images with minimal input parameters.[20] Briefly, a threshold is applied to the image to determine neuronal regions, which are then segmented into smaller sub regions. These are then compared to a known reference pattern, which was described using a sharpened sinusoidal function, by calculating the Pearson correlation coefficient at different rotational orientation of the image and phases of the pattern. Images above a predetermined threshold of this coefficient determined whether there was an MPS and the level of its structural quality. This method enabled the high-throughput analysis of neuronal images acquired from mice embryo neurons after various days *in vitro* and showed how the MPS develops as the embryo is growing.

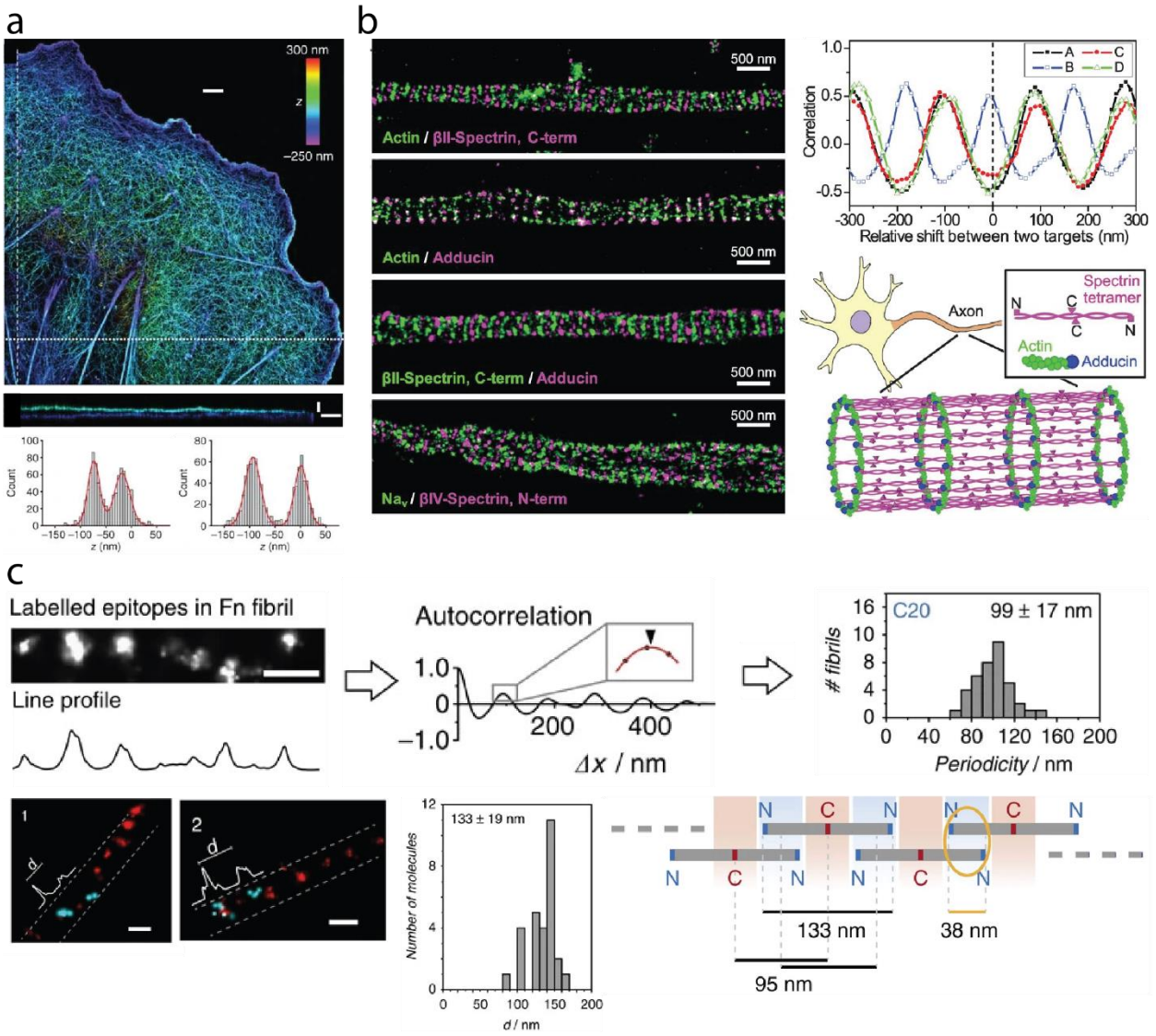

Figure 1.4. SRFM imaging of the cellular cytoskeleton. a. Dual-objective 3D STORM imaging of the actin cytoskeleton in the lamellipodia of BSC-1 cells, resolving the ventral and dorsal sides of the cell membrane to a z-resolution below 100 nm. Lateral and axial scale bars are 2 μm and 100 nm, respectively. Adapted from ref [17] with permissions. **b.** Two-colour STORM images of the membrane-associated periodic skeleton labeled for actin, βII-spectrin, adductin and Na_v proteins. Visualizing the distribution of the various proteins associated with the membrane-associated periodic skeleton (MPS) and their quantitative analysis with cross-correlation led to the proposed model of the MPS. Adapted from ref [19] with permissions. **c.** STORM imaging of fibronectin labeled at C-termini revealed a periodic molecular arraignment than can be characterized using the auto-correlation function. Combining this result with end-to-end measurements of N-terminal labeled fibronectin molecules, the arrangement of fibronectin were determined to be staggered with significant overlap when forming a fibril. All scale bars are 100 nm. Adapted from ref [21] with a Creative Commons CC BY license.

The study above utilized the simplest image correlation method, the Pearson correlation coefficient (R_p), which is the two-dimensional ratio of the covariance of two

images to the product of the standard deviations of the images (**Equation 4**), where m, n are pixel coordinates, and I, P being the intensities of the first and second image. However, given the reduced dimensionality of fibrillar structures, this coefficient can be simplified if intensity-distance profiles are acquired through line traces, and then expanded to a function on the relative displacements of two profiles. This yields the cross-correlation function (CCF) $\dot{I} \cdot P$ (**Equation 5**) of intensity plots I and P at points k with displacement τ, which can be used to study the colocalization of different components, such as proteins, within a structure. Calculating the cross-correlation function of an intensity plot with itself yields the auto-correlation function (ACF). The ACF of the intensity profile of a traced fibril can provide information on the presence and size of domains, and whether these domains are arranged in a periodic or random fashion. If the fibril contains no local domains then the ACF will quickly decay to zero. Otherwise, the size of the domains can be determined by the width of the first peak, and if these domains are periodic, then equally spaced neighbouring peaks in the ACF will be present. The average distance between these peaks can provide repeating distance of a labelling pattern. Through ACF and CCF analysis, the presence of different structural domains and their interactions can be determined on a fibril-by-fibril basis.

$$R_p = \frac{\sum_m \sum_n (I_{m,n} - \bar{I})(P_{m,n} - \bar{P})}{\sqrt{\sum_m \sum_n (I_{m,n} - \bar{I})^2 \sum_m \sum_n (P_{m,n} - \bar{P})^2}} \qquad \textbf{Equation 4}$$

$$I \cdot P(\tau) = \frac{\sum_k (I_{k+\tau} - \bar{I})(P_k - \bar{P})}{\sqrt{\sum_k (I_k - \bar{I})^2 \sum_k (P_k - \bar{P})^2}} \qquad \textbf{Equation 5}$$

The autocorrelation analysis approach is commonly used to analyze the periodic arrangement of proteins within sub-cellular structures imaged with SRFM. For instance, the molecular architecture of fibronectin fibrils, which are a critical component of extracellular matrices (ECM) that aid in cellular adhesion, growth, and migration, were quantitatively deciphered through autocorrelation.[21] Using STORM, the authors were able to measure the end-to-end length of individual N-terminal-labelled fibronectin molecules (Fn) to be ~133 nm. Labelling the C-terminus of Fn molecules and acquiring super-resolution images of fibronectin protofibrils revealed a labelling pattern, which was characterized in terms of its periodicity by the ACF to be ~95 nm (Figure 1.4c). This led to formulation of a molecular assembly model where Fn monomers are adjacently connected in an antiparallel fashion with ~38 nm overlap between N-termini. For bundled protofibrils, the intensity profiles yielded an irregular ACF, leading the authors to conclude that the self-assembly of fibronectin protofibrils was heterogeneous.

1.3.3 Molecular Assemblies and Growth Dynamics of Synthetic Polymers

Outside of the cell, correlative methods have also been used to probe the exchange pathways of synthetic one-dimensional aggregates. For example, fluorescently labeled 1,3,5-benzenetricarboxamide (BTA) that self-assemble into fibers were imaged using STORM.[22] Short-range decay of the ACF of intensity profiles and its comparison to ACF simulated profiles, which factor in the stochastic nature of STORM, showed that these fibrils were randomly labelled and did not possess sub-structural domains. To investigate the mechanism of interfibrillar exchange, pre-assembled fibrils labelled with either Cy5 or Cy3 were mixed and imaged following various incubation times. As time progressed, different coloured monomers were incorporated in each fibril and intensity profiles were obtained with two-colour STORM. The ACF of each colour channel along with the CCF of both channels revealed that the fibrils exchanged monomers homogenously and did not exhibit any end-to-end joining or the exchange of multimeric segments (Figure 1.5a). In another example, the self-assembly of synthetic, triblock protein nanofibrils that consist of a silk-structure sandwiched by two collagen domains has also been investigated by two-colour STORM with the aim of investigating how bifunctional fibrils can be made.[23] These synthetic proteins have the ability of forming a fibrillar hydrogel, which has applications in creating ECM-mimics for the growth and differentiation of cells within the context of regenerative medicine. Through time-series length measurements, the growth kinetics of these fibrils was shown to be linear and concentration-dependent, with higher monomer concentration yielding longer mean fibril lengths. In contrast to the BTA study, incubating different-colored fibrils or fibrils with different-colored monomers revealed that monomer exchange does not occur between fibrils and that growth was unidirectional (Figure 1.5b). Through the specificity of fluorescence and resolution offered by STORM, it was possible to study the structure, growth mechanisms and exchange pathways of these synthetic polymers.

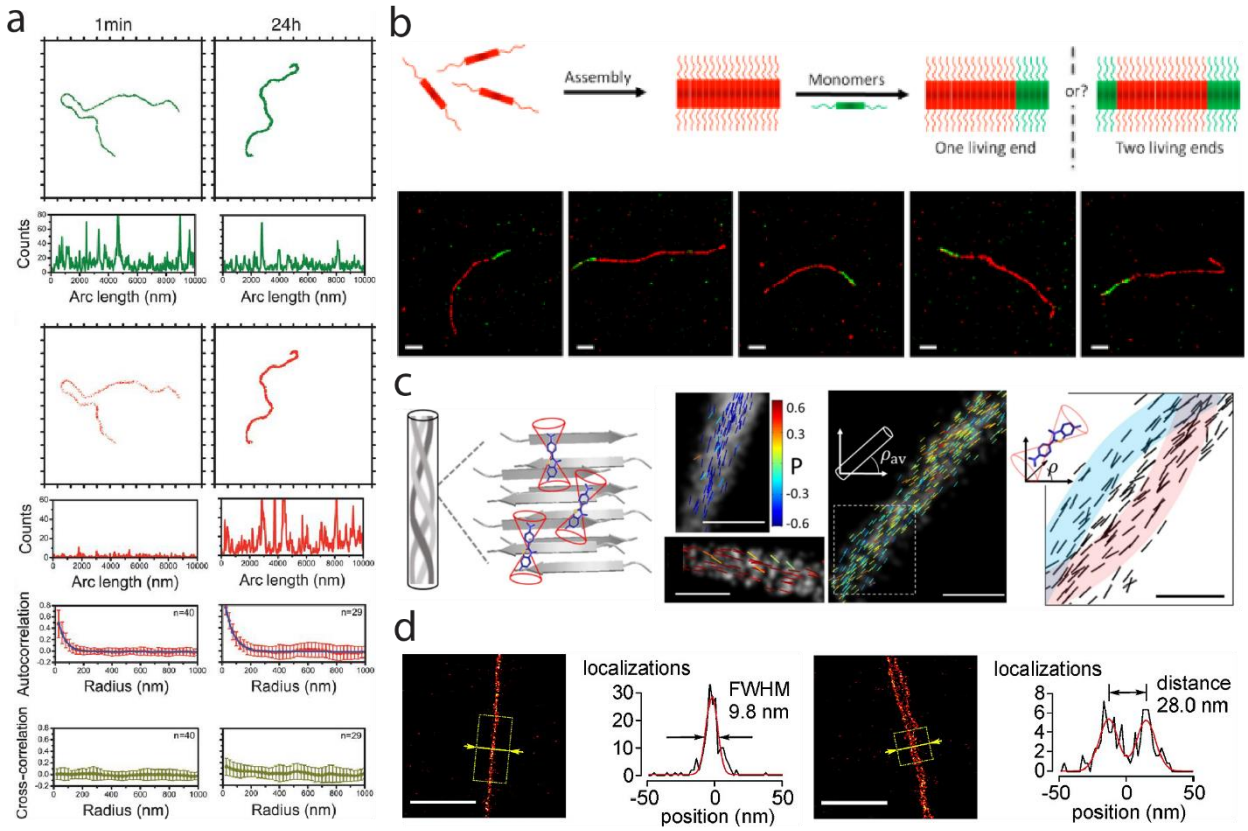

Figure 1.5. SRFM imaging of synthetic and natural fibrillar systems. a. The exchange of Cy5-labeled BTA monomers into Cy3-labeled BTA polymer fibrils was monitored at various time points using STORM, here only shown at 1 min and 24 h following mixing. The incorporation of Cy5-BTA into Cy5-BTA fibrils progressively increased overtime, in a homogenous fashion throughout the fibril as shown by the ACF and CCF functions of the two-colour channels. Adapted with permissions from ref [22]. **b.** Synthetic triblock protein polymer fibrils were initially self-assembled from Alexa647-labeled monomers then incubated with Alexa488-labeled monomers. STORM imaging showed that the growth of protein fibrils occurred unidirectionally from only one end. Adapted with permissions from ref [23]. **c.** Insulin amyloid ribbons labeled with Thioflavin T were imaged with polarization STORM, allowing the direction of individual protofilaments to be visualized due the restricted wobbling of the dye when bound to the protein β-sheets. Adapted from ref [24] with a Creative Commons CC BY license. **d.** BALM imaging of λ-phage DNA imaged with BALM using YOYO-1 intercalating dye achieved a maximal resolution below 10 nm with continuous mapping along DNA molecules. Adapted with permissions from ref [25].

1.3.4 Supramolecular Structure and Growth Kinetics of Amyloid Aggregates

The growth of fibrillar systems is highly relevant in the field of neurodegenerative diseases as they are often characterized by the formation of amyloid plaques within the brain. The aggregation and eventual fibrillar growth of disordered proteins, such as α-

synuclein, Tau and Aβ, and Huntingtin, have been shown to be the hallmark of Parkinson's, Alzheimer's and Huntington's diseases, respectively. Due to the diffraction-limited sizes of the highly-toxic protein oligomers, and the relatively short length of their fibrillar aggregates, these structures are usually visualized by EM, while their growth has been monitored by ensemble-averaged methods such as surface plasmon resonance, quartz crystal microbalance, and bulk fluorescence assays.[26–28] With the recent development of SRFM, these structures and their kinetic assembly can now be resolved and examined on a single-fibril basis with minimal perturbation from sample preparation. This allowed the evaluation of true population heterogeneity, which is an important aspect of amyloid fibrils as they exhibit polymorphic character with manifold growth processes.[29] Identification and characterization of subpopulations is important for the observation of intermediate states or anomalies that can act as a seed during the emergence of pathological behaviour.

To perform super-resolution imaging on amyloid structures, they were often covalently labelled with organic dyes at cysteine or lysine residues pre-assembly, or non-specifically labelled at their surface by binding dyes such as Nile Red or Thioflavin T. SRFM allowed the *in vitro* visualization of individual 90 nm Htt globular species and their time-dependent aggregation to form 100 nm wide fibrils with near 1 μm lengths that grew longer with increased incubation times.[29] Topographical studies by NSOM displayed high structural heterogeneity across β_2-microglobulin fibrils, an observation consistent with the polymorphic nature of amyloids.[30] Super-resolution imaging of amyloids has also been carried out *in vivo*, where intracellular uptake of both Aβ oligomers and fibrils was seen using STORM with structural lengths ranging from 0.3 to 2 μm.[31] Using STED, 3D images of tau aggregates, acquired from 50 μm brain sections, were able to resolve 70 – 80 nm wide puncta.[32]

Super-resolution imaging of amyloid fibrils has also been demonstrated with BALM using fluorescent probes that are activated upon their specific binding to the surface of amyloids. This can be advantageous due to reduced background signal from freely-diffusing labelled monomers, the elimination of possible interferences from labelled monomers, and the flexibility in avoiding the use of reducing buffers which may interfere with fibrillar growth. BALM imaging of α-synuclein fibrils was accomplished using the polyelectrolyte probe pentamer-formyl thiophene acetic acid and NIAD-4.[33,34] The latter study achieved impressive cross-sectional measurements of 14.3 nm, due to the high photon count of the fluorophore and the effective labeling density achieved by BALM. This enabled the observation of a 44 nm periodic labelling pattern, which was indicative of a twisted ribbon-like structure previously observed by AFM. In another study, the supramolecular

architecture of insulin amyloids was visualized through polarized STORM. This was achieved by exploiting the alignment of ThT with the axis of fibrils (Figure 1.5c).[24] Despite angular wobbling of the probe, the authors were able to visualize the helical intertwining of protofibrils and allowed a pitch measurement of 30 – 35 nm.

1.3.5 Super-Resolution imaging of Chromatin and DNA Fibrils

Investigations of ultrastructural organizations through SRFM has also been done on DNA fibrils both *in vivo* and *in vitro.* Typically, this involved DNA labelling with intercalating dyes YOYO-1, or the less cytotoxic and weaker-interacting YO-PRO and PicoGreen dyes. Super-resolution through STORM using these dyes has been demonstrated in a few *in vitro* studies that were able to achieve labelling densities every 15 nm with resolutions of ~30 nm. Using the same dyes, BALM achieved 1 nm labelling efficiencies and a remarkable resolution of 14 nm (Figure 1.5d).[24,35–36] These studies were expanded to *in vivo* environments, enabling the observation of nanoscale ischemic-induced changes in chromatin condensation within whole mouse and human nuclei.[37] Function-specific labeling allowed mapping the distribution of centromere-associated histone proteins, along with the visualization of 70 nm filament-like structures composed of 35 nm subfilaments, empty cavities and unstructured chromatin.[39]

1.4 Conclusion

In this review, we have seen how the development of SRFM has allowed scientists to study the supramolecular structure of various fibrillar systems, specifically in the cell cytoskeleton, synthetic fibrils, protein amyloids and DNA, contributing to our current understanding of the arrangement and function of the different components found within these structures. The ability to visualize multiple components in a specific and sensitive fashion at the nanoscale makes SRFM complementary to other high-resolution imaging techniques to study the complex molecular architecture of biological systems. With the development of new image analysis routines and the continued standardization of SRFM, this technique is expected to become more accessible and commonly employed by scientists in the fields of biological and materials science.

In the next chapter, I discuss the supramolecular structure of cellulose, an abundant fibrillar polymer that is naturally found in all plant cells. In the remainder of my thesis, I will demonstrate how the combination of SRFM and new fluorescence labeling tools can be used to study the structure and breakdown of bacterial cellulose fibrils at the nanoscale.

References

1. Gingerich, O. The Galileo Affair. *Scientific American* **247**, 132–143 (1982).

2. Lane, N. The unseen world: reflections on Leeuwenhoek (1677) 'Concerning little animals.' *Philosophical Transactions of the Royal Society B: Biological Sciences* **370**, 20140344 (2015).

3. Huang, B., Bates, M. & Zhuang, X. Super-Resolution Fluorescence Microscopy. *Annual Review of Biochemistry* **78**, 993–1016 (2009).

4. Betzig, E., Trautman, J. K., Harris, T. D., Weiner, J. S. & Kostelak, R. L. Breaking the Diffraction Barrier: Optical Microscopy on a Nanometric Scale. *Science* **251**, 1468–1470 (1991).

5. Gustafsson, M. G. L., Agard, D. A. & Sedat, J. W. I5M: 3D widefield light microscopy with better than 100 nm axial resolution. *Journal of Microscopy* **195**, 10–16 (1999).

6. Westphal, V. & Hell, S. W. Nanoscale resolution in the focal plane of an optical microscope. *Physical Review Letters* **94**, (2005).

7. Dyba, M. & Hell, S. W. Focal Spots of Size λ/23 Open Up Far-Field Florescence Microscopy at 33~nm Axial Resolution. *Physical Review Letters* **88**, 1639011–1639014 (2002).

8. Gustafsson, M. G. L. Nonlinear structured-illumination microscopy: Wide-field fluorescence imaging with theoretically unlimited resolution. *Proceedings of the National Academy of Sciences* **102**, 13081–13086 (2005).

9. van de Linde, S. *et al.* Direct stochastic optical reconstruction microscopy with standard fluorescent probes. *Nature protocols* **6**, 991–1009 (2011).

10. Huang, B., Wang, W., Bates, M. & Zhuang, X. Three-dimensional super-resolution imaging by stochastic optical reconstruction microscopy. *Science (New York, N.Y.)* **319**, 810–3 (2008).

11. Rust, M. J., Bates, M. & Zhuang, X. Sub-diffraction-limit imaging by stochastic optical reconstruction microscopy (STORM). *Nature Methods* **3**, 793–796 (2006).

12. Bates, M., Huang, B., Dempsey, G. T. & Zhuang, X. Multicolor super-resolution imaging with photo-switchable fluorescent probes. *Science* **317**, 1749–1753 (2007).

13. Schnitzbauer, J., Strauss, M. T., Schlichthaerle, T., Schueder, F. & Jungmann, R. Super-resolution microscopy with DNA-PAINT. *Nature Protocols* **12**, 1198–1228 (2017).

14. Hofmann, M., Eggeling, C., Jakobs, S. & Hell, S. W. Breaking the diffraction barrier in fluorescence microscopy at low light intensities by using reversibly photoswitchable proteins. *Proceedings of the National Academy of Sciences* **102**, 17565–17569 (2005).

15. Mikhaylova, M. *et al.* Resolving bundled microtubules using anti-tubulin nanobodies. *Nature Communications* **6**, (2015).

16. Lukinavičius, G. *et al.* Fluorogenic probes for live-cell imaging of the cytoskeleton. *Nature Methods* **11**, 731–733 (2014).

17. Xu, K., Babcock, H. P. & Zhuang, X. Dual-objective STORM reveals three-dimensional filament organization in the actin cytoskeleton. *Nature Methods* **9**, 185–188 (2012).

18. Izeddin, I. *et al.* Super-resolution dynamic imaging of dendritic spines using a low-affinity photoconvertible actin probe. *PLoS ONE* **6**, (2011).

19. Xu, K., Zhong, G. & Zhuang, X. Actin, spectrin, and associated proteins form a periodic cytoskeletal structure in axons. *Science* **339**, 452–456 (2013).

20. Barabas, F. M. *et al.* Automated quantification of protein periodic nanostructures in fluorescence nanoscopy images: Abundance and regularity of neuronal spectrin membrane-associated skeleton. *Scientific Reports* **7**, (2017).

21. Früh, S. M., Schoen, I., Ries, J. & Vogel, V. Molecular architecture of native fibronectin fibrils. *Nature Communications* **6**, (2015).

22. Albertazzi, L. *et al.* Probing exchange pathways in one-dimensional aggregates with super-resolution microscopy. *Science* **344**, 491–495 (2014).

23. Beun, L. H., Albertazzi, L., Van Der Zwaag, D., De Vries, R. & Cohen Stuart, M. A. Unidirectional Living Growth of Self-Assembled Protein Nanofibrils Revealed by Super-resolution Microscopy. *ACS Nano* **10**, 4973–4980 (2016).

24. Shaban, H. A., Valades-Cruz, C. A., Savatier, J. & Brasselet, S. Polarized super-resolution structural imaging inside amyloid fibrils using Thioflavine T. *Scientific Reports* **7**, (2017).

25. Schoen, I., Ries, J., Klotzsch, E., Ewers, H. & Vogel, V. Binding-activated localization microscopy of DNA Structures. *Nano Letters* **11**, 4008–4011 (2011).

26. Cannon, M. J., Williams, A. D., Wetzel, R. & Myszka, D. G. Kinetic analysis of beta-amyloid fibril elongation. *Analytical Biochemistry* **328**, 67–75 (2004).

27. White, D. A., Buell, A. K., Knowles, T. P. J., Welland, M. E. & Dobson, C. M. Protein aggregation in crowded environments. *Journal of the American Chemical Society* **132**, 5170–5175 (2010).

28. Cohen, S. I. A., Vendruscolo, M., Dobson, C. M. & Knowles, T. P. J. From macroscopic measurements to microscopic mechanisms of protein aggregation. *Journal of Molecular Biology* vol. 421 160–171 (2012).

29. Duim, W. C., Jiang, Y., Shen, K., Frydman, J. & Moerner, W. E. Super-resolution fluorescence of huntingtin reveals growth of globular species into short fibers and coexistence of distinct aggregates. *ACS Chemical Biology* **9**, 2767–2778 (2014).

30. Dalal, V., Bhattacharya, M., Narang, D., Sharma, P. K. & Mukhopadhyay, S. Nanoscale Fluorescence Imaging of Single Amyloid Fibrils. *The Journal of Physical Chemistry Letters* **3**, 1783–1787 (2012).

31. Kaminski Schierle, G. S. *et al.* In situ measurements of the formation and morphology of intracellular β-amyloid fibrils by super-resolution fluorescence imaging. *Journal of the American Chemical Society* **133**, 12902–12905 (2011).

32. Benda, A., Aitken, H., Davies, D. S., Whan, R. & Goldsbury, C. STED imaging of tau filaments in Alzheimer's disease cortical grey matter. *Journal of Structural Biology* **195**, 345–352 (2016).

33. Ries, J. *et al.* Superresolution imaging of amyloid fibrils with binding-activated probes. *ACS Chemical Neuroscience* **4**, 1057–1061 (2013).

34. Huh, H., Lee, J., Kim, H. J., Hohng, S. & Kim, S. K. Morphological analysis of oligomeric vs. fibrillar forms of A-synuclein aggregates with super-resolution BALM imaging. *Chemical Physics Letters* **690**, 62–67 (2017).

35. Flors, C. Photoswitching of monomeric and dimeric DNA-intercalating cyanine dyes for super-resolution microscopy applications. *Photochemical & Photobiological Sciences* **9**, 643 (2010).

36. Flors, C. DNA and chromatin imaging with super-resolution fluorescence microscopy based on single-molecule localization. *Biopolymers* vol. 95 290–297 (2011).

37. Szczurek, A. *et al.* Imaging chromatin nanostructure with binding-activated localization microscopy based on DNA structure fluctuations. *Nucleic Acids Research* **45**, (2017).

38. Flors, C. & Earnshaw, W. C. Super-resolution fluorescence microscopy as a tool to study the nanoscale organization of chromosomes. *Current Opinion in Chemical Biology* vol. 15 839–844 (2011).

39. Liesche, J., Ziomkiewicz, I. & Schulz, A. Super-resolution imaging with Pontamine Fast Scarlet 4BS enables direct visualization of cellulose orientation and cell connection architecture in onion epidermis cells. *BMC Plant Biology* **13**, (2013).

Chapter 2

The supramolecular structure and biosynthesis of plant and bacterial cellulose

Cellulose is a linear polysaccharide that is naturally produced by all plants and can be found in other species like bacteria, fungi and algae.[1] Annually produced at a rate of over a 100 billion tonnes, this biopolymer acts as the largest carbon sink in our biosphere as plants continuously capture sunlight energy through photosynthesis to produce and store cellulose in their cell walls.[2] The compact assembly of cellulose chains into fibrils, bundles and higher order structures provides plants with the necessary strength and protection to survive.[3] While endowing wood with the mechanical strength that makes it an attractive building material, cellulose can be extracted and deconstructed into nanofibrils and nanocrystals for applications in nanomedicine, biodegradable composite materials, biosensing, among other areas.[4,5] At the same time, cellulose can be completely broken down into soluble sugars and fermented to produce biofuels, allowing us to exploit the sunlight captured by plants through photosynthesis as a renewable source of energy. However, the conversion of cellulose to these different products is currently inefficient to the tight structural organization of cellulose, which makes it recalcitrant to depolymerization.[6] In order to develop new methods for processing cellulose and understand its function and biosynthesis within plants and other organisms, it is important to study the supramolecular structure and breakdown of this ubiquitous renewable material (Figure 2.1).[7]

Figure 2.1. Cellulose materials and their application. Cellulose forms the bulk material of wood and can be extracted to make paper products or regenerated fibers for clothing and textiles. Mechanical, enzymatic, and chemical processing of wood pulp allows the production of cellulose nanomaterials, including cellulose nanofibrils and nanocrystals, which have applications in drug delivery methods, biodegradable composite and biosensors. Complete depolymerization of cellulose yields soluble sugars, which can be fermented to produce renewable biofuels. The performance of cellulose materials and the ability to transform them from one form to another is directly linked to the hierarchical organization of cellulose chains into microfibrils, bundles and higher-order networks.

2.1 Cellulose chemical and crystalline structure

At the molecular level, cellulose is composed of long strings of up to 20,000 anhydroglucose units that are linearly connected through β-1→4 glycosidic linkages (Figure 2.2).[4,8] The abundant hydroxyl groups present on cellulose form an intermolecular hydrogen-bonding network that assembles multiple glucan chains into sheets, which stack on top of one another through van der Waals forces to form a highly ordered crystalline structure.[9–11] The covalent and intermolecular bonds involved in the crystalline packing of cellulose endow it with its high mechanical strength and a Young's modulus (>100 GPa) that is comparable to that of steel and Kevlar.[12,13] Most organisms that synthesize crystalline cellulose produce cellulose I, where contrary to the more thermodynamically stable structure of cellulose II, glucan chains are oriented in a parallel fashion.[14] Cellulose I contains a mixture of two different allomorphs, the triclinic I_α form that is predominant in bacterial

cellulose, and monoclinic I_β form that constitutes a higher fraction in plant cellulose.[10,11,15] Organisms producing crystalline cellulose assemble 16-36 glucan chains to form a microfibril.[16–18] The dimensions of cellulose microfibrils and their assembly into higher-order structures differs across species, as the supramolecular structure of cellulose is directly linked to the spatial organization of the enzymes responsible for its biosynthesis.[17,19]

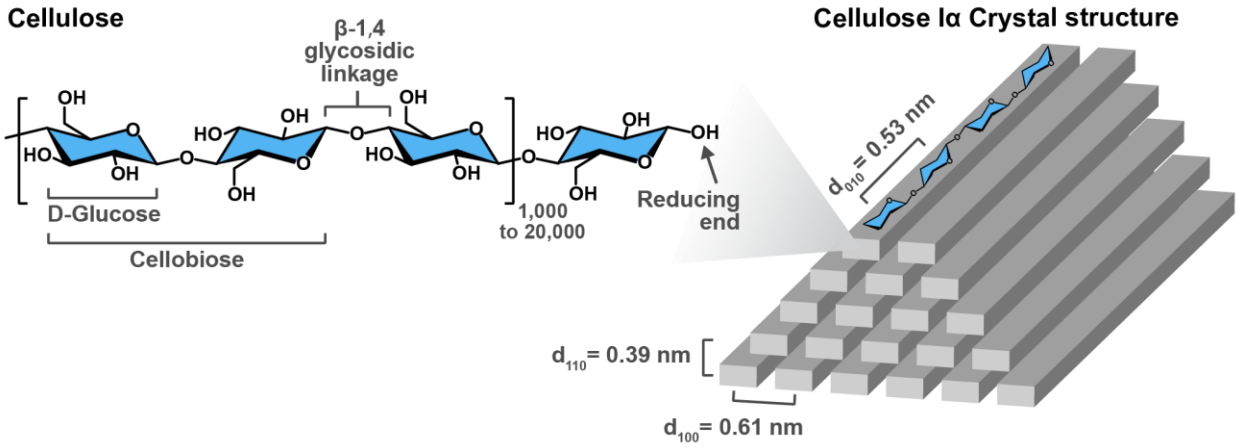

Figure 2.2. Chemical and crystalline structure of cellulose. Cellulose is a linear polymer of ahydroglucose molecules connected through β-1,4 glycosidic linkages, with degrees of polymerization of 1,000 to 20,000. The unreacted, free hemiacetal group present at the end of a cellulose chain is referred to as the reducing end. Multiple cellulose chains can assemble in an ordered fashion to make a crystalline structure. The d-spacings shown here are for the cellulose I_α allomorph.

2.2 Cell-directed hierarchical organization of cellulose

In plants, a rosette structure known as the cellulose synthase complex (CSC) synthesizes and extrudes cellulose microfibrils from the cell surface (Figure 2.3).[16] The CSC is composed of six rosette subunits, each containing three to four cellulose synthase proteins (CESA) that catalyze the synthesis of cellulose by using UDP-glucose to grow the nascent glucan chains. In this configuration, each CSC produces a 2 – 4 nm wide microfibril that contains 18 – 24 cellulose chains.[20] Unique to plant species, microfibrils are also surrounded by a sheath of lignin and hemicellulose, each composed of 5- or 6-carbon sugars and aromatic alcohols, respectively, that act as a glue to bundle multiple microfibrils into a bundle or macrofbril.[21,22] Macrofibrils further assemble into higher-order matrix that forms the scaffold of the plant cell wall.

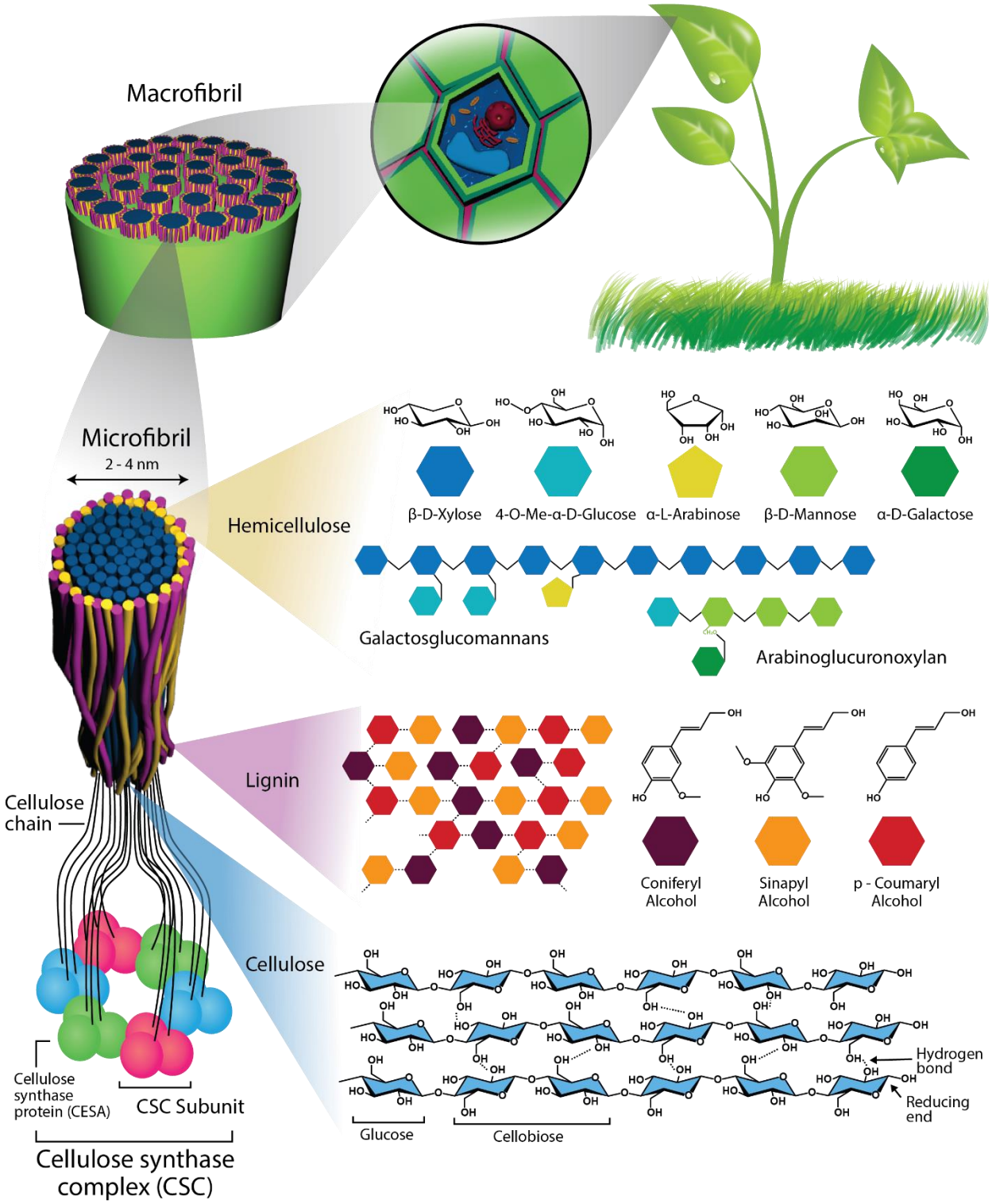

Figure 2.3. Supramolecular and chemical structure of plant hemicellulose. A cellulose synthase complex, composed of 6 CSC subunits that each contain 3 to 4 cellulose synthase proteins, is a rosette structure that synthesises 18 – 24 glucan chains to make a 2 – 4 nm wide microfibril. The microfibril

core consists of a crystalline arrangement of cellulose chains that are connected through a network of hydrogen bonds. The microfibril possesses a sheath of hemicellulose and xyloglucan that act to glue multiple microfibrils to form bundles and macrofibrils. Microfibrils assemble into higher-order structures that form the scaffold of the plant cell wall.

Some bacterial species, like the gram-negative *Komagataeibacter xylinus* (formerly known as *Gluconacetobacter xylinus* and *Acetobacter xylinus*)[23] produce large amounts of crystalline cellulose without a sheath of hemicellulose and lignin, making this organism a useful model for studying the native structure of cellulose and its biosynthesis.[24] *K. xylinus* and related organisms produce cellulose pellicles to form a biofilm, which offers protection and can be used as flotation device to help the bacterial cells capture oxygen.[25,26] Bacterial cellulose is synthesized by a complex of at least four protein subunits, traditionally known as a terminal complex (TC), that spans the inner and outer membranes of the bacterial envelope (Figure 2.4).[27] Residing in in the inner membrane, AcsA catalyzes the synthesis of cellulose while being bound to the accessory periplasmic protein AcsB.[28] This duo, sometimes referred to as AcsAB, has been shown by X-ray crystallography to organize into groups of four, such that four glucan chains pass through the helical passageways of AcsD[29] within the periplasm and are then extruded through a pore on the outer membrane formed by AcsC.[27] However, unlike plants, the arrangement of cellulose synthase enzymes into a higher order configuration like a rosette is yet to be observed in bacteria, which is why the dimensions of bacterial cellulose microfibrils remain elusive. At larger scales, freeze-fracture experiments have shown that TCs are organized linearly across the bacterium surface, causing cellulose microfibrils to laterally assemble and form ~10 nm wide bundles and ~50 nm wide ribbons.[30,31]

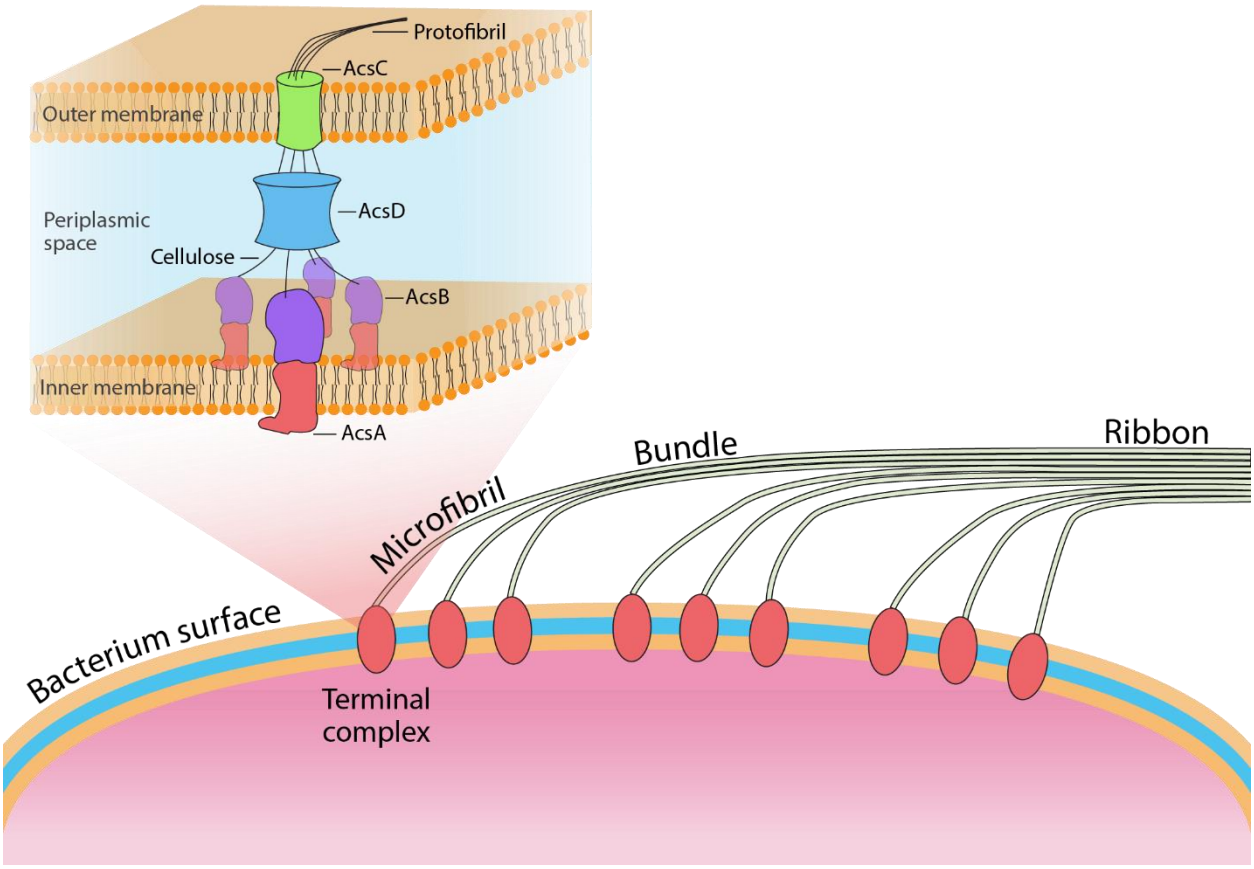

Figure 2.4. Biosynthesis and hierarchical structure of bacterial cellulose. Gram-negative bacteria, such as *K. xylinum*, synthesize crystalline cellulose from their surface through a linear series of terminal complex (TC) enzymes that resides within the inner and outer membranes of the bacterial envelope. TCs consist of four catalytic proteins, AcsAB, which synthesize four glucan chains that pass through AcsD in the periplasm before being extruded through a pore formed by AcsC. Cellulose protofibrils combine to make a microfibril, which aggregates linearly with other microfibrils to form bundles and ribbons.

Cellulose fibrils derived from various sources, including plants and bacteria, have been shown to twist at different structural hierarchy levels within microfibrils, bundles and ribbons. Twisting of cellulose fibrils has been largely studied using molecular dynamics (MD) simulations, which have consistently predicted that microfibrils adopt a persistent right-handed twist as the most thermodynamically stable state. The rate of twisting is independent of fibril length but decreases with higher cross-sectional widths, varying from 5 to 1.5 degrees/nm for a 3×3 to 6×6 chain configuration of the microfibril.[32–34] The molecular origin of cellulose twisting and the role of hydrogen-bonding, van der Waals forces and water solvation remains debatable. Some MD studies have suggested that the inherent chirality of cellulose molecules is the source of fibril twisting, which is then driven by hydrogen bonding

with the most notable contribution stemming from an intra-chain hydrogen bond that forms across glycosidic linkages.[34–36] However, other MD studies have reported that hydrogen bonding does not drive twisting, but acts in conjunction with solvent effects to counteract the twisting induced by van der Waals forces.[33,37]

While the source of twisting within cellulose microfibrils is yet to be fully understood, numerous MD studies have shown that twisting induces strain as surface chains must transverse longer distance than those at the core of the microfibril.[32,36] This strain can be alleviated by the regular presence of disordered regions, where misalignment of glucan chains from its ordered crystalline structure would compensate for the shear and compression forces that are produced through twisting.[32,38]

2.3 The Fringed-Micellar Model of Cellulose

The regular presence of disordered regions along cellulose microfibrils has been postulated for the past seven decades and is often used to explain the production of cellulose nanocrystals (CNCs) (Figure 2.5a).[4,39] During the acid hydrolysis of cellulose, microfibrils are quickly cleaved to produce needle-like, 100 – 300 nm long CNCs,[40] that become progressively shorter as they are hydrolyzed for longer periods of time.[41] Interestingly, after an extended period of hydrolysis, the degree of polymerization of CNCs levels-off (LODP) (Figure 2.5b).[41,42] This non-linear depolymerization suggested that the crystalline structure of the cellulose microfibril is interspersed with periodic disordered regions that are significantly more susceptible to hydrolysis.[41] Disordered areas of cellulose are expected to be less compact than their crystalline counterparts and in turn more susceptible to degradation as they are more easily accessible by small molecules. This alternating crystalline and disordered supramolecular structure of cellulose microfibrils was classically referred to as the “fringed micellar model”, where highly crystalline cellulose micelles are connected through more loose, fringed cellulose material.[8,43]

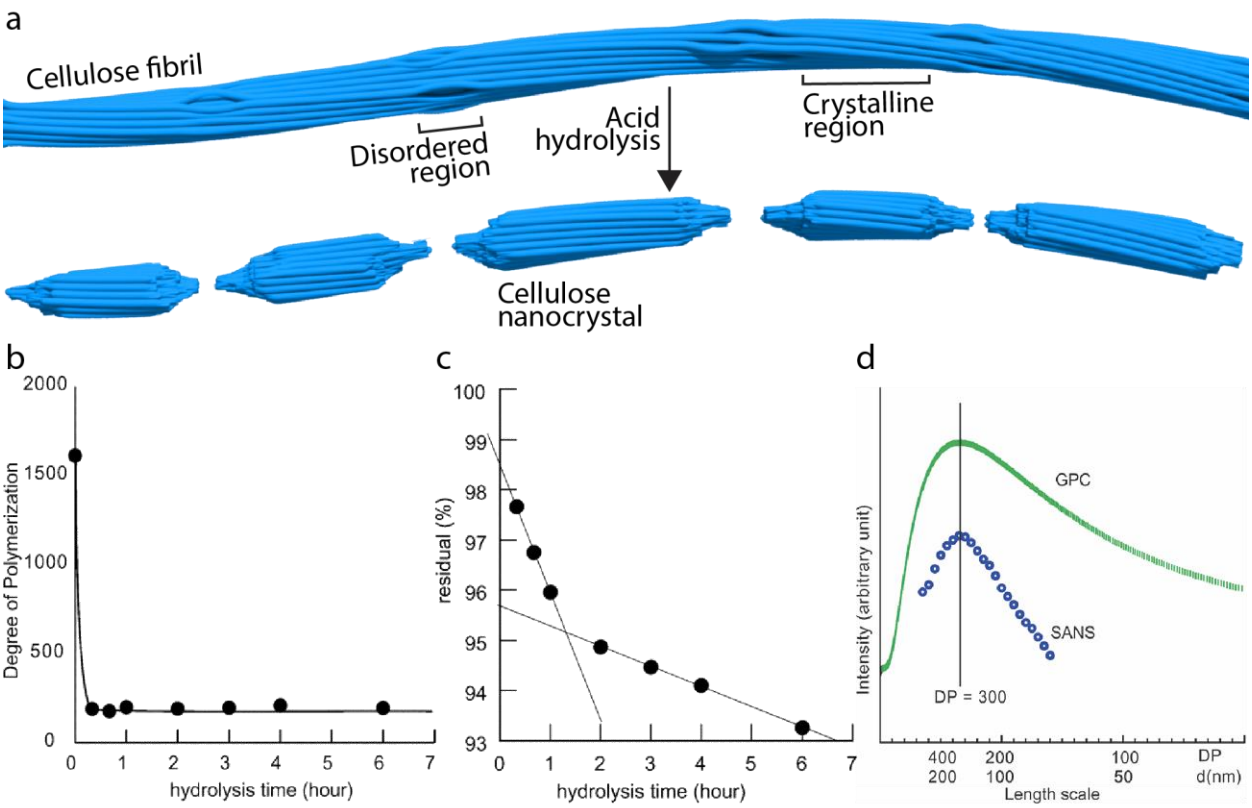

Figure 2.5. The fringed micellar model and non-linear hydrolysis of cellulose. a. Cellulose fibrils are thought to adopt a fringed-micellar superamolecular structure along their length, with alternating crystalline and disordered regions that exhibit different susceptibility to acid hydrolysis. The disordered regions are quickly cleaved to produce 100 – 300 nm long cellulose nanocrystals. **b.** The non-linear hydrolysis of cellulose is characterized by a level-off degree of polymerization, which occurs within the first few minutes of hydrolysis when ramie fibrils are reacted with 4 M hydrochloric acid at 80 °C. **c.** The time-course weight loss of cellulose during acid hydrolysis exhibited at least three phases. The first phase, not captured by the experiment here, resulted in weight a loss of ~1.5% during the first few minutes of hydrolysis. **d.** Good agreement between the gel permeation chromatograph of hydrolysed ramie fibers and the periodicity of disordered regions measured through SANS supported the fringed micellar model of cellulose fibrils. Panels b-d were adapted with permission from ref [49].

The disordered regions of the cellulose microfibril were initially regarded as "amorphous", due to powder X-ray diffraction (XRD) measurements that showed cellulose materials are never 100% crystalline.[44] Percent crystallinity (%Cr) can range between 50% to 90%, depending on the source and purity of the extracted cellulose material, and strongly varies between the different analysis methods used to interpret the X-ray diffractogram.[44] Moreover, %Cr measured using nuclear magnetic resonance (NMR) often yields significantly

lower values for the same materials analyzed with XRD. Since NMR %Cr measurements are based on the intermolecular interactions between cellulose chains, those on the surface of the microfibril that are interacting with water molecules are perceived as more disordered relative to those in the core of the microfibril.[45–47] Meanwhile, the contribution of amorphous material from impurities, such as hemicellulose and lignin which can constitute up to 40% of the starting plant raw material, to amorphous cellulose that is generated during extraction versus disordered regions present within cellulose particles are difficult to distinguish by bulk %Cr measurements.[48] These inconsistencies, combined with the limited spatial information offered by these techniques on the microfibril scale, have made the prevalence, size and distribution of disordered cellulose within the microfibril and its contribution to the overall crystallinity of cellulose unclear.

The distribution of disordered cellulose into local regions along the cellulose microfibril, as postulated by the fringed micellar model, is supported by only a few studies that directly characterize the supramolecular organization of cellulose microfibrils. This structure was detected for the first time by Nishiyama and colleagues, who used small-angle neutron scattering (SANS) to sense the presence of disordered regions as they exhibited enhanced accessibility to deuterated water compared to crystalline regions of ramie cellulose microfibrils.[49] The disordered regions possessed a periodicity of 150 nm, which corresponded well to the LODP of acid hydrolyzed fibers and strongly suggested the presence of alternating crystalline and disordered regions within the microfibril (Figure 2.5d). Since the weight loss at LODP was ~1.5%, the authors suggested that the disordered regions are comprised of 4 – 5 misaligned glucose residues (Figure 2.5c). Due to the expected small size of the dislocations, these regions of cellulose have more recently been referred to as “disordered” instead of “amorphous”. However, the origin of these dislocations and whether they occur naturally has been debatable, as kinks and nanoscale defects that show enhanced susceptibility to hydrolysis can be induced through mechanical stresses.[50,51] On the other hand, additional studies employing SANS, solid-state NMR, Fourier transform infrared spectroscopy and atomic force microscopy did not observe the presence of alternating disordered and crystalline regions, but instead suggested that the disordered fraction of cellulose lie on the surface of the microfibril.[52–54] Due to little direct evidence, the natural organization of native cellulose microfibrils in a fringed-micellar structure has been debated over the past two decades.[18,52,54]

2.4 Conclusion & Research Objectives

While the fringed-micellar model is supported by a limited number of studies, it is commonly used by the cellulose community to explain the production of CNCs.[4,55,56] However, the presence of alternating disordered and crystalline regions, and their size, morphology, origin and how they drive cellulose hydrolysis remain to be fully understood as they have never been directly visualized. To address these questions, the work presented in the remainder of my thesis will apply super-resolution fluorescence microscopy (SRFM) and combine it with other advanced imaging techniques to visualize the fringed-micellar structure and its associated nanoscale defects directly along individual cellulose fibrils. In order to employ super-resolution imaging, Chapter 3 introduces a versatile method of labeling cellulose with commercially available dyes and to high degrees of labeling that are optimal for SRFM. In Chapter 4, I leverage the resolution of SRFM to directly visualize regions of enhanced fluorescent labeling densities that are persistent along individual cellulose fibrils. The measured spacing lengths between these regions are compared to the length of CNCs produced during different hydrolysis times to support the fringed-micellar model of cellulose and propose a hydrolysis mechanism. In Chapter 5, the specificity of SRFM is combined with the high resolution of transmission electron microscopy in a correlative workflow to understand the structural origin of nanoscale dislocations that exist in bacterial cellulose fibrils. Understanding the supramolecular organization of cellulose and the role of nanoscale defects on cellulose hydrolysis is crucial for understanding cellulose biosynthesis, and for developing new and efficient methods of harnessing the energy stored within this renewable and abundant biomaterial.

References

1. Klemm, D., Heublein, B., Fink, H. P. & Bohn, A. Cellulose: Fascinating biopolymer and sustainable raw material. *Angewandte Chemie - International Edition* vol. 44 3358–3393 (2005).

2. Bar-On, Y. M., Phillips, R. & Milo, R. The biomass distribution on Earth. *Proceedings of the National Academy of Sciences* **115**, 6506–6511 (2018).

3. Paajanen, A., Ceccherini, S., Maloney, T. & Ketoja, J. A. Chirality and bound water in the hierarchical cellulose structure. *Cellulose 2019 26:10* **26**, 5877–5892 (2019).

4. Habibi, Y., Lucia, L. A. & Rojas, O. J. Cellulose nanocrystals: Chemistry, self-assembly, and applications. *Chemical Reviews* **110**, 3479–3500 (2010).

5. Habibi, Y. Key advances in the chemical modification of nanocelluloses. *Chemical Society reviews* **43**, 1519–42 (2014).

6. Himmel, M. E. *et al.* Biomass recalcitrance: Engineering plants and enzymes for biofuels production. *Science* **315**, 804–807 (2007).

7. Moran-Mirabal, J. M. The study of cell wall structure and cellulose-cellulase interactions through fluorescence microscopy. *Cellulose* **20**, 2291–2309 (2013).

8. Hon, D. N. S. Cellulose: a random walk along its historical path. *Cellulose* **1**, 1–25 (1994).

9. Björn Lindman *et al.* The relevance of structural features of cellulose and its interactions to dissolution, regeneration, gelation and plasticization phenomena. *Physical Chemistry Chemical Physics* **19**, 23704–23718 (2017).

10. Nishiyama, Y., Langan, P. & Chanzy, H. Crystal structure and hydrogen-bonding system in cellulose Iβ from synchrotron X-ray and neutron fiber diffraction. *Journal of the American Chemical Society* **124**, 9074–9082 (2002).

11. Nishiyama, Y., Sugiyama, J., Chanzy, H. & Langan, P. Crystal structure and hydrogen bonding system in cellulose Iα from synchrotron x-ray and neutron fiber diffraction. *Journal of the American Chemical Society* **125**, 14300–14306 (2003).

12. Gill, U. *et al.* Beyond buckling: Humidity-independent measurement of the mechanical properties of green nanobiocomposite films. *Nanoscale* **9**, 7781–7790 (2017).

13. Altaner, C. M., Thomas, L. H., Fernandes, A. N. & Jarvis, M. C. How cellulose stretches: Synergism between covalent and hydrogen bonding. *Biomacromolecules* **15**, 791–798 (2014).

14. O'Sullivan, A. C. Cellulose: the structure slowly unravels. *Cellulose 1997 4:3* **4**, 173–207 (1997).

15. Lehtiö, J. *et al.* The binding specificity and affinity determinants of family 1 and family 3 cellulose binding modules. *Proc. Natl. Acad. Sci. {U.S.A.}* **100**, 484–489 (2003).

16. Turner, S. & Kumar, M. Cellulose synthase complex organization and cellulose microfibril structure. *Philosophical Transactions of the Royal Society A: Mathematical, Physical and Engineering Sciences* **376**, 9–16 (2018).

17. Richard Malcolm Brown. The Biosynthesis of Cellulose. *http://dx.doi.org/10.1080/10601329608014912* **33**, 1345–1373 (2006).

18. Nishiyama, Y. Structure and properties of the cellulose microfibril. *Journal of Wood Science 2009 55:4* **55**, 241–249 (2009).

19. Haigler, C. H. & Benziman, M. Biogenesis of Cellulose I Microfibrils Occurs by Cell-Directed Self-Assembly in Acetobacter xylinum. in *Cellulose and Other Natural Polymer Systems* 273–297 (Springer, Boston, MA, 1982). doi:10.1007/978-1-4684-1116-4_14.

20. Song, B., Zhao, S., Shen, W., Collings, C. & Ding, S.-Y. Direct Measurement of Plant Cellulose Microfibril and Bundles in Native Cell Walls. *Frontiers in Plant Science* **0**, 479 (2020).

21. Gibson, L. J. The hierarchical structure and mechanics of plant materials. *Journal of The Royal Society Interface* **9**, 2749–2766 (2012).

22. Rose, M., Babi, M. & Moran-Mirabal, J. The study of cellulose structure and depolymerization through single-molecule Methods. *Industrial Biotechnology* **11**, 16–23 (2015).

23. Singhsa, P., Narain, R. & Manuspiya, H. Physical structure variations of bacterial cellulose produced by different Komagataeibacter xylinus strains and carbon sources in static and agitated conditions. *Cellulose 2018 25:3* **25**, 1571–1581 (2018).

24. Nobles, D. R. & Brown, R. M. Transgenic expression of Gluconacetobacter xylinus strain ATCC 53582 cellulose synthase genes in the cyanobacterium Synechococcus leopoliensis strain UTCC 100. *Cellulose 2008 15:5* **15**, 691–701 (2008).

25. Cook, K. E. & Colvin, J. R. Evidence for a beneficial influence of cellulose production on growth of Acetobacter xylinum in liquid medium. *Current Microbiology: An International Journal* **3**, 203–205 (1980).

26. Augimeri, R. v., Varley, A. J. & Strap, J. L. Establishing a role for bacterial cellulose in environmental interactions: Lessons learned from diverse biofilm-producing Proteobacteria. *Frontiers in Microbiology* **6**, 1282 (2015).

27. Du, J., Vepachedu, V., Cho, S. H., Kumar, M. & Nixon, B. T. Structure of the cellulose synthase complex of Gluconacetobacter hansenii at 23.4 Å resolution. *PLoS ONE* **11**, (2016).

28. Mehta, K., Pfeffer, S. & Brown, R. M. Characterization of an acsD disruption mutant provides additional evidence for the hierarchical cell-directed self-assembly of cellulose in Gluconacetobacter xylinus. *Cellulose 2014 22:1* **22**, 119–137 (2014).

29. Hu, S.-Q. *et al.* Structure of bacterial cellulose synthase subunit D octamer with four inner passageways. *Proceedings of the National Academy of Sciences* **107**, 17957–17961 (2010).

30. Kimura, S., Chen, H. P., Saxena, I. M., Brown, J. & Itoh, T. Localization of c-di-GMP-binding protein with the linear terminal complexes of Acetobacter xylinum. *Journal of Bacteriology* **183**, 5668–5674 (2001).

31. Brown, R. M., Willison, J. H. & Richardson, C. L. Cellulose biosynthesis in Acetobacter xylinum: visualization of the site of synthesis and direct measurement of the in vivo process. *Proceedings of the National Academy of Sciences* **73**, 4565–4569 (1976).

32. Zhao, Z. *et al.* Cellulose Microfibril Twist, Mechanics, and Implication for Cellulose Biosynthesis. *Journal of Physical Chemistry A* **117**, 2580–2589 (2013).

33. Hadden, J. A., French, A. D. & Woods, R. J. Unraveling cellulose microfibrils: A twisted tale. *Biopolymers* **99**, 746–756 (2013).

34. L, B., ME, H. & MF, C. The molecular origins of twist in cellulose I-beta. *Carbohydrate polymers* **125**, 146–152 (2015).

35. Paavilainen, S., Róg, T. & Vattulainen, I. Analysis of Twisting of Cellulose Nanofibrils in Atomistic Molecular Dynamics Simulations. *Journal of Physical Chemistry B* **115**, 3747–3755 (2011).

36. Conley, K., Godbout, L., Whitehead, M. A. & van de Ven, T. G. M. Origin of the twist of cellulosic materials. *Carbohydrate Polymers* **135**, 285–299 (2016).

37. Kannam, S. K. *et al.* Hydrogen bonds and twist in cellulose microfibrils. *Carbohydrate Polymers* **175**, 433–439 (2017).

38. Matthews, J. F. *et al.* Computer simulation studies of microcrystalline cellulose Iβ. *Carbohydrate Research* **341**, 138–152 (2006).

39. Nickerson, R. F. & Habrle, J. A. Cellulose Intercrystalline Structure. *Industrial & Engineering Chemistry* **39**, 1507–1512 (1947).

40. Reid, M. S., Villalobos, M. & Cranston, E. D. Benchmarking Cellulose Nanocrystals: From the Laboratory to Industrial Production. *Langmuir* **33**, 1583–1598 (2016).

41. Battista, O. A. Hydrolysis and Crystallization of Cellulose. *Industrial & Engineering Chemistry* **42**, 502–507 (1950).

42. Battista, A., Coppicic, S., Howsmon, J. A., Morehead, F. F. & Sisson, W. A. Level-off Degree of Polymerization: Relation to Polyphase Structure of Cellulose Fibrils. *Industrial & Engineering Chemistry* **48**, 333–335 (1956).

43. Scallan, A. M. A Quantitative Picture of the Fringed Micellar Model of Cellulose. *Textile Research Journal* **41**, 647–653 (1971).

44. Park, S., Baker, J. O., Himmel, M. E., Parilla, P. a & Johnson, D. K. Cellulose crystallinity index: measurement techniques and their impact on interpreting cellulase performance. *Biotechnology for biofuels* **3**, 10 (2010).

45. Newman, R. H. Estimation of the lateral dimensions of cellulose crystallites using 13C NMR signal strengths. *Solid State Nuclear Magnetic Resonance* **15**, 21–29 (1999).

46. Šturcova, A., His, I., Apperley, D. C., Sugiyama, J. & Jarvis, M. C. Structural Details of Crystalline Cellulose from Higher Plants. *Biomacromolecules* **5**, 1333–1339 (2004).

47. Wickholm, K., Larsson, P. T. & Iversen, T. Assignment of non-crystalline forms in cellulose I by CP/MAS 13C NMR spectroscopy. *Carbohydrate Research* **312**, 123–129 (1998).

48. Bychkov, A., Podgorbunskikh, E., Bychkova, E. & Lomovsky, O. Current achievements in the mechanically pretreated conversion of plant biomass. *Biotechnology and Bioengineering* **116**, 1231–1244 (2019).

49. Nishiyama, Y. *et al.* Periodic disorder along ramie cellulose microfibrils. *Biomacromolecules* **4**, 1013–1017 (2003).

50. Ciesielski, P. N. *et al.* Nanomechanics of cellulose deformation reveal molecular defects that facilitate natural deconstruction. *Proceedings of the National Academy of Sciences of the United States of America* **116**, 9825–9830 (2019).

51. Rowland, S. P. & Roberts, E. J. The nature of accessible surfaces in the microstructure of cotton cellulose. *Journal of Polymer Science Part A-1: Polymer Chemistry* **10**, 2447–2461 (1972).

52. Fernandes, A. N. *et al.* Nanostructure of cellulose microfibrils in spruce wood. *Proceedings of the National Academy of Sciences of the United States of America* **108**, 1195–1203 (2011).

53. Martinez-Sanz, M., Gidley, M. J. & Gilbert, E. P. Hierarchical architecture of bacterial cellulose and composite plant cell wall polysaccharide hydrogels using small angle neutron scattering. *Soft Matter* **12**, 1534–1549 (2016).

54. Usov, I. *et al.* Understanding nanocellulose chirality and structure–properties relationship at the single fibril level. *Nature Communications 2015 6:1* **6**, 1–11 (2015).

55. Mariano, M., el Kissi, N. & Dufresne, A. Cellulose nanocrystals and related nanocomposites: Review of some properties and challenges. *Journal of Polymer Science Part B: Polymer Physics* **52**, 791–806 (2014).

56. Salas, C., Nypelö, T., Rodriguez-Abreu, C., Carrillo, C. & Rojas, O. J. Nanocellulose properties and applications in colloids and interfaces. *Current Opinion in Colloid & Interface Science* **19**, 383–396 (2014).

Chapter 3

Efficient labelling of cellulose microfibrils and cellulose nanocrystals for high-resolution fluorescence microscopy applications

Mouhanad Babi,[1] Ayodele Fatona,[1] Xiang Li,[1] Christine Cerson,[1] Victoria M. Jarvis,[2] Tiffany Abitbol[3] and Jose M. Moran-Mirabal[1,4]*

[1] *Department of Chemistry and Chemical Biology, McMaster University, Hamilton, ON, Canada*

[2] *McMaster Analytical X-ray Diffraction Facility, McMaster University, Hamilton, ON, Canada*

[3] *RISE Research Institutes of Sweden, Stockholm, Sweden*

[4] *Centre for Advanced Light Microscopy, McMaster University, Hamilton, ON, Canada*

*Please address all correspondence to Jose Moran-Mirabal (mirabj@mcmaster.ca)

Abstract

The visualization of naturally derived cellulose nanofibrils (CNFs) and nanocrystals (CNCs) within nanocomposite materials is key to the development of packaging materials, tissue culture scaffolds, and emulsifying agents, among other applications. Here, we develop a versatile two-step approach, based on triazine chemistry, to fluorescently label nanocelluloses with a variety of commercially available dyes. We show that this method can be used to label bacterial cellulose microfibrils, plant-derived CNFs, carboxymethylated CNFs, and CNCs with Cy5 and fluorescein derivatives to high degrees of labelling using minimal amounts of dye, while preserving their native morphology and crystalline structure. The ability to tune the labelling density with this method allowed us to prepare optimized samples that were used to visualize nanostructural features of cellulose through super-resolution microscopy. The simplicity, cost-effectiveness and versatility of this method makes it ideal for labelling nanocelluloses and imaging them through advanced microscopy techniques for a broad range of applications.

3.1 Introduction

Cellulose, the main component of the plant cell wall, is the most abundant structural biopolymer on Earth and at the heart of traditional construction, textile, and paper industries.[1] Crystalline cellulose nanomaterials derived from plant biomass (*e.g.,* cellulose nanofibrils – CNFs and cellulose nanocrystals –CNCs) present high tensile strength, thermal stability, and surface area. This makes nanocelluloses excellent fillers and reinforcers for new composites, and attractive substrates for the fabrication of filtration membranes, batteries, and sensing devices.[2] Given the unique properties of sustainable nanocelluloses, they are being used in applications for nanomedicine, tissue engineering, biosensing, biodegradable plastics, energy storage, and water remediation.[3–5]

The use of nanocelluloses for practical applications often requires visualizing their distribution and interactions within complex matrices. This can be achieved with fluorescence microscopy techniques if the nanocelluloses are fluorescent, as the sensitivity and specificity of these methods permits visualizing nanoparticles and nanofibers within complex 3D systems. Previous work has shown that the uptake of fluorescent CNCs by macrophage and embryonic cells can be monitored, and their biodistribution within tissues visualized when they are used as drug delivery vehicles.[6–10] The distribution of CNCs and their interactions with components in new biocomposite materials, such as structured CNC-polymer hydrogels and CNC-protein-polymer matrices, has also been reported through confocal microscopy.[11,12] Fluorescent cellulose has also been used to further study the

impact of pre-treatments on the structure, accessibility and enzymatic depolymerization of cellulose with unprecedented resolution, contributing to the development of efficient biomass conversion strategies.[13–17] Yet, advanced imaging methods like super-resolution or light-sheet microscopy are rarely applied to cellulose studies. This is partly due to a lack of simple and cost-effective methods to fluorescently tag nanocelluloses without altering their unique properties.

The challenge of labelling cellulose in its native form arises from its relative chemical inertness and insolubility. Cellulose is made of linear $\beta - 1 \rightarrow 4$ anhydroglucose polymer (glucan) chains that through an elaborate hydrogen-bonding network assemble into tightly packed crystalline fibrils that are insoluble under aqueous conditions.[14] Reported fluorescence labelling methods often derivatize the mildly reactive hydroxyl groups on the cellulose surface with amine, maleimide or N-hydroxysuccinimide groups that are reactive with complementary moieties on commercially available dyes, and carry out the labelling as a heterogenous reaction.[8,18–21] Because such methods involve multiple reaction steps and use organic solvent exchanges that can lead to the aggregation of nanocelluloses, hydrazine- and triazinyl-substituted fluorophores have been used to develop aqueous one-step labelling schemes.[22,23] The most popular dye in these reactions is dichlorotriazinyl aminofluorescein (DTAF), a commercially available fluorophore that has been used to label bacterial cellulose (BC), CNFs and CNCs.[13,24,25] However, the large excess of DTAF needed to achieve high labelling densities (due to competing hydrolysis reactions in aqueous media) and the dye's low photostability are inherent limitations that preclude its use with high-resolution fluorescence microscopy.

In this work, we introduce a versatile, highly efficient, and broadly applicable methods for cellulose labelling to enable high resolution fluorescence imaging applications (Figure 3.1). First, we synthesize a new triazine-based dye, dichlorotriaznyl piperazine rhodamine (DTPR), that allows the one-step labelling of cellulose with a high-performance fluorophore. Second, we introduce a versatile method for labelling nanocelluloses using a two-step triazine- and click-chemistry reaction, which avoids complex syntheses and lowers the cost of labelling. In particular, the second step involves an efficient click-reaction that can be performed with any commercially available dye bearing an azide functionality, greatly expanding the range of fluorophores available for cellulose research. We demonstrate the power of this approach by labelling nanocelluloses with two commonly used dyes (fluorescein and Cy5) and show that high degrees of labelling are possible using low dye loads, without compromising the native morphological and crystalline properties of the

nanocellulose. This method is applied to BC to study the impact of fluorophore density on the quality of super-resolution images and the ability to visualize nanostructural features.

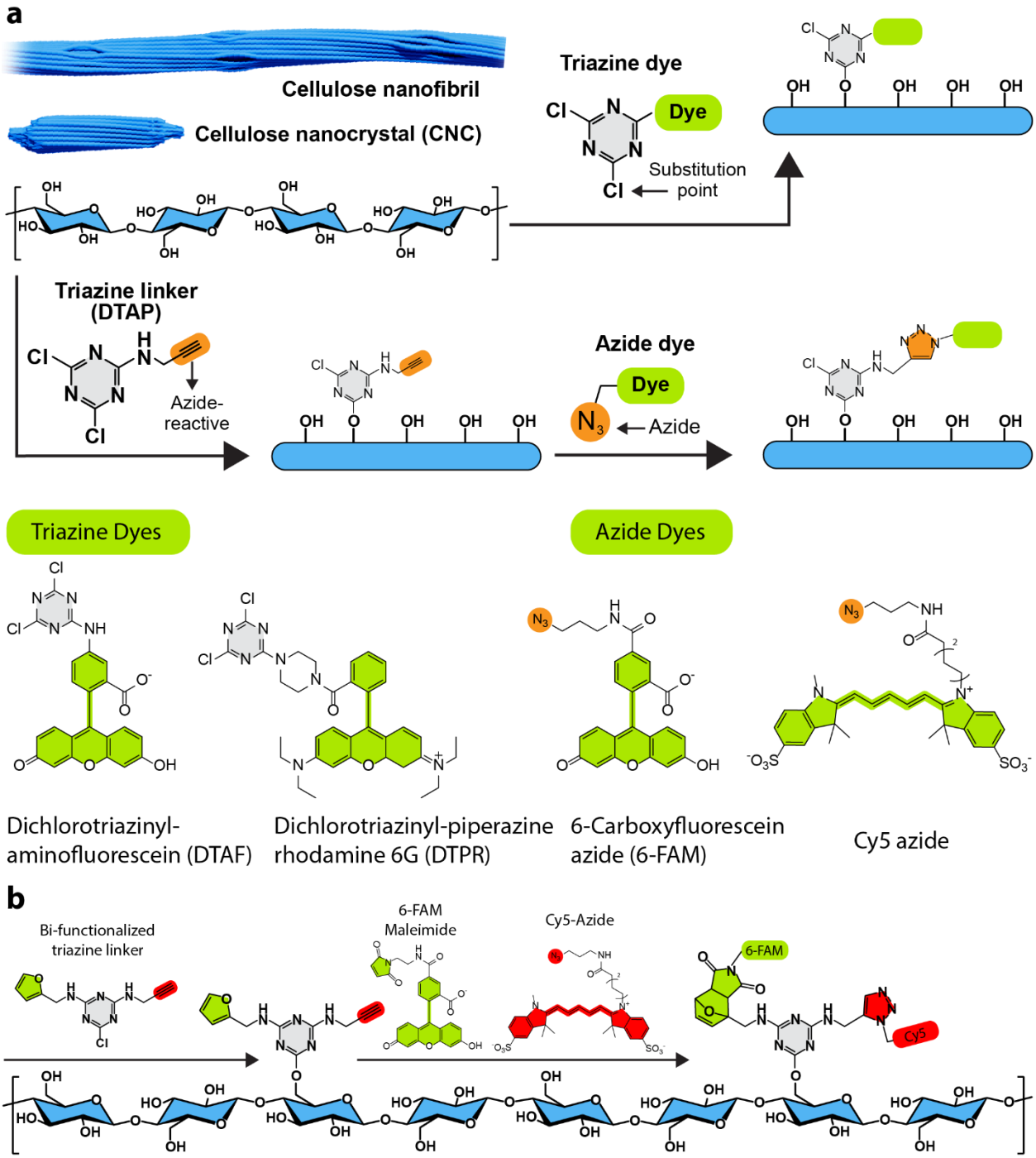

Figure 3.1. Fluorescence labelling of cellulose using a one- or two-step procedure based on triazine- and click-chemistry. a) Nanocellulose can be fluorescently labelled in a one-step reaction using triazine-based dyes, such as DTAF or the rhodamine-derivative DTPR, that directly graft onto

the surface hydroxyl groups of cellulose. An alternative two-step approach involves grafting onto cellulose a dichlorotriaznyl propargylamine (DTAP) linker, which introduces an alkyne group that can undergo a copper-catalyzed click-reaction with commercially available azide dyes such as 6-FAM-azide and Cy5-azide. b) The modularity offered by the two-step labelling approach allows a one-pot dual fluorescence labelling of nanocellulose through complementary orthogonal click-chemistries. This is achieved using a triazinyl linker bearing alkyne and furfuryl groups that are reactive with 6-FAM maleimide and Cy5 azide.

3.2 Results

3.2.1 DTPR – one-step labelling of cellulose with Rhodamine 6G

Triazinyl-based dyes provide a simple one-step route to label cellulose in aqueous solutions and in relatively mild conditions (Figure 3.1). BC fibrils (0.1 wt%) were labelled with 1 mM of DTAF (1 mmol/g cellulose) in an aqueous solution containing 0.1 M NaOH as previously described.[13,25] To extend the fluorophores amenable to this simple labelling method, a new triazine dye, dichlorotriazinyl piperazine Rhodamine 6G (DTPR), was synthesized in-house. This involved derivatizing the rhodamine carboxylate group with piperazine, which was used as a linker to reacts with trichlorotriazine (Scheme S3.1). The reaction conditions used to label BC with DTAF were also successful in labelling BC with DTPR to produce green/yellow fluorescent DTPR-BC (Figure 3.2).

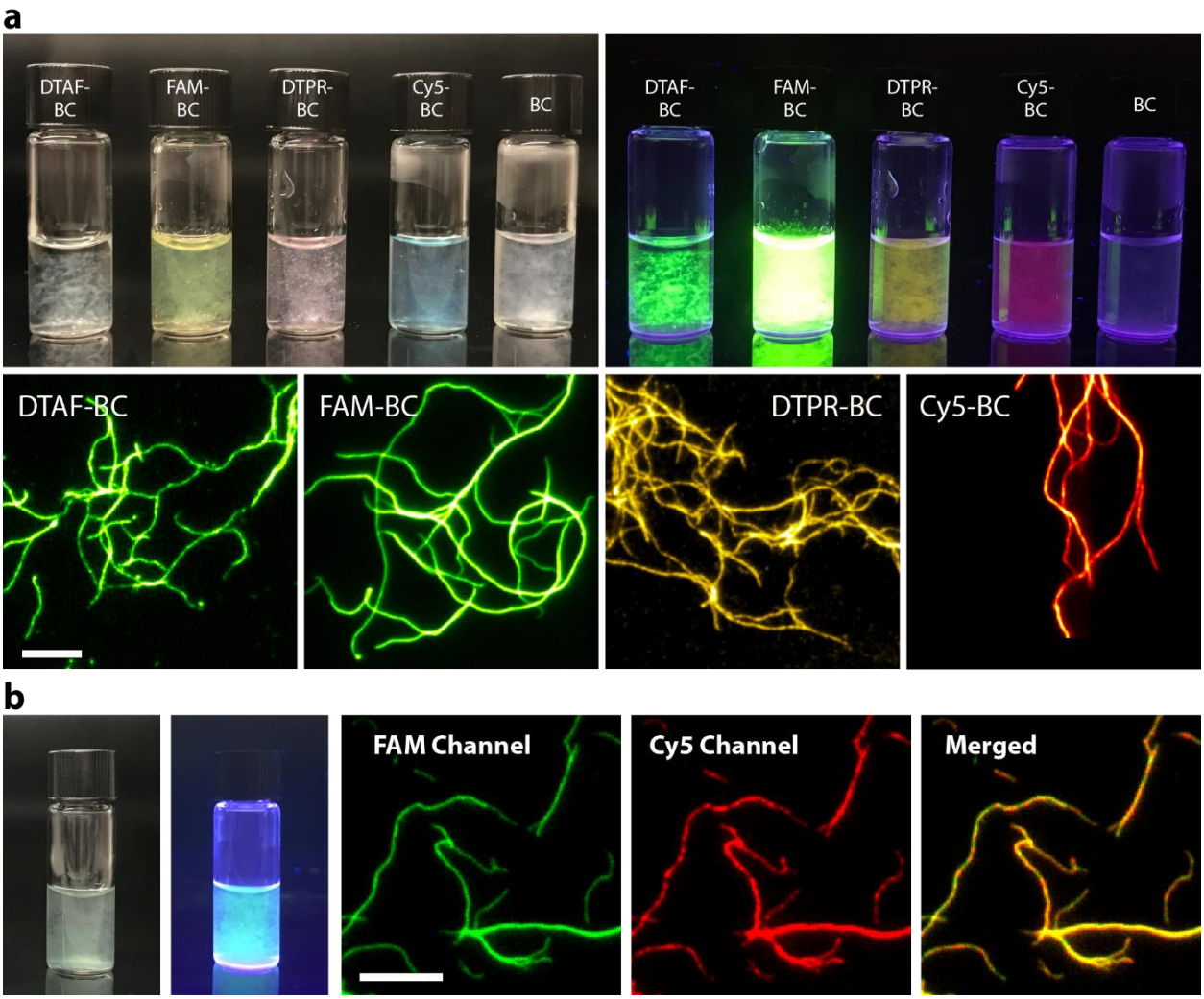

Figure 3.2. BC labelled with DTAF, 6-FAM, DTPR or Cy5. a) BC fibrils were labelled either using a one-step reaction with the triazine dyes DTAF and DTPR, or using a two-step reaction that first involved grafting a DTAP linker followed by a click-reaction with 6-FAM azide or Cy5 azide. Images of DTAF-BC, FAM-BC, DTPR-BC, Cy5-BC and unlabelled BC suspensions (0.1 wt%) under white light (top left) and UV light (top right) illumination. b) BC was also grafted with a triazinyl linker bearing both alkyne and furfuryl reactive groups. The bifunctional BC was then labelled with 6-FAM maleimide and Cy5 azide in a one-pot reaction. All epifluorescence images of immobilized fibrils were captured in buffer under oxygen-scavenging conditions. All scale bars represent 5 μm.

3.2.2 DTAP – a versatile route for labelling

Two-step labelling versus one-step labelling

While successful and simple, the one-step labelling strategy described above requires synthesizing a new derivative for each fluorophore, making it accessible only to groups with synthesis expertise. To bypass the need to synthesize new derivatives for every dye and

enable labelling of cellulose with a broad range of commercial fluorophores, we targeted the pre-functionalization of cellulose with a linker bearing an alkyne group commonly used in bio-orthogonal click reactions. An inexpensive dichlorotriazinyl propargylamine (DTAP) linker was made in-house through a scalable one-step reaction of propargylamine with Trichloro-triazine (Scheme S3.2).[26] DTAP was grafted onto 0.1 wt% BC at a concentration of 1 mM using an aqueous 0.1 M NaOH solution to yield DTAP-BC. The alkyne functionality on the cellulose surface enabled direct labelling with 1 mM of 6-carboxyfluorescein azide (6-FAM) through a copper-catalyzed azide-alkyne cycloaddition (CuAAC) reaction to yield FAM-BC. To compare the efficiency of this method versus traditional DTAF labelling, BC fibrils were labelled with both methods, imaged using epifluorescence and their average intensity determined by tracing >200 individual fibrils (Figure 3.3). The limiting step was identified, and labelling conditions were optimized for the two-step reaction. When the concentration of FAM in the second step was increased from 1 to 10 mM, the intensity of BC fibrils did not increase (Figure 3.3a). However, increasing the concentration of DTAP 10-fold from 1 to 10 mM, the fibril fluorescence increased by ~6-fold, indicating that grafting of DTAP onto cellulose is the limiting step for this labelling approach. Using a high concentration of an inexpensive linker ($2.49/mmol) in the first step yielded highly fluorescent fibrils that were significantly brighter than DTAF-BC despite using the same dye load (Figure 3.3a).

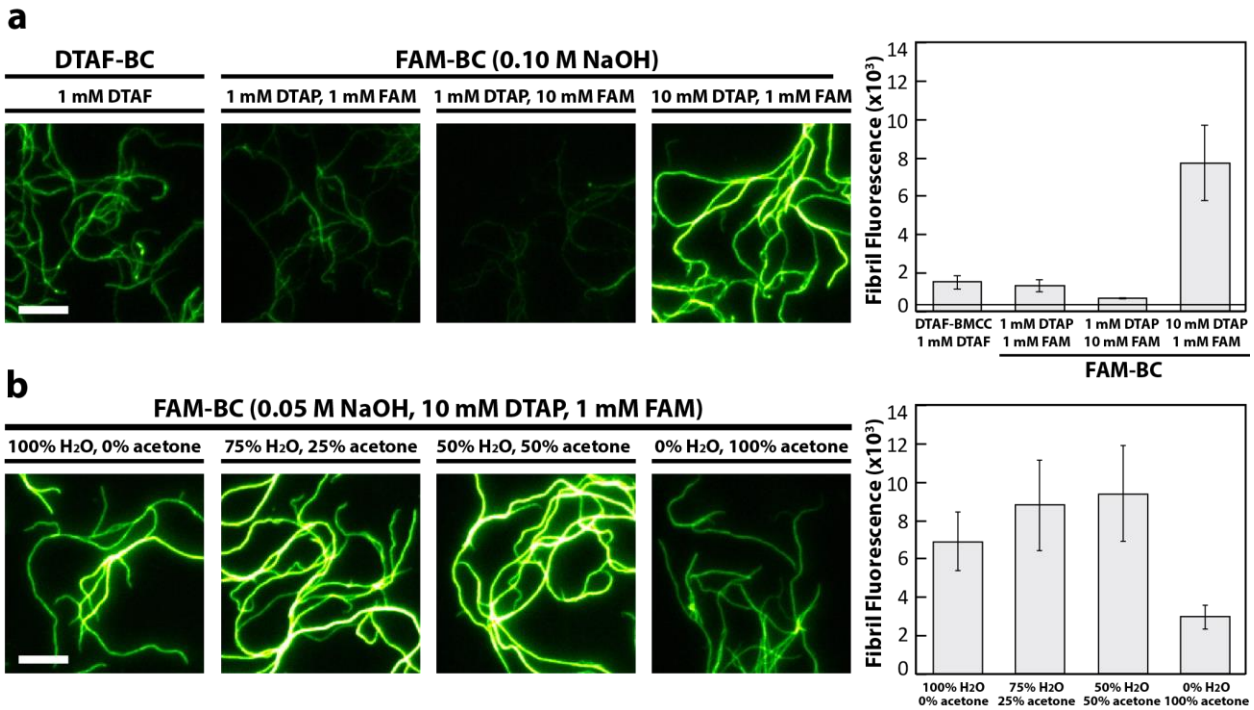

Figure 3.3. Impact of labelling reaction conditions on BC fluorescence. BC was labelled with fluorescein-based dyes through a one-step reaction with DTAF or a two-step reaction involving a

DTAP linker and 6-FAM azide. The labelling of BC by these approaches and the impact of various reaction conditions were assessed by the average fluorescence intensity of individually traced fibrils (n > 200 for each sample from > 50 images). Images were acquired under oxygen-scavenging conditions using the same gain, illumination power and exposure time and are displayed under the same brightness and contrast. a) Comparison of labelling efficiency of 1-step reaction with DTAF *vs.* 2-step reaction with DTAP and 6-FAM azide under various reaction conditions. b) Comparison of labelling efficiency with DTAP and 6-FAM azide when DTAP is grafted using acetone and/or water as solvent. All error bars represent the standard deviation of fluorescence intensity. Scale bars are all 5 μm.

Optimization of labelling with DTAP linker

We next explored whether the concentration of the base and solvent used to graft DTAP could further improve the labelling efficiency. The fact that DTAP is moderately soluble in water and chlorine-substituted triazine can be hydrolyzed under alkaline conditions suggested that the efficiency of the first grafting reaction could be improved by using lower base concentrations and less polar solvents. We explored varying the concentration of NaOH from 0.05 to 0.10 M, while using 10 mM of DTAP linker and 1 mM 6-FAM azide dye in the labelling reaction. Decreasing the concentration of base from did not hamper the reaction and yielded brightly fluorescent fibers (Figure 3.3b), so 0.05 M NaOH was used in all subsequent labelling reactions. Next, the solvent was changed to a water/acetone mixture since acetone solubilizes DTAP, is miscible with water, and does not aggregate nanocelluloses rapidly. Water/acetone volumetric ratios from 100/0 to 0/100 were tested, and we observed that increasing acetone resulted in higher cellulose fluorescence, except when using 100% acetone. This last sample was prepared by first deprotonating BC in 0.05 M NaOH aqueous solution for 24 hours, and then exchanging the solvent to 100% acetone for the linker grafting step. While this resulted in the most vividly coloured cellulose fibrils, their fluorescence intensity was lower than any of the other samples. These results suggest that the optimal conditions to graft DTAP onto nanocellulose are 0.05 M NaOH and 75/25 or 50/50 water/acetone ratio. To minimize the use of organic solvents, all subsequent grafting of DTAP was done using 75/25 water/acetone as the solvent.

3.2.3 One-pot, dual labelling via triazine chemistry

Trichloro-triazine contains three chlorine groups that can be substituted in a sequential fashion, which opens the possibility of designing bifunctional linkers for cellulose modification. To demonstrate this capability, we synthesized a bi-functionalized triazinyl linker bearing furfuryl and alkyne groups (Scheme S3.3). Since the resultant mono-chloro

triazine group is less reactive than the di-chloro DTAP linker, the bi-functional linker was grafted onto BC at 60 °C. The introduction of the chemically orthogonal furfuryl and alkyne moieties onto the surface of cellulose fibrils permitted a one-pot labelling reaction with azide and maleimide dyes (Figure 3.1b). This was demonstrated with 0.5 mM of each Cy5 azide and 6-FAM maleimide, which resulted in a green-coloured suspension of BC that was brightly fluorescent in both green and far-red channels (Figure 3.2b).

3.2.4 Tunable labelling for super-resolution imaging

The optimized reaction conditions for DTAP grafting were used to label BC with Cy5-azide, yielding a suspension of cellulose fibrils that were vividly coloured blue and showed intense fluorescence in the far-red spectrum (Figure 3.2). To prepare samples optimized for STORM super-resolution imaging, the concentration of Cy5 was varied from 100 μM to 1 μM, allowing the fluorescence intensity of cellulose fibrils to be tuned across one order of magnitude and resulted in labelling densities that spanned from complete, dense coverage to a sparse distribution of dye molecules (Figure 3.4a). During the acquisition of a STORM image sequence at high illumination power (0.49 kW/cm^2 at the image plane), the time needed to reach a density of emitting fluorophores where individual molecules could be precisely localized depended on the Cy5 labelling concentration (Figure 3.4d). The single molecule state was not reached within the 12,000-frame acquisition for BC labelled with 100 μM Cy5, while samples labelled with 50 or 10 μM reached it after 4,000 and 1,000 frames, respectively. In contrast, fibres labelled with 5 or 1 μM resulted in single-molecule densities immediately. These differences are reflected in the localization density observed on the microfibrils (Figure 3.4d), which was calculated as the total number of localizations per frame divided by the contour length of individual fibrils (Figure S3.1). As seen in the 4,000th frame acquired (Figure 3.4b), the ability to tune the labelling of BC microfibrils yielded localization densities that ranged from overcrowded emitters (100 μM) to high density single-emitters (50 μM), low density single-emitters (10 μM) and infrequent or absent emitters (5 and 1 μM).

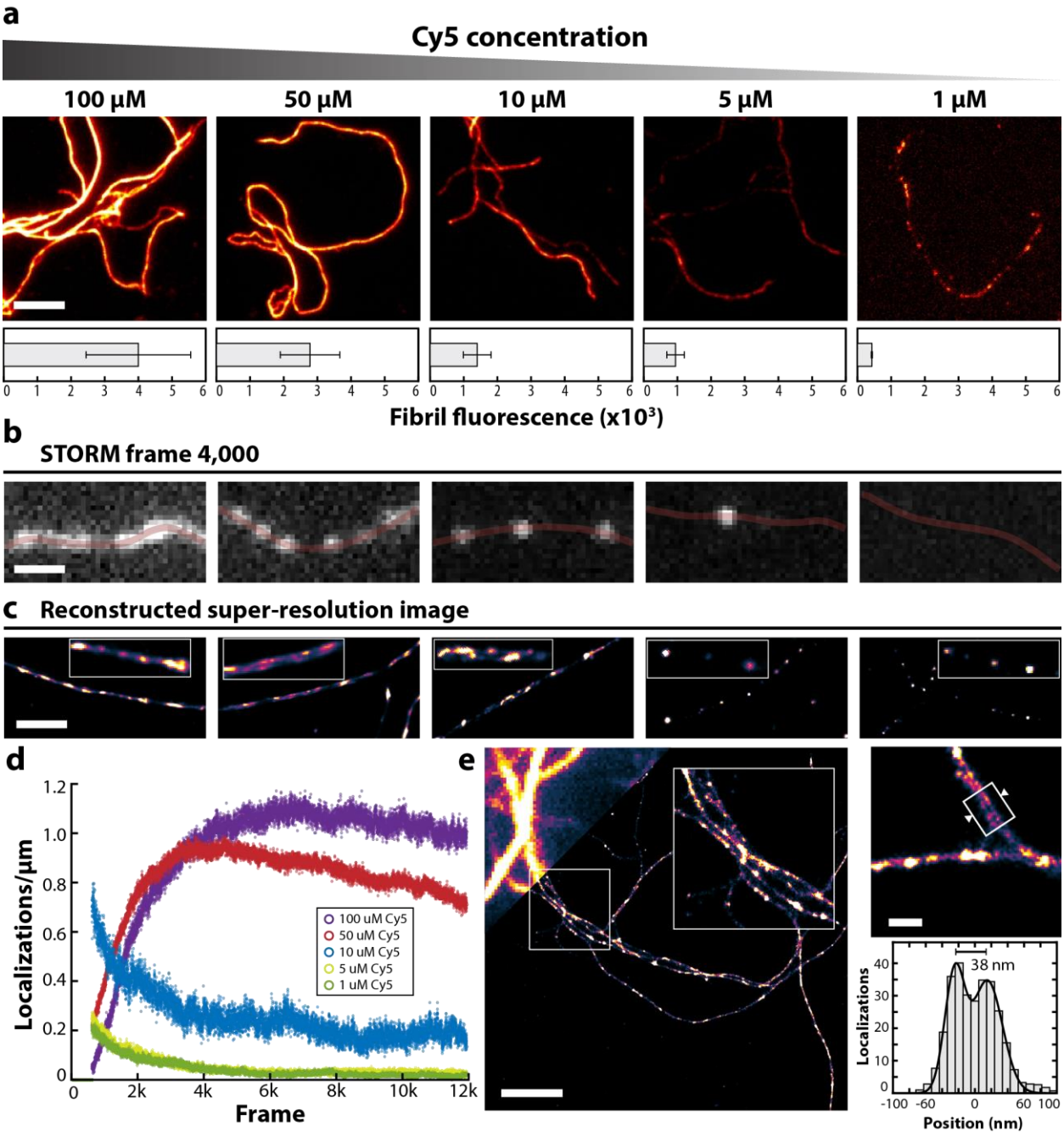

Figure 3.4. Optimization of BC labelling for super-resolution imaging. a) BC was labelled using a two-step reaction with various concentrations of Cy5 and average fluorescence was measured through line intensity traces of individual fibrils (>100/sample). b) Cy5-BC fibrils imaged after 4,000 frames of illumination with the 647 nm laser at a maximum power of 0.49 kW/cm^2. c) Super-resolution images reconstructed from a 12,000-frame acquisition under oxygen-scavenging conditions, 100 mM cysteamine and maximum illumination power without re-activation with the 405 nm laser. Sample drift was corrected using the cross-correlation method. d) Average localization

densities were determined by tracing individual cellulose fibrils (>10/sample) and dividing the total number of localizations within the region of interest by the fibril length. e) Using BC labelled with 10 μM Cy5, high quality super-resolution images of the fibrils were acquried, which showed resolvable cross-sectional features as small as 38 nm. All error bars represent the standard deviation of fluorescence intensity between fibrils. Scale bars are 5 μm (a), 1 μm (b, c), 2 μm (e) and 200 nm (e, inset).

The labelling density of Cy5-BC fibrils impacted the quality of reconstructed super-resolution images (Figure 3.4c). Fibrils labelled with 100 μM Cy5 exhibited an alternating pattern of bright and dim regions, representing the crystalline and disordered regions of cellulose. However, the overcrowding of emitters, due to the high labelling density, did not allow visualizing fine details such as the inherent twists of microfibrils. This feature was resolved using the 50 μM sample, while still clearly showing the crystalline and disordered regions (Figure 3.4c, second panel). Twisting was also observed in images reconstructed from the 10 μM Cy5 sample, but lower localization densities lead to worse mapping of the less densely labelled crystalline regions of cellulose microfibrils. In contrast, the sparse labelling of the 5 and 1 μM Cy5 samples produced highly discontinuous images that show well-spaced bright regions representing the more accessible dislocations along the cellulose microfibrils. From these observations, the 10 μM Cy5 sample was determined to have optimal labelling density, as the reactivation of Cy5 molecules using the 405 nm laser can tune the emission density and allow the visualization of fine details (<40 nm) within the sample while still continuously mapping the disordered and crystalline regions along the microfibrils (Figure 3.4e). Optimizing the labelling density of cellulose was critical to obtaining high quality super-resolution images with minimal acquisition time.

3.2.5 Highly labelled nanocelluloses with low Cy5 loads

The two-step labelling method was next applied to other nanocelluloses, including CNCs, CNFs and carboxymethylated CNFs. The optimized labelling conditions, which entailed 24 h reaction of 0.1 wt% nanocellulose with 10 mM DTAP (10 mmol/g of cellulose) followed by a 2 h CuAAC reaction with Cy5-azide at 10 μM concentration (dye load of 10 μmol/g cellulose, 100-fold lower than conditions used with DTAF!), yielded nanocellulose suspensions that were vividly coloured blue (Figure 3.5a) and brightly fluorescent under the microscope (Figure3. 5b). The degree of labelling (DoL) of the nanocellulose was determined by measuring the amount of unreacted dye present in the supernatants or eluates following extensive washing. A dye load of 10 μmol/g resulted in a DoL of approximately 7 μmol/g for all cellulose materials, except for CNCs, which had a slightly lower DoL of 5.7 μmol/g (Figure 3.5d). Varying the dye load from 5 to 25 μmol/g allowed tuning the DoL of BC from 3.8 to

10.5 μmol/g. As observed by atomic force microscopy (AFM), the labelling reaction did not alter the morphology of the nanocelluloses (Figure 3.5c, Figure S3.2 and Figure S3.3) and their measured dimensions remained unchanged (Table S3.1). Percent crystallinity (%Cr), which was determined through X-ray diffraction using the peak deconvolution method (Figure 3.5e), was approximately 90% for all cellulose materials and, within the 3% measured error of %Cr measurements; the native cellulose I_α crystalline structure was unaltered following fluorescence labelling (Figure 3.5e,f). The two-step florescence labelling method resulted in nanocellulose materials with high DoL, while using minimal amounts of dye and preserving their native structure.

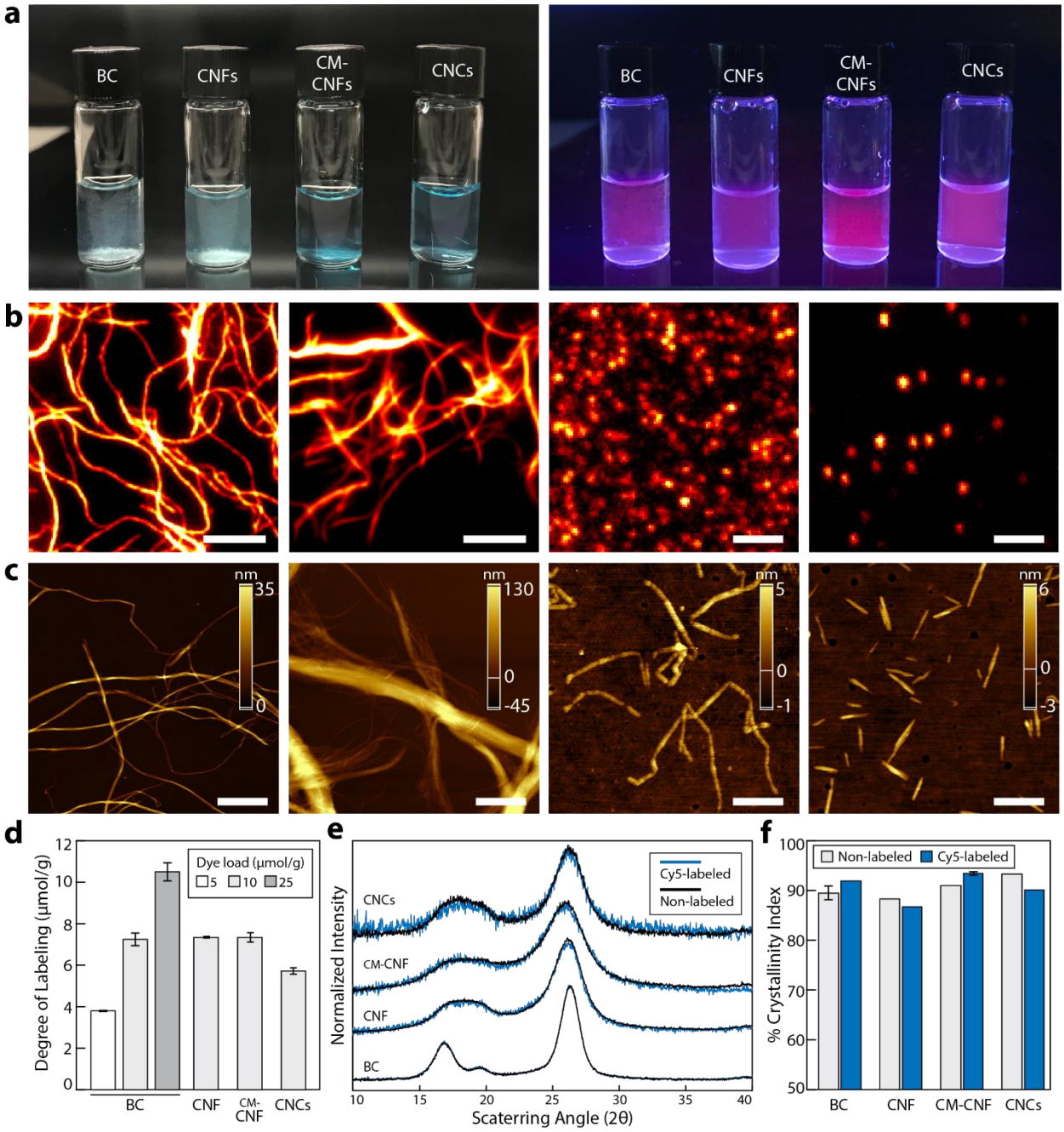

Figure 3.5. Characterization of nanocelluloses labelled with Cy5. a) Suspensions (0.1 wt%) of BC, wood-derived CNFs, carboxymethylated CNFs (CM-CNFs), and softwood-derived CNCs were labelled with Cy5 azide through a 24 hr reaction with DTAP linker (10 mM, 10 mmol/g cellulose) followed by a 2 hr reaction with Cy5 azide (10 uM, 10 µmol/g cellulose). The labelled nanocelluloses were prepared on glass substrates for b) epifluorescence and c) AFM imaging. The images are shown in the same order as the vials in (a). d) Degree of labelling was determined by measuring the dye remaining in the supernatant or eluent after washing the labelled nanocelluloses through centrifugation or stirred cell dialysis. Error bars represent the standard deviation associated with

three fluorescence measurements of the collected samples. e) X-ray diffractograms of Cy5-labelled and unlabelled nanocelluloses. f) Percent crystallinity of labelled and unlabelled materials were determined through X-ray diffraction using the peak deconvolution method. Error bars for %Cr of BC and CM-CNF represent the standard deviation of triplicate sample measurements. Error bars in (d) represent triplicate fluorescence measurements of residual dye in the supernatant. Scale bars, 5 μm (b, BC, CNF), 2 μm (b, CM-CNFs, CNCs), 1 μm (c, BC, CNF) and 200 nm (c, CM-CNFs, CNCs).

3.3 Discussion

Nanocellulose materials are increasingly being used to develop new composites, drug delivery vehicles, tissue engineering scaffolds, rheological modifiers, emulsifiers, health care products, and sensing devices, among many others.[27] This means that there is a demand for simple and versatile labelling methods that allow their visualization from the macro- to the nanometric scale in different contexts and within complex matrices. Potential applications include assessing the biodistribution and fate of CNCs in whole organisms using two-photon microscopy, leaching from packaging materials using fluorescence spectroscopy, visualizing the interaction of nanocelluloses with other components, their arrangement and distribution in composites via confocal or light sheet microscopy, monitoring the depolymerization of cellulose by cellulases using time-lapsed imaging or visualizing the nanostructure of cellulose fibers using super-resolution microscopy. All these examples require the use of spectrally distinct dyes that are compatible with the microscopy technique and the goal of the study.

The triazinyl-based dye DTPR allows nanocelluloses to be labelled in a simple one-step reaction with Rhodamine 6G, which is spectrally distinct than the commonly used DTAF dye and provides higher brightness and photostability.[28–30] Yet, the expertise and multiple synthetic and purification steps involved in the synthesis of this dye can limit its use by researchers outside the field of organic chemistry. Conversely, the two-step labelling reaction with the alkyne-bearing triazinyl linker DTAP, which can be easily and inexpensively produced in gram quantities and requires minimal purification, can render the surface of cellulose reactive with any fluorescent dye bearing an azide handle. The commercial availability of a wide variety of commonly used dyes as azide derivatives makes this method amenable to a broader range of applications and fields of research.

Compared to DTAF-BC, FAM-BC microfibrils were marginally dimmer in fluorescence intensity when both samples were prepared using the same concentrations of dye and linker. This is explained by the inclusion of a second step and the poor solubility of DTAP in water. However, the low cost of DTAP linker allows its use in high concentrations during the first step, causing cellulose to be densely functionalized with an alkyne group despite the

competing side reactions in water. Splitting the fluorescence labelling reaction of cellulose into two steps allowed us to decouple the low efficiency associated with the reactivity of cellulose with triazine from the labelling with the dye, thus limiting the waste of expensive dye. Since the second step is based on the highly efficient CuAAC reaction, the activated cellulose fibrils can be densely labelled using minimal amounts of dye.

The concentration of base and solvent used during the linker grafting reaction impacted the efficiency of labelling. When 100% water was used as a solvent, cellulose exhibited slightly higher fluorescence when 0.10 M NaOH was used over 0.05 M, which is consistent with Helbert *et al.* and is expected since the surface hydroxyl groups are activated in alkaline conditions.[13] Yet, a concentration of 0.05 M NaOH was selected to minimize the impact of the labelling reaction on the nanocellulose structure (e.g., swelling). At NaOH concentration of 0.05 M, decreasing the concentration of water to 75% or 50% correlated with increased nanocellulose fluorescence. This is explained by the fact that reducing the amount of water in the reaction minimizes the hydrolysis of the triazine moiety and increases the linker's solubility. However, when the reaction was run in 100% acetone, cellulose fluorescence dramatically decreased, despite the vivid colouration of the fibrils. This suggests that the fibrils are labelled to such a high density that the grafted dye molecules are in very close proximity to each other and undergo quenching. This has been previously observed in enzymatic hydrolysis experiments when using high DTAF concentrations on BC.[13] While the 25% acetone and 0.05 M NaOH reaction conditions are considered optimal, all of the tested reaction conditions can produce highly fluorescent fibrils when a linker load of 10 mmol/g of cellulose is used. Deprotonation of the cellulose fibrils in water followed by solvent exchange into 100% acetone for a grafting reaction can be particularly useful as a strategy for other reactions that are water sensitive but require the surface deprotonation of cellulose.

The two-step labelling method can be applied to nanocellulose materials derived from different sources and which have undergone various enzymatic or chemical treatments, ranging from large fibrillar aggregates seen in wood-derived enzymatically treated CNFs, to bacterial derived microfibrils, carboxymethylated CNFs and sulfated CNCs. Despite the presence of abundant surface carboxymethyl groups, the labelling density of CM-CNFs was similar to that of unmodified material (enzymatic CNFs) and BC at 7 μmol/g. On the other hand, CNCs exhibited a slightly lower degree of labelling at 5.7 μmol/g, which translates into ~10 Cy5 molecules per CNC, assuming a 110 nm long, 4.5 nm diameter nanoparticle and a cellulose density of 1.6 g/mL.[31,32] In comparison to the other nanocelluloses, the lower DoL of CNCs can most likely be attributed to the absence of

disordered regions, which would be more accessible to labelling but are cleaved during the acid hydrolysis that is used to make CNCs. Sulfuric acid hydrolysis also introduces sulfate half ester groups onto the cellulose surface and has been shown to significantly impact the labelling of CNCs with DTAF through electrostatic repulsion, which could also be applicable to the sulfated Cy5 azide dye used here.[25] Compared to previous work, the proposed method allowed nanocellulose to be fluorescently labelled under mild alkaline conditions and in much more efficient manner, yielding high labelling densities while using very low dye loads. Although other methods have achieved higher labelling densities of CNCs, they either used significantly higher dye loads or extended the total reaction period for up to 9 days (Table 3.1). The proposed labelling approach also preserves the native morphology and crystalline structure of these cellulose nanomaterials and retains their unique physical and biological properties, which is important for the development of new cellulose-based materials or for studying enzymes-cellulose interactions.

Table 3.1. Summary of reaction conditions and efficiencies reported for nanocellulose labelling.

Cellulose type	Dye	Base	Dye amount (µmol/g)	DoL (µmol/g)	Grafting efficiency	Number of steps / time	Reference
BC	Cy5 azide	0.05 M NaOH	5	3.8	76%	2 / 1 day 2 h	This work
BC	Cy5 azide	0.05 M NaOH	10	7.3	73%	2 / 1 day 2 h	This work
BC	Cy5 azide	0.05 M NaOH	25	10.5	42%	2 / 1 day 2 h	This work
CNFs	Cy5 azide	0.05 M NaOH	10	7.4	73%	2 / 1 day 2 h	This work
CM-CNFs	Cy5 azide	0.05 M NaOH	10	7.3	73%	2 / 1 day 2 h	This work
CNCs	Cy5 azide	0.05 M NaOH	10	5.7	57%	2 / 1 day 2 h	This work
CNCs	FITC	0.1 M NaOH	102	2.8	3%	1 / 4.5 days	[18]
CNCs	FAM-SE/ TAMRA-SE	1.92 mM DMAP	68 / 38	10.4 / 4.7	15%/12%	3 / 9 days	[18]
CNCs	TAMRA-SE/ OG-SE	1.92 mM DMAP	38 / 39	7.3 / 4.2	19%/11%	3 / 9 days	[18]
CNCs	DTAF	0.2 M NaOH	30	0.0045	0.2%	1 / 1 days	[25]
CNFs	DTAF	0.04 M NaOH	5.7	2	33%	1 day	[24]
CNCs	FITC	1 M NaOH	320	30	9.4%	3 / 5 days	[19]
CNCs	DTAF	0.2 M NaOH	28	0.08	0.3%	1 / 1 days	[31]
CNCs	RBITC	0.1 M NaOH	8	0.21	2.6%	1 / 2 days	[31]
CNCs	RBITC	0.1 M NaOH	37	1.2	3.2%	1 / 3 days	[31]
CNCs	RBITC	0.1 M NaOH	78	5.1	6.5%	1 / 4 days	[31]
BC	DTAF	0.2 M NaOH	1212	21.6	1.8%	1 / 1 days	[13]

The ability to tune the fluorescence of cellulose within at least one order of magnitude was demonstrated on BC by simply varying the concentration of dye used in the second reaction. This control allows the preparation of fluorescent nanocelluloses that are

optimized for different applications or imaging techniques. For example, the development of cellulose-based biosensors, such as those that measure pH or amine concentrations, would benefit from a high labelling density in order to maximize sensitivy.[18,33] The modular nature of this method, which we demonstrate by dual fluorescent labelling in a one-pot scheme, can be leveraged for the fabrication of such devices.[26] On the other hand, lower labelling densities may be needed when monitoring the enzymatic degradation of cellulose using fluorescence-based bulk assays or microscopy, as excess dye can interfere with the ability of enzymes to depolymerize cellulose.[13,15,16]

In this work, we demonstrated the ability to finely tune the labelling density of BC for preparing samples optimized for super-resolution fluorescence microscopy. Given that STORM-based super-resolution can be used to visualize features as small as 20 nm, it is important that samples are labelled with a density that is high enough to fully map structures in a continuous and detailed fashion; based on the Nyquist sampling criterion, this would require the presence of a fluorescent molecule at least once every 10 nm.[34] However, due to photobleaching and the stochastic nature of photoblinking, higher labelling densities would likely be required to acquire high quality super-resolution images. At the same time, it is important that the labelling density is not too high, as this could cause self-quenching or lead to overcrowding. Overcrowding of fluorescent molecules, which in super-resolution microscopy is described by the simultaneous emission of multiple fluorophores within a diffraction-limited area, can give rise to false localization and yield poor quality images with diminished resolution.[35] The effects of overcrowding and sparse localizations were both observed in Cy5-BC prepared using high or low concentrations of Cy5, where at the extremes fine details of microfibril twisting could not be resolved due to false localizations (at the high end) or because fibrils were discontinuously mapped due to a sparse localization density (low end). With the optimal labelling density of the 10 μM Cy5 sample, quickly reaching a single-molecule state combined with the fine tuning of fluorophore densities offered by the dye reactivation of the 405 nm laser allowed us to resolve features smaller than 40 nm within microfibrils while continuously mapping the disordered and crystalline regions of nanocellulose.

3.4 Conclusion

In this work, we have expanded the range of methods to label nanocelluloses by introducing a new triazine dye, DTPR, and a versatile and cost-effective two-step approach reliant on an alkyne functional triazinyl linker, DTAP. The cost-effectiveness and versatility of this approach in labelling cellulosic materials to tuneable degrees, while retaining the native properties of nanocelluloses, makes it possible to apply this method to label cellulose for a

wide range of fluorescence-based studies and imaging applications. The modularity offered by triazine chemistry can also be leveraged to create bi-functional linkers that allow labelling of nanocellulose with a dye for tracing purposes and introducing a second functionality that can be used for crosslinking, binding, or sensing. The methods introduced should provide much needed labelling routes for the visualization of cellulose nanomaterials that are the being used in a rapidly expanding range of applications.

3.5 Materials & Methods

Materials. Rhodamine 6G (95%), 6-aminofluorescein (95%), propargylamine (98%), phosphorus oxychloride ($POCl_3$, 99%), piperazine (99 %), Trichloro-triazine (99%), sodium hydroxide (NaOH), potassium carbonate (K_2CO_3), glucose, glucose oxidase (from *Aspergillus niger*, type X–S, 100–250 units/mg, 65–85% protein content), catalase (from bovine liver, ≥10 000 units/mg, ≥70% protein content) and cysteamine (98%) were purchased from MilliporeSigma (Oakville, ON, Canada) and used without any further purification. Poly(allylamine hydrochloride) (PAH) was purchased from Polysciences Inc. (Warrington, PA) and had a nominal molecular weight of 120-200 kDa. Nata de Coco (230 g drained weight, New Lamthong Food Industries, Bangkok, Thailand), consisting primarily of bacterial cellulose produced by *Komagataeibacter xylinus* cultures,[36] was purchased from a local food store. Spray-dried softwood-derived cellulose nanocrystals (CNCs) in hydrogen sulfate sodium salt form were generously provided by CelluForce (Montreal, QC, Canada). Sulfo-Cyanine5 azide and 5-fluorescein azide, 6-isomer (6-FAM-Azide) were purchased from Lumiprobe Corp. (Hunt Valley, MD), while DTAF and DTPR were synthesized in-house (see below). Glass-bottom petri dishes were purchased from MaTek (Ashland, MA). PS-Speck™ Microscope Point Source Kit (ThermoFisher, Waltham, MA) were used as fiducial markers for drift correction. Pictures of UV-illuminated suspensions of fluorescent cellulose were acquired on a TL-2000 Ultraviolet Translinker (Ultra-Violet Products, Upland, CA). Enzymatically pretreated CNFs and carboxymethylated -CNFs were derived from a never-dried dissolving grade pulp (Dissolving Pulp Plus from Domsjö-More). CNF pre-treatments were conducted on the pulp as have been described previously.[37,38] The total charge of the carboxymethylated CNF as determined by conductometric titration was ~600 μeq/g. Both pretreated pulps were fibrillated by microfluidization (M110-EH; Microfluidics; 1700 bar; Z-type interaction chamber, with 200 μm and 100 μm chamber dimensions) at a consistency of ~ 2 wt%, with the enzymatic CNF grade subjected to three passes through the microfluidizer and the carboxymethylated grade to one pass.

Characterization of synthesized compounds by nuclear magnetic resonance (NMR). ^{1}H and ^{13}C NMR spectra of all the synthesized compounds were acquired using a Bruker AV600-

600 MHz NMR Spectrometer, except for the ^{1}H spectrum of DTAP, which was acquired using a Bruker AV700-700 MHz NMR Spectrometer. All NMR and mass spectra of synthesized compounds are available in Supplementary Information (Figures S3.4 – S3.13).

Characterization of synthesized compounds mass spectrometry (MS). Mass spectra were acquired using a Micromass Ultima (LC-ESI/APCI) Triple Quadrupole mass spectrometer.

Isolation of BC from Nata De Coco. BC was isolated from commercial foodstuff Nata de coco (NDC, 250 g) through mild alkaline treatment.[36,39] NDC was drained of its syrup and thoroughly rinsed with 18.2 MΩ cm water, which is onwards simply referred to as "water". The material was combined with ~300 mL of water and blended at full speed in a MagicBullet blender (Nutribullet, Los Angeles, CA) for 10 minutes until the consistency was uniform. The slurry was then incubated in 0.1 M NaOH for 20 minutes at 80 °C. The reaction was quenched with chilled water using 10× the volume of the reaction and allowed to equilibrate to room temperature (RT). The suspension was rinsed with water by centrifugation at 1800*g* for 8-10 minutes (RC-5 Superspeed Refrigerated Centrifuge; DuPont Instruments), followed by supernatant decanting, until the pellet became white (5-7 cycles). The pellet was resuspended in water to create a 3 mg/mL bacterial cellulose slurry for later functionalization and labelling.

Synthesis of dichlorotriazine aminofluorescein (DTAF). The synthesis of DTAF was adapted from the method by Blakeslee.[26,40] The dye 6-aminofluorescein (0.5 g, 1.44 mmol) dissolved in cooled anhydrous methanol (0 – 5 ^{o}C, 15 ml) was added dropwise to a stirred solution of Trichloro-triazine (0.32 g, 1.74 mmol) in 3 ml of chloroform at 0 ^{o}C. After 2 h of stirring, 0.5 ml of concentrated HCl was added dropwise while maintaining the reaction for additional 1 hr. The resulting precipitate was filtered under vacuum to give a bright yellow powder as product (0.7 g, 91% yield). ^{1}H NMR (600 MHz, MeOD) δ 8.30 (d, *J* = 8.8 Hz, 1H), 8.02 (dd, *J* = 8.7, 2.2 Hz, 1H), 7.68 (d, *J* = 2.2 Hz, 1H), 7.51 (d, *J* = 9.2 Hz, 2H), 7.27 (d, *J* = 2.3 Hz, 2H), 7.12 (dd, *J* = 9.2, 2.3 Hz, 2H).

Synthesis of dichlorotriazine piperazine rhodamine 6G (DTPR) (Scheme S3.1). Under a nitrogen atmosphere, piperazine (72 mg, 0.836 mmol) and rhodamine 6G (200 mg, 0.418 mmol) were transferred into a 20 mL amber glass vial with a magnetic stirrer, sealed and heated at 110 ^{o}C for 4 h. After cooling to room temperature, the reaction mixture was carefully dissolved in 1 mL DCM (excluding sublimed excess piperazine attached to the upper walls of the glass vial) and added dropwise to 30 mL cold diethylether to give a red precipitate. The resulting precipitate was isolated by centrifugation and dried into red solid product (piperazine rhodamine 6G, 0.19 g, 94.1%). ^{1}H NMR (600 MHz, CD_2Cl_2, ppm) δ: 0.5-

2.0 (CH_2-CH_3, 12H), 2.0-3.3 (N-CH_2-CH_2-N, 4H). 3.3-4.2 (N-CH_2-CH_3, 4H), 6.5-8.5 (aromatic, 8H). MS (ESI): calculated for $C_{30}H_{35}N_4O_2^+$, 483.3; found, 483.4 (M+)

To a stirred solution of Trichloro-triazine (0.038 g, 0.207 mmol) dissolved in anhydrous tetrahydrofuran (THF, 2 ml) cooled to 0-5 ^oC, $NaHCO_3$ (0.0175 g, 0.208 mmol) was added. After 20 minutes, a solution containing rhodamine 6G piperazine (0.1 g, 0.207 mmol) in 2 ml anhydrous THF was added dropwise over a period of 30 minutes. The end of reaction was monitored via TLC (silica gel, DCM). The product was isolated by centrifugation followed by filtration of the supernatant, and precipitation in 40 mL cold diethylether to yield pure product (red precipitate) in quantitative yield (dichlorotriazine piperazine rhodamine 6G, 0.127 g, 97%). MS (ESI): calculated for $C_{30}H_{35}N_4O_2^+$, 630.2; found, 630.2 (M+)

Synthesis of dichlorotriazine propargylamine (DTAP) (Scheme S3.2). To a solution of Trichloro-triazine (2.00 g, 10.85 mmol) in THF (25 mL), a mixture of propargylamine (0.60 g, 0.70 mL, 10.93 mmol) and triethylamine (TEA, 1.21 g, 2.12 mL, 11.94 mmol) in THF (5 mL) was added dropwise over a 30-minute period at -20 °C. The temperature was maintained at -20 °C for an additional 30 minutes and the reaction was continued for an additional 12 hr between -20 °C and 21 °C while stirring. The mixture was centrifuged (17,500×*g*, 2 min) and the supernatant was dumped into ice water and the precipitate was filtered through vacuum to provide a tan coloured product in quantitative yield (2.2 g, ~99%). ^1H NMR (700 MHz, $CDCl_3$, ppm) δ: 5.96 (s, 1H), 4.27 (s, 2H), 2.32 (s, 1H). ^{13}C NMR (151 MHz, CD_2Cl_2, ppm) δ: 170.62, 166.10, 78.16, 72.73, 31.61. HRMS (ESI) *m/z*: $[M-H]^-$ calculated for $C_6H_3Cl_2N_4$, 201.0; found, 201.1.

Synthesis of alkyne-furfuryl bi-functionalized triazinyl linker (Scheme S3.3).

Synthesis of 4,6-dichloro-n-furfuryl-1,3,5-triazine-2-amine. To a vigorously stirred solution of Trichloro-triazine (1 g, 5.42 mmol) dissolved in 8 mL acetone in a 50 mL round-bottomed flask, 12 mL ice-water at 0 °C were added. A mixture of furfurylamine (0.53 g, 5.42 mmol) and $NaHCO_3$ (0.46 g, 5.42 mmol) in 10 mL of acetone/water solution (1:1, v/v) was then added slowly. The reaction mixture was stirred at 0 °C for 4 hr. The resulting white precipitate was filtered, rinsed with cold water, and dried in vacuo to give furfuryl-4,6-dichloro-[1,3,5]triazine-2-amine as a white solid (1.26 g, 95%). ^1H NMR ($CDCl_3$, δ) 4.70 (d, J = 5.8 Hz, 2H), 6.15 (br, 1H, NH), 6.34-6.38 (m, 2H), 7.37 (m, 1H); ESI-MS: m/z 245.0 (M+H+) [M = $C_8H_6Cl_2N_4O$, exact mass 245.06]

Synthesis of 6-dichloro-n-furfuryl-n'-propargyl-1,3,5-triazine-2,4-diamine. To a vigorously stirred solution of 4,6-dichloro-n-furfuryl-1,3,5-triazine-2-amine (0.5 g, 2.04 mmol) dissolved in 3 mL THF in a 20 mL round-bottomed flask, 5 mL water at room temperature

were added. A mixture of propargylamine (0.11 g, 2.0 mmol) and $NaHCO_3$ (0.17 g, 2.02 mmol) in 5 mL of THF/water solution (1:1, v/v) was then added slowly. The reaction mixture was stirred at room temperature for 6 hr. The resulting white precipitate was diluted with 20 mL of cold water, filtered, rinsed with more cold water, and dried in vacuo to give 6-dichloro-n-furfuryl-n'-propargyl-1,3,5-triazine-2,4-diamine as a white solid (0.49 g, 92%). ^1H NMR (CD_6SO, δ) 3.11 (s, 1H), 4.04 (m, 2H), 4.47 (m, 2H), 6.34 (m, 2H), 7.59 (m, 1H), 8.28 (m, 2H, 2 x NH) ; ESI-MS: m/z 264.1 (M+H+) [M = $C_{11}H_{10}ClN_5O$, exact mass 263.69]

Grafting triazinyl dyes on BC. BC was labelled using the rhodamine-based dye DTPR or the fluorescein-based dye DTAF in a one-step reaction using final cellulose, dye and base (NaOH) concentrations of 0.1 wt%, 1 mM and 0.1 M, respectively. The reaction proceeded in the dark at room temperature for 24 hr while mixing (Multi-Purpose Tube Rotator US, Fisherbrand, Ottawa, ON, CA) and free dye was removed through repeated cycles of centrifugation (21,100×g, 30 s, Sorvall Legend Micro 21R Centrifuge, Thermo Scientific), decanting and resuspension with 1× PBS (6 times) then water (3 times). Samples were re-dispersed after every third spin down using a ¼ inch point-probe (Branson SLPt, 40% amplitude, or 60 W, for 10 s) to liberate any unreacted dye trapped within cellulose aggregates.

Grafting Cy5-azide on nanocellulose materials. BC, CNCs, CNFs and CM-CNFs dispersed in a 3:1 mixture of water:acetone were first derivatized with DTAP linker using final cellulose, DTAP and NaOH concentrations of 0.1 wt%, 10 mM and 0.05 M, respectively. The reaction proceeded at room temperature for 24 hr while mixing and unreacted linker was removed from BC and CNF samples using the procedure described above with the following washing cycles: 3x water, 3x 1X PBS, 3x water. CM-CNFs and CNCs were difficult to pellet and therefore were cleaned with stirred cell dialysis (Amicon Stirred Cell 50 mL with Biomax 300 kDa Ultrafiltration Discs, Millipore Sigma, Oakville, ON, Canada) with 10 volume equivalents of water, 1X PBS, then water. CNCs were then extensively dispersed through point-probe sonication (60 W, 2 s on/off cycles, 3 minutes) while on ice.

Through centrifugation or stirred-cell dialysis, DTAP-functionalized cellulose was exchanged into 1× PBS containing 10% methanol and fluorescently labelled with Cy5 azide through a CuAAC click-reaction with final cellulose, dye, ascorbic acid and $CuSO_4$ concentrations of 0.1 wt%, 10 μM, 5 mM and 0.3 mM. The concentration of dye was also varied between 5 μM and 100 μM when labelling BC in order to tune the degree of labelling for optimized super-resolution imaging. The reaction proceeded at room temperature for 2 hr in the dark while mixing. Unreacted dye was removed and collected for determining the degree of labelling, using the same procedure described in the first step.

Grafting 6-FAM-azide on BC. DTAP linker was grafted onto BC in the same fashion as described above using various concentrations of NaOH, linker and mixture ratios of water:acetone. The click-reaction of 6-FAM azide dye with functionalized BC was performed similarly to the previous procedure but in a 1:1 mixture of water:methanol in order to solubilize the dye.

Orthogonal, dual-labelling of BC. A triazinyl linker bearing alkyne and furfuryl functional groups (of 6-dichloro-n-furfuryl-n'-propargyl-1,3,5-triazine-2,4-diamine) was grafted onto cellulose in a 3:1 water:acetone mixture containing 0.05 M NaOH, 10 mM linker and 0.1 wt% BC at 60 °C for 24 hr. Unreacted linker was washed using the same procedure written above and 6-FAM maleimide (0.5 mM) and Cy5 azide (0.5 mM) were grafted onto 0.1 wt% of functionalized cellulose suspended in 1× PBS through a one-pot reaction containing 0.3 mM $CuSO_4$ and 5 mM ascorbic acid at 60 °C for 24 hr.

Epifluorescence and super-resolution imaging of cellulose particles.

Microscope setup. Fluorescence microscopy images were acquired using a Leica DMI6000 B inverted fluorescence microscope equipped with a 100×/1.47NA HCXPLAPO oil-immersion objective. Illumination was provided by solid-state lasers housed within an Integrated Light Engine (ILE, Spectral Applied Research, Richmond Hill, ON, Canada) that controls illumination intensity and couples laser lines (405 nm, 488 nm, 561 nm and 647 nm) to a single output fiber. The laser light was coupled to the objective using a Borealis module (Spectral Applied Research, Richmond Hill, ON, Canada) using full field illumination and the samples were imaged in widefield epifluorescence mode. Emission light was directed towards the appropriate colour filter (460/50 nm, 525/50 nm, 593/40 nm or 700/75 nm) by a multiline dichroic mirror and the image was captured using an iXon Ultra DU-897U (10 MHz readout mode, frame transfer ON, 3.30 μs vertical clock speed, electron-multiplying mode). The projected pixel size was measured to be 96 nm.

Sample preparation. Glass-bottom Petri dishes (Mattek Corporation, Ashland, MA) were treated with air plasma for 3 mins at 700 mTorr (Harrick Plasma, Ithaca, NY). In the case where fiducial markers were used for drift-correction, 70 μL of 170 nm orange fiducial beads at a concentration of ~$2x10^7$ beads/mL (1:20,000 dilution) in 1:1 water:methanol were drop-casted and dried at 55 °C. Fluorescently labelled cellulose samples were prepared by drop casting 100 μL of a 0.01 wt% cellulose solution and drying at 55 °C for 10 minutes then washing three times with water before imaging.

Image acquisition. Epifluorescence images were acquired in Tris buffer under oxygen-scavenging conditions (50 mM Tris, pH 8.0, 10 mM NaCl, 10% glucose w/w, 84 u/mL glucose

oxidase and 510 u/mL catalase). Super-resolution images were also acquired in this buffer with the addition of 100 mM cysteamine.

STORM super-resolution images were acquired using maximum power (0.49 kW/cm^2) and a camera frame rate and exposure time of 30 Hz and 30 ms, respectively. Images of Cy5-BC with various degrees of labelling were acquired through a 12,000-frame image sequence without fluorophore re-activation by the 405 nm laser. Optimized super-resolution imaging of BC labelled using 10 μM Cy5 involved a 40,000 frame acquisition with dye re-activation using the 405 nm laser. Due to the high brightness of orange fiducial beads, it was possibly to simultaneously image them on the Cy5 channel using low power excitation (<0.1 kw/cm^2) with the 561 nm laser.

Image and data analysis. Average fluorescence intensities of individual BC fibrils were based on epifluorescence images and determined by manually tracing them in ImageJ software with the segmented-line tool using a thickness of 18 pixels.

Localization-fitting analysis for STORM acquisitions was performed using the ThunderSTORM[41] ImageJ plugin by applying a B-spline wavelet filter, approximating molecular positions through the local maximum method and calculating sub-pixel localizations by fitting a 2-dimesional integrated Gaussian function using the weighted least squares method (Figure S3.14). Single emitter molecule localizations were selected using the following filter parameters: sigma<(mean(sigma)+std(sigma)) & sigma>(mean(sigma)-std(sigma*1.3)) & uncertainty<40 & uncertainty >5 & intensity<1500. Sample drift was corrected using the cross-correlation method or by fiducial markers and consecutive emissions (with an OFF tolerance of 1 frame) within a 20 nm radius were merged. Average localization uncertainties of all STORM acquisitions were ~15 nm. Super-resolution image was rendered using the averaged shifted histograms method with a magnification factor of 10 (9.61 nm pixel size).

Molecular localization densities along individual fibrils were determined by manually tracing fibrils in super-resolution images with the segmented line tool in ImageJ using a line width of 34 (330 nm) pixels. The drawn regions-of-interest (ROIs) were converted from a line to area format ("Line to Area" in ImageJ) and the pixel perimeter was used to select the localizations associated with each traced fibril through a custom written MATLAB program (Figure S3.1). Fibrils possessing relatively high fluorescence were avoided as those likely represented fibril bundles as opposed to individual microfibrils, which were the objects of interest. Localization density frame traces for each sample were based on average values of at least 10 fibrils from >3 super-resolution images.

Determining degree of labelling of Cy5-labelled cellulose. Cellulose degree of labelling was calculated from the remaining amount of unreacted dye present in the first three eluates or supernatants collected during washing. Residual dye fluorescence was top read in a black Greiner 96-well transparent bottom plate using a Tecan Infinite 200 plate reader (Tecan Group Ltd, Männedorf, canton of Zürich, Switzerland). Measurements were acquired in 1× PBS buffer using excitation and emission wavelength/bandwidth of 646/9 nm and 730/20 nm, respectively, and dye concentrations were calculated using a Cy5 calibration curve (0 – 500 nM range). A correction factor based on the ratio of Cy5 fluorescence in PBS vs PBS containing 5 mM ascorbic acid and 0.3 mM $CuSO_4$ was used to account for the quenching of Cy5 fluorescence caused by the presence of copper in the supernatant. Degree of labelling of Cy5-CNCs was also determined by directly measuring the fluorescence of a 0.01 wt% solution and calculating the Cy5 concentration through the calibration curve.

The number of Cy5 molecules present on each CNC was calculated similarly to previous work, where the degree of labelling in μmol/g is converted to dye/particle based on the mass of an individual CNC.[31] This was calculated to be 2.8×10^{-18} g, assuming that each CNC is a cylinder that is 4.5 nm in diameter and 110 nm in length with a density of 1.6 g/mL.[32]

Atomic force microscopy imaging. BC and CNFs at a concentration of 0.01 wt% were drop-casted and dried on glass coverslips while CNCs and CM-CNFs at a concentration of 1 ppm were prepared on glass coverslips through layer-by-layer polyelectrolyte dip-coating using poly(allylamine hydrochloride) (PAH) as a binding agent, as described previously.[42] AFM images were acquired with a Bruker Dimension Icon AFM (Bruker Corporation, Billerica, MA) using a Bruker RFESP-75 AFM tip (k = 3 N/m). AFM images were processed and analyzed using Gwyddion open-source software.[43]

Determination of percent crystallinity using powdered X-ray diffraction. X-ray diffraction was performed at the McMaster Analytical X-ray (MAX) Diffraction Facility to determine the percent crystallinity of the samples. Films were deposited on (100) low background silicon wafers with a native oxide layer. A Bruker D8 DISCOVER diffractometer equipped with an Eiger2R 500K area detector positioned 20 cm from the sample and $CoK\alpha_{avg}$ radiation (λ=1.79026Å). Data was collected for a silicon wafer blank, which was subtracted from each measurement to account for scattering contribution to the sample data. Rietveld refinement (Topas v5, Bruker AXS) was used to model the crystalline and amorphous components of the profiles to determine the percent crystallinity. Crystallographic information files for cellulose I_α and I_β forms were obtained from the ICSD for modelling the crystalline component. A peak was inserted at 24.1° 2θ (fixed position) to model the amorphous contribution to the profile. Peak shapes were fitted with a pseudo-Voigt function

(PV TCHZ parameters U, V, W, and X). Preferred orientation was modelled with spherical harmonics and unit cell parameters were allowed to refine. A background function of 1/x was applied to account for air scatter.

Acknowledgments

Mouhanad Babi was supported through a Natural Sciences and Engineering Research Council (NSERC) of Canada Graduate Scholarship – Doctoral Award. Jose Moran-Mirabal is the Tier 2 Canada Research Chair in Micro and Nanostructured Materials and the recipient of an Early Researcher Award from the Ontario Ministry of Research and Innovation.

Author Contributions

MB analyzed and interpreted results and wrote first draft of the manuscript. AF synthesized DTAF, DTAP, DTPR and the bifunctional linker. MB and XI labelled cellulose samples and measured the degree of labelling. MB and CC acquired super-resolution and epifluorescence images and measured fibril intensities. VJ performed X-ray diffraction measurements. TA produced enzyme pre-treated CNF and carboxymethylated-CNF cellulose materials. JMM interpreted data, conceptualized the work and edited the manuscript. The final draft of the manuscript was reviewed and approved by all authors.

Competing Interests

The authors declare no competing interests.

References

1. Klemm, D., Heublein, B., Fink, H. P. & Bohn, A. Cellulose: Fascinating biopolymer and sustainable raw material. *Angewandte Chemie - International Edition* vol. 44 3358–3393 (2005).

2. Habibi, Y., Lucia, L. A. & Rojas, O. J. Cellulose nanocrystals: Chemistry, self-assembly, and applications. *Chemical Reviews* **110**, 3479–3500 (2010).

3. Petersen, N. & Gatenholm, P. Bacterial cellulose-based materials and medical devices: Current state and perspectives. *Applied Microbiology and Biotechnology* vol. 91 1277–1286 (2011).

4. Zhang, T., Yang, L., Yan, X. & Ding, X. Recent Advances of Cellulose-Based Materials and Their Promising Application in Sodium-Ion Batteries and Capacitors. *Small* **14**, 1802444 (2018).

5. Li, M., Li, X., Xiao, H. & James, T. D. Fluorescence Sensing with Cellulose-Based Materials. *ChemistryOpen* **6**, 685–696 (2017).

6. de France, K. J. *et al.* Tissue Response and Biodistribution of Injectable Cellulose Nanocrystal Composite Hydrogels. *ACS Biomaterials Science and Engineering* **5**, 2235–2246 (2019).

7. Sarparanta, M. *et al.* Multimodality labeling strategies for the investigation of nanocrystalline cellulose biodistribution in a mouse model of breast cancer. *Nuclear Medicine and Biology* **80–81**, 1–12 (2020).

8. Mahmoud, K. A. *et al.* Effect of surface charge on the cellular uptake and cytotoxicity of fluorescent labeled cellulose nanocrystals. *ACS Applied Materials and Interfaces* **2**, 2924–2932 (2010).

9. Hosseinidoust, Z., Alam, M. N., Sim, G., Tufenkji, N. & Ven, T. G. M. van de. Cellulose nanocrystals with tunable surface charge for nanomedicine. *Nanoscale* **7**, 16647–16657 (2015).

10. Endes, C. *et al.* Fate of Cellulose Nanocrystal Aerosols Deposited on the Lung Cell Surface In Vitro. *Biomacromolecules* **16**, 1267–1275 (2015).

11. de France, K. J. *et al.* 2.5D Hierarchical Structuring of Nanocomposite Hydrogel Films Containing Cellulose Nanocrystals. *ACS Applied Materials and Interfaces* **11**, 41 (2019).

12. Haghpanah, J. S. *et al.* Bionanocomposites: Differential Effects of Cellulose Nanocrystals on Protein Diblock Copolymers. *Biomacromolecules* **14**, 4360–4367 (2013).

13. Helbert, W., Chanzy, H., Husum, T. L., Schülein, M. & Ernst, S. Fluorescent cellulose microfibrils as substrate for the detection of cellulase activity. *Biomacromolecules* **4**, 481–487 (2003).

14. Rose, M., Babi, M. & Moran-Mirabal, J. The study of cellulose structure and depolymerization through single-molecule Methods. *Industrial Biotechnology* **11**, 16–23 (2015).

15. Luterbacher, J. S., Walker, L. P. & Moran-Mirabal, J. M. Observing and modeling BC degradation by commercial cellulase cocktails with fluorescently labeled Trichoderma reseii Cel7A through confocal microscopy. *Biotechnology and Bioengineering* **110**, 108–117 (2013).

16. Moran-Mirabal, J. M., Bolewski, J. C. & Walker, L. P. Thermobifida fusca cellulases exhibit limited surface diffusion on bacterial micro-crystalline cellulose. *Biotechnology and Bioengineering* **110**, 47–56 (2013).

17. Moran-Mirabal, J. M., Santhanam, N., Corgie, S. C., Craighead, H. G. & Walker, L. P. Immobilization of cellulose fibrils on solid substrates for cellulase-binding studies through quantitative fluorescence microscopy. *Biotechnology and Bioengineering* **101**, 1129–1141 (2008).

18. Nielsen, L. J., Eyley, S., Thielemans, W. & Aylott, J. W. Dual fluorescent labelling of cellulose nanocrystals for pH sensing. *Chemical Communications* **46**, 8929–8931 (2010).

19. Dong, S. & Roman, M. Fluorescently labeled cellulose nanocrystals for bioimaging applications. *Journal of the American Chemical Society* **129**, 13810–13811 (2007).

20. Navarro, J. R. G. *et al.* Multicolor Fluorescent Labeling of Cellulose Nanofibrils by Click Chemistry. *Biomacromolecules* **16**, 1293–1300 (2015).

21. Zhou, J. *et al.* Synthesis of Multifunctional Cellulose Nanocrystals for Lectin Recognition and Bacterial Imaging. *Biomacromolecules* **16**, 1426–1432 (2015).

22. Huang, J.-L., Li, C.-J. & Gray, D. G. Cellulose Nanocrystals Incorporating Fluorescent Methylcoumarin Groups. *ACS Sustainable Chemistry and Engineering* **1**, 1160–1164 (2013).

23. Grate, J. W. *et al.* Alexa Fluor-Labeled Fluorescent Cellulose Nanocrystals for Bioimaging Solid Cellulose in Spatially Structured Microenvironments. *Bioconjugate Chemistry* **26**, 593–601 (2015).

24. Reid, M. S., Karlsson, M. & Abitbol, T. Fluorescently labeled cellulose nanofibrils for detection and loss analysis. *Carbohydrate Polymers* **250**, 116943 (2020).

25. Abitbol, T., Palermo, A., Moran-Mirabal, J. M. & Cranston, E. D. Fluorescent labeling and characterization of cellulose nanocrystals with varying charge contents. *Biomacromolecules* **14**, 3278–3284 (2013).

26. Fatona, A., Berry, R. M., Brook, M. A. & Moran-Mirabal, J. M. Versatile Surface Modification of Cellulose Fibers and Cellulose Nanocrystals through Modular Triazinyl Chemistry. *Chemistry of Materials* **30**, 2424–2435 (2018).

27. Habibi, Y. Key advances in the chemical modification of nanocelluloses. *Chemical Society reviews* **43**, 1519–42 (2014).

28. Dempsey, G. T., Vaughan, J. C., Chen, K. H., Bates, M. & Zhuang, X. Evaluation of fluorophores for optimal performance in localization- based super-resolution imaging. *Nature methods* **8**, 1–44 (2011).

29. Spectrum [Rhodamine 6G] | AAT Bioquest. https://www.aatbio.com/fluorescence-excitation-emission-spectrum-graph-viewer/Rhodamine_6G.

30. 5-DTAF [5-(4,6-Dichlorotriazinyl)aminofluorescein] *CAS 51306-35-5* | AAT Bioquest. https://www.aatbio.com/products/5-dtaf-5-4-6-dichlorotriazinyl-aminofluorescein-cas-51306-35-5#jump_references.

31. Leng, T., Jakubek, Z. J., Mazloumi, M., Leung, A. C. W. & Johnston, L. J. Ensemble and Single Particle Fluorescence Characterization of Dye-Labeled Cellulose Nanocrystals. *Langmuir* **33**, 8002–8011 (2017).

32. Stefaniak, A. B., Seehra, M. S., Fix, N. R. & Leonard, S. S. Lung biodurability and free radical production of cellulose nanomaterials. *Inhalation toxicology* **26**, 733 (2014).

33. Jia, R. *et al.* Amine-responsive cellulose-based ratiometric fluorescent materials for real-time and visual detection of shrimp and crab freshness. *Nature Communications* **10**, 1–8 (2019).

34. van de Linde, S. *et al.* Direct stochastic optical reconstruction microscopy with standard fluorescent probes. *Nature protocols* **6**, 991–1009 (2011).

35. van de Linde, S., Wolter, S., Heilemann, M. & Sauer, M. The effect of photoswitching kinetics and labeling densities on super-resolution fluorescence imaging. *Journal of Biotechnology* **149**, 260–266 (2010).

36. Halib, N., Amin, M. C. I. M. & Ahmad, I. Physicochemical Properties and Characterization of Nata de Coco from Local Food Industries as a Source of Cellulose. *Sains Malaysiana 41(2)* 205–211 (2012).

37. Lars, W. *et al.* The Build-Up of Polyelectrolyte Multilayers of Microfibrillated Cellulose and Cationic Polyelectrolytes. *Langmuir* **24**, 784–795 (2008).

38. Henriksson, M., Henriksson, G., Berglund, L. A. & Lindström, T. An environmentally friendly method for enzyme-assisted preparation of microfibrillated cellulose (MFC) nanofibers. *European Polymer Journal* **43**, 3434–3441 (2007).

39. Toyosaki, H. & Naritomi, T. Screening of Bacterial Cellulose-producing Acetobacter Strains Suitable for Agitated Culture. *Biosci. Biotech. …* **59**, 1498–1502 (1995).

40. Blakeslee, D. & Baines, M. G. Immunofluorescence using dichlorotriazinylaminofluorescein (DTAF) I. Preparation and fractionation of labelled IgG. *Journal of Immunological Methods* (1976) doi:10.1016/0022-1759(76)90078-8.

41. Ovesný, M., Křížek, P., Borkovec, J., Švindrych, Z. & Hagen, G. M. ThunderSTORM: A comprehensive ImageJ plug-in for PALM and STORM data analysis and super-resolution imaging. *Bioinformatics* **30**, 2389–2390 (2014).

42. Gill, U. *et al.* Beyond buckling: Humidity-independent measurement of the mechanical properties of green nanobiocomposite films. *Nanoscale* **9**, 7781–7790 (2017).

43. Nečas, D. & Klapetek, P. Gwyddion: An open-source software for SPM data analysis. *Central European Journal of Physics* vol. 10 181–188 (2012).

Chapter 3 Supplementary Information

Efficient labelling of cellulose microfibrils and cellulose nanocrystals for high-resolution fluorescence microscopy applications

Mouhanad Babi,[1] Ayodele Fatona,[1] Xiang Li,[1] Christine Cerson,[1] Victoria M. Jarvis,[2] Tiffany Abitbol[3] and Jose M. Moran-Mirabal[1,4]*

[1] *Department of Chemistry and Chemical Biology, McMaster University, Hamilton, ON, Canada*

[2] *McMaster Analytical X-ray Diffraction Facility, McMaster University, Hamilton, ON, Canada*

[3] *RISE Research Institutes of Sweden, Stockholm, Sweden*

[4] *Centre for Advanced Light Microscopy, McMaster University, Hamilton, ON, Canada*

*Please address all correspondence to Jose Moran-Mirabal (mirabj@mcmaster.ca)

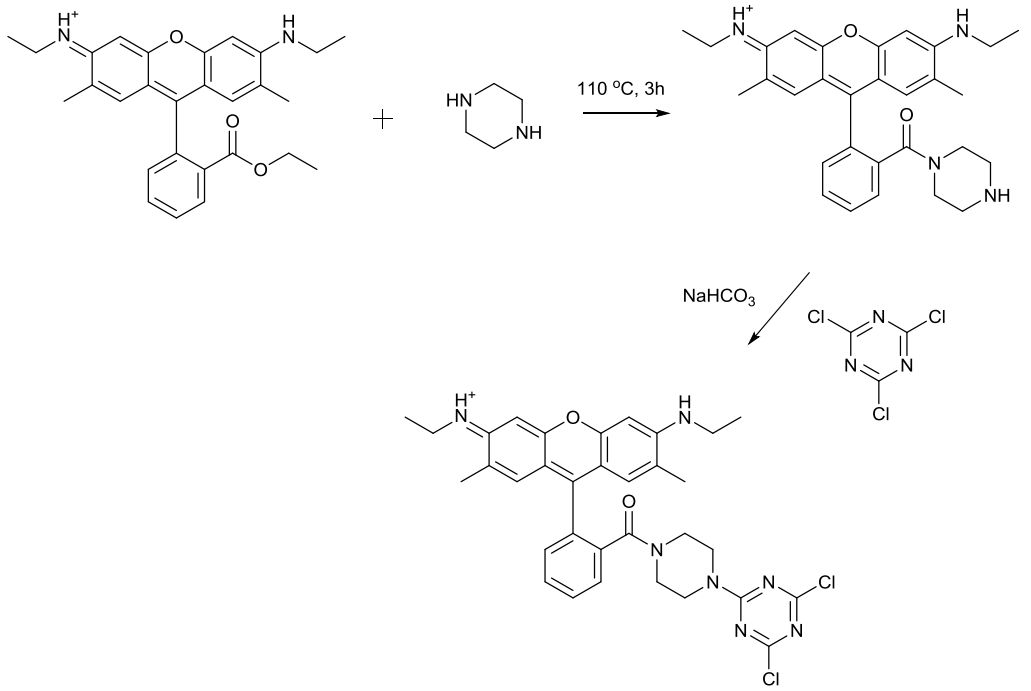

Scheme S3.1. Synthesis of dichlorotriaznyl piperazine rhodamine 6G (DTPR).

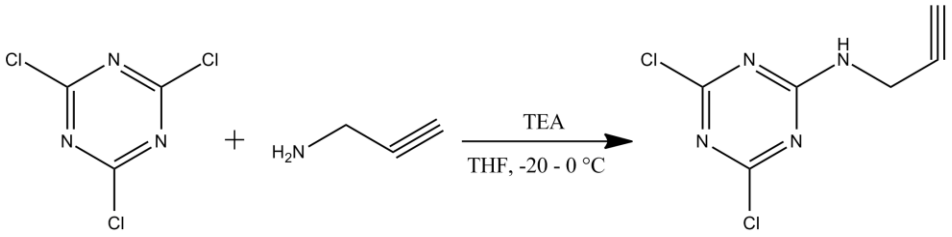

Scheme S3.2. Synthesis of dichlorotriaznyl propargyl amine (DTAP).

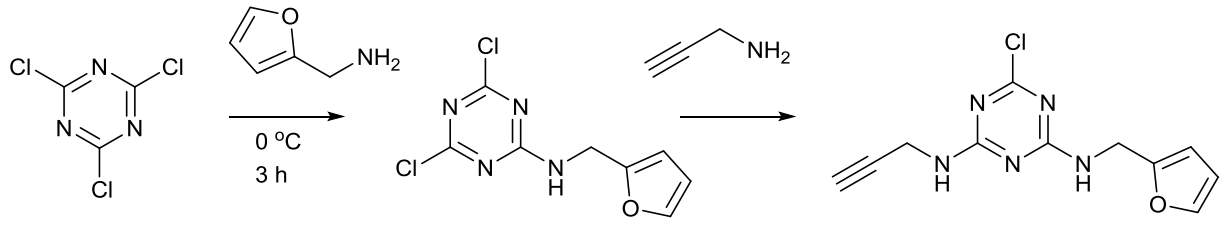

Scheme S3.3. Synthesis of a triaznyl linker that is bi-functionalized with furfuryl and alkyl groups (6-dichloro-n-furfuryl-n'-propargyl-1,3,5-triazine-2,4-diamine).

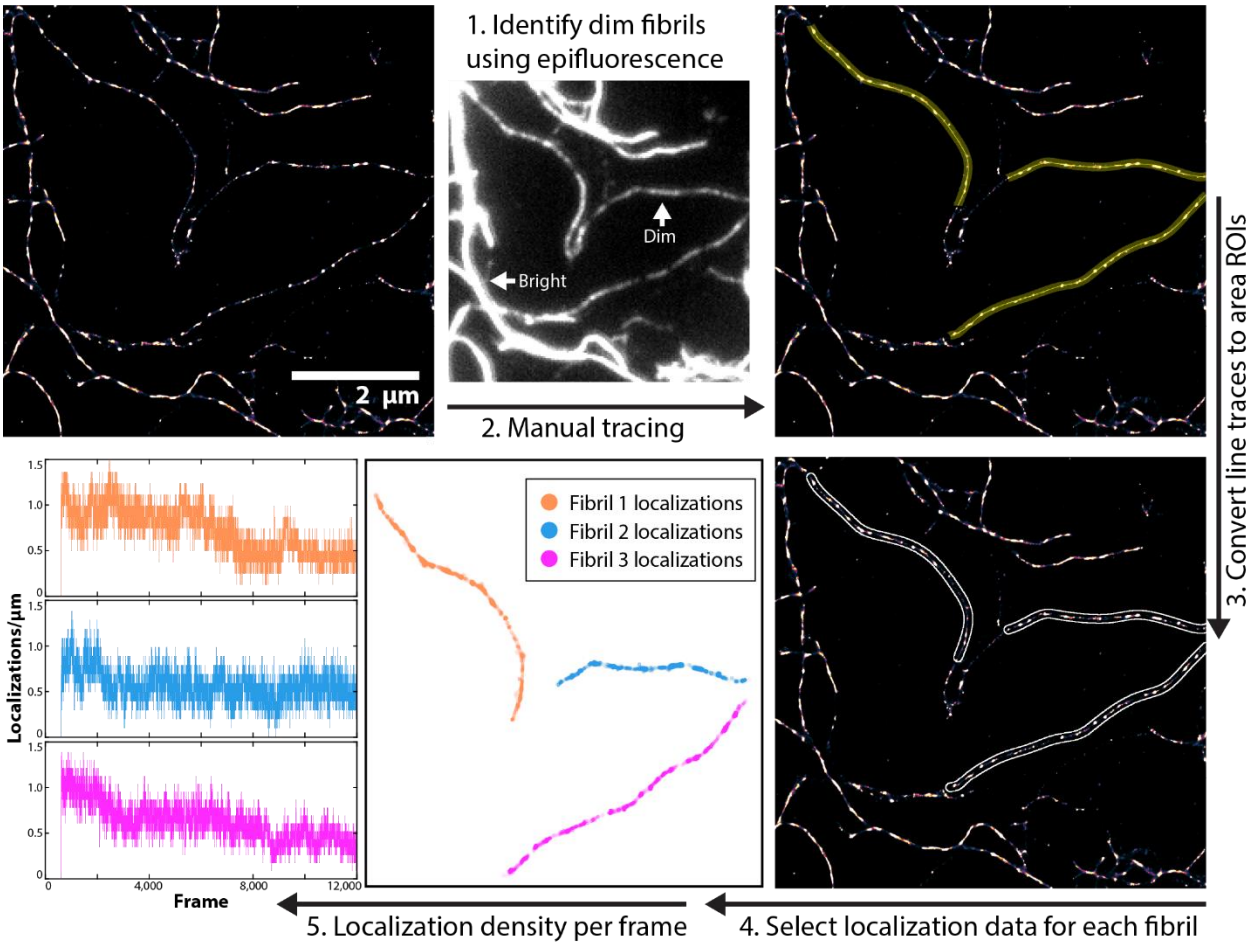

Figure S3.1. Localization data segmentation for individual fibrils. A diffraction-limited image of Cy5-BC was used to identify individual microfibrils based on their low fluorescence intensity. The fibrils were manually traced in the super-resolution image using the segmented line tool (width of 34 pixels) in ImageJ. The line trace is converted to an area ROI, which can be imported into a custom-written MATLAB program to segment the localization data for each fibril and determine their localization density at each frame throughout the STORM acquisition. The localization density was calculated as the total number of localizations within the fibril ROI divided by the contour length of the traced fibril.

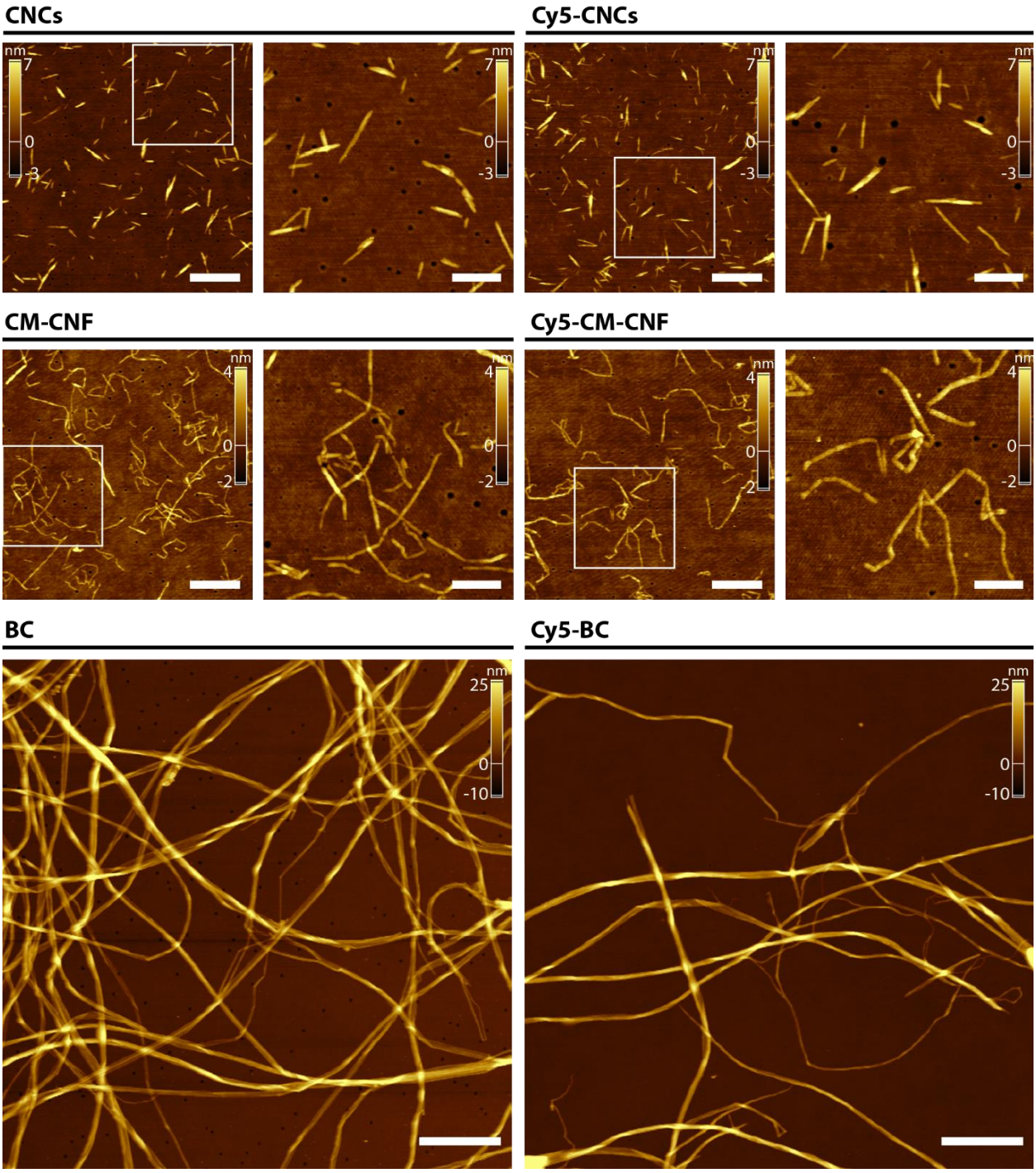

Figure S3.2. AFM height maps of fluorescently labelled and native CNCs, CM-CNFs and BC. Cellulose particles were prepared on glass coverslips either through dip-coating (for CNCs and CM-CNFs) or drop-casting (for BC) and imaged with AFM in tapping mode. Scale bars, 500 nm (top and middle row), 200 nm (insets), 1 μm (bottom row).

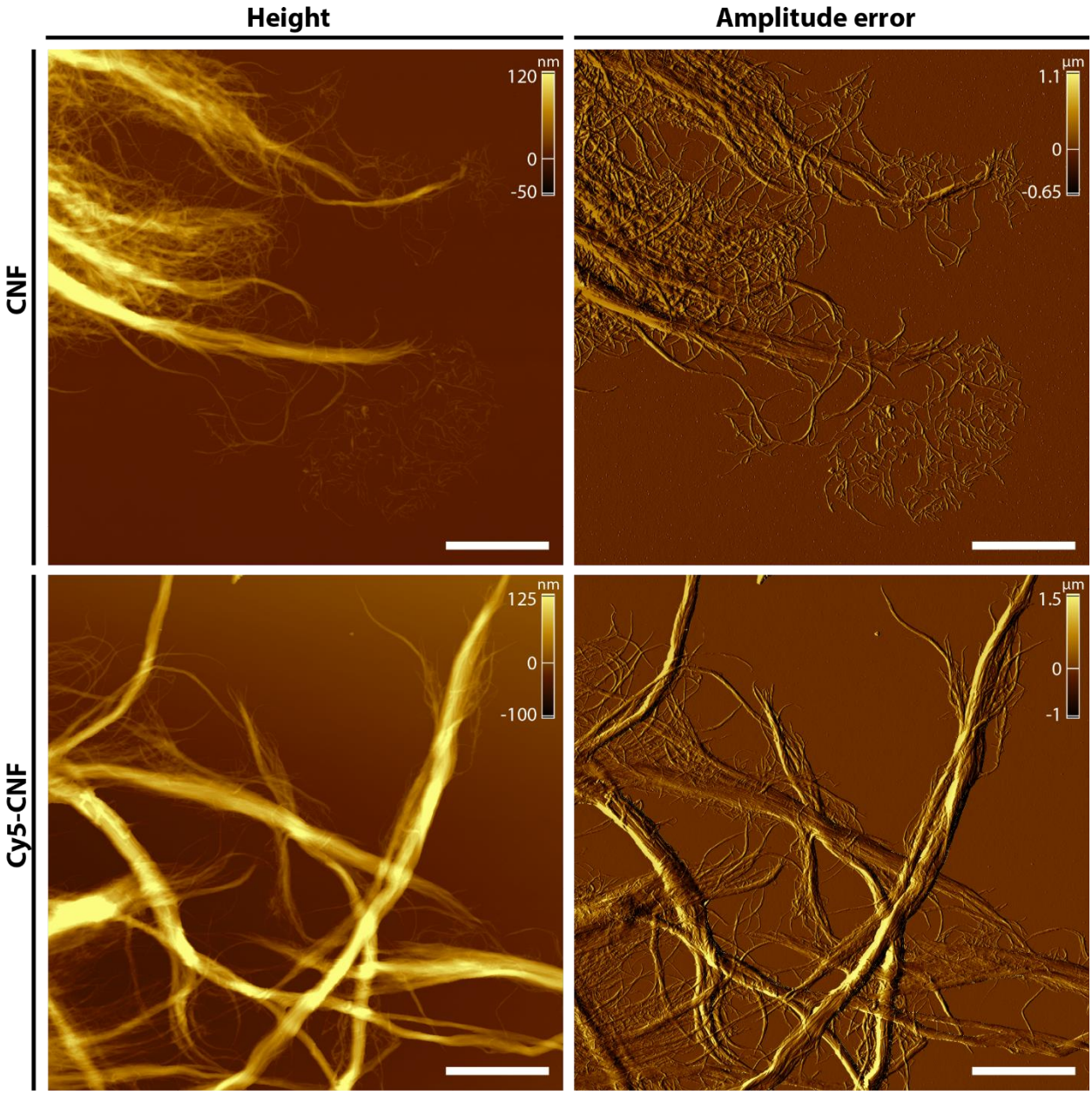

Figure S3.3. Height and error amplitude maps of labelled and enzyme-treated CNFs. CNFs were drop-casted and dried on glass coverslips and imaged with AFM in tapping mode. Amplitude error maps are displayed to clearly visualize both the thick bundles and nano-fibrillated cellulose. All scale bars are 2 µm.

Table S3.1. Height, length and percent crystallinity measurements of native and fluorescently labelled cellulose materials. The height and length of individual cellulose particles was measured through AFM by manually acquiring cross-sectional height profiles and tracing the contours of particles, respectively. Percent crystallinity was measured from XRD diffractograms using the peak-deconvolution method following background subtraction from a blank silicon wafer.

	Height (nm)	Length (nm)	%Cr
Cy5-CNCs	4.5 ± 1.5 (N>100)	110 ± 47 (N>100)	90%
CNCs	4.5 ± 1.5 (N>100)	110 ± 51 (N>100)	94%
Cy5-CM-CNFs	2.2 ± 0.6 (N>100)	360 ± 210 (N>70)	94%
CM-CNFs	2.5 ± 0.7 (N>100)	320 ± 150 (N>70)	91%
Cy5-BC	10.5 ± 4.5 (N>20)	N/A	92%
BC	8.9 ± 3.5 (N>20)	N/A	90%
Cy5-CNFs	3 – 100	N/A	87%
CNFs	3 – 100	N/A	89%

Mass and NMR spectra of synthesized compounds

All mass spectra were acquired using a Micromass Ultima (LC-ESI/APCI) Triple Quadrupole mass spectrometer. All ^{1}H NMR spectra were acquired using a Bruker AV600-600 MHz spectrometer, unless otherwise indicated.

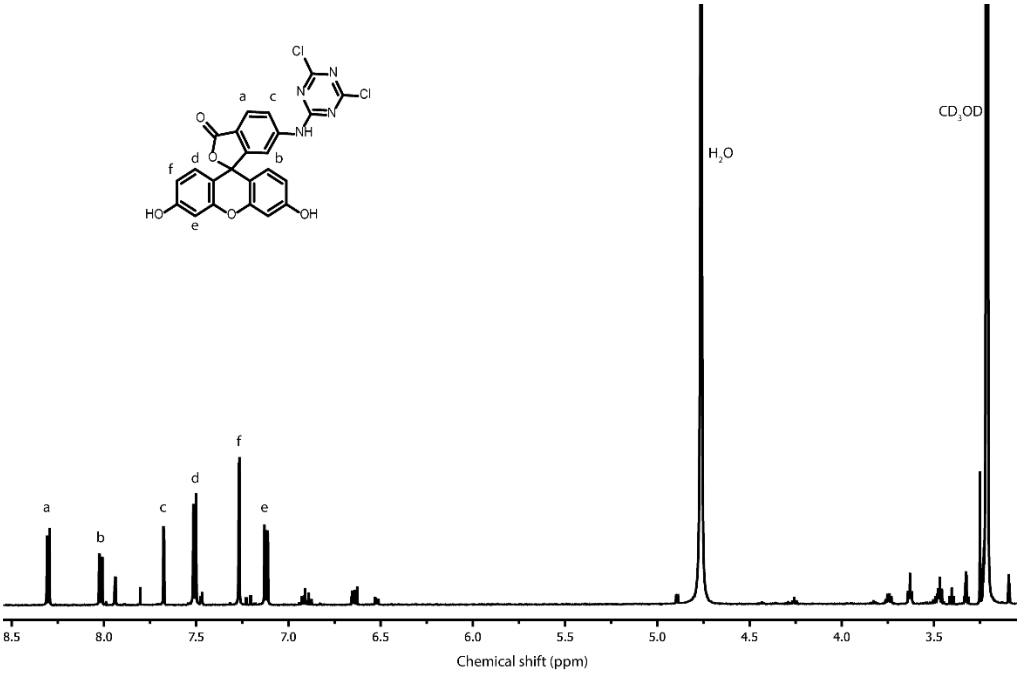

Figure S3.4. ^{1}H NMR spectrum of dichlorotriazine aminofluorescein (DTAF). The spectrum was acquired in deuterated methanol (CD_3OD).

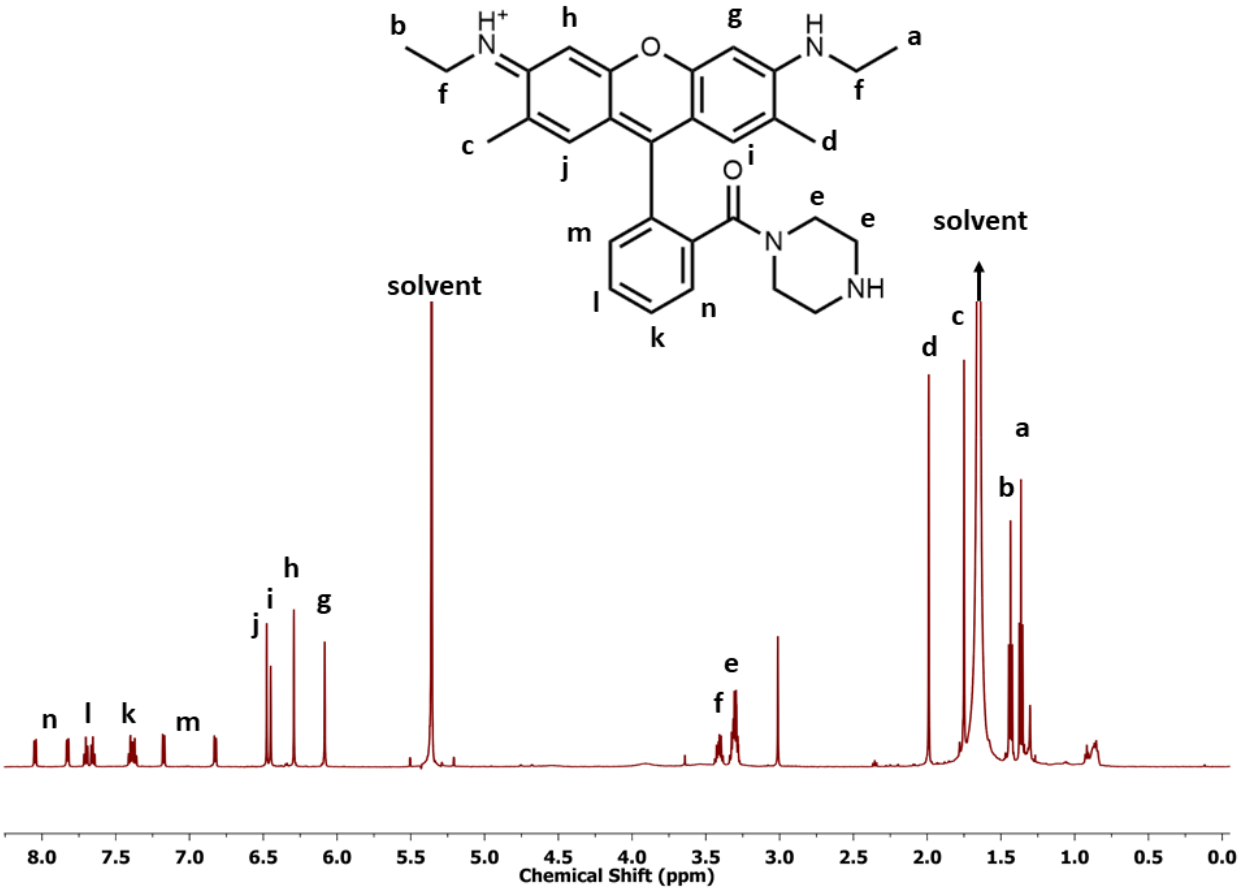

Figure S3.5. ^{1}H NMR spectrum of piperazine rhodamine 6G. The spectrum was acquired in deuterated dichloromethane (CD_2Cl_2). The upfield NMR solvent peak represents water.

a

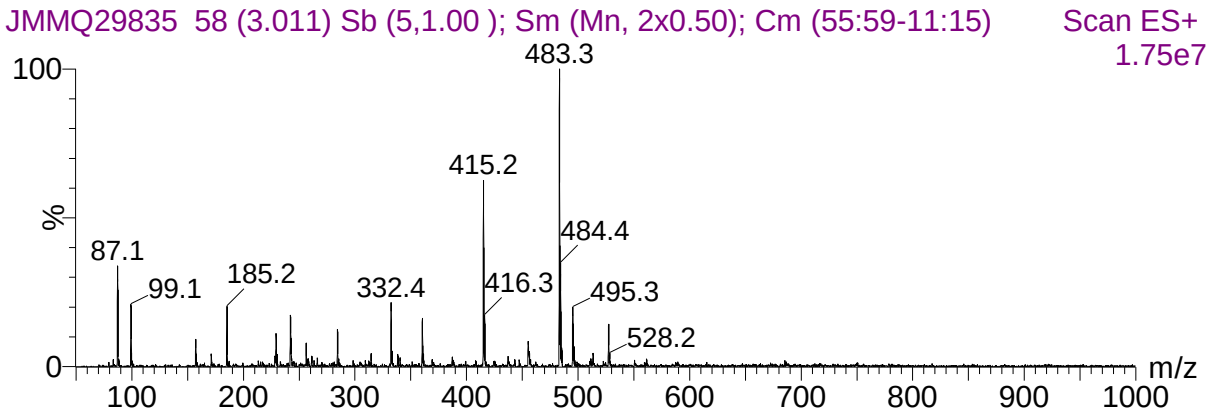

b

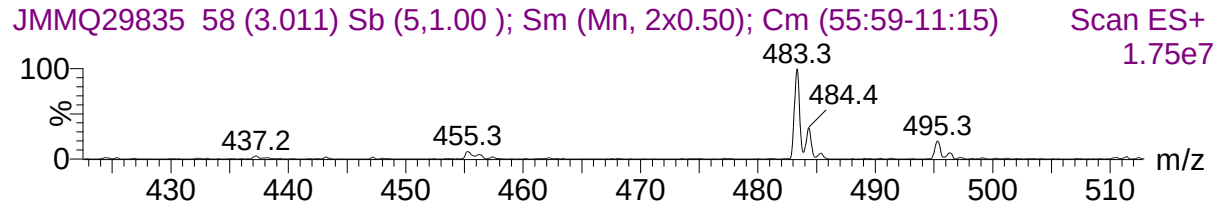

c

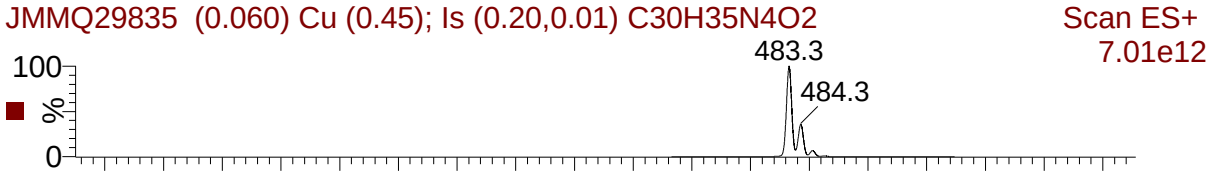

Figure S3.6. Mass spectrum of piperazine rhodamine 6G. a) The entire mass spectrum acquired through electrospray ionization in positive mode. **b)** An inset of the spectrum highlighting the most intense peaks in the 470 m/z region, which are in agreement with **(c)** the theoretical model MS spectrum calculated for the product $[M+H]^+$.

a

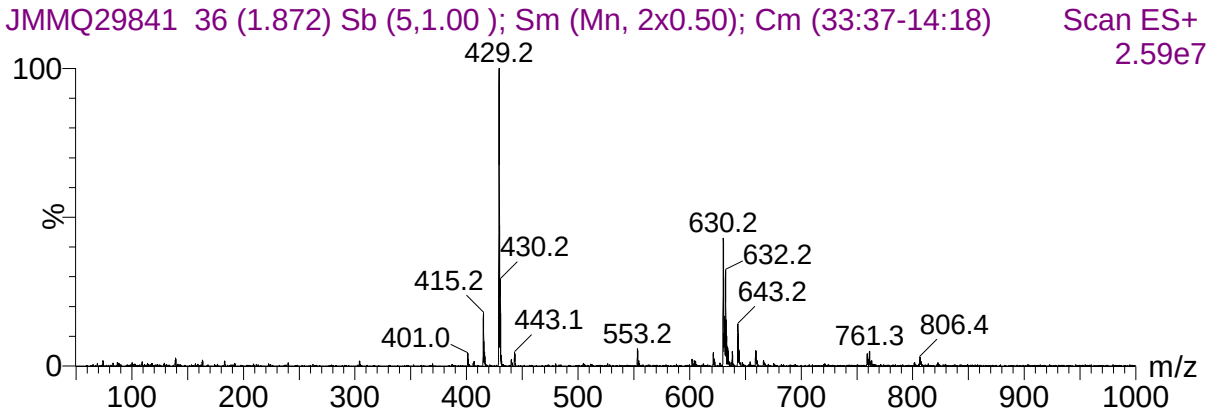

b

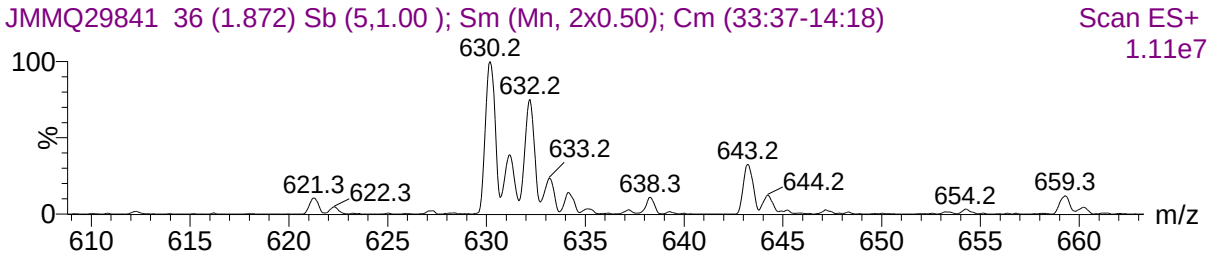

c

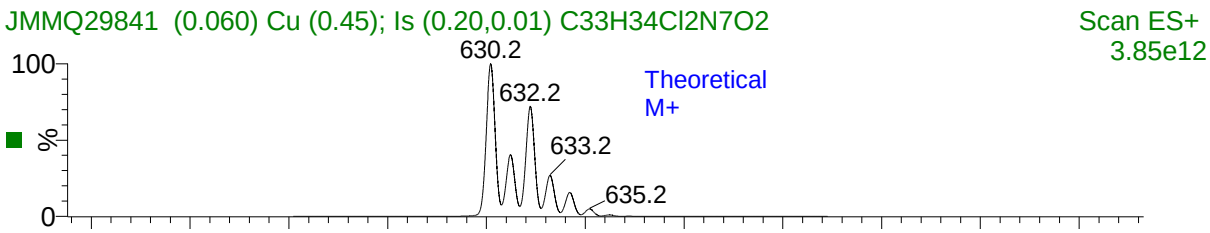

Figure S3.7. Mass spectrum of dichlorotriazine piperazine rhodamine 6G (DTPR). a) The entire mass spectrum acquired through electrospray ionization in positive mode. **b)** An inset of the spectrum highlighting the most intense peaks in the 635 m/z region, which are in agreement with **(c)** the theoretical model MS spectrum calculated for the produce $[M+H]^+$.

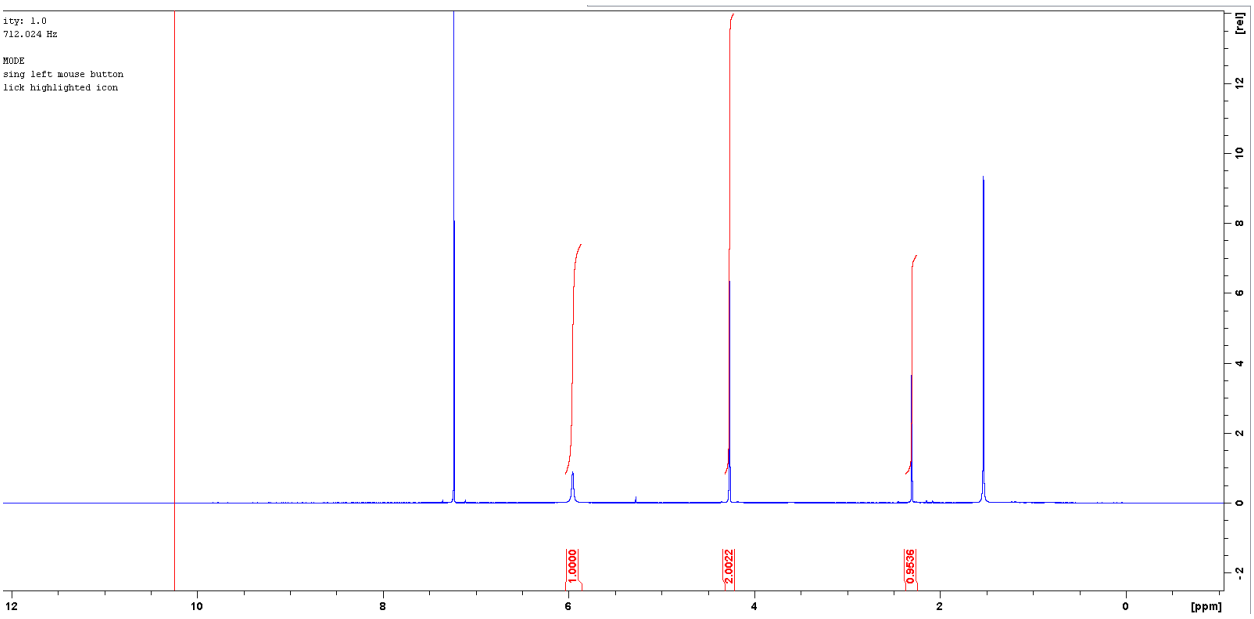

Figure S3.8. ^{1}H NMR spectrum of dichlorotriazine propargylamine (DTAP). The spectrum was acquired in deuterated dichloromethane (CD_2Cl_2) using a Bruker AV700 700 MHz NMR spectrometer.

a

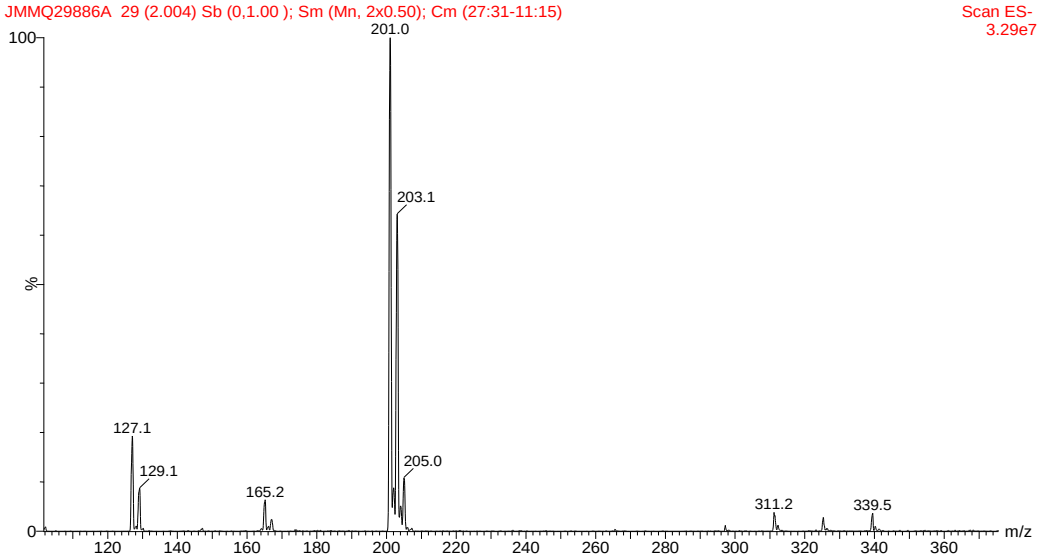

b

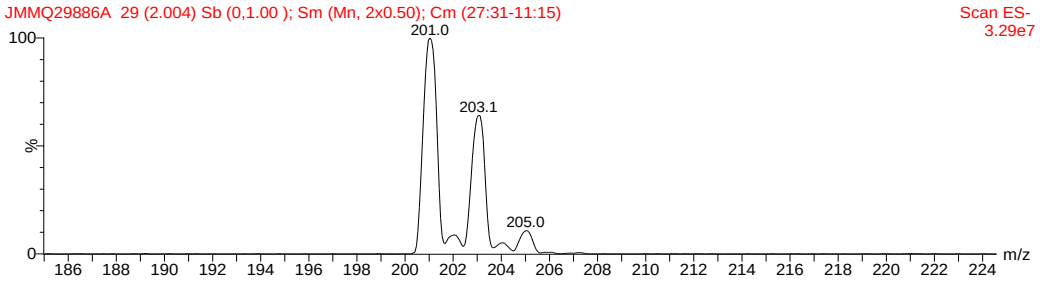

c

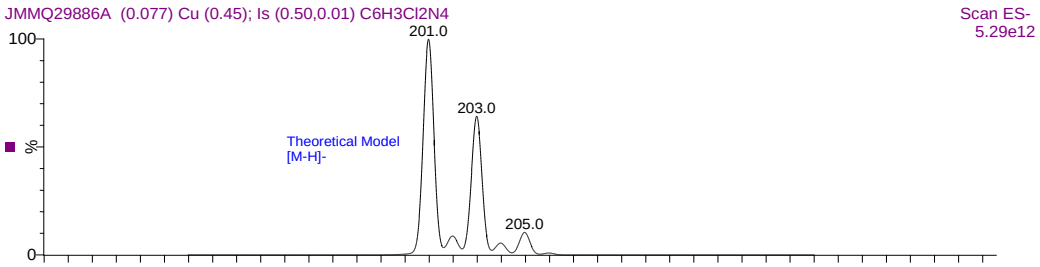

Figure S3.9. Mass spectrum of dichlorotriazine propargylamine (DTAP). a) The entire mass spectrum acquired through electrospray ionization in negative mode. **b)** An inset of the spectrum highlighting the most intense peaks in the 200 m/z region, which are in agreement with **(c)** the theoretical model MS spectrum calculated for DTAP $[M-H]^-$.

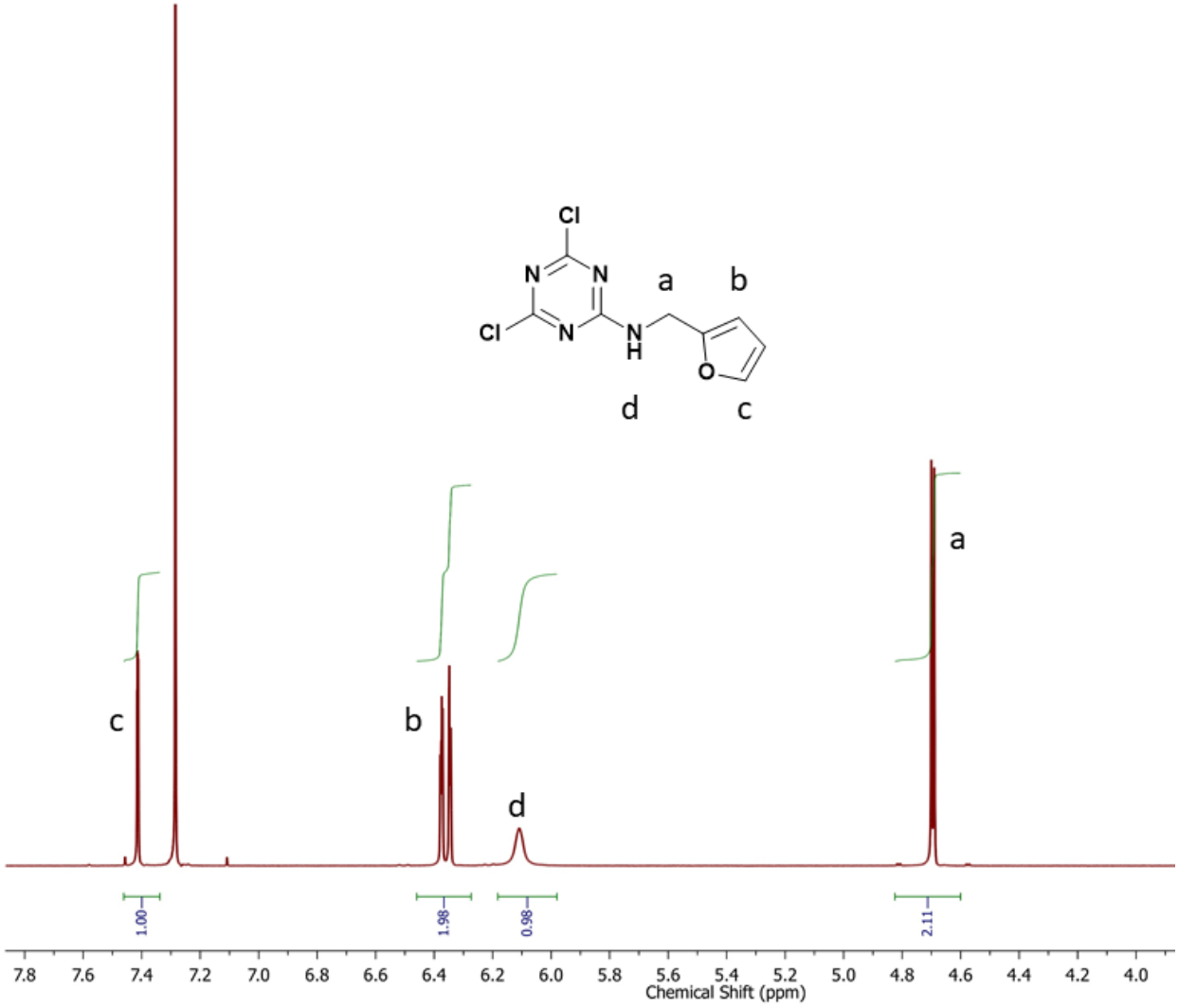

Figure S3.10. ^{1}H NMR spectrum of 4,6-dichloro-n-furfuryl-1,3,5-triazine-2-amine. The spectrum was acquired in deuterated chloroform ($CDCl_3$).

a

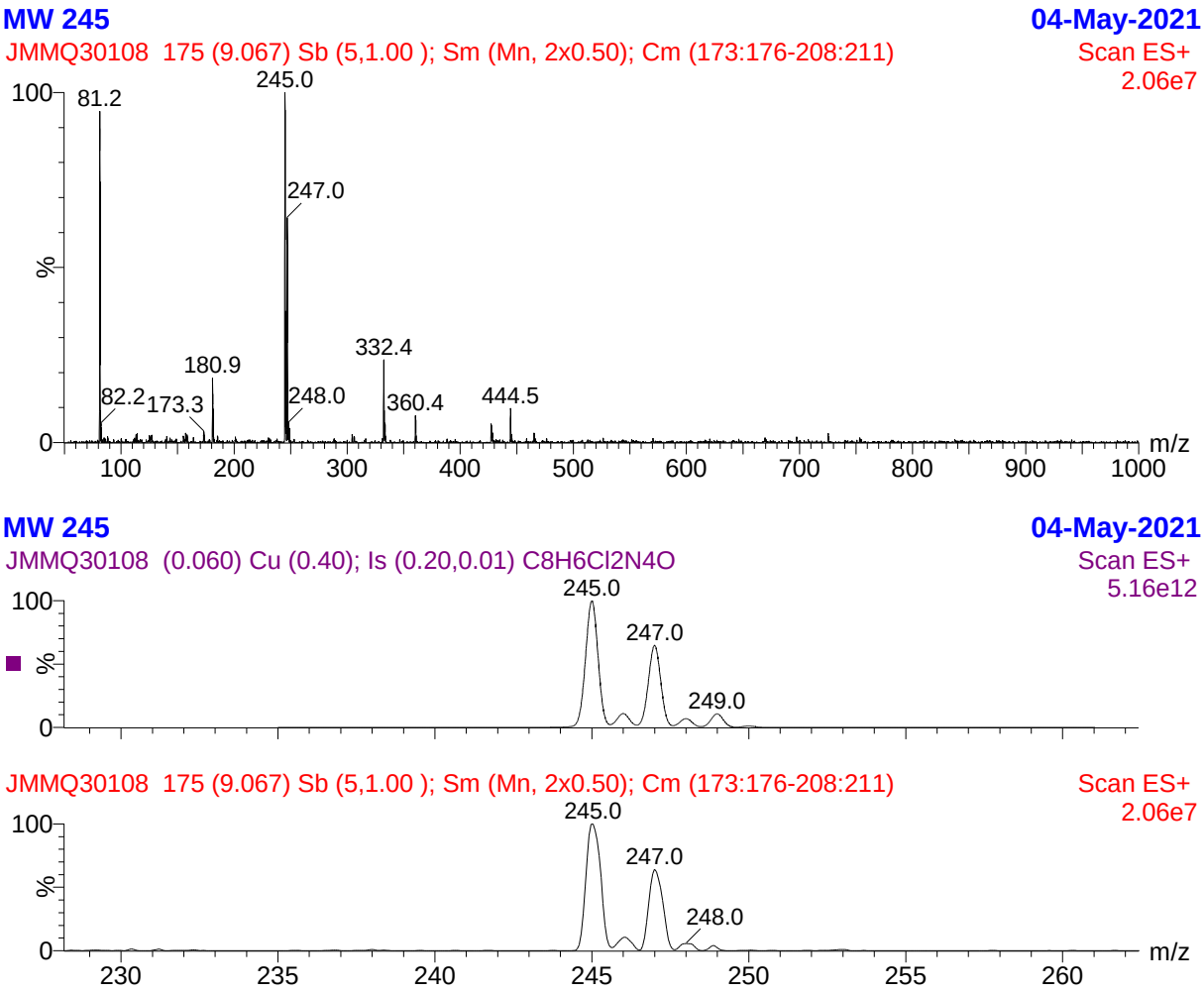

Figure S3.11. Mass spectrum of 4,6-dichloro-n-furfuryl-1,3,5-triazine-2-amine. a) The entire mass spectrum acquired through electrospray ionization in positive mode. **b)** An inset of the spectrum highlighting the most intense peaks in the 200 m/z region, which are in agreement with **(c)** the theoretical model MS spectrum calculated for DTAP $[M-H]^-$.

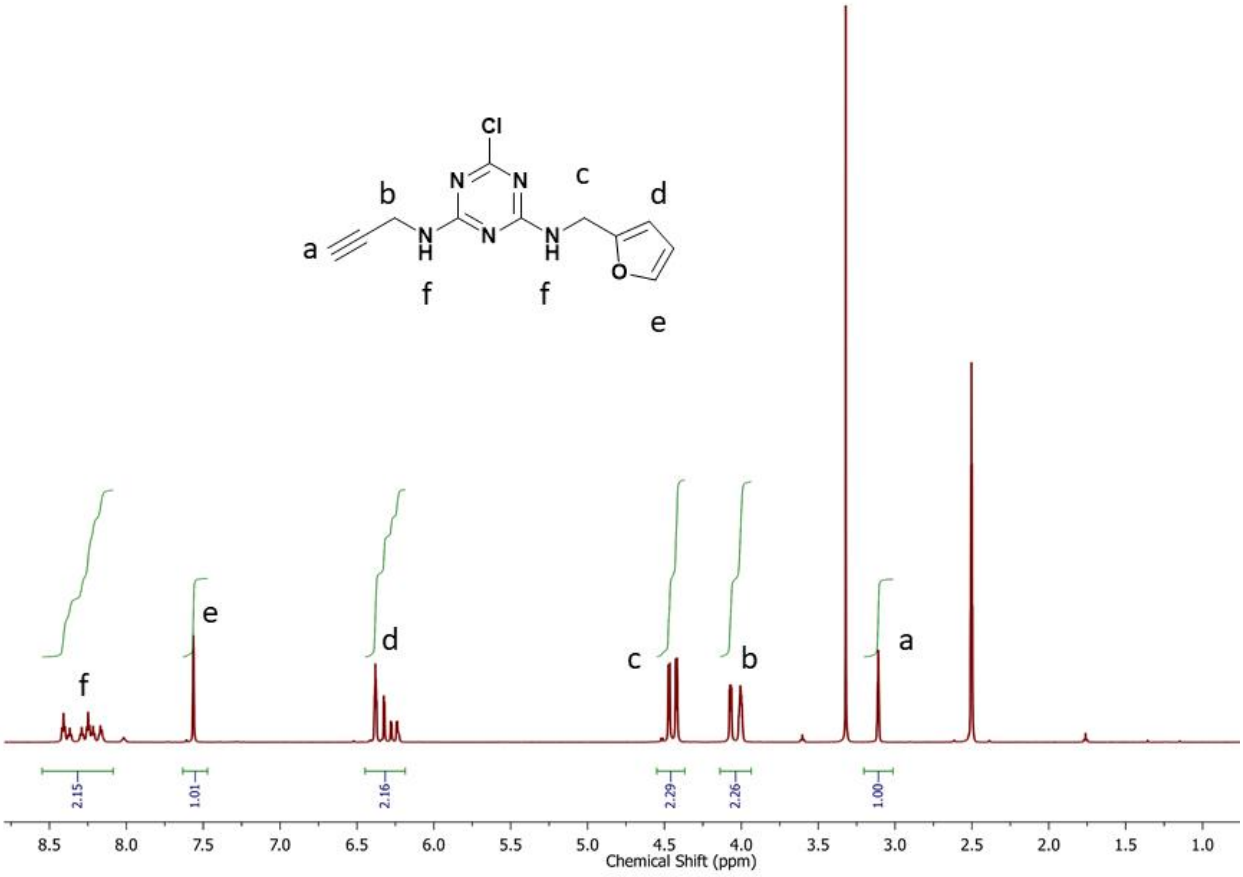

Figure S3.12 ^{1}H NMR spectrum of 6-dichloro-n-furfuryl-n'-propargyl-1,3,5-triazine-2,4-diamine. The spectrum was acquired in deuterated DMSO (CD_6SO).

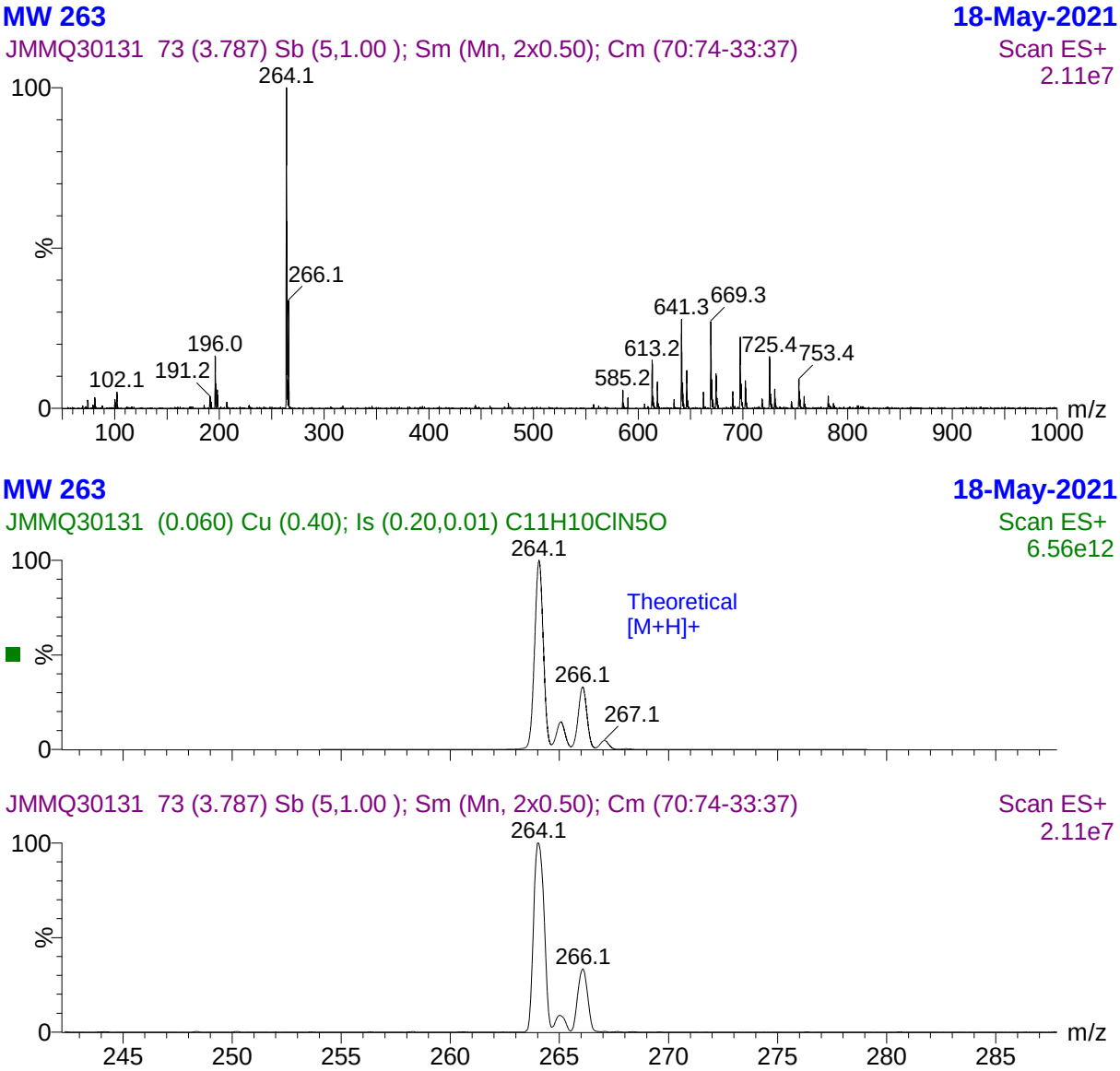

Figure S3.13. Mass spectrum of 6-dichloro-n-furfuryl-n'-propargyl-1,3,5-triazine-2,4-diamine. **a)** The entire mass spectrum acquired through electrospray ionization in positive mode. **b)** An inset of the spectrum highlighting the most intense peaks in the 200 m/z region, which are in agreement with **(c)** the theoretical model MS spectrum calculated for DTAP [M-H]-.

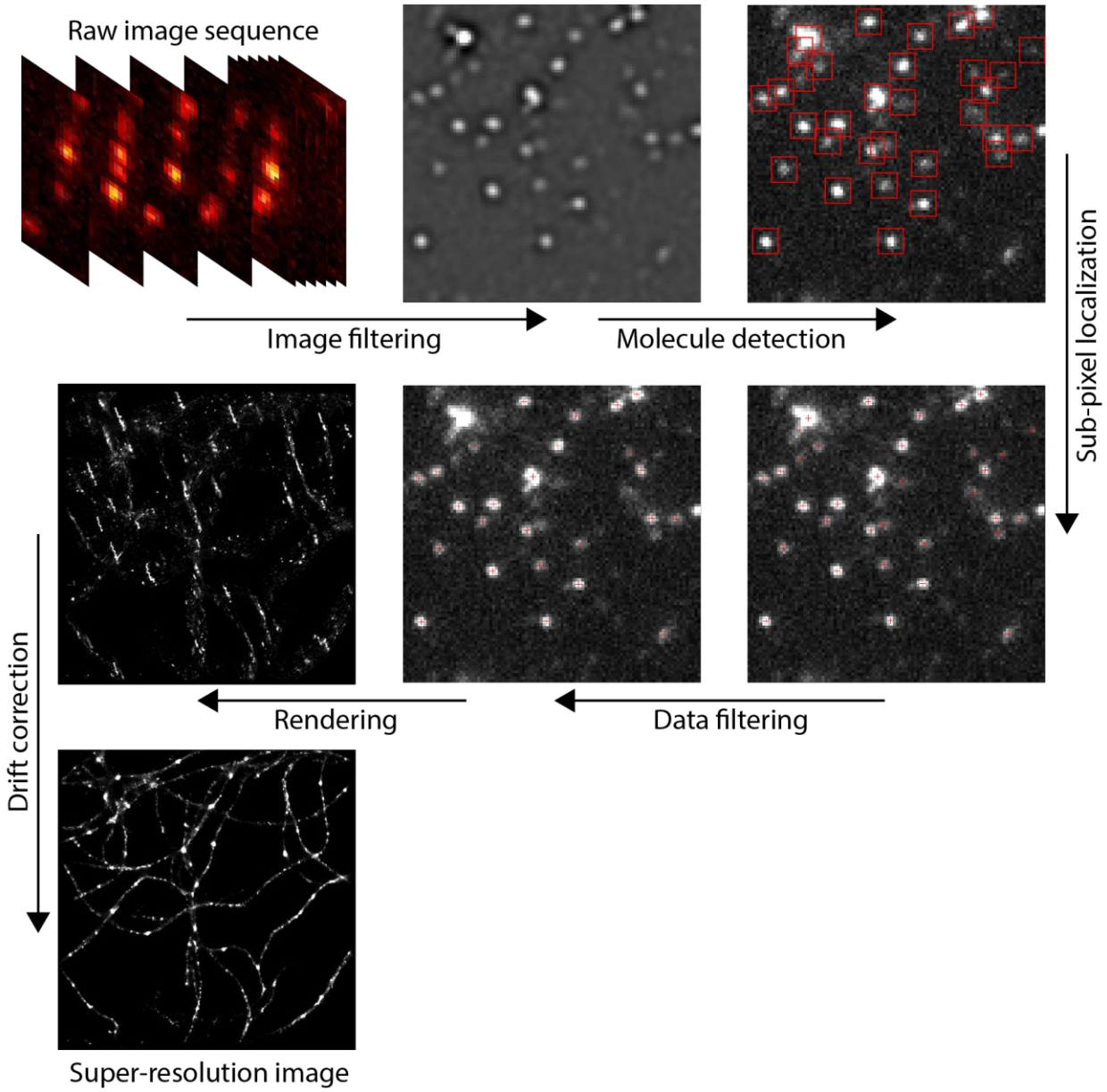

Figure S3.14. Analysis of super-resolution data with ThunderSTORM.

Chapter 4

Direct super-resolution imaging of the alternating disordered and crystalline structure of cellulose fibrils

Mouhanad Babi,[1] Anthony Palermo,[1] Tiffany Abitbol,[2] Ayodele Fatona[1], Victoria M. Jarvis,[3] Akanksha Nayak[1], Emily D. Cranston[4], and Jose M. Moran-Mirabal[1,5]*

[1] *Department of Chemistry and Chemical Biology, McMaster University, Hamilton, ON, Canada,*

[2] *RISE Research Institutes of Sweden, Stockholm, Sweden*

[3] *McMaster Analytical X-ray Diffraction Facility, McMaster University, Hamilton, ON, Canada*

[4] *Department of Wood Science, University of British Columbia, 2424 Main Mall, Vancouver, BC, Canada*

[5] *Centre for Advanced Light Microscopy, McMaster University, Hamilton, ON, Canada*

*Please address all correspondence to Jose Moran-Mirabal (mirabj@mcmaster.ca)

Abstract

Cellulose, the primary component of the plant cell wall, is ubiquitous in nature, has fueled the wood, pulp and paper industries for centuries, and has recently been exploited for the production of biofuels and renewable nanomaterials. The tight crystalline packing of glucan chains within cellulose microfibrils is responsible for the superior mechanical properties of cellulose, but it renders this material recalcitrant to biochemical and chemical depolymerization and limits its use as a green source of energy. The presence of dislocations as susceptible areas within cellulose microfibrils has been postulated for decades and is thought to be responsible for the production and size of cellulose nanocrystals (CNCs) following acid hydrolysis. However, these dislocations have never been directly visualized and their prevalence and size have remained elusive. In this study, we have used super-resolution (SR) fluorescence microscopy to directly visualize and measure, for the first time, alternating crystalline and disordered regions within individual fluorescently labelled bacterial cellulose microfibrils. The distribution of the measured crystalline regions range from 40 – 400 nm and show striking overlap with the length distribution of bacterial CNCs produced through sulfuric acid hydrolysis, supporting the fringed micellar model for the supramolecular structure of cellulose microfibrils. The disordered regions were measured to be 20 – 120 nm in length and we show that their heterogeneous accessibility directs fibril cleavage during the initial stages of cellulose acid hydrolysis. Two-colour SR imaging of cellulose microfibrils and bound cellobiohydrolases (Cel7A) in combination with degree of crystallinity measurements suggest the physical size of these dislocations are nanoscale and do not result in amorphous cellulose pockets large enough to accommodate enhanced cellulase binding. Through characterization of disordered regions in cellulose microfibrils, we have gained insight into the role of cellulose nanostructure in its breakdown by chemical and enzymatic means.

4.1 Introduction

Plants have evolved the machinery to efficiently capture sunlight energy and store it the form of the most abundant polymer in the biosphere – cellulose.[1] As a major constituent of the plant cell wall, cellulose provides the cell, and the plant as a whole, integrity and protection. This polysaccharide has been exploited by humans as building material in the form of wood, and has fueled many industries, including pulp, paper, and textiles, and more recently biocomposites and biofuels.[2–5] The biological function of cellulose and the performance of the materials derived from it are intimately linked to its hierarchical structure from the micro- to nanoscale. The crystalline packing of cellulose glucan chains (linear polymers of β-1→4 linked anhydroglucose units) give rise to higher order structures that result in the

unique physical and mechanical properties of cellulose. Glucan chains assemble into sheets through intermolecular hydrogen bonds and stack on top of one another through van der Waals forces to create a tightly packed, crystalline arrangement of 24-36 chains that form the elementary cellulose microfibril.[6,7] The individual glucan chains also possess a network of intramolecular hydrogen bonds that span the axis of the microfibril, giving rise to the exceptional mechanical strength of crystalline cellulose, with a reported elastic modulus of >100 GPa.[8,9] In higher-order plants, microfibrils are surrounded by a sheath of hemicellulose and lignin polymers, which are composed of 5- or 6-carbon sugars and aromatic alcohols, respectively.[10] The microfibrils, 5-20 nm in diameter, assemble together to form higher-order macrofibrils that intercalate into a mesh, forming the primary plant cell wall. Crystalline cellulose is also produced by other organisms, including some marine invertebrates (*e.g.,* tunicates), algae (*e.g., Valonia spp.*) and bacteria (*e.g., Komagataeibacter spp.*). In particular, bacteria produce cellulose microfibrils with comparable crystallinity to plants but without the lignin and hemicellulose sheath. This trait makes it a good source for native crystalline cellulose that can be isolated using mild treatments, which is why bacterial cellulose (BC) has been widely used as a model to study fundamental properties of cellulose, such as its nanoscale supramolecular structure.[11]

The structure of cellulose, specifically its ordered assembly at different length scales has been extensively studied using diffraction and scattering techniques. X-ray and neutron diffraction have given exquisite insight into the crystalline structure of cellulose and its inter- and intra-molecular hydrogen-bonding networks.[12,13] Related techniques, such as small-angle X-ray and neutron scattering (SAXS and SANS), Fourier transform infrared spectroscopy (FT-IR) and solid-state ^{1}H and ^{13}C NMR, have also been frequently used to study cellulose structure at larger scales. In combination, these techniques have informed on the supramolecular structure of cellulose microfibrils, including their shape, size, their higher-order bundling and alignment, along with their crystallinity and interaction with other non-cellulosic components.[6,14–17] Powder X-ray diffraction (XRD) experiments have shown that cellulose isolated from plant material, and to a lesser extent that derived from bacterial and other sources, is only partially crystalline and can contain amorphous or disordered components at different length scales.[18] Depending on the cellulose source, sample preparation, diffraction analysis, and fitting method used, the percent crystallinity (%Cr) of cellulose can range between 60% (raw kenaf fibers) to 82% (nanofibrilated flax) for plant cellulose and as high as 95% for bacterial cellulose from *Acetobacter xylinum*.[18–20] The presence of a disordered or amorphous component within cellulose has been supported by studies that have observed an increase in the crystallinity of cellulosic materials after they have undergone treatments such as base, acid, or enzymatic hydrolysis.[19–23] In particular, it

has been observed that subjecting cellulosic materials to strong acid hydrolysis, leads to the formation of highly crystalline, high-aspect ratio nanoparticles, known as cellulose nanocrystals (CNCs, Figure 4.1).[24] Interestingly, as cellulose is hydrolyzed for an extended period of time, the length of CNCs quickly decreases and eventually levels off.[25] These observations have suggested that the elementary cellulose microfibril structure conforms to a fringed-micellar model, where highly crystalline regions (or micelles) are separated by more accessible (disordered) regions that are much more susceptible to acid hydrolysis.[2,26–29]

At the macroscale, slip planes, kinks and pits within cellulose fibrils have been seen to play a key role in cellulose's mechanical strength, flexibility and susceptibility to breakdown by chemical and enzymatic hydrolysis.[30–34] These features, also known as macroscopic dislocations, have been previously visualized through polarized optical, fluorescence and electron microscopy in plant cell wall-derived materials. These studies have shown that macroscopic dislocations act as highly accessible reactive sites during the initial phase of acid or enzymatic hydrolysis of cellulose and quickly degrade to form breakages within fibrils.[30,35,36] On the other hand, the complementary role of nanoscale dislocations naturally present on individual microfibrils has not been fully elucidated. Signatures of nanoscale dislocations detected by diffraction and scattering techniques in combination with model fitting have provided indirect evidence of the presence of disordered regions within cellulose microfibrils.[6,14,15,37] Yet, these ensemble-averaged measurements have provided mostly cross-sectional information of the crystalline material, which makes it difficult to directly observe the disordered regions, especially if the dislocations are organized along the axis of the microfibril. The lack of direct visualization of nanoscale dislocations means that their presence, size, and prevalence within the crystalline structure of cellulose microfibrils remain highly elusive and controversial within the research community, and there is limited understanding of their role in cellulose hydrolysis or depolymerization.

The models of the supramolecular structure of cellulose developed to date could be complemented with microscopy techniques able to directly visualize nanoscale structural features. Cellulose has been extensively studied on a fibril-by-fibril basis using techniques such atomic force microscopy (AFM) and transmission electron microscopy (TEM), which has resulted in accurate measurements of the dimensions and topography of cellulose microfibrils.[38,39] However, these techniques have not been able to provide information about the disorder of cellulose chains along a microfibril axis because they lack the specificity to probe disorder or can damage the specimen during imaging. The obstacles in visualizing

nanoscale dislocations could be overcome by fluorescence microscopy, as the process of labeling cellulose with small organic dyes could probe the accessibility of different regions along the cellulose microfibril. Until recently, the resolution of conventional fluorescence microscopy was limited by the diffraction of light to ~200 nm, which prevented its use to study labelling patterns at the nanoscale. The development of super-resolution approaches over the last two decades has revolutionized the field of fluorescence microscopy and has allowed imaging with resolutions that surpass limitations imposed by diffraction. A subset of these super-resolution techniques exploit the photo-blinking behaviour of fluorophores to temporally deconvolve their emission and subsequently localize them with nanometer precision, resulting in reconstructed images with typical resolutions of 20 – 40 nm.[40,41] These developments have provided new tools to study cellulose structure at the nanoscale and opened the door to the visualization of dislocations in the crystalline arrangement of cellulose microfibrils.

In this work, stochastic optical reconstruction microscopy (STORM) was used to directly visualize, for the first time, nanoscale disordered regions within highly crystalline bacterial cellulose microfibrils. Following the grafting of small organic fluorescent dyes, the disordered and crystalline regions of the microfibrils were visualized using STORM and characterized in terms of their size, dispersity and relative degrees of accessibility (Figure 4.1, bottom). Additionally, temporally controlled sulfuric acid hydrolysis of BC microfibrils was used to produce bacterial CNCs (B-CNCs), which allowed us to compare the prevalence of nanoscale dislocations visualized through STORM with the length of the B-CNCs, providing insight into their mechanism of production (Figure 4.1, top). Our results strongly support the fringed-micellar model of cellulose microfibril structure and highlight the prevalence of the disordered regions within BC microfibrils (Figure 4.1, middle). We propose that this visualization technique can be further extended to directly characterize the nanoscale structure of cellulose microfibrils derived from other sources. The accurate characterization of nanoscale dislocations is key to our understanding of the structure-function relationship of cellulose in an industrial and biological context, and critical to the development of more efficient methods for the breakdown of this natural resource for the production of renewable materials, biofuels, and other sustainable consumer products.

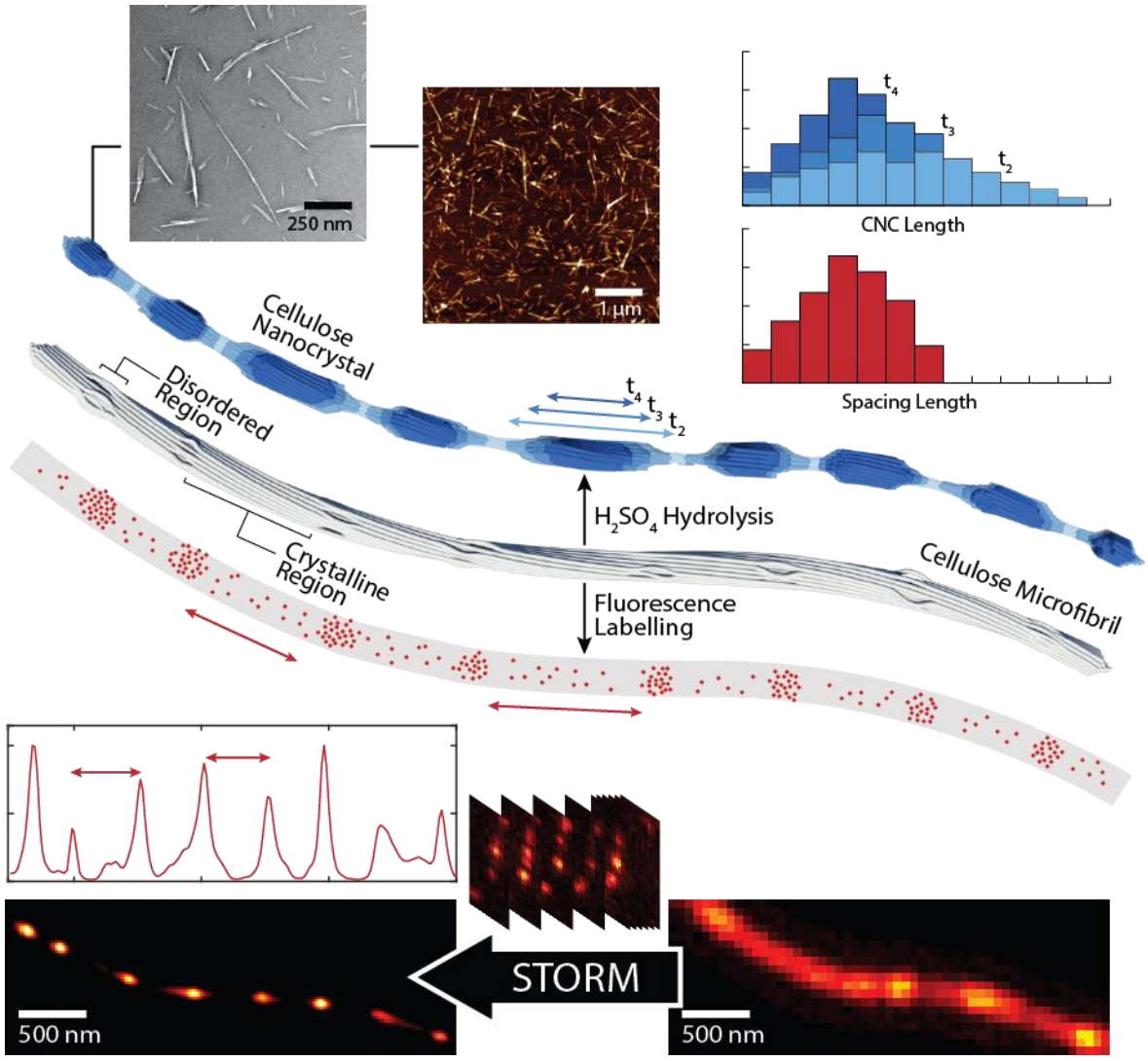

Figure 4.1 Visualizing dislocations in bacterial cellulose fibrils using super-resolution fluorescence microscopy. The fringed-micellar structural model of the cellulose microfibril (grey) postulates the presence of alternating regions of disordered and ordered glucan chains along the longitudinal axis. Areas of disorder are suspected to be more accessible to small molecules than those of high crystallinity, thus making them more susceptible to acid hydrolysis (blue) or labelling with fluorescent organic dyes (red). In this model, during acid hydrolysis, the disordered regions are preferentially degraded and eventually the cellulose fibril is cleaved at these regions, producing highly crystalline cellulose nanocrystals (B-CNCs). The length and height of these particles can be measured after different durations of acid hydrolysis using TEM and AFM, respectively. Fluorescent labelling of cellulose is expected to create clusters of fluorophores centered around the more accessible (i.e., disordered regions). The enhanced resolution offered by the STORM super-resolution technique yields a repeating pattern of alternating bright and dark segments that correspond to disordered and crystalline regions, respectively. The size of the latter can be determined by measuring the distance between the peaks, and their distribution (red histogram) should correspond

to that of the length of B-CNCs produced following acid hydrolysis (blue histogram). For the purpose of clearly showing the glucan dislocations, the microfibril is represented with a significantly lower length to width aspect ratio than in the real system.

4.2 Results & Discussion

Bacterial cellulose (BC) was purified from the foodstuff *nata de coco* (NDC) through mild alkaline treatment, producing micron-long cellulose ribbons (Figure 4.2a) with an average width of 40 ± 20 nm, as measured by TEM (n > 100 microfibrils). AFM imaging revealed that the fibrils have non-uniform cross-sections in the 10 – 50 nm range (Figure 4.2b), with frayed ends showing fibrils with diameters below 10 nm. The length, width and height observations agree with previous characterization of BC purified from NDC and *Acetobacter xylinum* cultures.[39,42] We also observed twists and striations along the longitudinal axis of the cellulose ribbons with widths of ~10 nm in both AFM and TEM images, consistent with previous observations of pure BC ribbons.[39] The morphology and texture of the purified BC samples suggest that the ribbons are bundles of elementary cellulose microfibrils, which typically have widths of 5-10 nm, and that the samples isolated form NDC are free from impurities, such as soluble sugars and proteins, that are found in the original foodstuff.

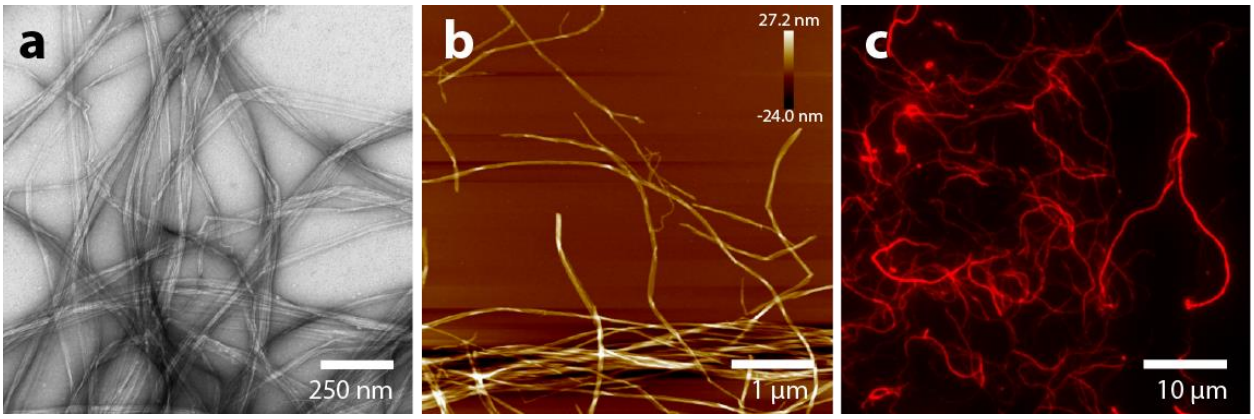

Figure 4.2 Images of purified bacterial cellulose (BC). (a) Transmission electron microscopy image of BC showing the striations of ribbons and their tendency to twist. (b) Atomic force microscopy (AFM) of cellulose elementary microfibrils and ribbons. (c) ACy5-BC imaged using epifluorescence, showing loosely bound meshes of cellulose microfibrils and ribbons. Microfibrils and ribbons appear larger in epifluorescence due to the limitations in resolution imposed by the diffraction of light.

To visualize the nanostructural features of microfibrils using STORM, BC was fluorescently labelled with organic dyes using two approaches based on triazinyl linkers. Triazine chemistry has been widely deployed to graft dyes and pigments onto the abundant primary hydroxyl groups present in cellulose. This chemistry also provides the advantage of

aqueous reactions under mild conditions, which ensure that the BC nanostructure and crystallinity remain unchanged.[43–45] In the first labeling approach, the commercially-available dichlorotriazinyl aminofluorescein (DTAF) and an in-house synthesized dichlorotriazinyl piperazine-rhodamine 6G (DTPR) derivative were directly grafted onto cellulose (Figure S4.1a) using previously reported protocols.[44,46,47] A second labelling strategy was also developed where BC was first functionalized with dichlorotriazinyl aminopropyne derivatives, which undergo click reactions with azide-bearing molecules. This enabled us to label cellulose with a higher density and a variety of commercially available dyes that possess an azide chemical handle, such as azidopropyl aminofluorescein (APAF) and azido-Cy5 (ACy5) (Figure S4.1b).

Under the microscope, fluorescently labelled BC displayed a range of hierarchical structures with lengths in the tens to hundreds of microns and widths that spanned from submicron-wide ribbons and fibril bundles to fibrils with widths below the diffraction-limited resolution of the optical microscope (~200 nm). These ribbons and fibrils were usually entangled, forming loose meshes (Figure 4.2c), in agreement with TEM and AFM observations (Figures 4.2a-b). Occasionally, isolated cellulose fibrils were found, which exhibited a variety of curved configurations due to their inherent flexibility.[4848] With widefield epifluorescence microscopy, the diffraction-limited microfibrils appeared uniformly labelled along their length. In contrast, imaging with STORM unveiled, for the first time, a consistent pattern of alternating dark and bright regions along the length of the fibrils (Figure 4.3a), while also resolving twisting features smaller than 50 nm (Figure 4.3b (inset), d).

The one-dimensional pattern was observed on fibrils labelled directly with DTAF or DTPR dyes, as well as on those labeled first with an alkyne-triazinyl derivative followed by click reaction with APAF or ACy5 dyes. In the case of ACy5-BC, the cellulose fibrils had a high localization density, were continuously mapped along their length and exhibited a similar labelling pattern when the dye concentration was doubled (Figures S4.2 and S4.3). These observations indicate that the pattern was not a labelling or imaging artifact, as it was independent of the dye, labelling concentration and grafting method used. Instead, it implies that the labeling pattern is a result of features encoded within the nanostructure of the cellulose microfibrils. The presence of highly contrasted dark and bright regions along the microfibril reflects regions with different density of the grafted fluorescent dyes, suggesting that some areas of the microfibril are more accessible to covalent grafting than others. We thus hypothesized that the dark regions of the fibril (less accessible to labelling) represent crystalline cellulose, while brighter regions (more accessible) represent dislocations or

areas where glucan chains (the linear polymers of anhydroglucose that make up the elementary microfibrils) are less ordered.

The size of the putative crystalline (dark) and disordered (bright) regions was quantified by tracing individual microfibrils (Figure 4.3b) and acquiring their line-intensity profiles (Figure 4.3c). The intensity profiles of labeled microfibrils exhibited many sharp, well-separated peaks with heterogeneous intensities and separation distances (Figure 4.3c). A semi-logarithmic histogram of the intensity values for pixels along the microfibril profiles displayed a bimodal distribution (Figure S4.3, bottom) for fibrils labeled with either DTAF or ACy5. For DTAF-BC, the first population was representative of the sparse labelling found in the dark regions, while the second population presented intensities 10-100-fold brighter, consistent with the densely labeled bright regions. The leftmost population was considerably less prominent in ACy5-BC and almost completely disappeared when the dye concentration was doubled. This indicates that the dark regions in DTAF-BC were completely absent of localizations and possessed an intensity similar to that of the image background, while ACy5-BC mainly exhibited continuous labelling throughout the fibrils. These differences are attributed to the higher grafting densities permitted by the two-step labelling method and superior photophysical properties of Cy5, including the ability to reactivate it using UV light, high photoswitching rate, and brightness. [49] This results in a higher dynamic range for the comparison of the intensities between the crystalline and disordered regions. [49]For these reasons, ACy5-BC was selected for further analysis and characterization of the labelling patterns observed in the microfibrils.

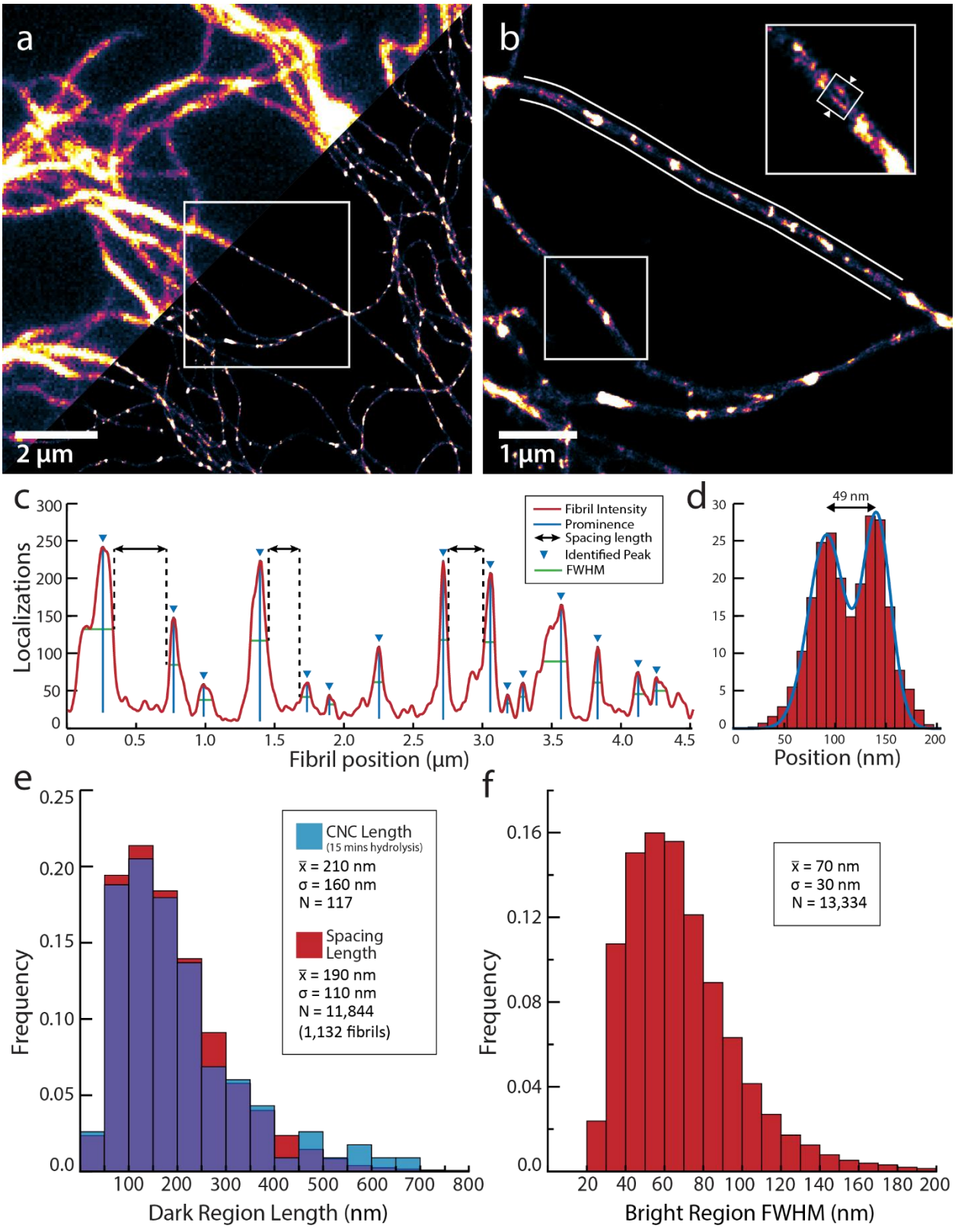
a
2 µm
b
1 µm
c
Localizations
Fibril position (µm)
Fibril Intensity
Prominence
Spacing length
Identified Peak
FWHM
d
49 nm
Position (nm)
e
Frequency
Dark Region Length (nm)
CNC Length
(15 mins hydrolysis)
x̄ = 210 nm
σ = 160 nm
N = 117
Spacing Length
x̄ = 190 nm
σ = 110 nm
N = 11,844
(1,132 fibrils)
f
Frequency
Bright Region FWHM (nm)
x̄ = 70 nm
σ = 30 nm
N = 13,334

Figure 4.3. Super-resolution images of ACy5-BC microfibrils and quantitative analysis of the labelling pattern. (a) Super-resolution images of ACy5-BC microfibrils unveiled a one-dimensional labeling pattern of alternating dark and bright regions that persists throughout the length of the microfibril. STORM imaging yielded average localization uncertainties of ~15 nm. (b) The pattern of repeating dark and bright regions was were analyzed by manually tracing the thinnest cellulose fibrils and acquiring intensity profiles along their longitudinal axis. (c) Intensity profiles evidenced the contrast in labelling densities of some regions on the fiber. The bright peaks were selected and characterized for their full width at half maximum (FWHM) and intensity. (d) Cross-sectional detail of BC microfibrils with sub-50 nm features, such as the fibril twisting shown in the inset of panel b, were occasionally seen in SR images (e) The length of the dark regions was calculated as the distance between adjacent peaks at half their intensity. Their distribution (red), closely mirrors the length measurements (through TEM) for B-CNCs produced by 15 minutes of acid hydrolysis (teal) with the overlap shown in purple. (f) The distribution of the FWHM of the peaks in comparison were at significantly smaller length scales (inset).

To systematically identify the brightly labeled peaks representative of the putative disordered cellulose regions, a median prominence threshold based on all the local maxima present in a given intensity profile was used (Figure S4.2). The size of the dislocations was then measured by determining the full width at half maximum (FWHM) intensity of the bright peaks and the size of the crystalline regions were calculated as the distance between adjacent peaks at half their intensity. The length of the disordered (bright) regions followed a normal distribution with an average of 70 nm and a standard deviation of 30 nm (Figure 4.3f). In contrast, the crystalline (dark) regions were significantly larger, with an average length of 190 nm and a standard deviation 110 nm (Figure 4.3e). The size distribution of the putative crystalline regions is in a range comparable to the reported length of CNCs produced through strong acid hydrolysis from bacterial and plant cellulose. This observation suggests a correlation between the frequency of the dislocations and the ultimate size of CNCs.

To investigate how the more accessible dislocations deduced from the microfibril labelling pattern could be related to the process of CNC isolation, we next studied the effects of strong acid hydrolysis on the morphology and structure of CNCs. To this end, sulfuric acid hydrolysis experiments were conducted on BC fibrils purified from NDC, where the acid concentration (64% w/w), temperature (70°C), and reaction time were tightly controlled. The dimensions and crystallinity index (CrI) of the resulting CNCs were characterized by TEM, AFM and XRD (Table 4.1). After 2 minutes of hydrolysis, the CNC length spanned from 50 to 1000 nm, as measured by TEM (Figure 4.4a). As the BC fibrils were hydrolyzed for longer periods of time, the length of the CNCs decreased, the distribution of their lengths narrowed, and eventually levelled off at 70 – 500 nm after 60 minutes of hydrolysis (typical

time used for the production of CNCs).[50,51] Previous studies have also observed longer particles and higher dispersity for CNCs produced from BC using acid hydrolysis under similar conditions.[42,52,53] We attribute the ability to control the length of CNCs and to observe the transition from a highly heterogeneous mixture of nanocrystal lengths to a more uniform population (similar to those obtained through hydrolysis of cotton linters or filter paper) to the use of freeze-dried BC as a starting material, which allowed us to precisely control the sulfuric acid concentration and acid/cellulose ratio. The CNC cross-section, as measured by AFM height analysis (Figure S4.4), decreased from 50 nm for untreated BC to 11 nm after 2 minutes of hydrolysis, but did not change significantly with longer hydrolysis times. This is also in agreement with previous reports that show that CNCs produced from a variety of cellulose sources do not show changes in cross-section with increasing hydrolysis "harshness" (i.e., reaction time, temperature, acid/cellulose ratio, acid strength).[54,55] Furthermore, the crystallinity of cellulose did not change (within error) after acid hydrolysis, and remained at >90% even for longer hydrolysis times (Table 4.1, Figure 4.4b). These results show that by carefully controlling the hydrolysis time, along with acid and cellulose concentrations, the length of the CNCs produced from bacterial cellulose can be tuned, but not their cross-sectional dimensions or surface charge.

Table 4.1. Characterization of purified BC and bacterial CNCs resulting from time-controlled acid hydrolysis.

Sample (Hydrolysis time)[a]	Length[b] (nm)	Cross-section[c] (nm)	% Sulfur[d] ($g_S/g_{B\text{-}B\text{-}CNC}\times100$)	CrI[e] ($A_{Cryst}/A_{Tot}\times100$)
BC (0 min)	> 1000	50 ± 20	–	92
B-CNC (2 min)	100 – 1300	11 ± 4	0.59 ± 0.07	91
B-CNC (5 min)	100 – 1300	14 ± 4	0.49 ± 0.07	93
B-CNC (15 min)	50 – 1000	9 ± 4	0.58 ± 0.03	91
B-CNC (30 min)	50 – 1000	12 ± 4	0.51± 0.15	91
B-CNC (60 min)	70 – 500	13 ± 4	0.56 ± 0.03	92

[a] All other hydrolysis conditions were kept constant; 70°C, 64% (w/w) H_2SO_4, 4.0 g freeze-dried BC, 10:1 acid-to-cellulose ratio

[b] Minimum and maximum lengths reported from n ≥ 100 measurements from TEM images

[c] Average and standard deviation is reported for n ≥ 100 AFM height measurements

[d] Average and standard deviation is reported for triplicate samples subjected to elemental analysis

[e] Triplicate measurements for B-CNC samples from 15- and 30-minute hydrolysis yielded a standard deviation of ±2% and ±1% for the CrI as measured by XRD.

The distribution of the length of the sparsely labeled regions shows strong correlation with the distribution of the length of CNCs produced after 15 minutes of sulfuric acid hydrolysis of BC (Figure 4.3e and Figure S4.5). This strongly suggests that the labelling pattern and the production of CNCs originate from the same process imposed by repeating regions of higher accessibility present along the length of mostly crystalline BC fibrils. Similar to how these pockets allow a high density of fluorophores to graft onto cellulose, they also act as vulnerable sites for acid hydrolysis and, in turn, microfibril cleavage to produce CNCs. Super-resolution microscopy results show that the dislocations can vary in accessibility within two orders of magnitude, as evidenced by the wide distribution of the intensities observed for the brightly labeled regions in the microfibril (Figure 4.3c and Supplementary Figure 4.5a). Measuring the distance between the more accessible dislocations, by setting a higher peak-picking threshold (to 15×median), resulted in increased lengths and broader distribution of the crystalline regions (Figure S4.5b) and overlapped with the length of CNCs produced by shorter acid hydrolysis times (Figure S4.5c). Decreasing the threshold, such that all the peaks presented by the bright regions are picked, resulted in the spacing lengths decrease and their distributions shorten and narrow, conforming to the length of CNCs produced after longer hydrolysis times.

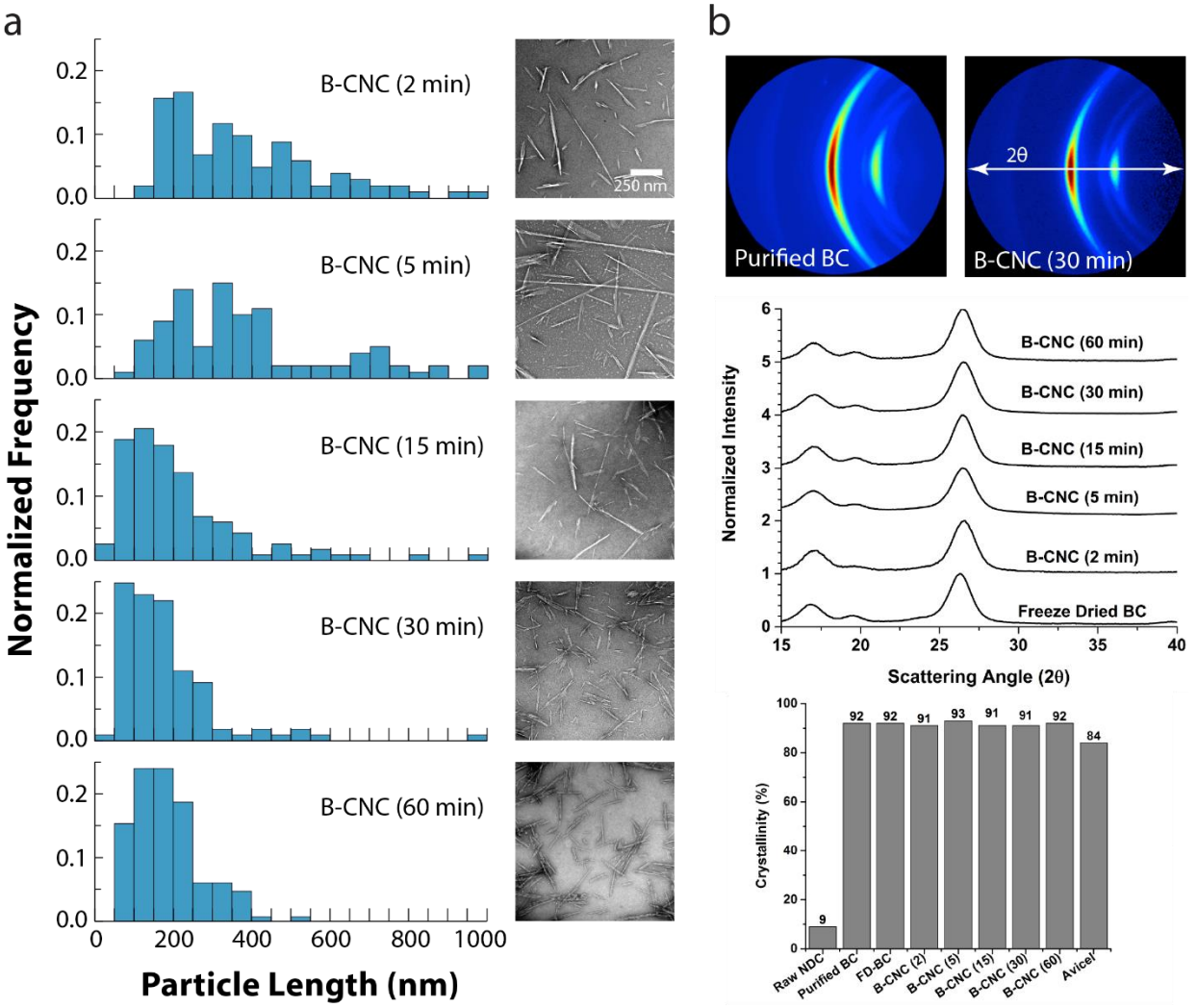

Figure 4.4. Length distribution, X-ray diffraction patterns and crystallinity of CNCs produced from time-series hydrolysis of bacterial cellulose. a) Particle lengths became shorter and more narrowly distributed with increasing hydrolysis times. Particles were measured directly from TEM images using image-processing software (N ≥ 100). The corresponding TEM images of the produced CNCs are shown on the right. b) One-dimensional diffraction plots of intensity vs. 2θ and CrI measurements showed that the cellulose Iα crystallinity of BC remained unchanged following prolonged periods of acid hydrolysis.

When combining the CNC length measurements with the super-resolution microscopy results it can be concluded that the strong acid treatment initially targets the larger, most accessible (brightly labeled) disordered regions and quickly hydrolyzes these sites to create long CNCs with a large size polydispersity (Figure S4.6). As the cellulose is further exposed to acid, the smaller, less accessible dislocations are hydrolyzed. This results in further cleaving of the cellulose particles, shortening their average length, and decreasing

their polydispersity. Once the intervening dislocations are hydrolyzed, continued exposure to acid results in a progressive shortening of the CNCs as they are hydrolyzed from the ends. Through super-resolution imaging, it is possible to simultaneously visualize dislocations of varying size and degree of accessibility along the length of cellulose microfibrils. Measuring the distance between these dislocations provides a distribution that strongly correlates with that of the length of CNCs produced after prolonged hydrolysis times. These results shed light on the mechanism behind the extraction of CNCs and provide strong evidence of the persistent occurrence of dislocations or disordered regions along bacterial cellulose microfibrils.

The combined super-resolution microscopy and controlled hydrolysis experiment observations support a supramolecular structure for cellulose that conforms to the fringed-micelle model. This model proposes that cellulose microfibrils are composed of highly crystalline portions – or micelles – interspersed with disordered cellulose – or fringes – that are more accessible and susceptible to acid hydrolysis.[2,56] While the presence of non-crystalline components within natural cellulose has been established by XRD diffractograms that evidence a broad baseline peak, in our experiments the crystallinity index of the CNCs did not increase significantly as the material was hydrolyzed for longer periods of time.[18] This suggests that the disordered regions are not a significant contributor to amorphous cellulose in the BC microfibrils or that the decrease in crystallinity due to hydrolysis is compensated by the appearance of "frayed" glucan chains at the tips of the CNCs. This interesting observation, in combination with the size of the bright regions (70 ± 30 nm), suggests that the disordered regions are small and arise from the misalignment (or dislocation) of the glucan chains, which results in decreased crystalline packing, rather than from highly-disordered or fully amorphous cellulose. This assessment is further supported by our observation that cellulases, with 5-10 nm hydrodynamic radii, do not show preferential binding or localization on the dislocations, as discussed further below (Figure 4.5).

Originally, the fringed-micelle model of the supramolecular structure of cellulose was proposed based on the observations of leveling-off in the degree of polymerization (LODP) of glucan chains following prolonged acidic hydrolysis.[25] The LODP of glucan chains from ramie fibers has further been correlated with SANS measurements, which show 2.5 nm long disordered regions along the cellulose microfibrils with a 150 nm periodicity.[15] From our results it can be deduced that in bacterial cellulose, the size of the crystalline and disordered regions exhibit less uniform distribution and are significantly larger than those in ramie fibers, with crystalline regions that can be as long as 500 nm. These observations are

consistent with previous measurements that show that CNCs produced from bacterial cellulose are longer and have a broader distribution than those produced from ramie.[42,57] While this work uses bacterial cellulose as a model cellulose substrate, it is possible that the observed irregular periodicity may also be present in plant-derived cellulose, given that the SANS measurements made are ensemble averages which could mask any heterogeneity present in plant microfibrils. We propose that the super-resolution microscopy method presented here could be similarly applied to the study of celluloses derived from other sources. Additionally, this method confers the advantage of being able to directly visualize and quantify regions of differing accessibility in a hydrated state and without sensitivity to aberrations that may arise from higher order phenomena, such as parallel fibril alignment or interfibrillar pores.[15] Thus, interesting subsequent studies could focus on a detailed assessment of cellulose microfibrils from other sources, such as plant, tunicates and algae, or on the impact of chemical and biological treatments on the nanostructure of elementary cellulose microfibrils.

An alternative model has been suggested, based on interpretations made from SANS, FT-IR, and solid-state NMR measurements, where the disordered fraction within cellulose microfibrils is thought to reside mostly on the surface of the crystalline regions.[6,14] Additional support for this model has been derived from kink angle and persistence length measurements of TEMPO-oxidized wood cellulose nanofibrils.[48] In this study, the non-normal distribution of kink angles was taken as evidence that the kinks could not represent intervening disordered regions within the microfibril, but were instead a result of the high energy mechanical treatment that the materials were subjected to within a microfluidizer. Our data suggests that the disordered regions, which may be as subtle as the dislocation of a single glucan chain, create significant accessibility pockets. Thus, this is compatible with the observations made on TEMPO oxidized nanofibrils, since such minor dislocations are not expected to have a significant impact on the flexibility (or modulus) of the fibrils or be the source of kinks. The remarkable contrast in intensity observed in the labeling pattern, the concomitant reduction in the length of CNCs due to acid hydrolysis and their constant cross-section strongly suggests that the intervening disordered regions reside along the fibrillar axis and have significantly higher accessibility than surface chains.

The distribution of the measured spacings and intensities of the pattern seen on labelled BC microfibrils indicate that the dislocations are heterogenous and their presence may not be the product of a controlled, canonical biological process. It is likely that they arise from built up tension or “seizing” of the molecular machinery at work in the biosynthesis of cellulose microfibrils. In *Acetobacter xylinum*, the bacterial cellulose is synthesized by a

cellulose synthase complex – or terminal complexes (TC) – that span across the inner and outer membranes while in a linear arrangement along the surface of the bacterium.[58] Downstream of the *acsAB* glucose transferase enzyme, which appends anhydroglucose units to the nascent glucan chain, *acsD* and *acsC* are presumed to be responsible for exporting the glucan chains and crystallizing them into elementary microfibrils, respectively.[59] Errors during this final step of the process could introduce misalignment between the glucan chains and thus be responsible for the presence of dislocations. The crystal structure of *acsC* has shown that this protein can simultaneously bind four glucopentose chains with a weak affinity through four helical passageways.[60] TCs missing this enzyme, or a transient inactivity of the enzyme, may produce intervening regions of dislocations. Moreover, the introduction of a chiral twist in a microfibril introduces tension on the outer chains of a cellulose fibril, as previously shown by molecular dynamics studies.[61] This strain could be thermodynamically relaxed by introducing misalignments and dislocations that could cause small breaks in the crystal structure in a periodic manner. [61]

There has been much speculation on the natural function of dislocations within crystalline cellulose microfibrils. Some studies speculate that they may provide flexibility to the microfibril, reducing the hindrance in bacterial mobility introduced by the cellulose matrix. The dislocations are also suspected to create water-accessible pockets that can partially swell the microfibrils and enhance the flotation of the cellulose mats, which the bacterium exploits to gain increased exposure to oxygen.[15,62] [63]In plants, dislocations could be active sites for hydrogen-bond disrupting proteins like expansins and swollenins, which have been shown to weaken cellulose fibers and increase their hydrolysis by cellulases.[64] It has also been speculated that disordered regions could be created from the integration of hemicellulose within the microfibril during its assembly, creating defects in the crystalline structure at that region.[65,66] Membrane-bound endoglucanses, which can break glycosidic linkages within a cellulose chain could act on these sites to release the microfibril from its association with hemicellulose and weaken its interaction to its surrounding matrix.[63,67] These processes have been shown to play a significant role in the relaxation and the remodelling of plant cells as they expand and change shape, highlighting the biological importance of nanoscale dislocations within cellulose microfibrils.[63] An additional implication of these nanostructural features is that they could create hotspots for cellulase binding, enhancing the ability of these enzymes to depolymerize the glucan chains into soluble sugars. To investigate this possibility, we incubated AF647-labeled *Trichoderma reseii* Cel7A – which we have previously shown retains enzymatic activity similar to its native counterpart[68] – with DTAF-labeled BC and acquired two-color super-resolution images. Analysis of the intensity profiles from the two channels revealed that the enzymes did not

show preferential binding to the dislocations in the microfibrils (Figure 4.5). This result reflects the binding mechanism of Cel7A, where the enzyme's carbohydrate binding module (CBM) tethers it randomly to the hydrophobic facet of crystalline cellulose.[69] This implies that the disorder introduced by the dislocations does not create pockets large enough for enzymes 5-15 nm in size to experience enhanced binding. These results open the door for the deployment of multicolour super-resolution microscopy for the exploration of the impact of nanoscale structure and pre-treatment strategies on cellulase-cellulose interactions.

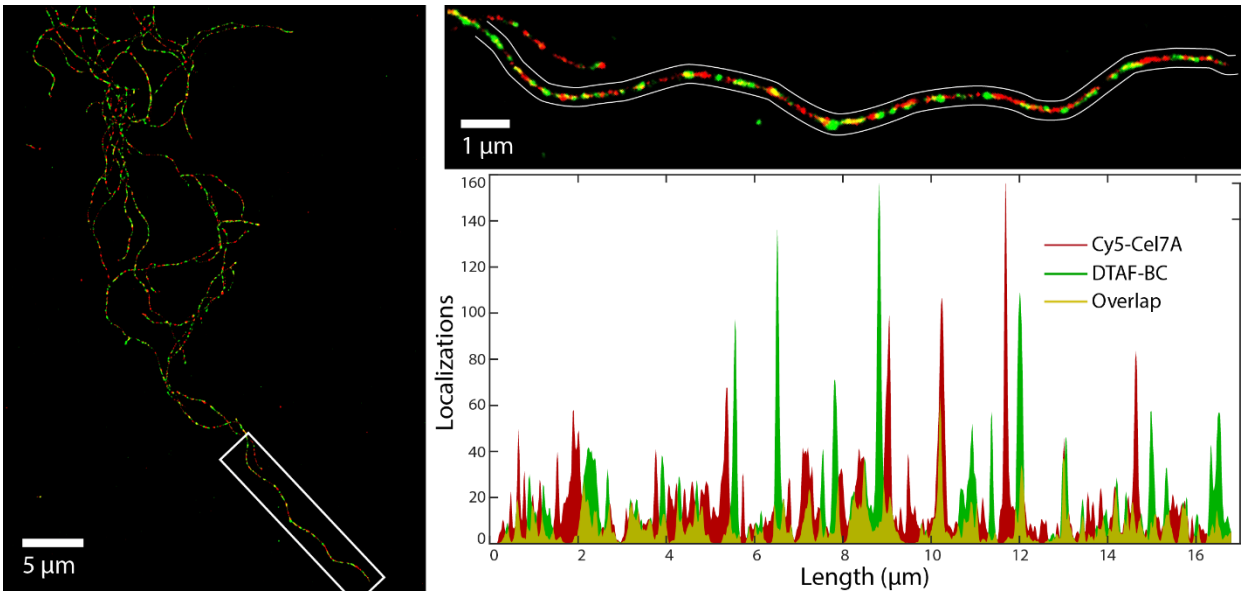

Figure 4.5. Two-colour super-resolution images of DTAF-labeled BC (green) and bound AF647-Cel7A (red). AF647-Cel7A was incubated on DTAF-labeled BC at concentrations of 5 nM. The super-resolution images were acquired at room temperature. Qualitative analysis of the colocalization of the dislocations and binding sites of Cel7A was done by highlighting overlapping regions of the intensity profiles of the fibril in the two-colour channels (shown in yellow). Epifluorescence images of AF647-Cel7A bound at high concentrations exhibited uniform intensities along the fiber.

4.3 Conclusion

The presence of an alternating crystalline and disordered structure along cellulose microfibrils has been an enigmatic and controversial topic within the field of cellulose, as this structure is generally hidden to techniques conventionally used to study cellulose supramolecular organization. By exploiting the process of fluorescence labelling to probe variations in accessibility, we used super-resolution fluorescence microscopy to visualize a repeating pattern of nanoscale dislocations present along bacterial cellulose microfibrils. This work shows that these dislocations are heterogenous in their size, separation distance

and accessibility, and through crystallinity and length measurements of CNCs produced after controlled acid hydrolysis, we elucidate the mechanism of how these dislocations govern the production of CNCs. The unaltered crystallinity of cellulose following acid hydrolysis and the non-preferential binding of cellulase Cel7A to the dislocations implied that while these dislocations create pockets of accessibility that are ~70 in length, their physical size is relatively small and precludes molecules larger than 5 nm. The ability to visualize these dislocations on cellulose microfibrils can act as a platform to detect amorphogenesis at the nanoscale, opening the door for future work on understanding how various proteins, enzymes and chemical agents can alter the structure of cellulose at the microfibril level. Understanding the nanostructure of cellulose and how it is altered through different treatments is critical for understanding its biological role and for the development of new cellulosic nanomaterials, biofuels, and bioplastics.

4.4 Materials & Methods

Materials. Nata de coco from (NDC, 230 g drained weight, New Lamthong Food Industries, Bangkok, Thailand) was purchased from a local Asian foods store. Rhodamine 6G (95%), 6-aminofluorescein (95%), cyanuric chloride (99 %), phosphorus oxychloride ($POCl_3$, 99%), piperazine (99 %), glucose oxidase (from *Aspergillus niger*, type X–S, 100–250 units/mg, 65–85% protein content), catalase (from bovine liver, ≥10 000 units/mg, ≥70% protein content), and cysteamine hydrochloride (≥98%) were purchased from MilliporeSigma (Oakville, ON, Canada) and used as is. Avicel 101 was purchased from MilliporeSigma (St. Louis, MO). APAF and sulfo-Cy5 azide (ACy5) was purchased from Lumiprobe (Hunt Valley, MD, USA). Poly(allylamine hydrochloride) was purchased from Polysciences Inc. (Warrington, PA, USA) and had a nominal molecular weight of 120-200 kDa. Glass-bottom petri dishes were purchased from MaTek (insert country, city). *Thermofibda fusca* Cel7A was expressed, purified and labelled with Alexa-Fluor 647, to a degree of labeling of 2.95, as described previously.[51]

Nata de coco purification. Nata de coco was drained of its syrup and thoroughly rinsed with 18.2 MΩ cm purified water, which from now on will be referred to as "water". The material was then combined with ~300 mL of water and blended at full speed in a Magic Bullet blender (Nutribullet, Los Angeles, CA, USA) for 10 minutes until the consistency was uniform. The slurry was then incubated in 0.1 M NaOH for 20 minutes at 80°C.[70] The reaction was quenched with chilled water using 10× the volume of the reaction and allowed to equilibrate to room temperature (RT). The suspension was rinsed with water by centrifugation at 1800*g* for 8-10 minutes (RC-5 Superspeed Refrigerated Centrifuge; DuPont Instruments), followed by supernatant decanting, until the pellet became white (5-7 cycles). The pellet was

resuspended in water to create a 3 mg/mL bacterial cellulose slurry for later functionalization and labelling. For controlled acid hydrolysis, the pellet was freeze-dried and blended for 2 minutes to produce a coarse white powder referred to as purified bacterial cellulose (BC).

Synthesis of DTAF. The synthesis of DTAF was adopted to the method of D. Blakeslee.[71] Thus, 0.5 g (1.44 mmol) of 6-aminofluorescein dissolved in cooled anhydrous methanol (0 – 5 ^{o}C, 15 ml) was added dropwise to a stirred solution of cyanuric chloride (0.32 g, 1.74 mmol) in 3 ml of chloroform at 0 ^{o}C. After 2 h of stirring, 0.5 ml of concentrated HCl was added dropwise while maintaining reaction for additional 1 hr. The resulting precipitate was filtered under vacuum to give a bright yellow powder as product (0.7 g, 91% yield). ^{1}H NMR (600 MHz, MeOD) δ 8.30 (d, *J* = 8.8 Hz, 1H), 8.02 (dd, *J* = 8.7, 2.2 Hz, 1H), 7.68 (d, *J* = 2.2 Hz, 1H), 7.51 (d, *J* = 9.2 Hz, 2H), 7.27 (d, *J* = 2.3 Hz, 2H), 7.12 (dd, *J* = 9.2, 2.3 Hz, 2H).

Synthesis of DTPR. To a stirred solution of rhodamine 6G (0.50 g, 1.04 mmol) in 12 ml of 1,2 dichloroethane under nitrogen was added dropwise phosphorus oxychloride (0.30 mL, 0.48 g, 3.12 mmol) over a period of 10 minutes and refluxed for 4 h. The resulting solution was cooled and evaporated under vacuum to give rhodamine acid chloride as a dark solid that was directly used for next step without further purification. To a stirred solution of piperazine (0.69 g, 8.0 mmol) dissolved in dichloromethane (50 mL) was added dropwise a solution containing rhodamine 6G acid chloride (0.50 g, 1.0 mmol) in acetonitrile (50 mL) over a period of 3 h with the help of a dropping funnel. The reaction mixture was stirred continuously for 24 h at room temperature in the dark. After which the solvent was removed under vacuum at 50 °C and exchanged with 50 mL of diethyl ether leading into precipitation. The resulting precipitate was isolated by filtration, dried and dissolved in 40 mL of water followed by acidification using conc. HCl. The solution was saturated with sodium chloride and extracted with a 1:2 dichloromethane/isopropanol mixture until colourless (five 20 mL portions). The combined organic fractions were dried over anhydrous sodium sulfate for 3 h, filtered, and evaporated under vacuum to give a purple solid as pure product (0.45 g, 88%). ^{1}H NMR (600 MHz, CD_2Cl_2, ppm) δ: 0.5-1.6 (CH2-CH3, 12H), 2.0-3.3 (N-CH2-CH2-N, 7H). 3.3-4.2 (N-CH2-CH3, 8H), 6.5-8.5 (aromatic, 10 H); ^{13}C NMR (151 MHz, C_2D_6SO, ppm) δ: 12 (CH3, - polarity), 42-47 (CH2, + polarity, 3 signals), 110-170(aromatic, 13+ signals), 172 (C=O, + polarity). MS (ESI): calcd for $C_{32}H_{39}N_4O_2^+$, 511.6; found, 511.4 (M+)

To a stirred solution of cyanuric chloride (0.072 g, 0.39 mmol) dissolved in anhydrous tetrahydrofuran (THF, 2 ml) cooled to 0 -5 ^{o}C was added $NaHCO_3$ (0.033 g, 0.39 mmol). After 20 minutes of addition, a solution containing rhodamine 6G piperazine (0.2 g, 0.39 mmol) in 5 ml anhydrous THF was added dropwise over a period of 30 min. The end of reaction was

monitored via TLC (silica gel, DCM). The product was isolated by centrifugation followed by filtration of the supernatant, and evaporation under vacuum to yield a pure product (purple precipitate) in quantitative yield (0.25 g, 97%).

Labeling of BC. DTAF and DTPR were grafted onto BC by stirring a 5 mL solution of 0.1 M NaOH, 1 mg/mL BC and 1 mM of the dye for 24 hrs. The samples were washed with 15 cycles of centrifugation (21,100×g, 30 s, Sorvall Legend Micro 21R Centrifuge, Thermo Scientific), decanting and resuspension in 1X PBS by vortexing. Samples were sonicated every third spindown using a ¼ inch point-probe (Branson SLPt, 40% amplitude, or 90 W, for 10 s) to disperse any cellulose that remained lumped even after vortexing. The sample was washed with water for 5 cycles to ensure all of the buffer was removed and the volume was adjusted to reach a final cellulose concentration of 1 mg/mL.

To graft APAF and ACy5, BC was first functionalized with a dichlorotriazinyl-aminopropyne (DTP) group, synthesized in house as previously reported.[45] Briefly, a 5 mL solution of 3:1 water:acetone containing 0.05 M NaOH, 1 mg/mL BC and 10 mM DTP was mixed using a rotating mixer for 24 hrs. Similarly to the previous cleaning procedure, the suspension was cleaned by centrifugation cycles 3 times with water, 3 times with acetone, 3 times with 1X PBS then 3 times with water and diluted to a final cellulose concentration of 1 mg/mL. The DTP-functionalized BC was then labeled with either ACy5 or APAF by mixing a 1X PBS (for ACy5) or 1:1 water:methanol (for APAF) solution of 1 mg/mL of DTP-BC, 1 mM of APAF or 5 μM of Cy5 or 10 μM of ACy5, 0.3 mM $CuSO_4 \cdot 5H_2O$ and 5 mM ascorbic acid for 24 hours. The ACy5-BC sample was cleaned with a minimum of 10 cycles of water washing, centrifugation, decanting and resuspension, while APAF-BC was cleaned with 5 washing cycles of 50% methanol, 3 cycles of PBS and 3 cycles of water washing and diluted to a final cellulose concentration of 1 mg/mL.

Super-resolution cellulose imaging. All cellulose samples were prepared on Matek glass-bottom petri dishes by drop casting 100 μL of a ~0.1 mg/mL solution of labelled BC and drying at 70ºC. For enzyme binding experiments, dried cellulose samples were first blocked with 3 mL of 10 mg/mL BSA (purified using a 0.045 μm syringe filter) in a 50 mM sodium acetate (NaAc), pH 5.0 buffer. The sample was incubated overnight, washed three times with buffer and incubated with 2 mL of 5 nM AF647-Cel7A for 2 hours at 4 ºC in NaAc buffer. Prior to imaging, all samples were washed three times with water and were imaged in Tris buffer under oxygen-scavenging and reducing conditions (50 mM Tris, pH 8.0, 10 mM NaCl, 10% glucose w/w, cysteamine, 0.56 mg/mL (56 u/mL) glucose oxidase and 40 μg/mL (381 u/mL) catalase). The concentration of cysteamine for imaging APAF-BC, $ACy5_{10\ \mu M}$-BC and $ACy5_{10\ \mu M}$-BC were 100 mM, 100 mM and 50 mM, respectively.

The samples were imaged using a Leica DMI6000 B inverted fluorescence microscope with adaptive focus control and equipped with a 100x/1.47NA HCXPLAPO oil-immersion objective. Illumination was provided by solid-state lasers housed within a Integrated Light Engine (ILE, Spectral Applied Research, Richmond Hill, ON, Canada) that controls illumination intensity and couples laser lines (405 nm, 488 nm, 561 nm and 647 nm) to a single output fiber. The laser light was coupled to the objective using a Borealis module (Spectral Applied Research, Richmond Hill, ON, Canada) using full field illumination and the samples were imaged in widefield, epifluorescence mode. Emission light was directed towards the appropriate colour filter (40-60 nm bandwidth) by a multiline dichroic mirror and the image was captured using an iXon Ultra DU-897U camera in single-molecule mode (10 MHz readout mode, frame transfer ON, 3.30 µs vertical clock speed, electron-multiplying mode) and a binning mode of 1. The projected pixel size was measured to be 96 nm. Diffraction-limited, well-dispersed and dim microfibrils, as such to avoid fibrillar bundles, were selectively imaged using STORM by illuminating the sample with 60% for DTAF-BC, 80% for ACy5$_{5\ \mu M}$-BC to 100% laser powers and an image sequence of 6000 for DTAF-BC or 24,000 frames for ACy5-BC was acquired with an exposure time of 30 ms (30 Hz actual frame rate). For samples labelled with ACy5, fluorophores were occasionally reactivated with a fixed, pre-recorded pulse sequence of 405 nm laser at 0.2% to 10% power so as to optimize the emission density within the dimmest cellulose fibrils. Average localization uncertainties were approximately 14 nm for ACy5-BC and 18 nm for DTAF-BC.

Image and Data Analysis. Image stacks were cropped to a time point where individual, discernable single molecule emission can be seen on the microfibrils, which was at 3,000 for DTAF-BC and ACy5$_{5\ \mu M}$-BC or 4,000 for ACy5$_{10\ \mu M}$-BC. Localization-fitting analysis was performed using the ThunderSTORM ImageJ plugin by applying a B-spline wavelet filter, approximating molecular positions through the local maximum method and calculating sub-pixel localizations by fitting a 2-dimesional integrated Gaussian function using the weighted least squares method.[72] Single emitter molecule localizations were selected using the following filter parameters: sigma<(mean(sigma)+std(sigma)) & sigma>(mean(sigma)-std(sigma*1.3)) & uncertainty<40 nm & uncertainty >5 nm & intensity<2500 photons. Consecutive emissions (with an OFF tolerance of 1 frame) within a 20 nm radius were merged. Sample drift was corrected using the cross-correlation method and the super-resolution image was rendered with a magnification factor of 5 (19.2 nm pixel size) or 10 (9.6 nm pixel size) for APAF-BC and ACy5-BC samples, respectively.

Using the ImageJ segmented line tool, isolated and dim microfibrils from at least twenty acquisitions of each sample were traced with a line width value of 18 pixels for APAF-

BC or 40 pixels for ACy5-BC and spline-fitted to acquire an intensity profile. Using MATLAB (MathWorks, Massachusetts), the 'findpeaks' function was used to identify the location and width of bright emission peaks, using threshold values of 40 nm inter-peak distance and 20 nm peak width. The peak prominence threshold was determined using one of two methods. The global thresholding method relied on the background population seen in the cumulated intensity distribution of all fibril profiles (Figure S4.3). In DTAF-BC fibrils, the image background was representative of the dark regions and three standard deviations above this population, which was determined through a bimodal fitting of the distribution, of 1.2 localizations was used. The second method was a local thresholding method based on the median peak prominence of all local maxima present in a profile. Without any thresholds, the "findpeaks" function was used to identify all local maxima and the median prominence of the identified peaks was used as the prominence threshold, in conjunction with 40 nm inter-peak distance and 20 nm peak width thresholds, to identify peaks that were representative of the bright regions (Figure S4.2). Peaks with a signal-to-background ratio below 2 were discarded. Using the peak position and widths that were determined through either of these thresholding methods, the length of the dark regions was calculated using the following equation, where x_i is the position of the ith peak:

$$Spacing\ length = x_{i+1} + \frac{FWHM_{i+1}}{2} - \left(x_i + \frac{FWHM_i}{2}\right) \qquad \textbf{(Equation 3)}$$

Spacing values lower than 20 nm were discarded, as this was the lower bound resolution of our super-resolution images.

Sulfuric acid hydrolysis of bacterial cellulose. In a water bath, 65% H_2SO_4 (w/w) was heated to 70°C and then 4.0 g of dry, purified BC was added with continuous mechanical stirring (final acid to cellulose ratio = 10 mL/g). Hydrolysis reaction times were varied from 2–60 minutes (as listed in Table 4.1) and all other conditions were kept constant. The hydrolyzed slurries were quenched in 10x volume of chilled water and allowed to equilibrate to RT. Cycles of centrifugation (1800g, 10-15 minute), decanting, and resuspension in water were used to remove the acid from the reaction mixture until the cellulose pellet was no longer stable (~4 rinses). The suspensions were extensively dialyzed (using Spectra Por dialysis tubing with 14 kDa MWCO from Sigma-Aldrich) against water for 2-3 weeks, with daily water changes, until constant pH. The suspensions were then sonicated for 2-3 minutes at 60% amplitude (equivalent to 90W, Sonifier 450; Branson Ultrasonics, Danbury, CT), and concentrated to ~1 wt% using an ultrafiltration stirred cell operating at ~140 kPa N_2 pressure (solvent-resistant stirred cell fitted with 76 mm ultrafiltration discs; Millipore). The

resulting suspensions were stored in acid-form in the refrigerator and labeled as bacterial cellulose nanocrystals (CNCs) along with the hydrolysis time used to produce them.

Conductometric titrations. To determine the surface sulfate half ester content of CNCs, 0.1 g of CNCs were added to 75 mL of 1 mM NaCl solution (used to increase the baseline conductivity of the suspension) and titrated with 2 mM NaOH. Injections of 0.2 mL of titrant were added every 30 seconds and the conductivity was measured upon each addition. An auto-titrator (Mandel, Man-Tech PLM-100214) was used with a Man-Tech 991 electrode, and titrations were done in triplicate for each suspension. The sulfur content (%S, g sulfur/100 g cellulose) was calculated from the equivalence point of the titration through the following equation (Dong et al 1998):

$$\%S = \frac{(V_{NaOH} C_{NaOH} MW_S)}{V_{susp} C_{susp}} \times 100\% \qquad \textbf{(Equation 4)}$$

Where V_{NaOH} is the volume of base used to reach the equivalence point, C_{NaOH} is the molar concentration of base, MW_S is the molecular weight of sulfur, V_{susp} is the volume of the B-CNC suspension, and C_{susp} is the B-CNC concentration in g/L.

Transmission electron microscopy (TEM). Images of B-CNC samples were obtained using a JEOL JEM 1200 EX TEMSCAN Transmission Electron Microscope operating at 56 kV. B-CNC suspensions (3.5 µL, 0.001% w/w) were dried onto freshly prepared 200-mesh carbon coated Cu grids. Grids were glow discharged prior to use in order to improve material dispersion. The grids were then stained with a 1% (w/v) solution of uranyl acetate for 2 minutes.

Atomic force microscopy (AFM). Square silicon wafer pieces (~1 cm^2) were cleaned using Piranha (3:1 H_2SO_4 (12M):H_2O_2 (30%)) and then thoroughly rinsed with water prior to use. Using a spin coater, 0.1 wt% polyallylamine hydrochloride was deposited onto each square followed by a rinse with water. Then, a drop of 0.01 wt% B-CNC suspension was spin-coated at 3000 rpm for 30 seconds in a G3P-12 Spin Coater (Specialty Coating Services, Indianapolis, IN), and a final rinse with water was performed. Images were acquired in tapping mode using a Nanoscope IIIa Multimode Scanning probe Microscope with cantilevers from Asylum Research (AC160TS type, 42 N/m spring constant, and 300 kHz nominal resonance frequency).

X-Ray diffraction. Two-dimensional diffraction patterns were collected using a D8 Davinci diffractometer (Bruker, Billerica, MA) equipped with a sealed tube cobalt source. All analysis of the resulting patterns was conducted using the Bruker TOPAS software. The beam was collimated to a diameter of 0.5 mm (35mA, 45kV). Cellulose samples were drop-cast and

oven dried onto clean Si wafer pieces for the analysis. A still frame of a blank piece of Si was initially examined to correct for background. The background intensity was subtracted from each sample frame prior to integration of the data. A 2θ range of 13–42° was used for the crystallinity index (CrI) analysis. Integration along relative angle χ for every 2θ value was performed to obtain one-dimensional diffraction plots of intensity versus 2θ (cf. wireframe in Figure 4.4b). The background corrected intensity vs. 2θ plots were fitted to five symmetric Lorentzian peaks, four peaks corresponding to the (100), (010), (002), and (040) crystalline planes[73], and one broad amorphous peak fixed at 24.1°. The CrI was calculated by the peak deconvolution method as the ratio of the area for the crystalline peaks over the total area for the diffraction plots. The CrI was calculated for Avicel 101 as reference to validate the deconvolution method. In addition, texture analysis was conducted to assess the degree of preferred orientation of the cellulose samples.

Acknowledgments

Mouhanad Babi was supported through a Natural Sciences and Engineering Research Council (NSERC) of Canada Graduate Scholarship – Doctoral Award. Jose Moran-Mirabal is the Tier 2 Canada Research Chair in Micro and Nanostructured Materials and the recipient of an Early Researcher Award from the Ontario Ministry of Research and Innovation.

Author Contributions

MB acquired super-resolution images, analyzed and interpreted results and wrote the first draft of the manuscript. AP and TA performed the time-course hydrolysis and CNC characterization experiments. AF and MB synthesized DTAF, DTAP and DTPR and fluorescently labeled cellulose. VJ performed X-ray diffraction measurements. JMM interpreted data and edited the manuscript. JMM and EDC conceptualized the work. The final draft of the manuscript was reviewed and approved by all authors.

Competing Interests

The authors declare no competing interests.

References

1. Calvin, M. The Path of Carbon in Photosynthesis. *Angewandte Chemie International Edition in English* **1**, 65–75 (1962).

2. Hon, D. N. S. Cellulose: a random walk along its historical path. *Cellulose* **1**, 1–25 (1994).

3. Delmer, D. P. Cellulose biosynthesis: exciting times for a difficult field of study. *Annual Review of Plant Physiology and Plant Molecular Biology* **50**, 245–276 (1999).

4. Klemm, D., Heublein, B., Fink, H. P. & Bohn, A. Cellulose: Fascinating biopolymer and sustainable raw material. *Angewandte Chemie - International Edition* vol. 44 3358–3393 (2005).

5. Moon, R. J., Martini, A., Nairn, J., Simonsen, J. & Youngblood, J. Cellulose nanomaterials review: structure, properties and nanocomposites. *Chemical Society Reviews* **40**, 3941–3994 (2011).

6. Fernandes, A. N. *et al.* Nanostructure of cellulose microfibrils in spruce wood. *Proceedings of the National Academy of Sciences of the United States of America* **108**, 1195–1203 (2011).

7. Nishiyama, Y. Structure and properties of the cellulose microfibril. *Journal of Wood Science* **55**, 241–249 (2009).

8. Altaner, C. M., Thomas, L. H., Fernandes, A. N. & Jarvis, M. C. How cellulose stretches: Synergism between covalent and hydrogen bonding. *Biomacromolecules* **15**, 791–798 (2014).

9. Matsuo, M., Sawatari, C., Iwai, Y. & Ozaki, F. Effect of Orientation Distribution and Crystallinity on the Measurement by x-ray Diffraction of the Crystal Lattice Moduli of Cellulose i and ii. *Macromolecules* **23**, 3266–3275 (1990).

10. Rose, M., Babi, M. & Moran-Mirabal, J. The study of cellulose structure and depolymerization through single-molecule Methods. *Industrial Biotechnology* **11**, 16–23 (2015).

11. Fink, H.-P., Purz, H. J., Bohn, A. & Kunze, J. Investigation of the supramolecular structure of never dried bacterial cellulose. *Macromolecular Symposia* **120**, 207–217 (1997).

12. Nishiyama, Y., Langan, P. & Chanzy, H. Crystal structure and hydrogen-bonding system in cellulose Iβ from synchrotron X-ray and neutron fiber diffraction. *Journal of the American Chemical Society* **124**, 9074–9082 (2002).

13. Nishiyama, Y., Sugiyama, J., Chanzy, H. & Langan, P. Crystal structure and hydrogen bonding system in cellulose Iα from synchrotron x-ray and neutron fiber diffraction. *Journal of the American Chemical Society* **125**, 14300–14306 (2003).

14. Martinez-Sanz, M., Gidley, M. J. & Gilbert, E. P. Hierarchical architecture of bacterial cellulose and composite plant cell wall polysaccharide hydrogels using small angle neutron scattering. *Soft Matter* **12**, 1534–1549 (2016).

15. Nishiyama, Y. *et al.* Periodic disorder along ramie cellulose microfibrils. *Biomacromolecules* **4**, 1013–1017 (2003).

16. Peura, M. *et al.* X-ray microdiffraction reveals the orientation of cellulose microfibrils and the size of cellulose crystallites in single Norway spruce tracheids. *Trees - Structure and Function* (2008) doi:10.1007/s00468-007-0168-5.

17. Martínez-Sanz, M., Gidley, M. J. & Gilbert, E. P. Application of X-ray and neutron small angle scattering techniques to study the hierarchical structure of plant cell walls: A review. *Carbohydrate Polymers* (2015) doi:10.1016/j.carbpol.2015.02.010.

18. Park, S., Baker, J. O., Himmel, M. E., Parilla, P. A. & Johnson, D. K. Cellulose crystallinity index: Measurement techniques and their impact on interpreting cellulase performance. *Biotechnology for Biofuels* **3**, 1–10 (2010).

19. Kargarzadeh, H. *et al.* Effects of hydrolysis conditions on the morphology, crystallinity, and thermal stability of cellulose nanocrystals extracted from kenaf bast fibers. *Cellulose* **19**, 855–866 (2012).

20. Chen, W. *et al.* Isolation and characterization of cellulose nanofibers from four plant cellulose fibers using a chemical-ultrasonic process. *Cellulose* **18**, 433–442 (2011).

21. Hernandez, C. C., Ferreira, F. F. & Rosa, D. S. X-ray powder diffraction and other analyses of cellulose nanocrystals obtained from corn straw by chemical treatments. *Carbohydrate Polymers* **193**, 39–44 (2018).

22. Cao, Y. & Tan, H. Study on crystal structures of enzyme-hydrolyzed cellulosic materials by X-ray diffraction. *Enzyme and Microbial Technology* **36**, 314–317 (2005).

23. Cao, Y. & Tan, H. Effects of cellulase on the modification of cellulose. *Carbohydrate Research* **337**, 1291–1296 (2002).

24. Habibi, Y., Lucia, L. A. & Rojas, O. J. Cellulose nanocrystals: Chemistry, self-assembly, and applications. *Chemical Reviews* **110**, 3479–3500 (2010).

25. Battista, O. A. Hydrolysis and Crystallization of Cellulose. *Industrial & Engineering Chemistry* **42**, 502–507 (1950).

26. Wiman, M. *et al.* Cellulose accessibility determines the rate of enzymatic hydrolysis of steam-pretreated spruce. in *Bioresource Technology* vol. 126 208–215 (Elsevier Ltd, 2012).

27. Thompson, D. N., Chen, H. C. & Grethlein, H. E. Comparison of pretreatment methods on the basis of available surface area. *Bioresource Technology* **39**, 155–163 (1992).

28. Jeoh, T. *et al.* Cellulase digestibility of pretreated biomass is limited by cellulose accessibility. *Biotechnology and Bioengineering* **98**, 112–122 (2007).

29. Ryu, D. D. Y., Lee, S. B., Tassinari, T. & Macy, C. Effect of compression milling on cellulose structure and on enzymatic hydrolysis kinetics. *Biotechnology and Bioengineering* **24**, 1047–1067 (1982).

30. Thygesen, L. G., Hidayat, B. J., Johansen, K. S. & Felby, C. Role of supramolecular cellulose structures in enzymatic hydrolysis of plant cell walls. *Journal of Industrial Microbiology and Biotechnology* **38**, 975–983 (2011).

31. Andersons, J., Poriķe, E. & Spārniņš, E. Modeling strength scatter of elementary flax fibers: The effect of mechanical damage and geometrical characteristics. *Composites Part A: Applied Science and Manufacturing* **42**, 543–549 (2011).

32. Aslan, M., Chinga-Carrasco, G., Sørensen, B. F. & Madsen, B. Strength variability of single flax fibres. in *Journal of Materials Science* vol. 46 6344–6354 (2011).

33. Thygesen, L. G., Eder, M. & Burgert, I. Dislocations in single hemp fibres-investigations into the relationship of structural distortions and tensile properties at the cell wall level. *Journal of Materials Science* **42**, 558–564 (2007).

34. Hidayat, B. J., Felby, C., Johansen, K. S. & Thygesen, L. G. Cellulose is not just cellulose: A review of dislocations as reactive sites in the enzymatic hydrolysis of cellulose microfibrils. *Cellulose* **19**, 1481–1493 (2012).

35. Novy, V. *et al.* Quantifying cellulose accessibility during enzyme-mediated deconstruction using 2 fluorescence-tagged carbohydrate-binding modules. *Proceedings of the National Academy of Sciences of the United States of America* **116**, 22545–22551 (2019).

36. CLEAVAGE OF SOFTWOOD KRAFT PULP FIBRES BY HCL AND CELLULASES | Ander | BioResources. https://ojs.cnr.ncsu.edu/index.php/BioRes/article/view/BioRes_03_2_0477_Ander_HD_Cleavage_Kraft_Fibers/196.

37. Astley, O. M. & Donald, A. M. A small-angle X-ray scattering study of the effect of hydration on the microstructure of flax fibers. *Biomacromolecules* **2**, 672–680 (2001).

38. Hanley, S., Revol, J.-F., Godbout, L. & Gray, D. Atomic force microscopy and transmission electron microscopy of cellulose from Micrasterias denticulata; evidence for a chiral helical microfibril twist. *Cellulose* **4**, 209–220 (1997).

39. Tokoh, C., Takabe, K., Fujita, M. & Saiki, H. Cellulose synthesized by Acetobacter xylinum in the presence of acetyl glucomannan. *Cellulose* **5**, 249–261 (1998).

40. van de Linde, S. *et al.* Direct stochastic optical reconstruction microscopy with standard fluorescent probes. *Nature protocols* **6**, 991–1009 (2011).

41. Rust, M. J., Bates, M. & Zhuang, X. Sub-diffraction-limit imaging by stochastic optical reconstruction microscopy (STORM). *Nature Methods* **3**, 793–795 (2006).

42. Araki, J. & Kuga, S. Effect of trace electrolyte on liquid crystal type of cellulose microcrystals. *Langmuir* **17**, 4493–4496 (2001).

43. Reid, M. S., Karlsson, M. & Abitbol, T. Fluorescently labeled cellulose nanofibrils for detection and loss analysis. *Carbohydrate Polymers* **250**, 116943 (2020).

44. Helbert, W., Chanzy, H., Husum, T. L., Schülein, M. & Ernst, S. Fluorescent cellulose microfibrils as substrate for the detection of cellulase activity. *Biomacromolecules* **4**, 481–487 (2003).

45. Fatona, A., Berry, R. M., Brook, M. A. & Moran-Mirabal, J. M. Versatile Surface Modification of Cellulose Fibers and Cellulose Nanocrystals through Modular Triazinyl Chemistry. *Chemistry of Materials* **30**, 2424–2435 (2018).

46. Moran-Mirabal, J. M., Santhanam, N., Corgie, S. C., Craighead, H. G. & Walker, L. P. Immobilization of cellulose fibrils on solid substrates for cellulase-binding studies through quantitative fluorescence microscopy. *Biotechnology and Bioengineering* **101**, 1129–1141 (2008).

47. Luterbacher, J. S., Walker, L. P. & Moran-Mirabal, J. M. Observing and modeling BC degradation by commercial cellulase cocktails with fluorescently labeled Trichoderma reseii Cel7A through confocal microscopy. *Biotechnology and Bioengineering* **110**, 108–117 (2013).

48. Usov, I. *et al.* Understanding nanocellulose chirality and structure-properties relationship at the single fibril level. *Nature Communications* **6**, 1–11 (2015).

49. Dempsey, G. T., Vaughan, J. C., Chen, K. H., Bates, M. & Zhuang, X. Evaluation of fluorophores for optimal performance in localization- based super-resolution imaging. *Nature methods* **8**, 1–44 (2011).

50. Kargarzadeh, H. *et al.* Effects of hydrolysis conditions on the morphology, crystallinity, and thermal stability of cellulose nanocrystals extracted from kenaf bast fibers. *Cellulose* **19**, 855–866 (2012).

51. Reiniati, I., Hrymak, A. N. & Margaritis, A. Recent developments in the production and applications of bacterial cellulose fibers and nanocrystals. *Critical Reviews in Biotechnology* **37**, 510–524 (2017).

52. Martínez-Sanz, M., Lopez-Rubio, A. & Lagaron, J. M. Optimization of the nanofabrication by acid hydrolysis of bacterial cellulose nanowhiskers. *Carbohydrate Polymers* **85**, 228–236 (2011).

53. Roman, M. & Winter, W. T. Effect of sulfate groups from sulfuric acid hydrolysis on the thermal degradation behavior of bacterial cellulose. *Biomacromolecules* **5**, 1671–1677 (2004).

54. Stephanie Beck-Candanedo, †, Maren Roman, ‡ and & Derek G. Gray*, †. Effect of Reaction Conditions on the Properties and Behavior of Wood Cellulose Nanocrystal Suspensions. *Biomacromolecules* **6**, 1048–1054 (2005).

55. Vanderfleet, O. M., Osorio, D. A. & Cranston, E. D. Optimization of cellulose nanocrystal length and surface charge density through phosphoric acid hydrolysis. *Philosophical Transactions of the Royal Society A: Mathematical, Physical and Engineering Sciences* **376**, (2018).

56. Scallan, A. M. A Quantitative Picture of the Fringed Micellar Model of Cellulose. *Textile Research Journal* **41**, 647–653 (1971).

57. Habibi, Y. *et al.* Bionanocomposites based on poly(ε-caprolactone)-grafted cellulose nanocrystals by ring-opening polymerization. *Journal of Materials Chemistry* **18**, 5002 (2008).

58. Zaar, K. Visualization of pores (export sites) correlated with cellulose production in the envelope of the gram-negative bacterium Acetobacter xylinum. *Journal of Cell Biology* **80**, 773–777 (1979).

59. Du, J., Vepachedu, V., Cho, S. H., Kumar, M. & Nixon, B. T. Structure of the cellulose synthase complex of Gluconacetobacter hansenii at 23.4 Å resolution. *PLoS ONE* **11**, (2016).

60. Hu, S.-Q. *et al.* Structure of bacterial cellulose synthase subunit D octamer with four inner passageways. *Proceedings of the National Academy of Sciences* **107**, 17957–17961 (2010).

61. Zhao, Z. *et al.* Cellulose microfibril twist, mechanics, and implication for cellulose biosynthesis. *Journal of Physical Chemistry A* **117**, 2580–2589 (2013).

62. Cook, K. E. & Colvin, J. R. Evidence for a beneficial influence of cellulose production on growth of Acetobacter xylinum in liquid medium. *Current Microbiology: An International Journal* **3**, 203–205 (1980).

63. Cosgrove, D. J. Growth of the plant cell wall. *Nature Reviews Molecular Cell Biology* vol. 6 850–861 (2005).

64. Mcqueen-Mason, S. & Cosgrove, D. J. Disruption of hydrogen bonding between plant cell wall polymers by proteins that induce wall extension. *Proceedings of the National Academy of Sciences of the United States of America* **91**, 6574–6578 (1994).

65. Hayashi, T., Ogawa, K. & Mitsuishi, Y. Characterization of the adsorption of Xyloglucan to Cellulose. *Plant and Cell Physiology* **35**, 1199–1205 (1994).

66. Localization of xyloglucan in the macromolecular complex composed of xyloglucan and cellulose in pea stems. https://agris.fao.org/agris-search/search.do?recordID=JP9501830.

67. Park, Y. W. *et al.* Enhancement of growth by expression of poplar cellulase in Arabidopsis thaliana. *Plant Journal* **33**, 1099–1106 (2003).

68. Moran-Mirabal, J. M., Corgie, S. C., Bolewski, J. C., Smith, H. M. & Walker, L. P. Fluorescence Labeling And Purification Of Cellulases For Single Molecule Spectroscopy. *Biophysical Journal* **96**, 45a (2009).

69. Lehtiö, J. *et al.* The binding specificity and affinity determinants of family 1 and family 3 cellulose binding modules. *Proc. Natl. Acad. Sci. {U.S.A.}* **100**, 484–489 (2003).

70. Toyosaki, H. & Naritomi, T. Screening of Bacterial Cellulose-producing Acetobacter Strains Suitable for Agitated. *Biosci. Biotech. …* **59**, 1498–1502 (1995).

71. Blakeslee, D. & Baines, M. G. Immunofluorescence using dichlorotriazinylaminofluorescein (DTAF) I. Preparation and fractionation of labelled IgG. *Journal of Immunological Methods* (1976) doi:10.1016/0022-1759(76)90078-8.

72. Ovesný, M., Křížek, P., Borkovec, J., Švindrych, Z. & Hagen, G. M. ThunderSTORM: A comprehensive ImageJ plug-in for PALM and STORM data analysis and super-resolution imaging. *Bioinformatics* **30**, 2389–2390 (2014).

73. Briois, B. *et al.* Iα → Iβ transition of cellulose under ultrasonic radiation. *Cellulose* vol. 20 597–603 (2013).

Chapter 4 Supplementary Information

Direct super-resolution imaging of the alternating disordered and crystalline structure of cellulose fibrils

Mouhanad Babi,[1] Anthony Palermo,[1] Tiffany Abitbol,[2] Ayodele Fatona[1], Victoria M. Jarvis,[3] Akanksha Nayak[1], Emily D. Cranston[4], and Jose M. Moran-Mirabal[1,5]*

[1] *Department of Chemistry and Chemical Biology, McMaster University, Hamilton, ON, Canada,*

[2] *RISE Research Institutes of Sweden, Stockholm, Sweden*

[3] *McMaster Analytical X-ray Diffraction Facility, McMaster University, Hamilton, ON, Canada*

[4] *Department of Wood Science, University of British Columbia, 2424 Main Mall, Vancouver, BC, Canada*

[5] *Centre for Advanced Light Microscopy, McMaster University, Hamilton, ON, Canada*

*Please address all correspondence to Jose Moran-Mirabal (mirabj@mcmaster.ca)

a **b**

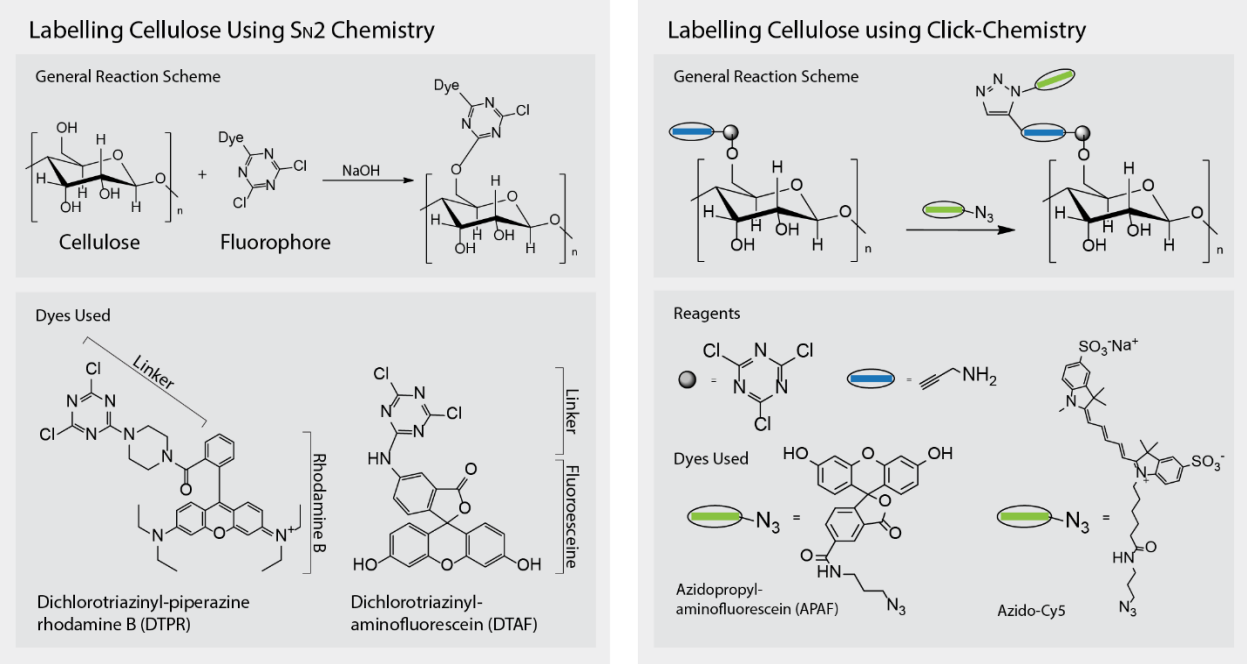

Figure S4.1 Labelling BC with different dyes and using different reactions. In a first approach (a) BC was fluorescently labelled directly grafting using two different dyes: fluorescein (DTAF) and rhodamine 6G (DTPR). Both reactions utilized a dichlorotriazinyl group to act as an electrophilic linker that can be nucleophilically attacked by the free C6 hydroxyl group present on the glucose monomers of cellulose. In a second reaction scheme (b), fluorescein and Cy5 were also grafted onto BC using click chemistry. BC was first functionalized with a propyne group using dichlorotriazinyl as a linker. This group then underwent a click reaction with the azide moiety of APAF or ACy5, allowing them to be covalently linked to BC. All grafting reactions were followed by a cleaning procedure involving repeated centrifugation, decanting and resuspension.

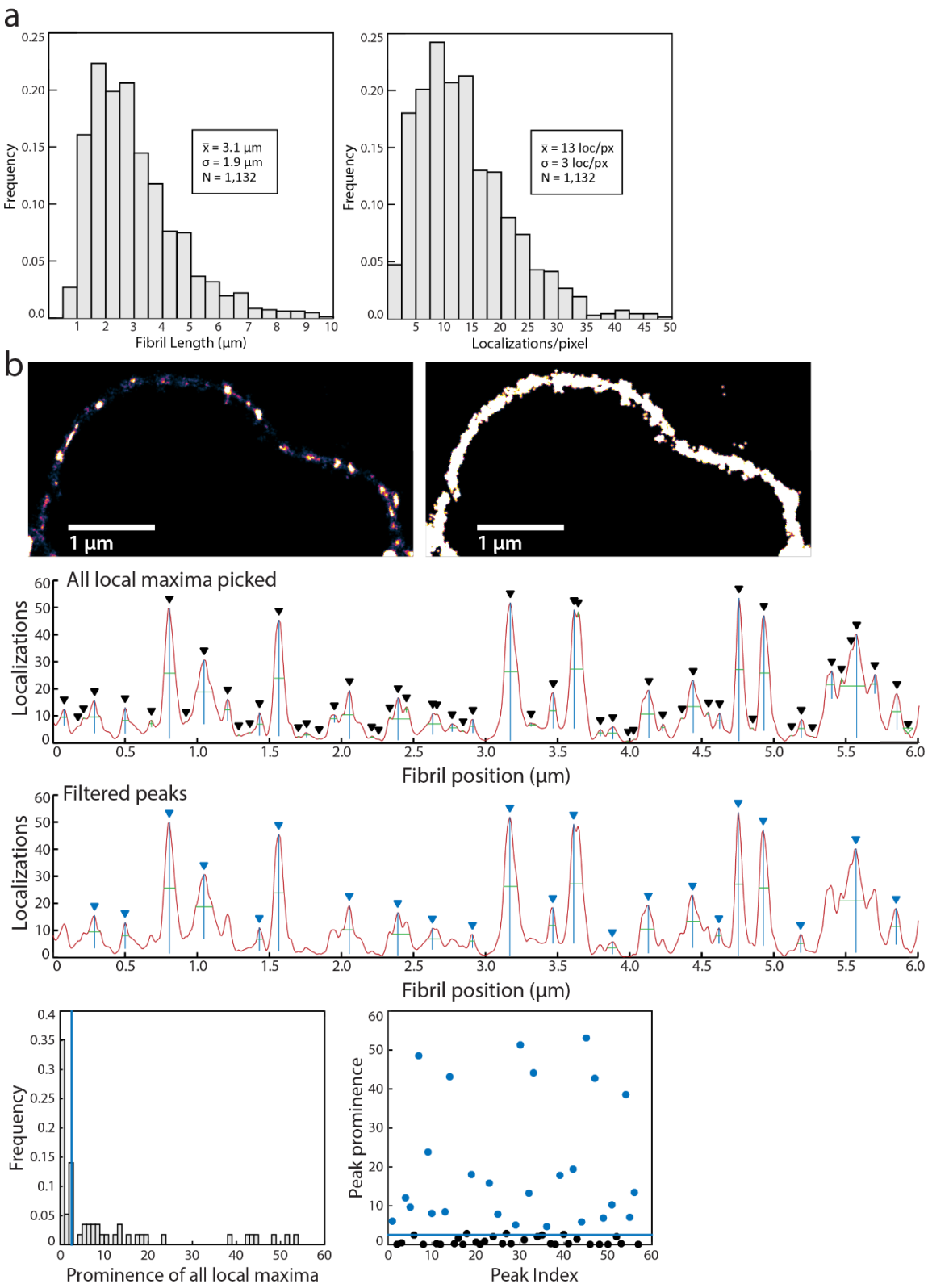

Figure S4.2 Localization continuity of ACy5-BC microfibrils and the identification of bright regions using the local median threshold method. (a) Contour length (left) and average

localization density (right, 9.61 nm pixel size) distributions of traced $Cy5_{5\ \mu M}$-BC fibrils imaged using STORM. (b) STORM image of a representative $Cy5_{5\ \mu M}$-BC fibril showing an alternating labelling pattern of dark and bright regions (left) while being continuously mapped by molecular localizations, as seen in the binary image (right). (c) Line-intensity profile of the traced cellulose fibril exhibited many local maxima (top profile, black triangles), which can be filtered using a median prominence threshold and a local signal-to-background ratio of 2 to select peaks that are representative of the bright regions (bottom profile, blue triangles). As seen in the histogram and scatter plot of the prominence of all local maxima, this filtering method disregards the most abundant population of local maxima (population to the left of the blue line in histogram and black dots in the scatter plot) that arise from minor intensity fluctuations within the dark region of the fibril.

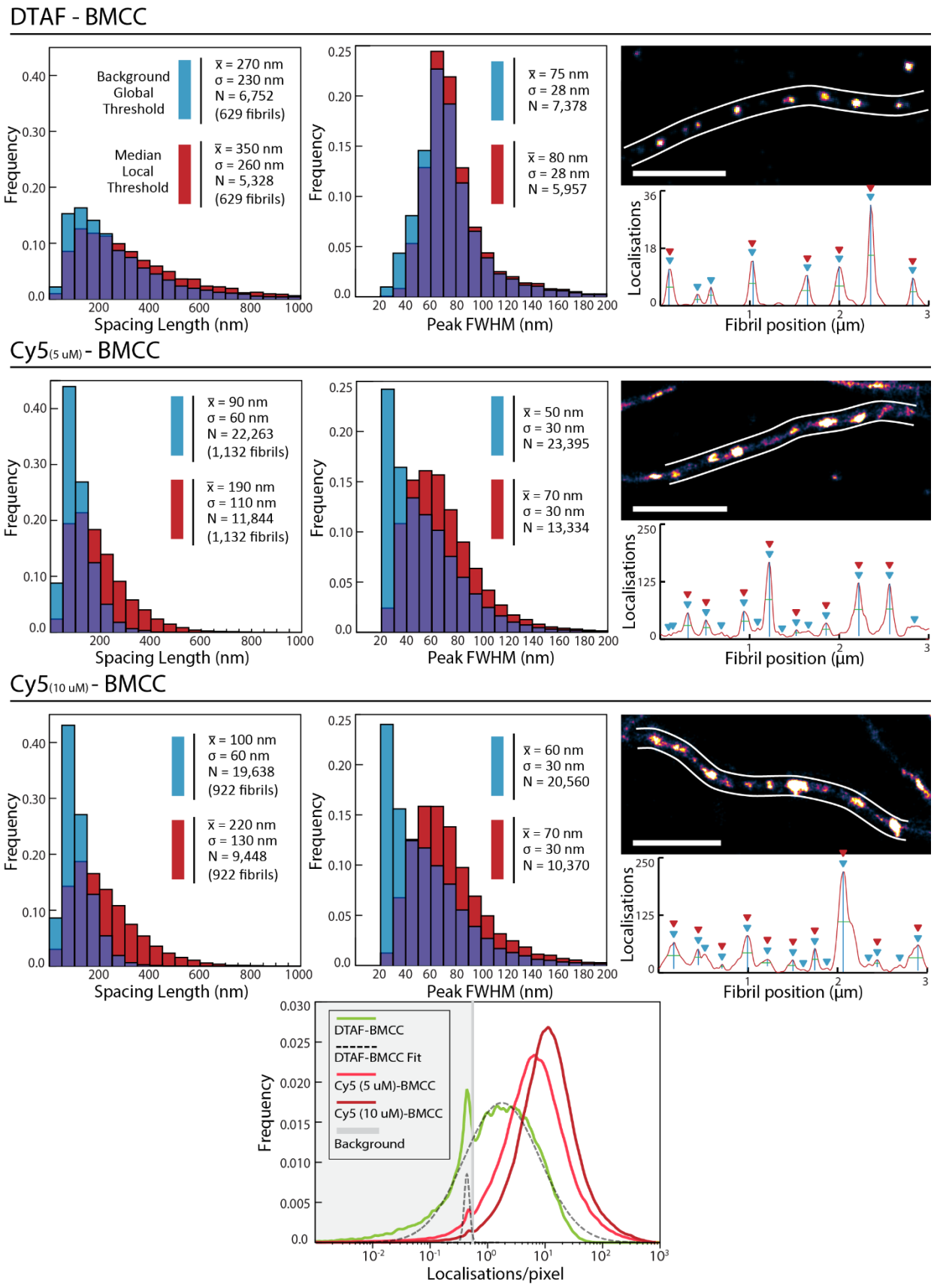
DTAF - BMCC
Background Global Threshold
x̄ = 270 nm
σ = 230 nm
N = 6,752
(629 fibrils)
Median Local Threshold
x̄ = 350 nm
σ = 260 nm
N = 5,328
(629 fibrils)
Frequency
Spacing Length (nm)
x̄ = 75 nm
σ = 28 nm
N = 7,378
x̄ = 80 nm
σ = 28 nm
N = 5,957
Peak FWHM (nm)
Localisations
Fibril position (µm)
Cy5(5 uM) - BMCC
x̄ = 90 nm
σ = 60 nm
N = 22,263
(1,132 fibrils)
x̄ = 190 nm
σ = 110 nm
N = 11,844
(1,132 fibrils)
x̄ = 50 nm
σ = 30 nm
N = 23,395
x̄ = 70 nm
σ = 30 nm
N = 13,334
Cy5(10 uM) - BMCC
x̄ = 100 nm
σ = 60 nm
N = 19,638
(922 fibrils)
x̄ = 220 nm
σ = 130 nm
N = 9,448
(922 fibrils)
x̄ = 60 nm
σ = 30 nm
N = 20,560
x̄ = 70 nm
σ = 30 nm
N = 10,370
DTAF-BMCC
DTAF-BMCC Fit
Cy5 (5 uM)-BMCC
Cy5 (10 uM)-BMCC
Background
Localisations/pixel

Figure S4.3 Different thresholding methods used for quantitatively characterizing the labelling pattern of DTAF-BC and ACy5-BC microfibrils. Bacterial cellulose was fluorescently labelled in one step with a fluorescein-based dye, DTAF, or using a two-step reaction with 5 uM or 10 μM of azido-Cy5. A semi-logarithmic histogram representation of intensity values of DTAF-BC profiles (based on 10 nm pixels) shows a bimodal distribution (bottom), with the overlapping leftmost population representing a background intensity that resided within the sparsely labelled regions of cellulose microfibrils. To systematically identify the brightly labeled peaks representative of the putative disordered cellulose regions, two Gaussian functions were fit to the histogram, and an intensity threshold of 3 standard deviations above the sparsely labeled (low intensity) population was used for peak selection. The size of these regions was measured by the full width at half max (FWHM) of the peaks, and the spacing length between the peaks at their FWHM was used to measure the size of the dark regions. The global thresholding method correctly identified the bright regions for DTAF-BC fibril profiles (top row, right, blue triangles) and yielded reasonable spacing length and peak width values (top row, left and middle). In the case of ACy5-BC, the background intensity population that was seen in DTAF-BC was still present, although it was considerably lower in intensity when 5 μM of dye was used and almost completely disappeared at 10 μM. Compared to DTAF-BC, the increased labelling density offered by the two-step labelling reaction and the superior photostability and re-activatability ACy5 dye permitted more localizations within the putative crystalline regions, causing the dark regions to have an intensity above the image background. As a result, the global thresholding method, which was based on the background population, selected many small peaks in the ACy5-BC profiles that stemmed from minor intensity fluctuations within the dark regions and yielded small size distributions of the apparent dark and bright regions. A second thresholding method based on the median prominence of all local maxima in any given intensity profile, in combination with a filter that disregarded all identified peaks whose local signal-to-background ratio was below 2 (see Supplementary Figure 2), correctly identified peaks associated with the bright regions (red triangles) in both ACy5-BC samples and resulted in spacing length distributions that were in close agreement with the length of CNCs produced after at least 15 mins of acid hydrolysis (see Supplementary Figure 5). The two thresholding methods yielded similar spacing length and peak width measurements for DTAF-BC, although the median local threshold occasionally missed peaks as it relied on the presence of molecular localization within the dark regions.

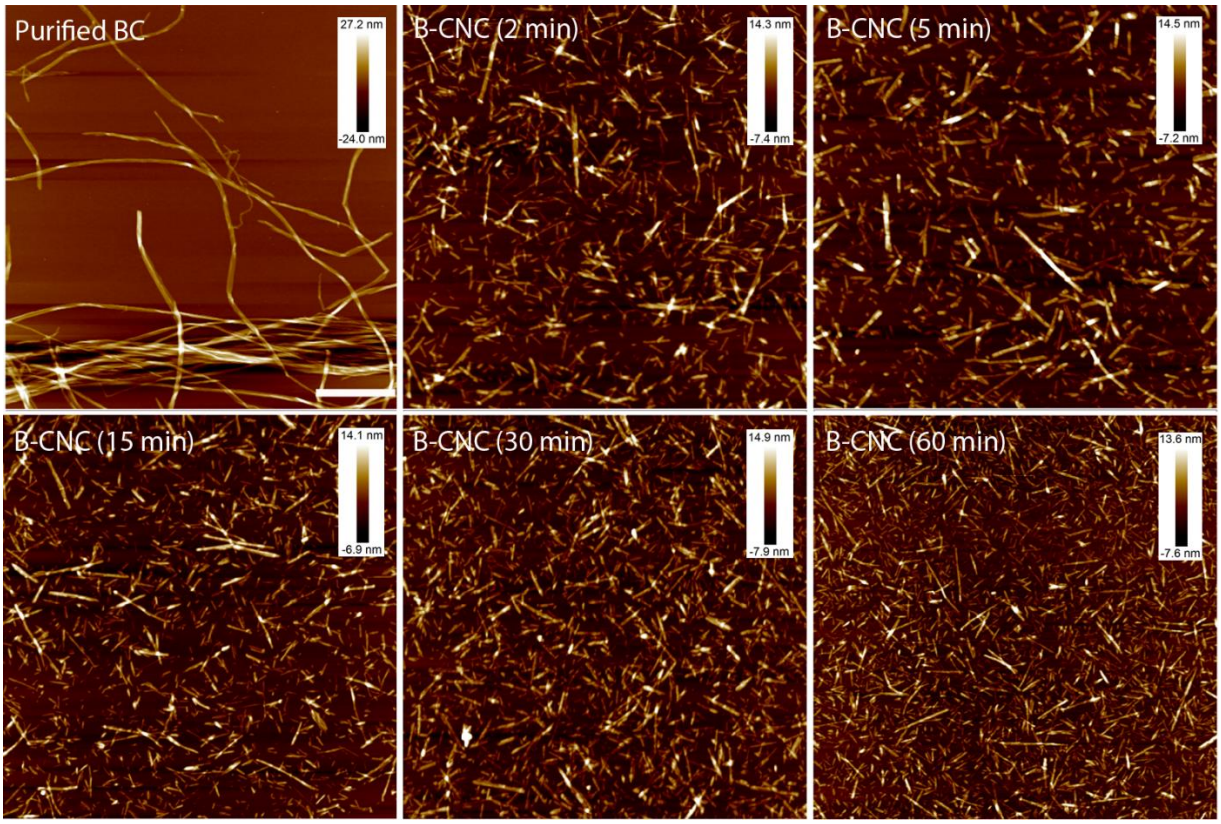

Figure S4.4 AFM images of BC and CNCs produced following various times of acid hydrolysis. BC was hydrolyzed using sulphuric acid for 2 – 60 minutes and the height of the resultant CNCs were measured using AFM.

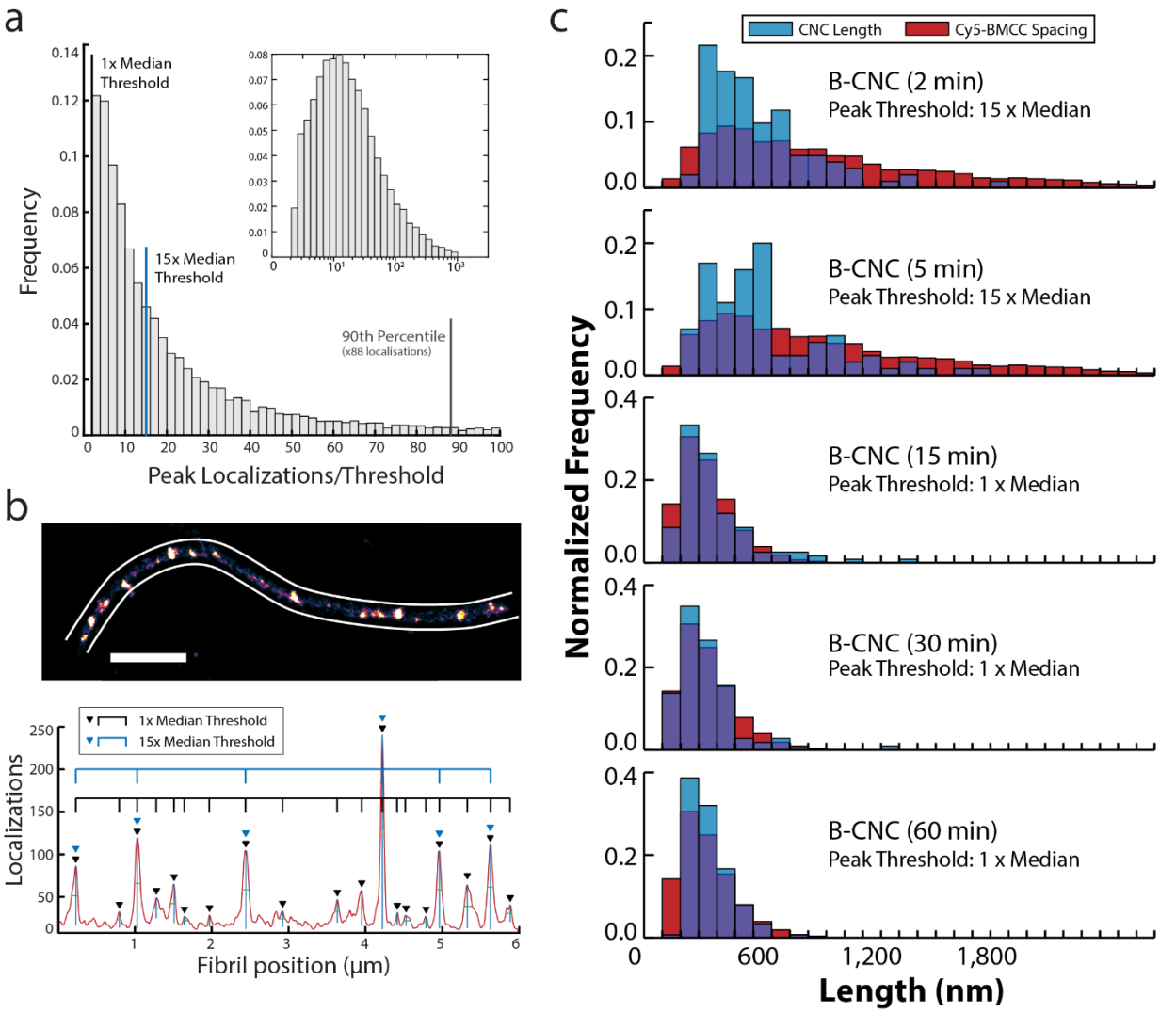

Figure S4.5. Lengths of CNCs produced from BC with different acid hydrolysis times compared to ACy5 5 µM-BC spacing lengths measured with varying peak-picking thresholds. (a) Intensity distribution of the bright regions relative to the peak-picking threshold (i.e. intensity of dark regions) shows that the disordered regions were heterogeneous, with 3 to 100 times more accessibility than the putative crystalline regions. (b) Using a median prominence threshold of all local maxima (black line in figure a), the spacing length was measured between all bright regions on the fibril, while increasing the peak-picking threshold by 15-fold (blue line in figure b) results in the measurements of spacing lengths only between the most intense peaks. (c) Distribution of spacing lengths measured using varying peak-picking thresholds compared to the length distribution of CNCs produced using different acid hydrolysis times shows how variable accessibility of the disordered regions leads to a time-dependent cleavage of the fibrils.

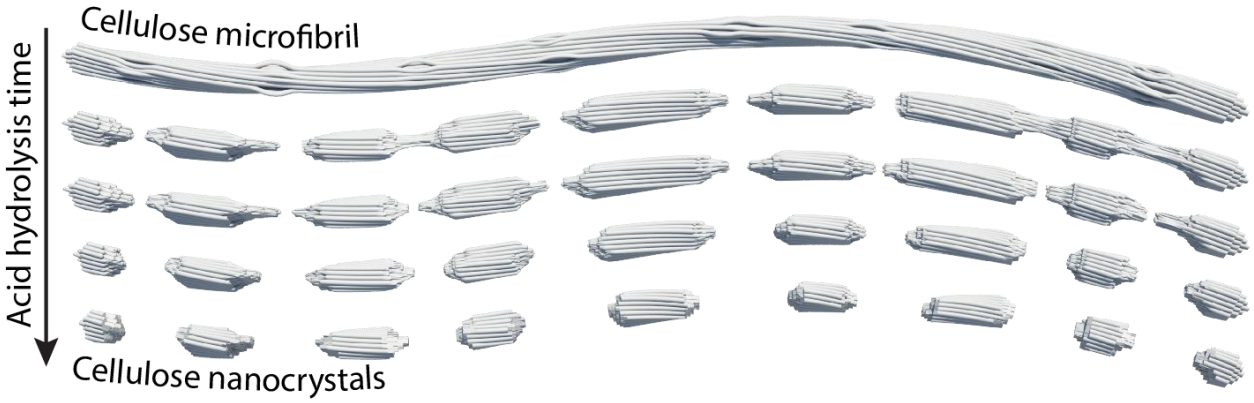

Figure S4.6. Proposed mechanism for the acid hydrolysis cellulose microfibrils in the production of cellulose nanocrystals. Super-resolution imaging of BC microfibrils unveiled the recurring presence of disordered regions with heterogenous accessibility to small molecules. This result, in combination with the length distribution of CNCs produced after various durations of sulfuric acid hydrolysis (2 - 60 mins), suggests that cellulose microfibrils are first cleaved at their most disordered regions to yield CNCs with polydisperse lengths (2 - 5 mins hydrolysis). As the acid hydrolysis progress for longer durations, the smaller (less accessible) dislocations are hydrolyzed, causing long CNCs to be cleaved and resulting in a more homogenous population of CNCs (15 mins hydrolysis). At longer hydrolysis times of 30 to 60 mins, the CNCs are slowly degraded from their ends and the reduction of their length begins to plateau, yielding a monodispersed and relatively short population of CNCs.

Chapter 5

Unraveling the supramolecular structure and nanoscale dislocations of bacterial cellulose ribbons using correlative super-resolution light and electron microscopy

Mouhanad Babi,[1] Alyssa Williams,[2] Marcia Reid,[3] Kathryn Grandfield,[2,4] Nabil Bassim,[2,3,4] and Jose M. Moran-Mirabal[1,2,5,6]*

[1] *Department of Chemistry and Chemical Biology, McMaster University, Hamilton, ON, Canada*

[2] *School of Biomedical Engineering, McMaster University, Hamilton, ON, Canada*

[3] *Canadian Center for Electron Microscopy, McMaster University, Hamilton, ON, Canada*

[4] *Department of Materials Science and Engineering, McMaster University, Hamilton, ON, Canada*

[5] *Brockhouse Institute for Materials Research, McMaster University, Hamilton, ON, Canada*

[6] *Center for Advanced Light Microscopy, McMaster University, Hamilton, ON, Canada*

*Please address all correspondence to Jose Moran-Mirabal (mirabj@mcmaster.ca)

Abstract

Cellulose is a structural linear polysaccharide that is naturally produced by plants and bacteria, making it the most abundant biopolymer on Earth. The biosynthesis and ability to process this sustainable resource for materials applications is intimately linked to the hierarchical structure of cellulose from the nano to microscale. The morphology of bacterial cellulose microfibrils and their assembly into higher order structures, in addition to the structural origins of the alternating crystalline and disordered supramolecular structure of cellulose, have remained elusive. In this work, we employed high resolution and cryogenic transmission electron microscopy to study the morphology of bacterial cellulose ribbons at different levels of its structural hierarchy and provide direct visualization of nanometer wide microfibrils. The non-persistent twisting of cellulose ribbons was characterized in detail, and we found that twists are associated with nanostructural defects at the bundle and microfibril levels. To investigate the structural origins of the persistent disordered regions that are present along cellulose ribbons, we employed a correlative super-resolution light and electron microscopy workflow and observed that most of the disordered regions that can be seen in super-resolution fluorescence microscopy correlated with the ribbon twisting observed in electron microscopy. Unraveling the hierarchical assembly of bacterial cellulose and the ultrastructural basis of its disordered regions provides insight into its biosynthesis and susceptibility to hydrolysis. These findings are important for understanding the cell-directed assembly of cellulose, for developing new cellulose-based nanomaterials, and to develop more efficient biomass conversion strategies.

5.1 Introduction

Cellulose is a linear polymer of glucose that is naturally assembled into nanometer wide microfibrils, higher order bundles and networks that provide the plant cell wall with the strength and structural integrity that is needed to protect and support plant life.[1] The different structural hierarchy levels of cellulose possess unique properties that make them useful for a variety of applications. On the macroscale, cellulose is the primary constituent of wood and endows it with the mechanical strength that makes it an excellent building material,[2] while the properties of wood derived pulp are leveraged for the production of paper, fabrics and clothing products.[3,4] Further mechanical, enzymatic and chemical processing of wood pulp deconstructs it into highly crystalline cellulose nanomaterials, including cellulose nanofibrils and nanocrystals (CNCs), which possess high surface area and can be functionalized for use in new biodegradable plastics, nanocomposites, cellular scaffolds, sensing devices and drug delivery vehicles.[5,6] Furthermore, cellulose can be completely depolymerized into its constituent sugar building blocks and fermented to

produce renewable biofuels, but this process is currently inefficient due to the recalcitrant crystalline packing of cellulose fibrils.[7] In order to realize the full potential of this ubiquitous and sustainable material, it is essential to understand the structure of cellulose at different hierarchical levels.

It is generally accepted that the hierarchical structure of cellulose is driven by the spatial organization of the enzymes responsible for its biosynthesis.[8,9] Bacteria like *Komagataeibacter xylinus* (formerly known as *Gluconacetobacter xylinus* or *Acetobacter xylinus*)[10] has been used as a model organism to study cellulose biosynthesis and morphology as it produces large amounts of crystalline cellulose with minimal impurities or additional components that are otherwise produced in plants, like lignin and hemicelluloses.[11] During bacterial cellulose synthesis, a complex of cellulose synthases and associated proteins that reside between the inner and outer membranes of the bacterial envelope synthesize cellulose glucan chains and assemble them into a microfibril.[12] Since these terminal complexes (TCs) are arranged linearly along the bacterium surface, microfibrils laterally assemble to form bundles and ribbons.[13,14] The supramolecular structure of cellulose, particularly microfibrils, and the presence of other hierarchical levels like the elementary fibril (also known as a protofibril and sub-elementary fibril) remain debatable since they have never been visualized in high resolution directly within cellulose ribbons. Studying the morphology of these structures is important for understanding cellulose biosynthesis in bacteria and for gaining insight into the spatial organization of TCs that encodes cellulose assembly at this scale.

At the single fibril level, it has been long postulated that cellulose is organized into alternating crystalline and disordered regions with varying susceptibility to hydrolysis.[15,16] This model is based on the nonlinear hydrolysis of cellulose, which initially involves rapid cleavage of the fibrils into 100 – 200 nm long CNCs followed by a leveling off of the degree of polymerization.[17] The first evidence for this supramolecular organization of the microfibril was provided by small-angle neutron scattering, which detected the presence of periodic disordered regions along plant microfibrils that exhibited enhanced accessibility for deuterium exchange.[18] Recent work in our group involving super-resolution fluorescence microscopy (SRFM) provided direct visualization of the alternating crystalline and disordered regions along individual bacterial fibrils, and showed that the disordered regions vary in their accessibility and do not constitute a significant amorphous cellulose fraction that can be directly detected using x-ray diffraction.[19] Yet, the structural origin of these disordered regions and the level of hierarchy that they exist in remains unclear.

In this work, we use high resolution and cryogenic transmission electron microscopy (TEM) to study the hierarchical organization of bacterial cellulose ribbons, and combine this technique with SRFM in a correlative super-resolution light and electron microscopy (SR-CLEM) workflow to gain insight into the structural origins of the disordered regions. The morphology of cellulose was studied at the ribbon, bundle and microfibril levels and the non-persistent twisting of cellulose ribbons was characterized in detail. Through SR-CLEM, the persistent dislocations that can be seen in SRFM were correlated with the locally twisted regions of cellulose ribbons and their associated nanostructural defects. Studying the morphology of cellulose and the susceptible areas present across its structural hierarchy is critical for understanding cellulose biosynthesis and the development of efficient methods to partially or fully depolymerize cellulose to generate cellulose nanomaterials and fermentable sugars for bioplastic and biofuel production.

5.2 Results

5.2.1 TEM characterization of bacterial cellulose

The morphology and hierarchical organization of bacterial cellulose were characterized at various scales using brightfield transmission electron microscopy (TEM). Unstained cellulose prepared on formvar-coated grids consisted of a loose mesh of ribbons, each exhibiting a right-handed twist that appeared as a thin dark strip along the ribbon (Figure 5.1a). Negative staining with uranyl acetate revealed more detailed structural features (Figure 5.1b), including 10–16 nm wide striations or banding (Figure 5.1c). These striations were identified as cellulose bundles, which were measured to be 12 ± 2 nm wide (N = 63) using peak minima-to-minima distances of ribbon cross-sectional profiles (Figure 5.1d). In the cases where individual bundles were seen in the tapering ends of the ribbons (Figure S5.1), their twisted morphology allowed measuring their thickness, which was found to be ~6 nm (Figure 5.1e). Cellulose ribbons usually consisted of 3–4 bundles and had an average width of 50 ± 20 nm (N=100), with the measured widths ranging from 20–100 nm and in some cases nearly 200 nm wide (Figure 5.1f, g).

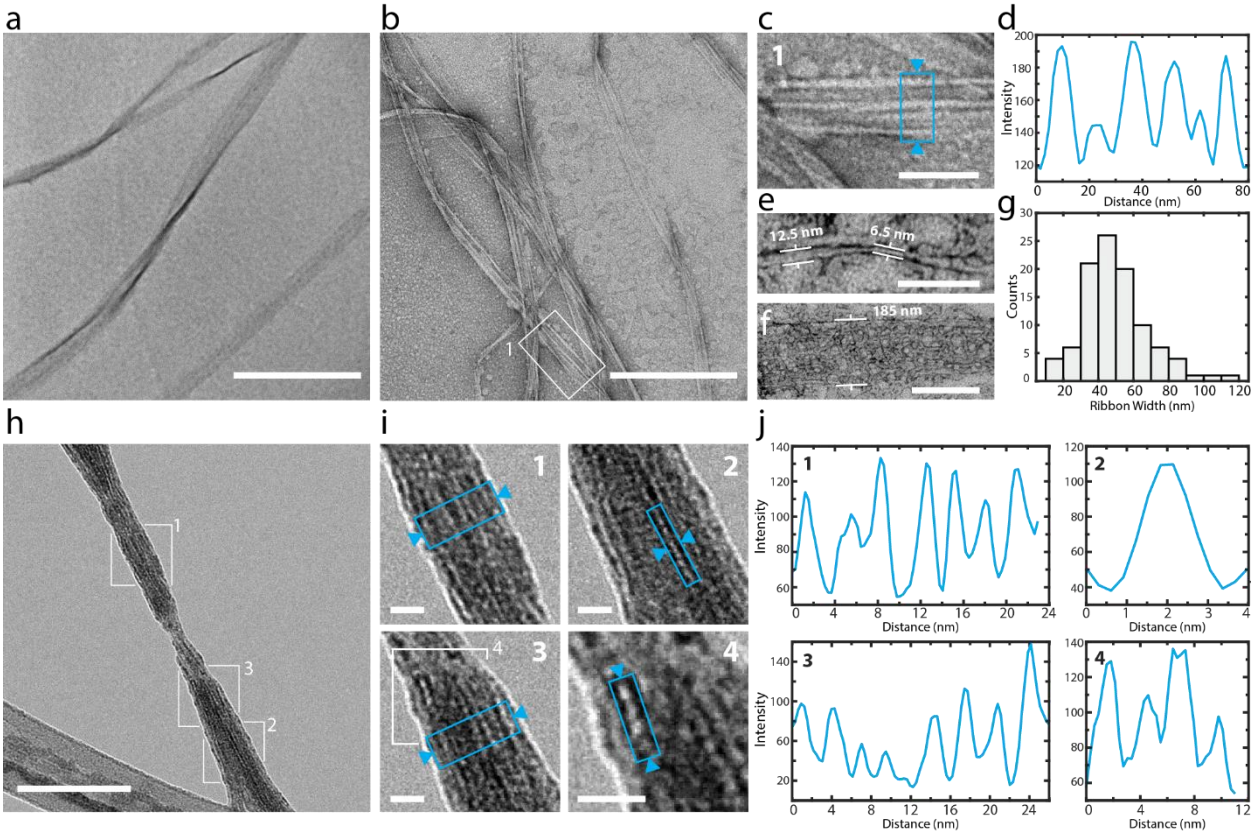

Figure 5.1. Characterization of the hierarchical structure of bacterial cellulose ribbons using TEM. Brightfield TEM images of bacterial cellulose ribbons prepared on formvar copper grids that were either (a) unstained or (b) negatively stained with 1 wt% uranyl acetate. c) Zoomed-in region of interest from (b) showing striations across individual cellulose ribbons whose cross-section intensity profile (d) consisted of periodically spaced microfibrils. e) Width and thickness of an individual cellulose microfibril. f) Representative image of a large cellulose ribbon. g) Distribution of measured ribbon widths, acquired from flat regions of individual ribbons (N > 100). h) Cryo-TEM of a cellulose ribbon suspended across a holey carbon film with (i) insets highlighting the presence of microfibrils within each bundle. j) Intensity profiles of the insets in (i) showing the spatial arrangement (graphs 1 and 3), cross-sectional width (graph 2) and longitudinal structure (graph 4) of microfibrils. Scale bars are 500 nm (a, b), 100 nm (c, e), 200 nm (f), 100 nm (h) and 10 nm (I, all insets).

Cryogenic imaging conditions were used to visualize unstained cellulose at higher resolution while minimizing the effects of electron beam damage. Cryo-TEM imaging of a single cellulose ribbon suspended across the lacey carbon film (Figure 5.1h) unveiled that it was composed of two bundles, each containing an ordered arrangement of 3 to 4 fibrils (Figure 5.1i, 1,3 and Figure 5.1j, 1,3). These nanometer striations were identified as microfibrils, whose width was measured to be 2.6 ± 0.2 nm (N = 18) (Figure 5.1i,2 and 5.1j,

2). The microfibrils exhibited a symmetric periodic structure along their length (Figure 5.1i,4), whose intensity profile presented peaks with an average width and separation of 2.6 ± 0.4 nm and 2.5 ± 0.4 nm (N = 11), respectively (Figure 5.1j,4). The narrow width of the microfibril at the trough of its periodic structure was measured to be approximately 1.6 ± 0.1 nm (N = 9). TEM analysis of bacterial cellulose ribbons revealed their hierarchical organization to consist of 3 or 4 laterally assembled 12 nm-wide bundles, each composed of 3 to 4, 2.6 nm-wide microfibrils.

The twisting morphology of cellulose ribbons was characterized in more detail using TEM. While twisting was consistently right-handed, it was non-persistent as ribbons preferred to lay flat with their wider axis facing the formvar film (Figure 5.2a). The twists appeared as short, quick 180° turns with an average length of 240 ± 100 nm (N = 121) (Figure 5.2b), as measured from the points where the ribbon begins to narrow around the twisted region. In contrast, the flat portion of the ribbon was uniform in width and longer, with an average length of 530 ± 400 nm (Figure 5.2d). The spacing between adjacent twists was measured from the center of each twist, where the rectangular ribbon appeared thinnest, and found to be 880 ± 400 μm (N = 152) (Figure 5.2c). Wider ribbons often folded onto themselves (Figure 5.1a, Figure 5.2a) and, as seen by the plot between twist spacing and ribbon width (r=0.49), exhibited larger spacing between adjacent twists (Figure 5.2e). In higher magnification images of stained ribbons, we observed nanostructural defects associated with the twisting regions, such as fine “cracks” travelling along the ribbon and bulges between bundles (Figure 5.2f). Under cryo-TEM we could clearly observe bulges, or ballooning, of individual bundles near the twisted portion of the ribbon (Figure 5.2g); in addition, we observed the presence of less ordered arrays of microfibrils and microfibril termination points flanking the twisted regions (Figure 5.2h). TEM characterization showed that cellulose ribbons possessed distinct flat and twisting regions, the latter of which is associated with defects that occur at various scales and ranged from “cracks” and bulges between microfibrils, to disorder and misalignment at the microfibril level.

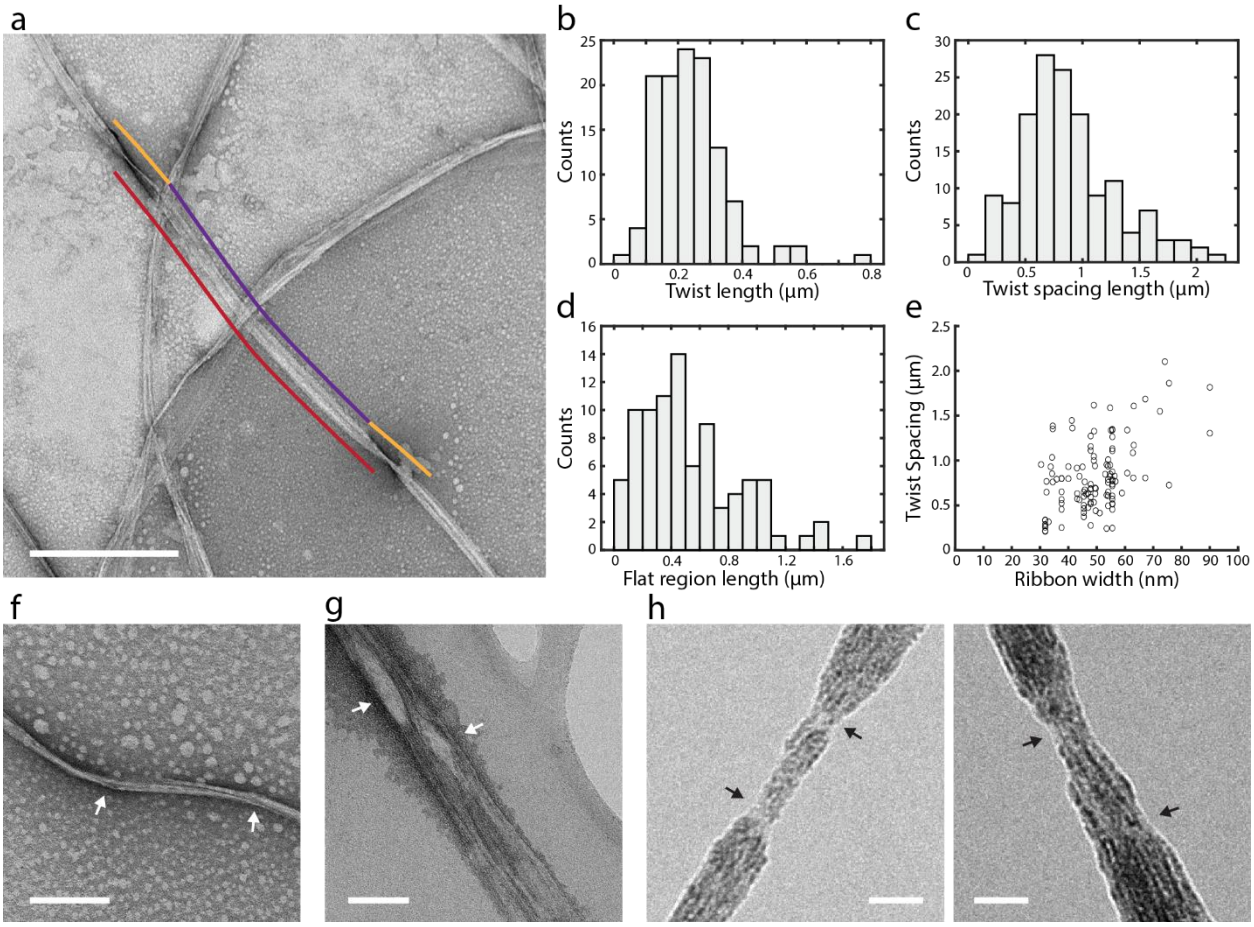

Figure 5.2. Characterization of twisting morphology and nanostructural dislocations within cellulose ribbons via TEM. a) Non-persistent twisting of bacterial ribbons was characterized in terms of twisting length (orange line), flat region length (purple line) and twist spacing (red line). (b – e) Distribution of twist length (N > 120), twist spacing length (N > 120) and length of flat regions (N>80) measured across individual cellulose ribbons. e) Plot of twist spacing versus ribbon width. (f – h) Nanostructural defects (black and white arrows) associated with ribbon twisting, seen in uranyl acetate-stained fibrils imaged with (f) *room temperature TEM* or (g, h) cryo-TEM. Scale bars are 500 nm (a), 200 nm (f), 50 nm (g) and 20 nm (h).

5.2.2 SRFM and TEM imaging of Cy5-labelled cellulose

To explore the possible relationship of the observed nanostructural defects to the alternating crystalline and disordered structure of cellulose, we analyzed Cy5-labeled bacterial cellulose (Cy5-BC) fibrils using TEM and SRFM. As previously reported in detail, SRFM using stochastic optical reconstruction microscopy (STORM) allows the direct visualization of crystalline and disordered regions along individual, fluorescently labeled cellulose fibrils. The bacterial cellulose fibers imaged present alternating dark and bright labeling patterns (Figure 5.3a, b) that represent areas with different susceptibility to

fluorescence labeling. The disordered regions were measured to be ~100 nm long, while the intervening dark crystalline regions ranged from 50 to 500 nm in length (Figure 5.3c). Under TEM, Cy5-BC ribbons occasionally presented 10 to 30 nm wide, round structures that appeared to associate with the twisted regions of the ribbon (Figure 5.3d). These aggregates were observed only in some parts of the sample, and their presence was confined to isolated areas. Upon negative staining with uranyl acetate and washing with deionized water, these structures disappeared and were not observed on any of the imaged ribbons (Figure 5.3e).

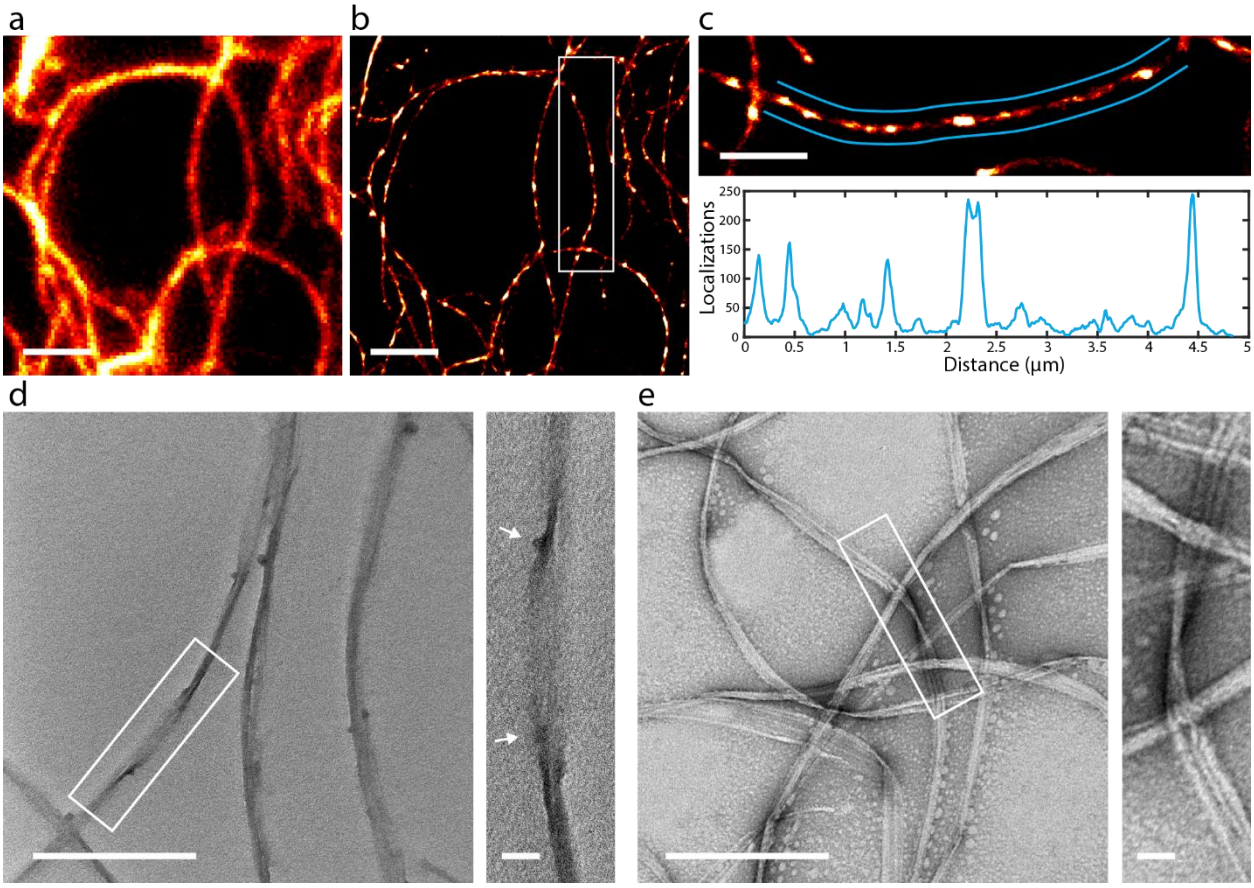

Figure 5.3. Super-resolution and TEM imaging of Cy5-labelled bacterial cellulose. Cy5-BC imaged on a glass coverslip using **(a)** conventional epifluorescence and **(b)** super-resolution fluorescence microscopy. **c)** Inset image from (*b*) with an intensity profile showing the alternating disordered and crystalline structure of cellulose fibrils being represented by bright and dark regions. **d)** Brightfield TEM image of unstained Cy5-BC showing aggregate particles that formed around the twisted regions (white arrows). **e)** Brightfield TEM image of Cy5-BC following negative staining with 1 wt% uranyl acetate. Scale bars are 2 μm *(a, b)*, 500 nm *(c, d, e)*, and 50 nm for insets in (d) and (e).

The presence of aggregates near the twisted regions of Cy5-BC ribbons suggested that the persistent dislocations visualized in SRFM might be associated with ribbon twisting. To

explore this possibility, super-resolution and transmission electron microscopy images of Cy5-BC were acquired and correlated using a SR-CLEM workflow (Figure 5.4). This involved the immobilization of Cy5-BC fibrils onto a formvar-coated copper grid with alphanumerical markings, which were crucial in locating the same fibrils across both imaging modalities. The fibrils were first imaged in SRFM as TEM imaging would likely destroy the Cy5 dye that is needed to visualize the dislocations. To image the sample in SRFM, an imaging chamber was assembled by sandwiching the grid between two glass coverslips containing a droplet of STORM switching buffer, supplemented with 30% v/v of glycerol to reduce spherical aberration. This configuration allowed the copper grid to be mounted onto the inverted microscope and to be within the focal distance of the high numerical aperture oil-immersion objective, while being exposed to the buffering conditions needed for fluorophore photoblinking. Following the acquisition of STORM image sequences and chamber disassembly, the sample was cleaned and a brightfield microscope was used to verify the integrity and cleanliness of the areas imaged with SRFM; this minimized unnecessary efforts in subsequent imaging steps. STORM sequences acquired at areas that were free of large debris and where the formvar film remained intact were processed to reconstruct super-resolution images. Dim fibrils, which represent thin, individual ribbons, were highlighted as regions of interest (ROI) for TEM imaging, where low- and high-magnification images of unstained ribbons were acquired. High-magnification TEM images were stitched together then aligned with SRFM images in either ec-CLEM software or manually in Photoshop, using junctions, fibril ends and bending points as natural fiduciary markers. We found that the quality of alignment using both methods by two different researchers were comparable, but those manually performed in Adobe Photoshop were faster. This workflow allowed us to acquire SR-CLEM images of cellulose ribbons in a simple fashion, and combine the functional information provided by SRFM with the high-resolving power of TEM.

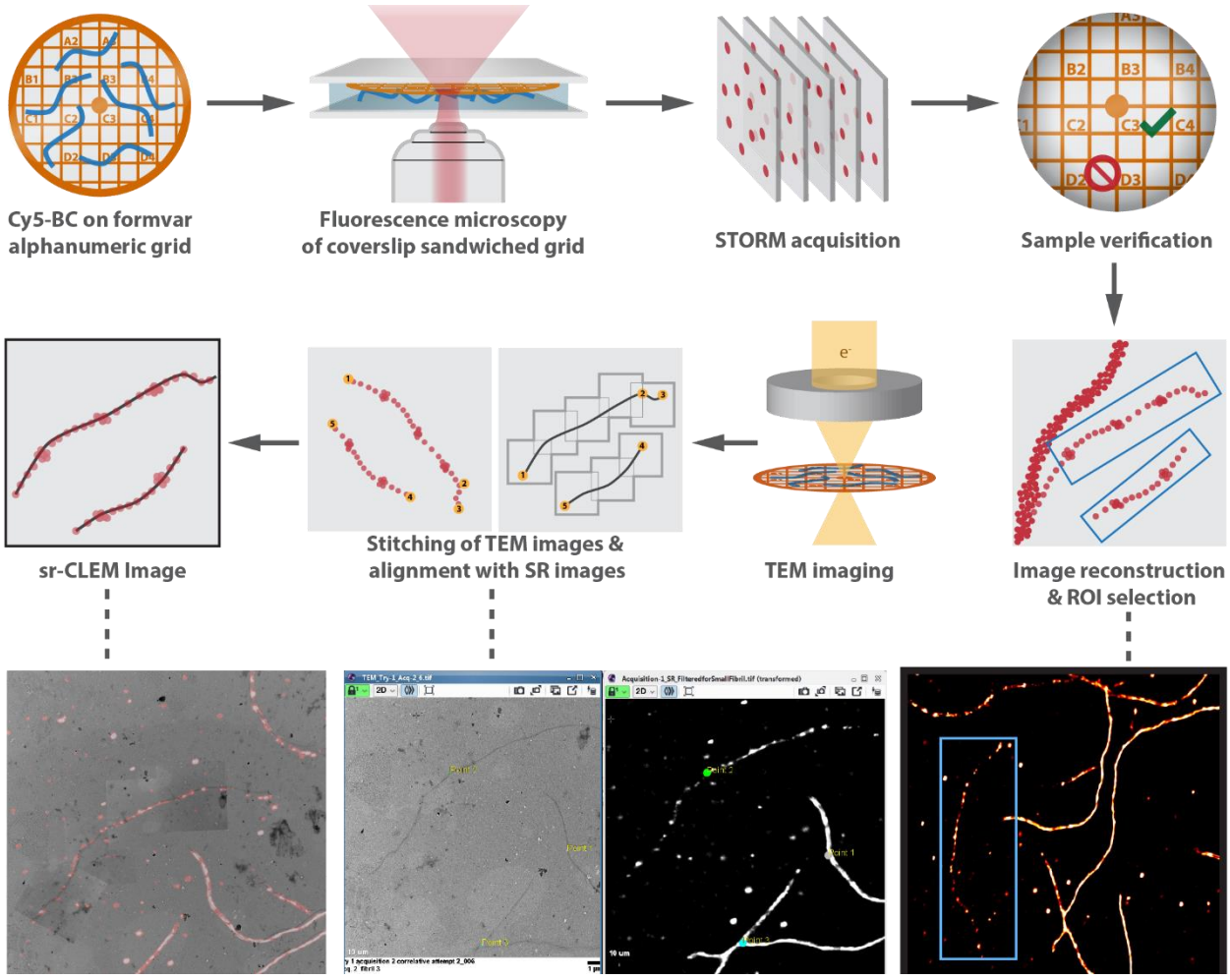

Figure 5.4. Correlative Super-Resolution Fluorescence and Electron Microscopy workflow for cellulose fibrils. Cy5-BC fibrils were first immobilized on alphanumeric, formvar-coated copper grids. Following washing with MilliQ water, the sample was sandwiched between two No. 1.5 glass coverslips containing a small volume of STORM imaging buffer and mounted on the inverted microscope with the fibrils facing the objective. 24,000-frame STORM acquisitions were taken at different areas within the sample, before the sample was removed from the coverslip chamber and washed with deionized water. A brightfield microscope was used to assess the integrity of the imaged regions and identify areas where the formvar film may have ripped or large debris were deposited. Acquisitions taken at intact areas were processed to produce super-resolution image reconstructions and individual fibrils were selected as regions of interest to image with TEM. At the TEM microscope, alphanumeric markings are used to locate the fibrils of interest and both high and low magnification brightfield images were taken. In Adobe Photoshop, low magnification TEM images were used as a templates to stitch high-magnification images and the corresponding super-resolution image was translated and rotated linearly to align with the stitched TEM image. Alternatively, the images were aligned using the ec-CLEM plugin in Icy software by using fibril ends and bending features as

alignment markers to produce the final *SR-CLEM* image of cellulose fibrils. Representative images of the SRFM, TEM stitching and final CLEM steps are shown in the bottom row.

5.2.3 SR-CLEM imaging of Cy5-labelled cellulose

SR-CLEM images of cellulose ribbons were used to contextualize the persistent dislocations seen along cellulose ribbons in SRFM with the ultrastructural details provided by TEM (Figure 5.5). We observed that 76% (n=49) of the dislocations, which are represented by bright spots in SRFM, colocalized with the twisting regions of the unstained cellulose ribbon that appeared as dark stripes in TEM (Figure 5.5, inset). Here, we regard a colocalization as less than 50 nm from one edge of a feature in SRFM to that in TEM, to account for errors associated with image alignment. Similarly, the large majority of the twisted regions (92.5%, n=40) were associated with dislocations, where multiple dislocations were often colocalized with a single twist. However, ribbon twisting did not account for all the dislocations observed in SRFM; this was particularly evident for those smaller in size and weaker in intensity, which instead localized with the flat regions of the ribbon (Figure 5.5, inset, white arrows). These results show that the large, bright cellulose dislocations seen in SRFM are often associated with ribbon twisting, and that most of the twisted regions colocalized with at least one dislocation.

While the SR-CLEM workflow provided a simple route for correlating information from SRFM and TEM imaging modalities, we faced some challenges during the process. Alignment of TEM and SRFM images was sometimes imperfect, as the fibrils, especially at their thinner, more flexible ends, can slightly move during washing and drying of the sample after SRFM imaging. Deformation of the formvar film, including stretching and ripping (Figure S5.2a), also prevented the complete alignment of fibrils that covered long distances. Additionally, the formvar film was auto-fluorescent, resulting in high background levels during the STORM acquisition (Figure S5.2b). Attempts to reduce this autofluorescence by washing the formvar coated grids with acetone, methanol or isopropyl alcohol beforehand were unsuccessful. Despite supplementation of the switching buffer with 30% v/v glycerol, spherical aberration can still be clearly seen (Figure S5.2c), resulting in hazy single molecule emissions with higher localization uncertainties (~23 nm) compared to fibrils imaged on glass coverslips (~15 nm). We also observed reduced fluorophore brightness, photostability and switching when imaging the fibrils in the coverslip sandwich, likely due to faster oxygen diffusion into the imaging buffer. Finally, the accumulation of debris and deformation of the sample, either through the formation of a thin film from the imaging buffer during drying or embedding of the fibrils within the formvar film during imaging, yielded blurry or obstructed TEM images. (Figure S5.2d). Overall, these challenges resulted in reduced SRFM and TEM

image quality with lower levels of structural and functional detail than what is typically offered by these imaging modalities when performed independently.

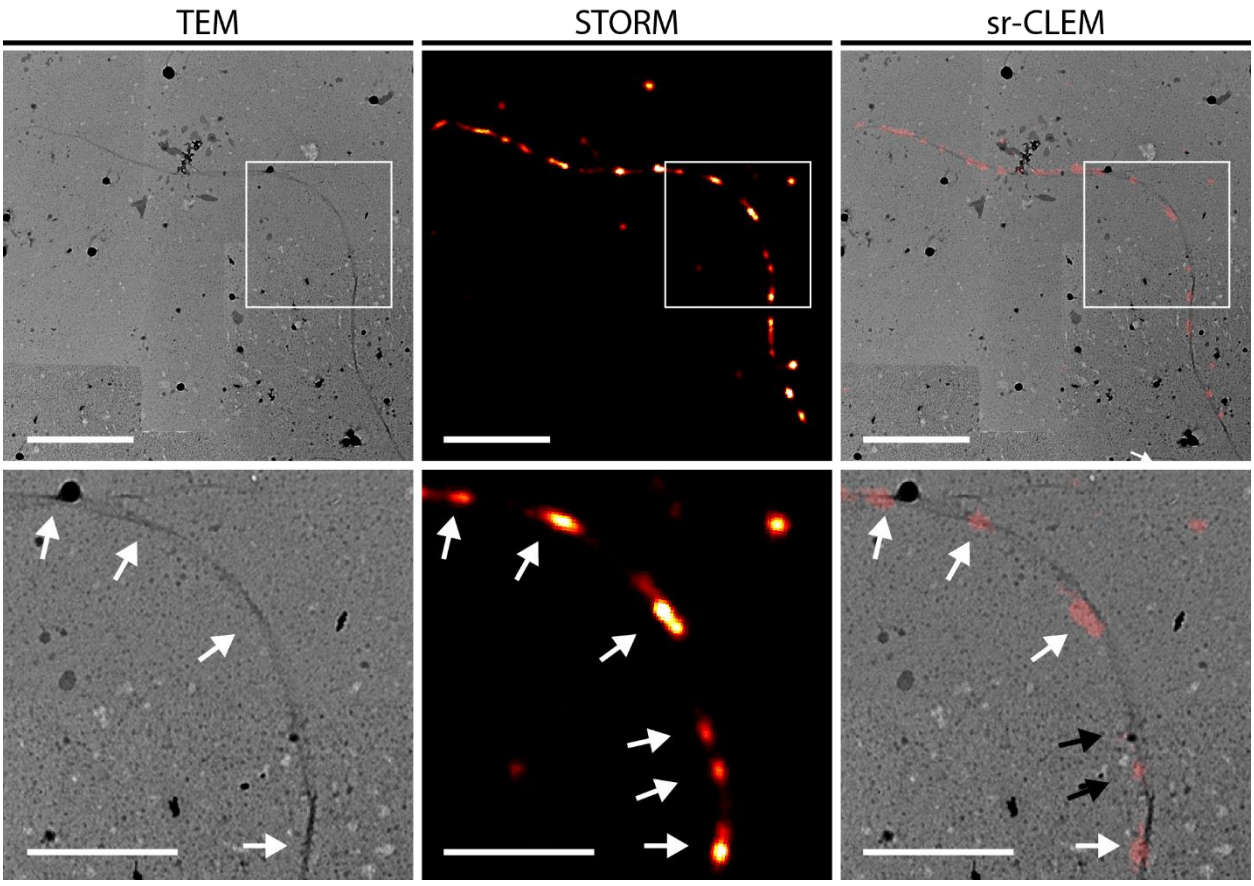

Figure 5.5. SR-CLEM image of bacterial cellulose fibrils. High magnification TEM (20,000×) images of unstained fibrils were manually stitched and aligned onto the corresponding STORM super-resolution image in Adobe Photoshop. The STORM image was reconstructed from a 12,000-frame image sequence acquired at a framerate of 30 Hz. White arrows indicate the presence of twists and dislocations on the TEM and SRFM image, respectively. On the CLEM overlay, regions where the dislocations and twisting regions overlapped are highlighted by white arrows, while black arrows represent dislocations that were not associated with any visible twists. Scale bars are 2 μm (top row) and 1 μm (insets).

5.3 Discussion

High resolution TEM imaging of bacterial cellulose ribbons allowed a detailed analysis of their morphology at three distinct hierarchy levels. Ribbons were on average 50 nm wide and typically consisted of 3 or 4, 12×6 nm laterally aggregated bundles (Figure 5.1c-e). Ribbon width measurements and observed morphology are in agreement with previous characterization of bacterial cellulose, however, we saw that ribbon width can vary significantly, ranging from 20 to 120 nm, and in some rare cases up to 200 nm wide (Figure 5.1g).[14,20–22] Additionally, while the specific bundle dimensions reported here are consistent with previous measurements using TEM[14,21] or X-ray scattering and NMR[23], a wide range of width values, of 5 – 16 nm, have been reported in the literature.[20,24,25] The heterogeneity in ribbon width and inconsistency of bundle dimensions to other reported values may arise from differences in the fermentation conditions used during the production of bacterial cellulose, such as bacterial strain type and dynamic versus static culture, which are known to alter the morphology and crystallinity of the cellulose ribbons.[10]

Beyond ribbons and bundles, a recent study employing electron cryotomography revealed a new structural hierarchical level, where bacterial cellulose ribbons consist of a stack of two to three sheets of bundles.[21] While we note the presence of a similar number of striations on the twisted portion of the ribbons, the two-dimensional TEM images acquired here did not allow for the clear visualization and measurement of sheets within ribbons. These sheets are distinct from a “bundle of microfibrils” or “bundle”, a structure that is identified as “microfibrils” in other papers.[21,24] In order to remain consistent with previous nomenclature established to describe cellulose structural hierarchy in both plants and bacteria, we define microfibrils as 2-3 nm wide structures (consisting of a crystalline arrangement of glucan chains) that assemble to form a bundle, which aggregate to form a ribbon.[14,26,27]

The high resolution and minimal electron beam damage offered by cryo-TEM allowed the direct visualization of unstained microfibrils within cellulose ribbons, showing that they are laterally organized in groups of 3 – 4 to form a bundle (Figure 5.1h-j). These observations are consistent with freeze-fracture studies showing that the linear array of TCs are organized in discontinuous groups of 3 or 4, supporting the cell-directed hierarchical organization of cellulose produced by bacteria.[20,28] The width of bacterial cellulose microfibrils has been previously measured to be 3 to 4 nm through TEM imaging directly within ribbons[14] or on individual microfibrils produced using agents that disrupt the assembly of ribbons and bundles, such as carboxymethylcellulose[20] or fluorescent brightening agents like Calcofluor White.[29] The high resolution offered by cyro-TEM allowed the precise measurement of the

cross-sectional dimensions of the microfibril, which were determined to be 2.6×1.6 nm; this suggests a 4×4 chain model of the microfibril since the crystal structure of cellulose I_α would predict dimensions of 2.44 × 1.56 nm for this arrangement.[30,31] Previous crystallographic data of the cellulose synthase complex have shown that it is composed of four catalytic subunits, AcsAB, which are bound to the inner membrane and synthesize four glucan chains, that are then crystallized by AcsD in the periplasmic space and extruded by AcsC on the outer membrane to form an elementary fibril.[12,32,33] However, unlike plant species, the higher level spatial ordering of TCs that may drive the microfibril production in bacteria remains unclear. Based on the cross-sectional measurements of the cellulose microfibril, we propose that the bacterial cellulose TCs are spatially organized in a 2×2 arrangement, such that four elementary fibrils combine to form a microfibril composed of 16 glucan chains. While evidence for this is yet to be reported in the literature, it would not be surprising that bacterial cellulose TCs form clusters since this has been observed in plant species, where a hexameric rosette of TCs extrude an 18 to 24 chain cellulose microfibril.[34,35]

Cellulose ribbons presented regions of non-persistent, right-handed 180° twists that are separated by longer segments that laid flat on the formvar carbon film (Figure 5.2a). Non-persistent twisting has been previously seen across different hierarchical levels of cellulose materials, including ribbons[36,37], microfibrils[38] and CNCs[39] extracted from various species like bacteria, algae, and tunicates. These observations are in contradiction with molecular dynamic simulations, which almost always result in a stable, low energy conformation of cellulose fibrils that involves continuous right-handed twisting.[40–43] Cryogenic TEM imaging of tunicate CNCs embedded in vitreous ice indeed showed these cellulose rods adopting a continuous helical morphology when suspended in liquid, but laying flat with short twisted segments when on a carbon film.[39] It is thought that this phenomenon occurs while cellulose particles are drying on a substrate, where capillary forces from water during evaporation lead to unwinding of the fibril and leave discontinuous twisting segments.[37] The wide distribution of inter-twist spacing (Figure 5.2c) highlights the irregularity of the sharp twists that are introduced during cellulose drying; however it was unclear whether their positions are random or driven by an underlying structure. The latter is supported by the presence of nanostructural defects within bundles and microfibrils near the twisted regions (Figure 5.2f-h), suggesting that these morphological features can act as flexible hotspots that give way to the discontinuous sharp twists during drying. While structural defects of cellulose are known to occur at the microscale[44], high-resolution TEM imaging provided evidence for nanoscale dislocations within cellulose twists.

By combining the specificity of SRFM with the ultrastructural information provided by TEM, SR-CLEM allowed us to study the relationship between the twisted regions, and their associated nanoscale defects, with the alternating crystalline and disordered structure of cellulose ribbons. The ability to visualize disordered and crystalline regions along cellulose fibres by SRFM is rooted in the observation of variations of fluorophore density that reflect the different susceptibility of crystalline and disordered regions to fluorescent labeling.[19] The connection between the disordered and locally twisted regions in the ribbons was first highlighted by the presence of small aggregates on the twists of Cy5-labeled ribbons. Since these aggregates were electron dense, they may represent salts that nucleate on regions with high density of Cy5. We propose that this salt is $CuSO_4$ since it was used as a catalyst during the labeling reaction with Cy5 and can nucleate on the two sulfate groups present on the dye. We considered using electron energy loss spectroscopy (EELS) to corroborate the identity of the electron dense components in the particles, but their small size would have made it challenging to acquire a spectrum with EELS. SR-CLEM further showed that most of the twisted regions were associated with at least one dislocation, indicating that the nanostructural defects were more susceptible to fluorescent labeling. Recent work employing scanning electron diffraction has shown that local crystallographic ordering is preserved through the twisted regions.[38] This is consistent with our previous observations that the disordered regions identified by SRFM are smaller than 5 nm and do not contribute a significant amorphous fraction that can be detected by X-ray diffraction crystallinity measurements.[19] Contrary to the common notion that the periodic disordered regions present along cellulose fibrils occur at the molecular level within the crystalline structure of cellulose, the colocalization of the bright regions seen in SRFM with the twisted regions of cellulose ribbons indicates that bulges between bundles and misalignment of microfibrils act as sites susceptible to labeling and acid hydrolysis. At least for bacterial cellulose, this mechanism is supported by the dimensions of CNCs, whose width of 12 nm[19] is in excellent agreement with that of the bundle of microfibrils measured here; this observation further supports that acid hydrolysis occurs initially at defects present at the bundle and microfibril level.

While the SR-CLEM workflow was adequate for correlating the dislocations in SRFM to the twisted regions of cellulose ribbons, the imaging quality across both modalities prevented correlation of the dislocations with finer morphological details, including nanoscale defects. The quality of SRFM can be improved by employing silicon nitride substrates, which can be cleaned with basic reagents and may give lower background fluorescence levels than the formvar film.[45] Higher index of refraction buffers, such as those containing high concentrations of sucrose, could further reduce spherical aberrations and

improve the localization uncertainty and, in turn, the resolution of SRFM images.[45] Notwithstanding these potential improvements, the current SR-CLEM workflow provides a simple route for combining the functional and morphological information that is directly offered by the two imaging modalities on individual cellulose ribbons.

5.4 Conclusion

The supramolecular organization of bacterial cellulose ribbons was characterized in detail using high resolution TEM and SRFM, allowing the different hierarchical levels of the ribbon to be unraveled from the micro to nanoscale. The observed arrangement and dimensions of microfibrils directly within ribbons provides insight into the cell-directed biosynthesis of bacterial cellulose, which should be corroborated with future studies on the clustering of TCs across the bacterial surface. The adapted SR-CLEM workflow afforded a simple route for contextualizing the persistent disordered regions of cellulose ribbons to its ultrastructure and showed that the disordered regions were often associated with the non-persistent twists of the ribbon. The presence of hairline cracks and misalignment at the bundle and microfibril levels within the twisted regions indicated that these nanostructural defects act as sites that are susceptible to chemical modification and drive the initial stages of CNC production through strong acid hydrolysis. Future research should explore the existence of these defects in cellulose fibrils derived from other sources, such as plants, algae and tunicates, and investigate whether they originate during cellulose biosynthesis or other processes.

5.5 Materials & Methods

Materials. Glucose, sodium hydroxide (NaOH), glucose oxidase (from *Aspergillus niger*, type X–S, 100–250 units/mg, 65–85% protein content), catalase (from bovine liver, ≥10 000 units/mg, ≥70% protein content) and cysteamine (98%) were purchased from MilliporeSigma (Oakville, ON, Canada) and used without any further purification. Dichlorotriazinyl propargyl amine (DTAP) was synthesized in-house as previously described. Bacterial cellulose was extracted from foodstuff Nata de Coco (230 g drained weight, New Lamthong Food Industries, Bangkok, Thailand), a fermented desert consisting of a bacterial culture of *Komagataeibacter xylinus*, using the same procedure described previously. All mentions of water refer to distilled 18.2 MΩ water, generated from a Milli-Q Direct purifier system (Millipore Sigma). Uranyl acetate was obtained from Electron Microscopy Sciences (Hatfield, PA).

Fluorescence labeling of cellulose fibrils. Bacterial cellulose fibrils were fluorescently labeled with sulfo-Cy5 azide dye in a two-step reaction scheme as previously described.[46] Briefly, a triazinyl linker bearing an alkyne group (DTAP) was grafted onto BC through a

reaction involving 0.1 wt% suspension of BC fiblrils in a 3:1 water:acetone solution containing 10 mM of linker and 0.05 M of sodium hydroxide while mixing at room temperature for 24 hr. Unreacted linker was removed through centrifugation (21,100×g, 60 s with a Sorvall Legend Micro 21R Centrifuge, Thermo Scientific), decanting and resuspension cycles with water (3×), acetone (3×), PBS (3×) then water (3×). Cellulose fibrils were dispersed using a 0.25 inch point-probe (Branson SLPt, 40% amplitude, or 60 W, for 10 s) every third spin-down. The introduction of an alkyne group onto cellulose allowed a copper-catalyzed azide-alkyne click-reaction with sulfo-Cy5 azide (Lumiprobe, Cockeysville, MD) by mixing a 0.1 wt% suspension of DTAP-BC in 1× PBS, 10% methanol containing 10 μM of Cy5 dye, 5 mM ascorbic acid and 0.3 mM copper sulfate pentahydrate for 2 hr at room temperature. Unreacted dye was removed through a similar cleaning procedure described above using 10 washing cycles with water.

Transmission electron microscopy. Three microliters of 0.01 wt% cellulose suspension were drop casted onto prepared electron microscopy grids (Electron Microscopy Sciences, Hatfield, PA), excess liquid was wicked away using Whatman filter paper and the sample was allowed to completely air dry before imaging. Samples were either imaged unstained, or negative stained with 1 wt% uranyl acetate to improve contrast. In this procedure, after BC was air-dried and adhered to TEM grids, a drop of 1 wt% uranyl acetate was deposited onto the sample, and after a designated time the excess liquid was removed from the TEM grid using blotting paper. After blotting, the TEM grid was left to air dry at room temperature before being placed into the microscope. The exposure time of cellulose to uranyl acetate was optimized by imaging BC fibrils exposed to uranyl acetate for 1-10 minutes. Bright field TEM imaging of BC fibrils were performed on a JEOL 1200EX TEMSCAN microscope (JEOL, Peabody, MA, USA) operating at an accelerating voltage of 80 kV.

Transmission Electron Microscopy Images at Cryogenic Temperatures. Bacterial cellulose was prepared on 200 mesh lacey carbon electron microscopy grids (Structure Probe Inc., West Chester, PA)(Ted Pella, Inc., Redding, CA, USA) using the same procedure described above. The sample was inserted into the cooled to cryogenic temperatures using a Gatan cryo-holder filled and then transferred to with liquid nitrogen then the holder unit was transferred to the Talos L120C TEM (Thermo Fisher Scientific, MA, USA). Liquid nitrogen is then added to the Gatan cryoholder system and using the attached controller the temperature is monitored and maintained around -170 ^{O}C. Images were acquired using an acceleration voltage of 120 kV and a 4k × 4k CETA CMOS Camera.

Super-resolution fluorescence microscopy. STORM super-resolution images were acquired as previously reported.[19,46] Briefly, imaging was performed in widefield, epifluorescence

mode on a Leica DMI6000B inverted microscope equipped with a Borealis module (Spectral Applied Research, Richmond Hill, ON, Canada) that couples 405, 488, 561 and 647 nm laser lines from an Integrated Light Engine (Spectral Applied Research, Richmond Hill, ON, Canada) to a 100×/1.47NA oil-immersion objective. Emitted light passes through a multiline dichroic mirror and is filtered through a 700/75 nm filter before being captured by an Andor iXon Ultra DU-897U EMCCD with a projected pixel size of 96 nm.

STORM super-resolution images of Cy5-BC were acquired on plasma treated (air, 3 mins, 700 mTorr, Harrick Plasma, Ithaca, NY) glass-bottom petri dishes (Mattek, Ashland, MA) using a traditional STORM imaging buffer (50 mM tris, pH 8.0, 10 mM NaCL, 10 wt% glucose, 100 mM cysteamine, 84 u/mL glucose oxidase and 510 u/mL catalase). An image sequence of 24,000 frames (30 ms exposure, 30 Hz framerate) was acquired using maximal 647 nm laser power (47 kW/cm^2) and short, low power bursts of the 405 nm laser for dye reactivation. STORM analysis was performed in the ThunderSTORM ImageJ plugin using the local maximum method for single-molecule localization, cross-correlation for drift correction, merging of consecutive emitters and the averaged shifted histogram method for image reconstruction.[47]

SR-CLEM image acquisition and correlation.

Super-resolution imaging. Cy5-BC fibrils were prepared on formvar-coated, alphanumeric copper grids (G200F1-CP, Electron Microscopy Sciences, Hatfield, PA) by drop-casting 2 µL of a 0.01 wt% cellulose suspension onto the grid and allowing the fibrils to bind for 3 mins before excess liquid was wicked away with a Kimwipe tissue. The sample was washed three times by drop-casting and wicking away a 3 µL droplet of water. The sample was air dried for 5 mins then placed on a 1.5 glass coverslip with the fibrils facing up. The copper grid was mounted for SRFM similarly to previous work.[48] STORM switching buffer, supplemented with 30% v/v glycerol to reduce spherical aberration, was prepared 15 minutes before use and a 30 µL droplet was drop-casted onto the grid. A second 1.5 glass coverslip was gently placed on top to create a coverslip sandwich, which was mounted onto the microscope such that the fibrils were facing towards the objective.

Areas where the formvar film appeared undisturbed and the fluorescent fibrils were well dispersed and in focus over a large were selected for super-resolution imaging. A 24,000-frame image sequence was acquired as described above and the image position was determined by locating the nearest alphanumerical marking in brightfield transillumination mode. The number of acquisitions were limited to two or three areas within the sample since the lifetime of the buffer was short and drying of the sample must be avoided in order to

minimize the irreversible deposition of debris onto the copper grind. These issues can be alleviated by sealing the coverslip sandwich chamber with nail polish, which would reduce the rates of evaporation and oxygen diffusion. Following imaging, the coverslips were gently separated, the copper grid was removed and washed three times with water by pipetting a 3 µL droplet and wicking after 10 seconds.

Sample verification, image reconstruction and ROI selection. Imaged areas were verified under a brightfield microscope to ensure that no large debris were deposited and the formvar film remained intact following disassembly of the coverslip chamber and washing of the copper grid. Clean areas without significant deformation of the formvar film, such as tears and large stretch marks, were selected for further analysis and imaging by TEM. Super-resolution images were reconstructed similarly to what is described above and individual cellulose fibrils were selected as regions of interest (ROIs) for correlative TEM imaging.

TEM imaging. Using the alphanumeric grid system, the grid space containing the fibrils of interest was located. Initially, low magnification images (1000×) of the entire grid space were acquired to gauge the orientation of the TEM grid and adjust it accordingly to match the orientation of SRFM images and assist in ribbon identification. Medium magnification (5000×) images encompassing the entirety of individual fibrils were acquired to facilitate stitching of higher magnification images and alignment with SRFM data. Once identified, high magnification (50,000× - 100,000×) images were acquired along the ribbon length to capture ultrastructural details.

Negative staining with uranyl acetate was not employed to prevent debris accumulation or the contrast enhancement of existing debris on the sample surface. These potential artifacts could obscure structural features along cellulose ribbons and cause deformation to the formvar film layer, which could change the orientation and appearance of the ribbons and hinder image processing and correlation in later stages within this workflow.

Correlative TEM images were taken on a JEOL JEM 1200EX TEMSCAN TEM (JEOL, Peabody, MA, USA) at an accelerating voltage of 80 kV and spot size of 3 to minimize sample beam damage. A 4MP digital camera (Advanced Microscopy Technique Corp., Danvers, MA, USA) and AmtV600 software were used to capture and analyze TEM images.

Image alignment with Photoshop. Super-resolution fluorescence, high magnification (high-mag) TEM (20,000× - 50,000×) and low magnification (low-mag) TEM (5,000× - 10,000×) images were imported as individual layers into Adobe Photoshop v13.0 and scaled to match the pixel size of the low-mag TEM image containing the entire fibril of interest. High-mag

images were stitched together by overlaying them with medium opacity onto the low-mag image and using the continuous fibril as a reference. Following stitching, the opacity of high-mag TEM images was increased back to 100%. The super-resolution fluorescence image was overlaid onto the TEM data by reducing its opacity to 25% and setting the layer blending option to vivid light. The image was translated to align a distinct feature that can be seen in both TEM and fluorescence images, such as a fibril intersection or end point, then rotating the image while using the aligned spot as a pivot until both images were adequately aligned.

Image alignment with ec-CLEM. The multi-microscopy modality data sets were aligned, registered, and correlated using the ec-CLEM software on the Icy bioimage platform.[49] SR images were matched to the TEM images using natural fiducial markers along the microfibril structures including, endpoints of the microfibril and intersection points between two microfibrils, as well as notable structural features of the TEM grid, including grid boundaries along the perimeter. Approximately 20-25 registration markers were found to be sufficient to produce an accurate overlay between SR and TEM images. After evaluating the produced images through rigid and non-rigid registration, the decision was made to perform the rigid registration method. Utilization of the non-rigid registration may introduce unnecessary warping and lead to misalignment between SR and TEM images. The final SR and TEM composite overlaid image was produced by applying the transformation to the SR image to match the TEM images.

Acknowledgements

Electron microscopy preparation and correlative work was conducted at the Canadian Centre for Electron Microscopy (CCEM) in the Faculty of Health Science division. The CCEM facility is supported by governmental agencies including NSERC.

Author Contributions

MB wrote the first draft of the manuscript. MB and AW analyzed all the data. MB labeled cellulose and acquired super-resolution images. AW and MR acquired TEM images. MB and AW developed the SR-CLEM workflow. NB and JMM conceptualized the study. All authors reviewed the manuscript.

Competing Interests

The authors declare no competing interests.

References

1. Gibson, L. J. The hierarchical structure and mechanics of plant materials. *Journal of The Royal Society Interface* **9**, 2749–2766 (2012).

2. Reiterer, A., Lichtenegger, H., Tschegg, S. & Fratzl, P. Experimental evidence for a mechanical function of the cellulose microfibril angle in wood cell walls. *http://dx.doi.org/10.1080/01418619908210415* **79**, 2173–2184 (2008).

3. Cellulose (Dissolving Pulp) Manufacturing Processes and Properties: A Mini-Review | Chen | BioResources. https://ojs.cnr.ncsu.edu/index.php/BioRes/article/view/BioRes_11_2_Review_Chen_Cellulose_Manufacturing_Processes.

4. Chen, J. Synthetic Textile Fibers: Regenerated Cellulose Fibers. *Textiles and Fashion: Materials, Design and Technology* 79–95 (2015) doi:10.1016/B978-1-84569-931-4.00004-0.

5. Habibi, Y. Key advances in the chemical modification of nanocelluloses. *Chemical Society reviews* **43**, 1519–42 (2014).

6. Habibi, Y., Lucia, L. A. & Rojas, O. J. Cellulose nanocrystals: Chemistry, self-assembly, and applications. *Chemical Reviews* **110**, 3479–3500 (2010).

7. Rose, M., Babi, M. & Moran-Mirabal, J. The study of cellulose structure and depolymerization through single-molecule Methods. *Industrial Biotechnology* **11**, 16–23 (2015).

8. Haigler, C. H. & Benziman, M. Biogenesis of Cellulose I Microfibrils Occurs by Cell-Directed Self-Assembly in Acetobacter xylinum. in *Cellulose and Other Natural Polymer Systems* 273–297 (Springer, Boston, MA, 1982). doi:10.1007/978-1-4684-1116-4_14.

9. Richard Malcolm Brown. The Biosynthesis of Cellulose. *http://dx.doi.org/10.1080/10601329608014912* **33**, 1345–1373 (2006).

10. Singhsa, P., Narain, R. & Manuspiya, H. Physical structure variations of bacterial cellulose produced by different Komagataeibacter xylinus strains and carbon sources in static and agitated conditions. *Cellulose 2018 25:3* **25**, 1571–1581 (2018).

11. Nobles, D. R. & Brown, R. M. Transgenic expression of Gluconacetobacter xylinus strain ATCC 53582 cellulose synthase genes in the cyanobacterium Synechococcus leopoliensis strain UTCC 100. *Cellulose 2008 15:5* **15**, 691–701 (2008).

12. Du, J., Vepachedu, V., Cho, S. H., Kumar, M. & Nixon, B. T. Structure of the cellulose synthase complex of Gluconacetobacter hansenii at 23.4 Å resolution. *PLoS ONE* **11**, (2016).

13. Brown, R. M., Willison, J. H. & Richardson, C. L. Cellulose biosynthesis in Acetobacter xylinum: visualization of the site of synthesis and direct measurement of the in vivo process. *Proceedings of the National Academy of Sciences* **73**, 4565–4569 (1976).

14. Mehta, K., Pfeffer, S. & Brown, R. M. Characterization of an acsD disruption mutant provides additional evidence for the hierarchical cell-directed self-assembly of cellulose in Gluconacetobacter xylinus. *Cellulose 2014 22:1* **22**, 119–137 (2014).

15. Battista, O. A. Hydrolysis and Crystallization of Cellulose. *Industrial & Engineering Chemistry* **42**, 502–507 (1950).

16. Hon, D. N. S. Cellulose: a random walk along its historical path. *Cellulose* **1**, 1–25 (1994).

17. Calvini, P. The Influence of Levelling-off Degree of Polymerisation on the Kinetics of Cellulose Degradation. *Cellulose* **2005**, 445–447 (2005).

18. Nishiyama, Y. *et al.* Periodic disorder along ramie cellulose microfibrils. *Biomacromolecules* **4**, 1013–1017 (2003).

19. Babi, M. *et al.* Direct super-resolution imaging of the alternating disordered and crystalline structure of cellulose fibrils. *In submission*.

20. Haigler, C. H., White, A. R., Brown, R. M. & Cooper, K. M. Alteration of in vivo cellulose ribbon assembly by carboxymethylcellulose and other cellulose derivatives. *Journal of Cell Biology* **94**, 64–69 (1982).

21. Nicolas, W. J., Ghosal, D., Tocheva, E. I., Meyerowitz, E. M. & Jensen, G. J. Structure of the bacterial cellulose ribbon and its assembly-guiding cytoskeleton by electron cryotomography. *bioRxiv* 2020.04.16.045534 (2020) doi:10.1101/2020.04.16.045534.

22. Hirai, A., Tsuji, M. & Horii, F. TEM study of band-like cellulose assemblies produced by Acetobacter xylinum at 4 °C. *Cellulose 2002 9:2* **9**, 105–113 (2002).

23. Fink, H.-P., Purz, H. J., Bohn, A. & Kunze, J. Investigation of the supramolecular structure of never dried bacterial cellulose. *Macromolecular Symposia* **120**, 207–217 (1997).

24. Tokoh, C., Takabe, K., Fujita, M. & Saiki, H. Cellulose synthesized by Acetobacter xylinum in the presence of acetyl glucomannan. *Cellulose* **5**, 249–261 (1998).

25. Astley, O. M., Chanliaud, E., Donald, A. M. & Gidley, M. J. Structure of Acetobacter cellulose composites in the hydrated state. *International Journal of Biological Macromolecules* **29**, 193–202 (2001).

26. Song, B., Zhao, S., Shen, W., Collings, C. & Ding, S.-Y. Direct Measurement of Plant Cellulose Microfibril and Bundles in Native Cell Walls. *Frontiers in Plant Science* **0**, 479 (2020).

27. Cousins, S. K. & Brown, R. M. Photoisomerization of a dye-altered β-1,4 glucan sheet induces the crystallization of a cellulose-composite. *Polymer* **38**, 903–912 (1997).

28. Kimura, S., Chen, H. P., Saxena, I. M., Brown, J. & Itoh, T. Localization of c-di-GMP-binding protein with the linear terminal complexes of Acetobacter xylinum. *Journal of Bacteriology* **183**, 5668–5674 (2001).

29. Haigler, C. H., Brown, R. M. & Benziman, M. Calcofluor white ST alters the in vivo assembly of cellulose microfibrils. *Science* **210**, 903–906 (1980).

30. Lehtiö, J. *et al.* The binding specificity and affinity determinants of family 1 and family 3 cellulose binding modules. *Proc. Natl. Acad. Sci. {U.S.A.}* **100**, 484–489 (2003).

31. Castro, C. *et al.* Structural characterization of bacterial cellulose produced by Gluconacetobacter swingsii sp. from Colombian agroindustrial wastes. *Carbohydrate Polymers* **84**, 96–102 (2011).

32. Hu, S.-Q. *et al.* Structure of bacterial cellulose synthase subunit D octamer with four inner passageways. *Proceedings of the National Academy of Sciences* **107**, 17957–17961 (2010).

33. Krasteva, P. V. *et al.* Insights into the structure and assembly of a bacterial cellulose secretion system. *Nature Communications 2017 8:1* **8**, 1–10 (2017).

34. Vandavasi, V. G. *et al.* A Structural Study of CESA1 Catalytic Domain of Arabidopsis Cellulose Synthesis Complex: Evidence for CESA Trimers. *Plant Physiology* **170**, 123–135 (2015).

35. Turner, S. & Kumar, M. Cellulose synthase complex organization and cellulose microfibril structure. *Philosophical Transactions of the Royal Society A: Mathematical, Physical and Engineering Sciences* **376**, 9–16 (2018).

36. Colvin, J. R. Twisting of bundles of bacterial cellulose microfibrils. *Journal of Polymer Science* **49**, 473–477 (1961).

37. Hanley, S., Revol, J.-F., Godbout, L. & Gray, D. Atomic force microscopy and transmission electron microscopy of cellulose from Micrasterias denticulata; evidence for a chiral helical microfibril twist. *Cellulose* **4**, 209–220 (1997).

38. Willhammar, T. *et al.* Local Crystallinity in Twisted Cellulose Nanofibers. *ACS Nano* **15**, 2730–2737 (2021).

39. Ogawa, Y. Electron microdiffraction reveals the nanoscale twist geometry of cellulose nanocrystals. *Nanoscale* **11**, 21767–21774 (2019).

40. Conley, K., Godbout, L., Whitehead, M. A. & van de Ven, T. G. M. Origin of the twist of cellulosic materials. *Carbohydrate Polymers* **135**, 285–299 (2016).

41. Zhao, Z. *et al.* Cellulose Microfibril Twist, Mechanics, and Implication for Cellulose Biosynthesis. *Journal of Physical Chemistry A* **117**, 2580–2589 (2013).

42. Paavilainen, S., Róg, T. & Vattulainen, I. Analysis of Twisting of Cellulose Nanofibrils in Atomistic Molecular Dynamics Simulations. *Journal of Physical Chemistry B* **115**, 3747–3755 (2011).

43. Hadden, J. A., French, A. D. & Woods, R. J. Unraveling cellulose microfibrils: A twisted tale. *Biopolymers* **99**, 746–756 (2013).

44. Nyholm, K., Ander, P., Bardage, S. & Geoffrey, D. Dislocations in pulp fibres – their origin, characteristics and importance – a review. *Nordic Pulp & Paper Research Journal* **16**, 376–384 (2001).

45. Kim, D. *et al.* Correlative Stochastic Optical Reconstruction Microscopy and Electron Microscopy. *PLOS ONE* **10**, e0124581 (2015).

46. Babi, M. *et al.* Efficient labelling of nanocellulose for high-resolution fluorescence microscopy applications. *In submission*.

47. Ovesný, M., Křížek, P., Borkovec, J., Švindrych, Z. & Hagen, G. M. ThunderSTORM: A comprehensive ImageJ plug-in for PALM and STORM data analysis and super-resolution imaging. *Bioinformatics* **30**, 2389–2390 (2014).

48. van Elsland, Dr. D. M. *et al.* Ultrastructural Imaging of Salmonella–Host Interactions Using Super-resolution Correlative Light-Electron Microscopy of Bioorthogonal Pathogens. *Chembiochem* **19**, 1766 (2018).

49. Paul-Gilloteaux, P. *et al.* eC-CLEM: flexible multidimensional registration software for correlative microscopies. *Nature Methods 2017 14:2* **14**, 102–103 (2017).

Chapter 5 Supplementary Information

Unraveling the supramolecular structure and nanoscale dislocations of bacterial cellulose ribbons using correlative super-resolution light and electron microscopy

Mouhanad Babi,[1] Alyssa Williams,[2] Marcia Reid,[3] Kathryn Grandfield,[2,4] Nabil Bassim,[2,3,4] and Jose M. Moran-Mirabal[1,2,5,6]*

[1] *Department of Chemistry and Chemical Biology, McMaster University, Hamilton, ON, Canada*

[2] *School of Biomedical Engineering, McMaster University, Hamilton, ON, Canada*

[3] *Canadian Center for Electron Microscopy, McMaster University, Hamilton, ON, Canada*

[4] *Department of Materials Science and Engineering, McMaster University, Hamilton, ON, Canada*

[5] *Brockhouse Institute for Materials Research, McMaster University, Hamilton, ON, Canada*

[6] *Center for Advanced Light Microscopy, McMaster University, Hamilton, ON, Canada*

*Please address all correspondence to Jose Moran-Mirabal (mirabj@mcmaster.ca)

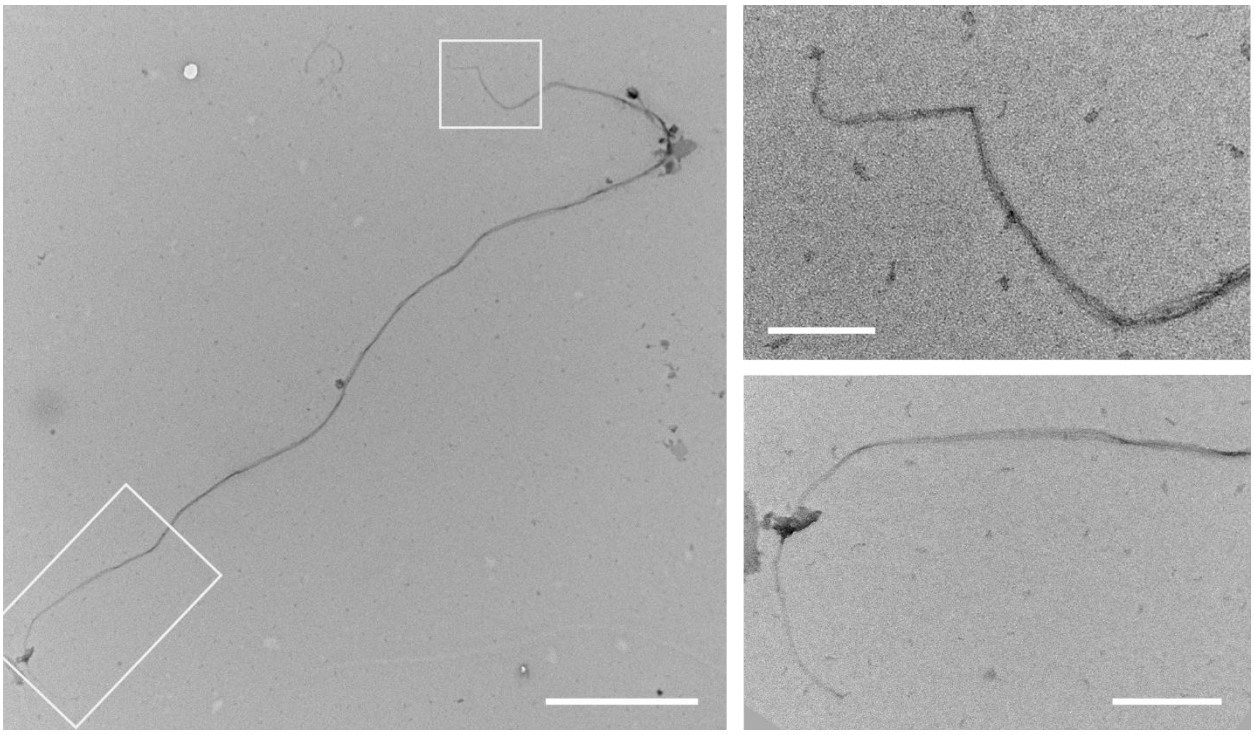

Figure S5.1. Cellulose ribbons taper off at their ends. Scale bars are 2 μm (left) and 500 nm (top right and bottom right).

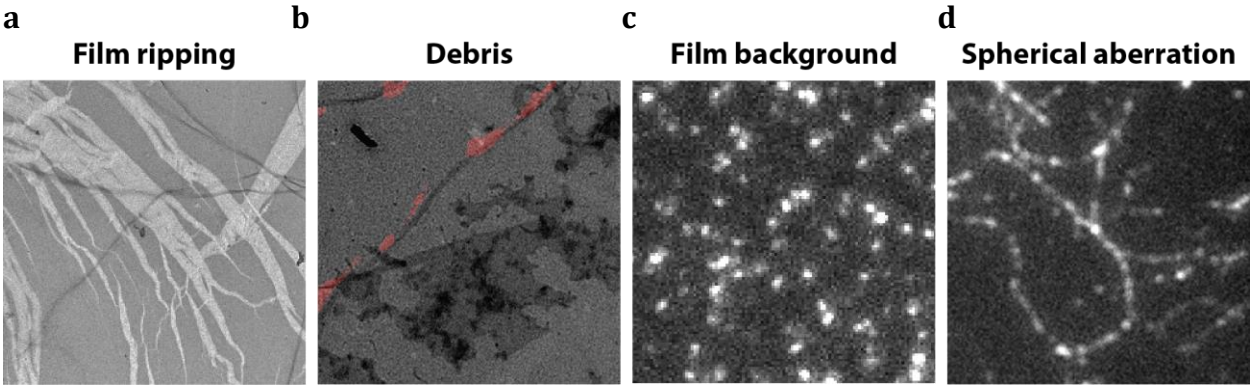

Figure S5.2. Challenges associated with the SR-CLEM workflow.

Chapter 6

Concluding remarks

The overarching research objective of this thesis, in unraveling the supramolecular structure of cellulose fibrils and its role on the breakdown of this material, was achieved by developing new chemical tools for fluorescently labeling cellulose and applying state-of-the-art imaging techniques.

In the process of preparing samples for super-resolution fluorescence microscopy (SRFM), we developed a new approach of labeling celluloses with azide-bearing dyes. The high efficiency of this method and the fact that it is amenable to a variety of commercially available fluorophores makes it cost-effective and versatile. This opens the door for integrating fluorescence-based assays and microscopy techniques in the pipeline of methods routinely used by researchers in the field to characterize the structure and performance of new cellulose materials. The ability to fluorescently label nanocelluloses to high degrees of labeling without compromising their attractive native properties would facilitate the use of advanced imaging techniques, including SRFM, light-sheet and two-photon microscopy. These methods can be instrumental to unraveling fundamental aspects of cellulose, including its nanostructure and enzymatic breakdown, or the development of new cellulose-based technologies for applications in drug delivery, biosensing, biodegradable composites and tissue engineering. The potential for these applications is further supported by the modular nature of the triazine chemistry employed in this labeling method, which was used to prepare di-labeled cellulose as a proof of concept. This should be expanded upon in future work, with the integration of cross-linking, sensing and other functional moieties onto cellulose.

The labeling strategy presented in Chapter 3 allowed the fluorescence labeling of bacterial cellulose with a high-performance dye compatible for SRFM. The development of SRFM has revolutionized the field of fluorescence microscopy by bringing this commonly used technique to the nanoworld. In Chapter 4, SRFM was used to visualize, for the first time, the alternating crystalline and disordered structure of cellulose directly along individual

bacterial cellulose fibrils. This supramolecular structure has been fundamental to our understanding of cellulose and has been often used to explain the production of cellulose nanocrystals (CNCs), but it has been largely hidden to techniques conventionally used to study supramolecular structure of cellulose. The near-perfect overlap between the length distributions of the dark regions seen in SRFM and the length of CNCs produced following acid hydrolysis provides very strong support for the fringed micellar model of cellulose structure. As a follow up, future research should explore whether this structure is also found in cellulose fibrils derived from other sources, including plants and algae. The ability to directly visualize susceptible areas within cellulose fibrils also provides a platform for assessing the impact of different pretreatments on the nanostructure and depolymerization of cellulose. These studies would play a critical role in the development of new and efficient methods of breaking down cellulose to produce renewable biofuels.

To contextualize the disordered regions observed in SRFM to the ultrastructure and morphology of bacterial cellulose ribbons, the last research chapter of this thesis applied a super-resolution correlative light and electron microscopy (SR-CLEM) workflow to combine the specificity of SRFM with the high resolution offered by transmission electron microscopy (TEM). Through SR-CLEM, we saw that the disordered regions were associated with the twisted segments of cellulose ribbons, which possessed nanostructural defects at the bundle and microfibril levels. These observations contribute to the evolving studies on cellulose twisting and the role of nanoscale defects on cellulose depolymerization. In the process of studying cellulose structure with high-resolution TEM, the hierarchical assembly of cellulose into microfibrils, bundles and ribbons was characterized in detail and shed light on the biosynthesis and cell-directed assembly of bacterial cellulose. The optimized SR-CLEM workflow presented in this chapter can be extended to other cellulose-related research questions that would benefit from directly combining the functional information provided by SRFM with the ultrastructural details offered by TEM.

Altogether, the work presented in this thesis has advanced our fundamental understanding of the supramolecular structure of bacterial cellulose and the role of nanoscale dislocations on the breakdown of this ubiquitous material. With the development of new labeling strategies and the continued standardization of SRFM and its integration into multi-modal workflows, we anticipate that advanced imaging techniques will evolve as an invaluable tool for future studies on cellulose structure and depolymerization.

Appendix

Tuning the nanotopography and chemical functionality of 3D printed scaffolds through cellulose nanocrystal coatings

Mouhanad Babi,[1] Roberto Riesco,[2] Louisa Boyer,[2] Ayodele Fatona,[1] Angelo Accardo,[3] Laurent Malaquin,[2] and Jose M. Moran-Mirabal[1,3,4,5]*

[1] *Department of Chemistry and Chemical Biology, McMaster University, Hamilton, ON, Canada*

[2] *LAAS CNRS, Université Toulouse III - Paul Sabatier, 31400 Toulouse, France*

[3] *Department of Materials Science and Engineering, McMaster University, Hamilton, ON, Canada*

[4] *Brockhouse Institute for Materials Research, McMaster University, Hamilton, ON, Canada*

[5] *Center for Advanced Light Microscopy, McMaster University, Hamilton, ON, Canada*

*Please address all correspondence to Jose Moran-Mirabal (mirabj@mcmaster.ca)

Babi, M.; Riesco, R.; Boyer, L.; Fatona, A.; Accardo, A.; Malaquin, L.; Moran-Mirabal, J. Tuning the Nanotopography and Chemical Functionality of 3D Printed Scaffolds through Cellulose Nanocrystal Coatings. *ACS Applied Bio Materials* **2021**.
https://doi.org/10.1021/acsabm.1c00970.

ACS APPLIED BIO MATERIALS

www.acsabm.org Article

Tuning the Nanotopography and Chemical Functionality of 3D Printed Scaffolds through Cellulose Nanocrystal Coatings

Mouhanad Babi, Roberto Riesco, Louisa Boyer, Ayodele Fatona, Angelo Accardo, Laurent Malaquin, and Jose Moran-Mirabal*

Cite This: https://doi.org/10.1021/acsabm.1c00970 Read Online

ACCESS | Metrics & More | Article Recommendations | Supporting Information

ABSTRACT: In nature, cells exist in three-dimensional (3D) microenvironments with topography, stiffness, surface chemistry, and biological factors that strongly dictate their phenotype and behavior. The cellular microenvironment is an organized structure or scaffold that, together with the cells that live within it, make up living tissue. To mimic these systems and understand how the different properties of a scaffold, such as adhesion, proliferation, or function, influence cell behavior, we need to be able to fabricate cellular microenvironments with tunable properties. In this work, the nanotopography and functionality of scaffolds for cell culture were modified by coating 3D printed materials (DS3000 and poly(ethylene glycol)diacrylate, PEG-DA) with cellulose nanocrystals (CNCs). This general approach was demonstrated on a variety of structures designed to incorporate macro- and microscale features fabricated using photopolymerization and 3D printing techniques. Atomic force microscopy was used to characterize the CNC coatings and showed the ability to tune their density and in turn the surface nanoroughness from isolated nanoparticles to dense surface coverage. The ability to tune the density of CNCs on 3D printed structures could be leveraged to control the attachment and morphology of prostate cancer cells. It was also possible to introduce functionalization onto the surface of these scaffolds, either by directly coating them with CNCs grafted with the functionality of interest or with a more general approach of functionalizing the CNCs after coating using biotin−streptavidin coupling. The ability to carefully tune the nanostructure and functionalization of different 3D-printable materials is a step forward to creating *in vitro* scaffolds that mimic the nanoscale features of natural microenvironments, which are key to understanding their impact on cells and developing artificial tissues.

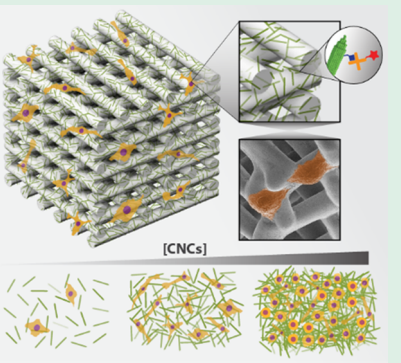

KEYWORDS: *bioprinting, additive manufacturing, cell culture, mechanobiology, biomimetic, cell microenvironment*

1. INTRODUCTION

Recent advances in three-dimensional (3D) printing technologies and biomaterials have given rise to a variety of scaffold designs and compositions designed to mimic natural microenvironments and culture cells *in vitro*. Examples of this include the fabrication of artificial bone grafts through fused deposition modeling of calcium phosphate and collagen composites, extrusion-photopolymerization printing of poly(ethylene glycol)diacrylate (PEG-DA)/alginate hydrogel composites, and electrohydrodynamic jet printing of polycaprolactone/poly(vinylpyrrolidone) scaffolds.[1−3] In addition to incorporating a variety of complex geometrical features, these materials present a broad range of mechanical, physical, and chemical properties. These differences reflect the desire to mimic cellular niches that are found within the various types of tissues that make up multicellular organisms. While artificial scaffolds are effective in producing bulk 3D structures to encapsulate and support cells, they often still require tuning and functionalization to mimic the extracellular matrix (ECM) features found in real tissues. Micro- to nanoscale features of the ECM, such as topography, stiffness, and decoration with various biochemical motifs play an important role in the proliferation, migration, differentiation, and overall function of the cell.[4] Thus, whether to understand the role of the ECM on cellular behavior, study cells in their native environment, or create artificial tissues, it is important to fabricate 3D cellular scaffolds with properties similar to those of tissues.

The *in vivo* extracellular environment possesses nanoscale structures and topography that play a key role in determining the behavior and function of cells both in healthy and diseased tissues. The main structural component of tissue, the ECM, provides biochemical and mechanical support to cells by virtue of a fibrous network, primarily composed of proteins like collagen and elastin that possesses nanoscale dimensions and introduces nanotopography in the cellular microenvironment.

Received: September 9, 2021
Accepted: November 9, 2021

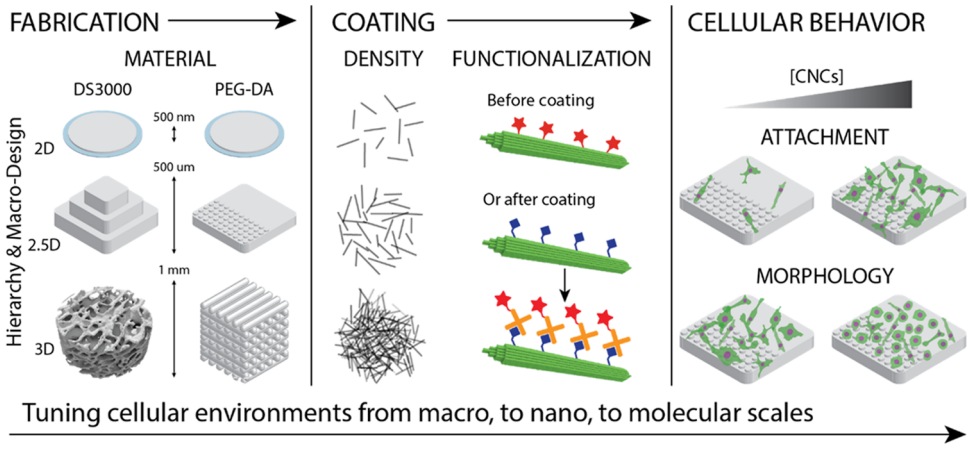

Figure 1. Fabrication of cellular microenvironments with tunable nanotopography and functionality. Spin-coating (followed by flood exposure to UV-light) and one- or two-photon 3D printing were used to fabricate scaffolds of increasing complexity, ranging from 2D thin films to 2.5D and 3D structures. The topography of these scaffolds can be finely tuned by the LbL deposition of a coating of CNCs with densities spanning from sparse to dense coverage of the surface. Using chemically modified CNCs, the scaffold surface can be functionalized during coating with a moiety of interest (red star in the schematic) that is directly grafted on the CNC surface, or after coating with a molecule that targets the functionality encoded on the coated CNCs. Careful tuning of the CNC coating density on the 3D printed scaffolds permits control of cell adhesion and phenotype.

This fibrous network provides structural and mechanical cues that direct cellular adhesion, morphology, migration, and differentiation.[5−7] For instance, collagen fibrils, which have a width of 20−200 nm and a periodic ridged structure with 67 nm spacing and 5−15 nm grooves, present nanostructures that cells interact with through integrin-mediated focal or 3D matrix adhesions.[8−10] Through these contact points, the alignment of collagen fibrils has been shown to guide the migration of fibroblast, epithelial, and carcinoma cells within the 3D matrix.[11−13] *In vivo* substratum nanotopography can also be found in endothelial and corneal epithelium basement membranes, which present a 3D fibrous texture rich in nanoscale (20−200 nm) pores and ridges that are vital for cellular adhesion and act as the foundation of large-scale multicellular architectures including tissues and organs.[14−16] Given the ubiquitous presence and importance of nanoscale topography *in vivo*, the incorporation of surface nanostructures and roughness during the fabrication of artificial microenvironments is key to promoting relevant behavior and function of cells cultured *in vitro*.

Nanostructured surfaces can be made through various fabrication and patterning techniques and have been previously shown to modulate cellular behavior. Ordered and regular nanoscale features, such as nanopillars, nanogrooves, and nanopits, can be produced using colloidal, electron beam, or soft lithography.[17−19] Solely from the anisotropic topography presented by nanogrooves (320−2100 nm wide), human corneal cells elongate and align themselves with the pattern, and in the case of human embryonic stem cells, also differentiate into neuronal lineages without the use of any biochemical differentiation factors.[18,19] Electrospinning of synthetic or natural polymers can be used to create highly porous 3D networks of fibers with controllable widths and pores at the submicron scale and have been used to study human ligament fibroblast alignment and proliferation.[20] In a benchtop fabrication approach, thermoresponsive substrates can be used to wrinkle thin films to produce micro/nanostructured surfaces. Silicon dioxide thin films structured through this method were shown to alter the morphology of murine macrophages into star-shaped cells that displayed enhanced phagocytic abilities.[21]

Incorporating nanoscale structures in artificial scaffolds can play a pivotal role in controlling cell phenotype. However, despite the abundance of nanostructuring techniques, they are often limited to transforming flat surfaces into more complex 2.5D structures or 3D scaffolds with limited depth. While these structures are a significant improvement over commonly used two-dimensional (2D) cell culture dishes, they still fall short in recapitulating the nanotopography present within the 3D environment of biological systems.

Light-assisted 3D printing techniques have become an attractive route for the fabrication of cell and tissue culture scaffolds. These techniques use inks containing photosensitive resins and initiators that result in cross-linking when exposed to light either through a projected image or a scanned laser source. By translating the sample or the source of illumination, a 3D structure can be printed layer-by-layer (LbL) or voxel-by-voxel. This additive manufacturing technology allows the fabrication of scaffolds with complex architectures and precisely defined geometries from the macro- to the microscopic scale. While the resolution offered by light-assisted 3D printing is superior to those of other 3D printing techniques, the natural diffraction of light limits its resolution to ∼200 nm and prevents nanoscale features from being printed onto scaffolds for cell culture.[22] As a result, 3D printed scaffolds are often smooth and require subsequent modifications to incorporate surface nanotopography.

A way to incorporate nanotopography on the surface of 3D scaffolds is to dope the bulk material with nanoparticles (NPs). The high surface-area-to-volume ratio of NPs makes them easily dispersible and ideal to blend with other materials through bulk mixing or surface coating. Attractive properties of NPs, such as piezoelectricity (TiO_2), magnetism (Fe_3O_4), conductivity (carbon nanotubes), antimicrobial effects (Ag), and biodegradability (nanocellulose) can be imparted to the scaffold with the added benefit of mechanical reinforcement. For example, the antioxidant properties of polydopamine/puerarin nanoparticles have been shown to enhance the wound healing properties of PEG-DA-based hydrogel materials.[23] The dimensions of NPs also increase the roughness of scaffolds and have been shown to modify the way cells interact with them. The incorporation of

https://doi.org/10.1021/acsabm.1c00970
ACS Appl. Bio Mater. XXXX, XXX, XXX−XXX

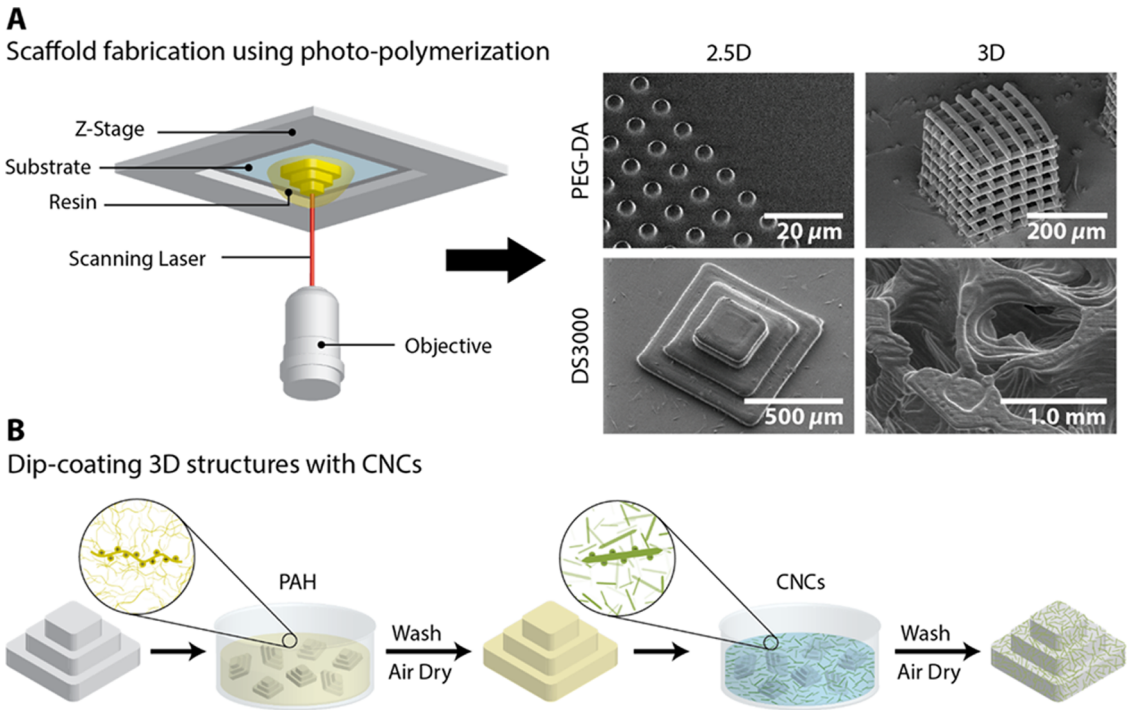

Figure 2. Three-dimensional (3D) printing and dip coating of scaffolds. (A) 2.5D and 3D structures made of DS3000 and PEG-DA were fabricated using single-photon and two-photon polymerization 3D printing, respectively. This technique involves a moveable laser source that polymerizes the resin and prints the structure in a layer-by-layer fashion. (B) Two-dimensional (2D) thin films and 3D printed structures were coated with CNCs using a LbL dip-coating approach, which uses the linear cationic polymer poly(allylamine hydrochloride) (PAH) as an adhesive layer to bind anionic CNCs to the surface of the structures.

carbon nanotubes, poly(lactic-*co*-glycolic acid), hydroxyapatite, and silica nanoparticles within 3D scaffolds has been shown to enhance the adhesion and proliferation of stem cells and promote their differentiation to adipogenic, osteogenic, and neurogenic lineages.[24−28] Yet, in most cases the NPs are incorporated within the bulk material before or during fabrication of the 3D scaffolds, which limits their availability on the surface and can significantly change the bulk mechanical properties of the whole scaffold.[29] Another challenge for their incorporation into 3D printing inks is that NPs can introduce significant light scattering that hinders the photopolymerization of the inks. Given the difficulty in modifying the surface roughness of 3D printed scaffolds, it is not surprising that few studies have quantitatively characterized the nanotopography of composite scaffolds or its impact on cellular adhesion and morphology. A simple method of modifying the surface of 3D printed scaffolds through NP coatings could thus significantly aid in the study of how nanotopography can control the behavior of cells cultured in artificial 3D microenvironments.

In this work, we develop a simple and versatile method (Figure 1) for tuning the nanotopography and functionality of 3D printed scaffolds via dip coating with cellulose nanocrystals (CNCs). CNCs are rod-shaped, rigid, and highly crystalline nanoparticles produced from cellulosic materials through strong acid hydrolysis.[30] CNCs have typical lengths of 100−200 nm and widths of 5−20 nm[31] and exhibit excellent mechanical properties, and high thermal and chemical stability.[32] The abundant hydroxyl groups present on the surface of CNCs can be used to graft small molecules or polymers, endowing them with targeted functionalities; to this end, a variety of surface modification approaches have been reported in the literature.[33−36] Their intrinsic physicochemical properties, non-cytotoxicity, biodegradability (primarily by fungal and bacterial enzymes), and low production cost are advantages that have made CNCs attractive materials to incorporate into *in vitro* scaffolds for applications in tissue engineering and regenerative medicine.[37,38]

We have leveraged the intrinsic surface charge of CNCs to coat 3D printed structures via a layer-by-layer (LbL) dip-coating approach, which relies on a cationic polymer to electrostatically bind CNCs to the surface.[39] Such a LbL method has been previously used to coat 2D surfaces to produce thin CNC films for biosensing, optical, drug delivery, and controlled adhesion applications but to our knowledge has not been used to coat 3D structures or to confer nanotopography and modulate cellular behavior.[40] Our simple and versatile approach is demonstrated on thin films, 2.5D and 3D structures fabricated from commercially available resins using photopolymerization and 3D printing. We showcase the ability to tune the nanoscale roughness and coating density on the 3D printed scaffolds by characterizing the coatings through atomic force microscopy (AFM) and confocal microscopy. The ability to functionalize 3D printed scaffolds with chemically modified CNCs is also shown using two approaches: (i) precoating functionalization, where the moiety of interest is first grafted onto CNCs and then the functionality is transferred to the scaffold surface during coating; (ii) postcoating functionalization, where the scaffold is first coated with functional CNCs and then a second molecule of interest is specifically bound to the CNCs on the scaffold surface. The impact of CNC coatings and their density on the adhesion and morphology of PC3 prostate cancer cells is evaluated to understand how tuneable nanoscale roughness and surface chemistry can be used to influence cell phenotype. We anticipate that this simple method for tuning the nanotopography and

https://doi.org/10.1021/acsabm.1c00970
ACS Appl. Bio Mater. XXXX, XXX, XXX−XXX

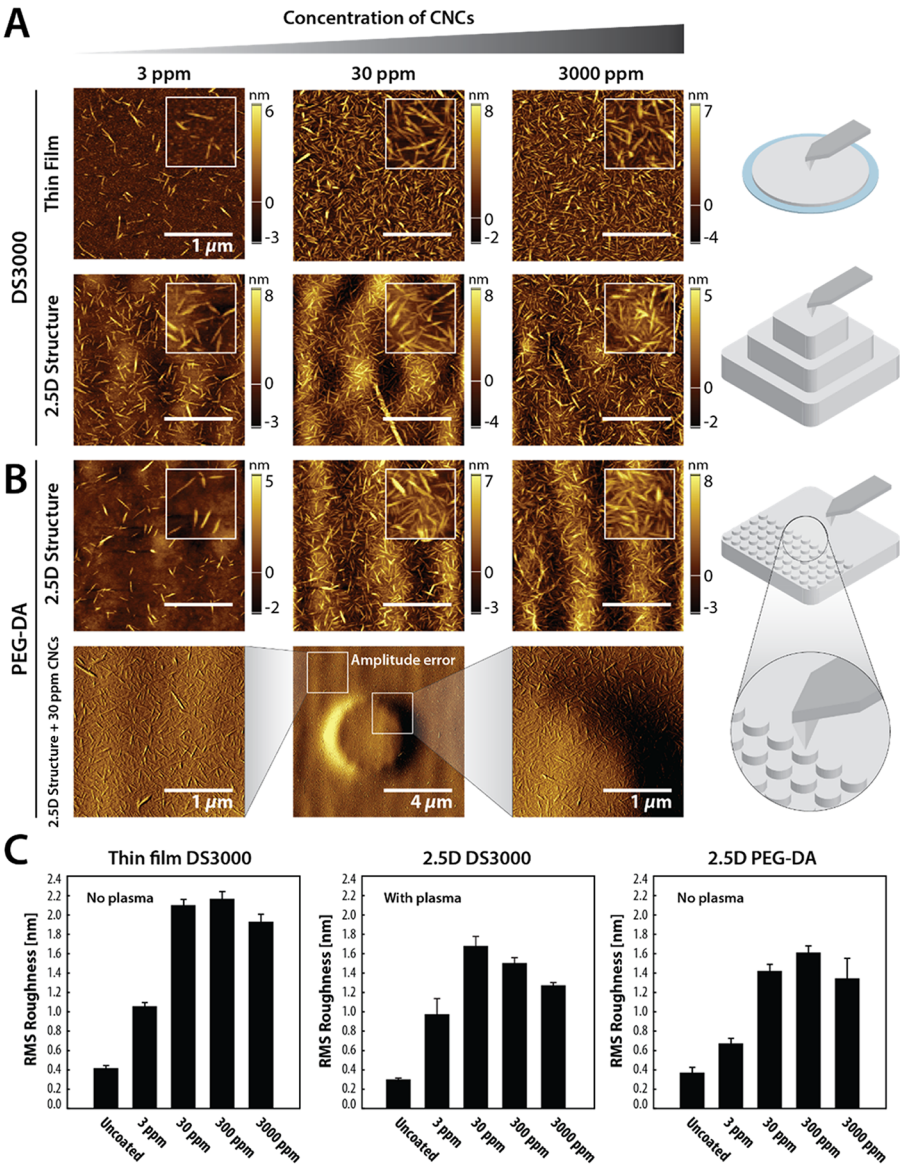

Figure 3. Characterization of the CNC coating density using AFM. (A, B) 2D thin films and 3D printed 2.5D structures made from PEG-DA or DS3000 were coated with CNCs using suspensions with concentrations of 3, 30, 300, and 3000 ppm. As opposed to the DS3000 pyramid, the DS3000 thin-film and PEG-DA pillars were not activated with plasma before coating. The resulting surface density and RMS roughness were characterized by AFM, in three different areas of the thin film, the top surface of the DS3000 pyramid, or the flat half of PEG-DA pillar structures. The image insets are a 0.5 μm × 0.5 μm portion of the image. An amplitude error map of a scan of the PEG-DA pillar was generated to highlight the ability to uniformly coat the wall and top surfaces of 3D printed structures. (C) RMS roughness was calculated from at least three images, and in the case of 2.5D structures, polynomial background subtraction of the underlying large order topography was performed beforehand.

functionality of 3D printed scaffolds will aid in the development of biomimetic cellular microenvironments for applications in tissue engineering and regenerative medicine.

2. RESULTS AND DISCUSSION

2.1. Fabrication of Cellular Scaffolds via 3D Printing.

To investigate the ability of the LbL method to coat 3D printed structures with CNCs, scaffolds of various sizes and geometrical complexities were fabricated using two commercially available photosensitive materials with contrasting properties: (i) PEG-DA, a polymeric material that is hydrophilic, protein-repellent, and relatively soft (under the fabrication conditions and fully hydrated) and (ii) DS3000, a material that is hydrophobic, protein-binding, and mechanically stiff. DS3000 was 3D printed using a single-photon polymerization stereolithography printer (DWS 028J+, DWS Systems, Italy), which allowed the rapid fabrication of centimeter size structures, with feature sizes down to 30−40 μm.[41] On the other hand, a two-photon polymerization (2PP) 3D printing system (Photonic Professional GT, Nanoscribe, Germany) was used to fabricate PEG-DA structures with submicron resolution but was limited to sub-millimeter sized designs. PEG-DA scaffolds were printed on glass substrates spin-coated with a thin film of DS3000 to improve adhesion.[42] Thin films of PEG-DA and DS3000 were also used as flat, 2D surfaces to accurately characterize CNC coatings with AFM. This surface characterization was extended to simple 2.5D structures that had planar facets compatible with AFM imaging, which included a 300 μm × 300 μm × 15 μm base of PEG-DA half-covered with 5 μm diameter, 5 μm high pillars, or DS3000 square pyramids with 700, 500, and 300 μm bases (Figure 2A).

https://doi.org/10.1021/acsabm.1c00970
ACS Appl. Bio Mater. XXXX, XXX, XXX−XXX

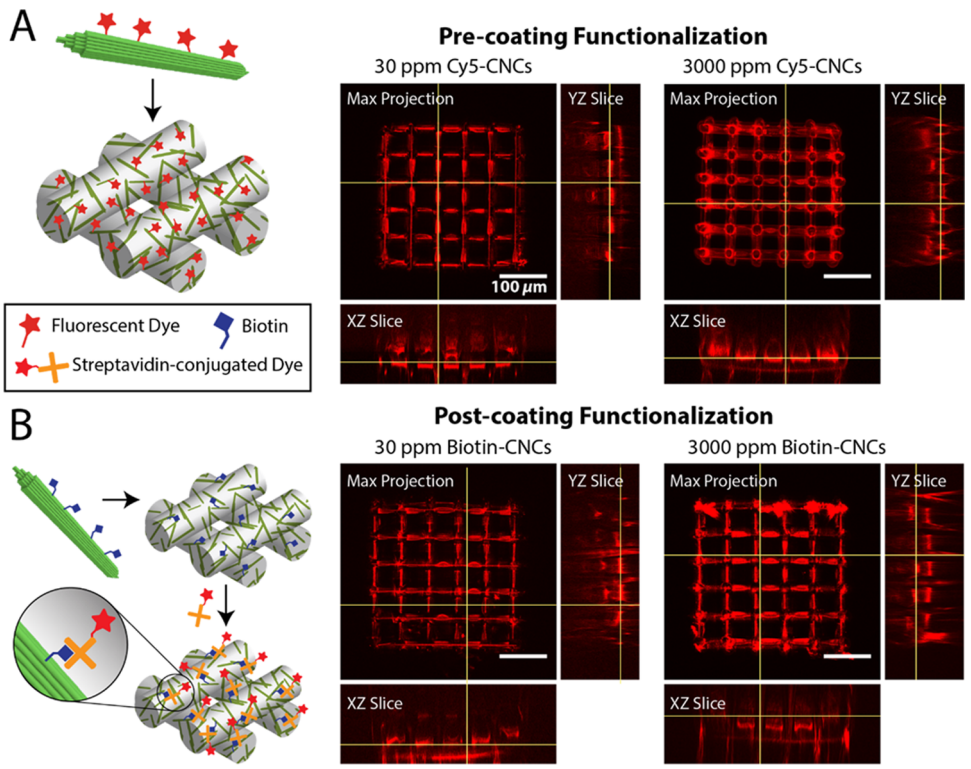

Figure 4. Coating and functionalization of 3D PEG-DA woodpiles with chemically modified CNCs. The ability to functionalize 3D printed PEG-DA structures through (A) precoating functionalization or (B) postcoating functionalization of CNCs was evaluated using the Cy5 dye as a reporter and was characterized using laser scanning confocal microscopy. Fluorescence *z*-stack images were acquired in the far-red channel with a slice thickness of 1.2 μm and a total depth of 180 μm. *XY* images were obtained using a maximum sum projection of the stack while *YZ* and *XZ* orthogonal projections were single slices taken at the positions indicated by the yellow lines.

The coating was then tested on 3D structures that contained overhanging features, such as the 270 μm × 270 μm × 270 μm PEG-DA woodpile and a complex, centimeter-sized DS3000 scaffold with a design reconstructed from 3D tomography of a horse trabecular bone. Thus, 2D, 2.5D, and 3D structures with macroscopic and microscopic features were fabricated from PEG-DA and DS3000 through photopolymerization and 3D printing and were subsequently used to study the ability to coat these scaffolds with CNCs.

2.2. Tunable Surface Coating of 3D Printed Scaffolds with CNCs. Thin-films and 3D printed structures made from DS3000 and PEG-DA were coated with CNCs using the LbL dip coating method. Because of the hydrophobic character of the DS3000 samples, samples with 2.5D and 3D structures were first activated with air plasma to increase the surface wettability and avoid the formation of air pockets that could decrease the coating efficiency. The samples were then immersed in a bath containing PAH, a linear polycation, which adsorbed onto the surface and introduced positive charges (Figure 2B). After washing away excess PAH, the structures were placed into a bath containing a suspension of CNCs, which electrostatically bound to the PAH adhesive layer and effectively coated the scaffold surface. The importance of the PAH layer in coating surfaces with CNCs can be seen by the lack of nanoparticles adsorbed on bare PEG-DA thin films even when a high concentration of CNCs was used (Figure S1A). Furthermore, a two-step washing of the PAH-coated structures was essential to remove the excess or loosely bound polymer and obtain uniform and reproducible coatings (Figure S1C,D). When using low CNC concentrations, inadequate removal of excess PAH through a single washing step resulted in nonuniform coatings with large areas that were devoid of CNCs and the presence of CNC aggregates; similarly, when using high CNC coating concentrations, incomplete PAH washing led to the formation of a dense, fibrillated cellulose film (Figures S1A and S2A). In the case of 3D PEG-DA woodpile structures, incomplete washing of PAH also caused clogging, webbing, and bridging of the scaffolds with cellulose films (Figure S1E). By thoroughly washing excess PAH, it was possible to reproducibly coat thin films and 3D printed structures with various concentrations of CNCs.

AFM was used to characterize the surface of coated thin films and 2.5D structures, where the coating density and surface roughness were evaluated as a function of plasma activation and the CNC concentration used during the coating process. For DS3000 thin films coated without plasma activation and a low CNC concentration (3 ppm), the surface was sparsely covered with individual CNCs, and the root mean square (RMS) surface roughness increased from 0.4 to 1.0 nm (Figure 3A,B). At a 10-fold higher concentration of 30 ppm, the coating density significantly increased and yielded a connected network of CNCs with a roughness of 2.1 nm. This effect leveled off at higher CNC concentrations, with more complete coverage of the thin film and a maximum roughness of 2.2 nm (at 300 ppm CNCs) and a slight decrease to 1.8 nm when a 3000 ppm CNC solution was used. The decrease in RMS roughness at the highest concentration is attributed to the formation of a complete CNC layer where the roughness is no longer dictated by the difference in height between the diameter of the nanoparticles and the surface but by the packing between the CNCs themselves, as evidenced by line scans obtained from AFM measurements (Figure S2B). The coating of PEG-DA thin films yielded similar results with low concentrations resulting in

https://doi.org/10.1021/acsabm.1c00970
ACS Appl. Bio Mater. XXXX, XXX, XXX−XXX

sparse coatings and high concentrations leading to complete surface coverage with CNCs (Figure S2C).

The dip-coating approach also allowed the controlled deposition of CNC coatings with tunable density on structures made through 3D printing from DS3000 and PEG-DA inks (Figure 3A,B). Unlike spin-coated flat films, which had an RMS roughness of 0.4 nm (Figure S1A), the surface of 2.5D structures presented intrinsic inhomogeneous topographies either from the 3D printing process or caused by drying and wrinkling. Thus, the RMS roughness of uncoated surfaces varied from 0.5 to 4.0 nm, making it necessary to perform a polynomial background subtraction to determine the roughness introduced solely by the CNC coating (Figure S3A). Surprisingly, the observed roughness of coated 2.5D structures was lower than that of thin films (Figure 3C). This can be seen when comparing the height profiles of CNCs imaged on a DS3000 thin film, which were 4−6 nm high, to those on a PEG-DA 2.5D structure, which had a height of 2−4 nm (Figure S3B). The observed discrepancy is attributed to the inability of the AFM to map the full height of CNCs when they are overlaid on large-scale topography and to over smoothing by the polynomial fit. The coating efficiency, as visualized from the density of surface-bound CNCs, was similar for both thin films and the PEG-DA 2.5D structures. However, the 2.5D DS3000 pyramid was coated more efficiently, which can be seen by the higher coating density when a dilute CNC solution of 3 ppm was used. This can be explained by the activation of the surface with plasma, which introduces negative surface charges and enhances the adsorption of the positively charged PAH polymer chains. The higher coating efficiency introduced by plasma activation caused the maximum roughness and complete coverage of the surface to occur at more dilute CNC concentrations (Figure 3C). Finally, to demonstrate the ability of this method to uniformly coat microscale features, an AFM scan was acquired from a 5 μm diameter PEG-DA pillar that was coated using a 30 ppm CNC suspension (Figure 3B, bottom row). Through the amplitude error map, it is possible to see homogeneous coverage by CNCs across the base, walls, and top surfaces of the pillar. Altogether, these results show that the dip-coating process allows easy tuning of the roughness and density of CNCs on thin films and 3D printed structures made from DS3000 and PEG-DA by simply changing the CNC concentration used.

2.3. Functionalization of 3D Printed Scaffolds with Chemically Modified CNCs. The use of chemically modified CNCs opens the door to a simple route for the functionalization of 3D printed scaffolds via dip coating. Through chemical derivatization of CNCs, functionalities of interest can be grafted onto the nanoparticle surface and introduced onto the scaffolds using two strategies: (i) precoating functionalization, where the moiety of interest is first grafted onto the CNC and then transferred to the scaffold surface during coating or (ii) postcoating functionalization, amenable to biomolecules sensitive to drying, where the scaffold is first coated with CNCs grafted with a binding group and then a second molecule of interest is specifically targeted to the CNCs containing the binding group on the scaffold surface (Figure 4). The precoating functionalization was demonstrated by coating the PEG-DA woodpile and DS3000 bone 3D scaffolds with CNCs grafted with the far-red dye Cy5, which allowed their visualization with laser scanning confocal microscopy. With as little as 30 ppm CNCs, 10% of which were grafted with the Cy5 dye, the PEG-DA woodpile scaffold displayed a fluorescent coating (Figures 4A and S4A). At a higher concentration of 3000 ppm CNCs, the full surface of the beams was easily visible in the orthogonal projections and 3D rendering (Figures 4A and S4A) of confocal microscopy images. Coating a trabecular bone scaffold, made from DS3000 resin, with Cy5-CNCs allowed the visualization of the highly complex architecture of the reconstructed bone and demonstrated the ability to coat and functionalize small, free-standing features within the structure (Figure S4B) using as little as a 3 ppm suspension of Cy5-CNCs. However, due to the heterogeneity in features presented by the scaffold, it was not possible to consistently visualize similar areas within individual prints and study the impact of CNC concentrations or other conditions on coating.

The postcoating functionalization approach was demonstrated by first coating the scaffolds with CNCs, 10% of which had biotin grafted onto their surface, and then incubating the coated scaffolds with a solution containing Cy5-labeled streptavidin. Functionalization of the structures after coating with Cy5-streptavidin yielded fluorescence images like those obtained with the prefunctionalization approach (Figure 4B) but with a ∼4× lower fluorescence intensity. This was attributed to differences in the degree of functionalization of the CNCs and streptavidin with Cy5. With both functionalization scenarios, it was only possible to visualize the first two layers of the woodpile structure due to limitations to how deep the confocal laser could penetrate (typically 40 μm) and how much of the emitted fluorescence could be recorded. However, in cases where the scaffolds were partially detached from the glass substrate, it was possible to acquire an image of the tilted structure and visualize the outer beams of the whole woodpile, which confirmed that the CNC coating was uniform across the whole structure (Figure S3B). Using chemically modified CNCs, it was possible to functionalize 3D scaffolds with Cy5 dyes either through direct functionalization of the CNCs or streptavidin−biotin coupling. The latter strategy is amenable to a variety of commercially available functionalities that are biologically relevant but sensitive to drying, such as structural proteins, enzymes, receptors, and differentiation factors which are key members of cellular microenvironments found in tissues. Functionalization through this route would preserve the native structure and activity of these biochemical factors that otherwise might not survive the steps involved in directly grafting them to CNCs or coating the scaffolds with the nanoparticles.

The LbL dip-coating method has been previously used for the fabrication of multilayered, nanostructured composite biomaterials that consist of CNCs, polyelectrolyte, and other scaffolding polymers like collagen, chitosan, and poly(oligoethyleneglycol-methacrylate).[43−45] While this method has been traditionally used for creating thin films or 2.5D structures, we have demonstrated that this approach can be extended to coat 3D printed scaffolds with tunable densities of CNCs. We have also observed that these coatings remain on the structures for several months under hydrated conditions and for years when stored under dry conditions, highlighting their excellent stability. The ability to coat both DS3000 and PEG-DA, which possess contrasting physical and chemical properties, suggests that this method can be applied to other biomaterials commonly used in 3D printing to confer nanotopography and functionalization. The versatility of this approach stems from the ability of PAH to nonspecifically interact with various charged and uncharged materials, as we observed that the introduction of surface negative charges through plasma treatment was not necessary to achieve coating. The interactions between the

https://doi.org/10.1021/acsabm.1c00970
ACS Appl. Bio Mater. XXXX, XXX, XXX−XXX

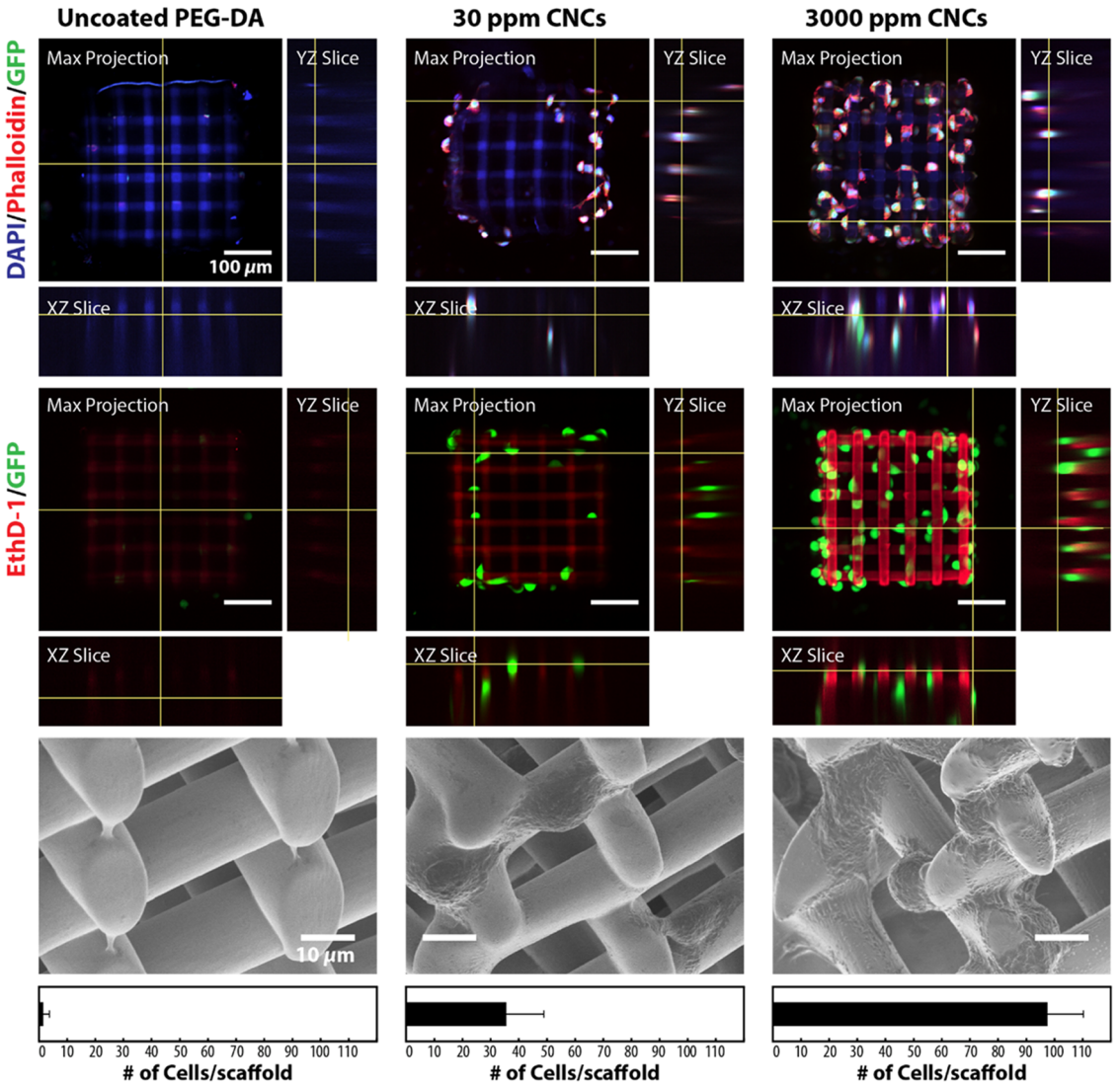

Figure 5. The adhesion of PC3-GFP prostate cells to PEG-DA 3D woodpile structures could be tuned by the density of CNC coatings. PC3-GFP prostate cancer cells, which constitutively expressed green fluorescence protein (GFP) in the cytoplasm, were seeded on the PEG-DA scaffolds at a density of 10 000 cells/cm^2 for 1 h, supplemented with media, and cultured for 2 days. Images in the top row are of formalin-fixed cells stained for the nucleus and actin filaments using 4′,6-diamidino-2-phenylindole (DAPI) and rhodamine−phalloidin, respectively, and were acquired using spinning-disk confocal microscopy. The cells in the second row were cultured under the same conditions and stained with ethidium bromide homodimer (EthD-1), which causes dead cells to fluoresce orange (false-colored red). The sample in the first row was dehydrated and imaged by SEM (bottom row). Cells were manually counted from the raw *z*-stack confocal images, and the bars at the bottom represent the average and standard deviation from at least three independently prepared samples for each condition.

cationic PAH layer and the anionic CNCs are responsible for the excellent stability of these coatings.

Despite the simplicity of this method, some obstacles were encountered when coating 3D hydrogel scaffolds. Compared to DS3000, coating 3D printed PEG-DA structures using this procedure was more challenging as the small hydrogels were delicate, exhibited high water retention, and were easily detachable from the substrate. As a result, the numerous coating, washing, and drying steps involved required careful handling of samples and avoiding harsh drying methods such as the use of an air gun. As previously discussed, a key step to obtaining uniform and reproducible coatings was thoroughly washing away excess PAH, which would otherwise result in the formation of aggregate cellulose fibers and films. Achieving this required an intermediary drying step between washing, which we suspect is necessary for the PAH chains to collapse onto the PEG-DA scaffold to irreversibly coat it. This requirement may pose issues when coating more delicate scaffolds, where the process of dehydration could significantly deform or collapse fine structures.

2.4. Impact of CNC Coatings on Cellular Attachment and Morphology. The impact of CNC coatings and their density on the adhesion and morphology of PC3-GFP human prostate cancer cells was studied on PEG-DA and DS3000 3D printed scaffolds. In the absence of CNCs, PC3 cells did not adhere to PEG-DA woodpiles (2 ± 2 bound cells/scaffold), as seen by spinning-disk confocal microscopy (Figure 5). In contrast, coating the scaffold with CNCs using a 30 ppm solution caused some cells to bind to the PEG-DA hydrogel (35 ± 14 cells/scaffold) and a high coating concentration of 3000 ppm resulted in complete coverage of the woodpile with cells (97 ± 13 cells/scaffold). As seen in the fluorescence orthogonal projections and scanning electron microscopy (SEM) micrographs, the cells were able to reside deep within the woodpile

https://doi.org/10.1021/acsabm.1c00970
ACS Appl. Bio Mater. XXXX, XXX, XXX−XXX

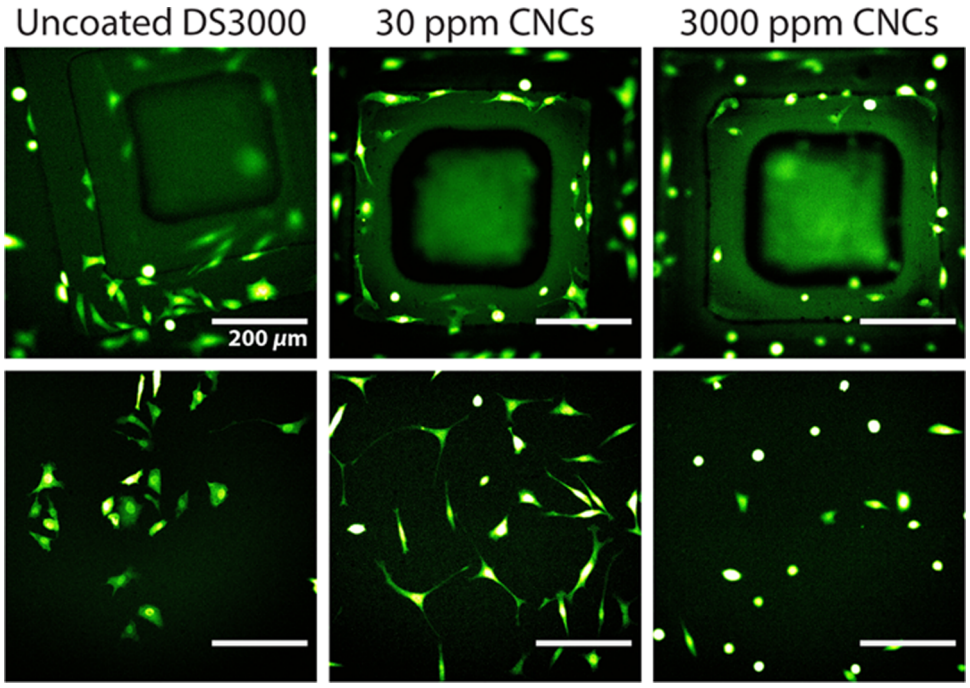

Figure 6. Epifluorescence images of PC3-GFP cells cultured on DS3000 2.5D pyramids. Cells were seeded at a density of 15 000 cells/cm^2 for 1 h, supplemented with media, and cultured for 3 days. Live-cell images were acquired in the green channel using an epifluorescence microscope at room temperature. The top row consists of representative images of cells adhering to the pyramid while the images in the bottom row were acquired on the flat part of the DS3000 pyramid array.

and occasionally suspended between beams when not lying flat or wrapping them. Staining with ethidium bromide homodimer (EthD-1) did not result in red fluorescence from any of the cells, indicating that CNCs did not hinder cellular viability at both high and low coating concentrations after 2 days of cell culture. Unexpectedly, this dye was able to nonspecifically stain CNCs and in this case highlighted the scaffold coating with a fluorescence intensity that was proportional to the density of CNCs.

Coating PEG-DA with CNCs permitted attachment of the PC3 cells to the 3D scaffold in a fashion that could be tuned by controlling the surface density of CNCs. The ability of these nanoparticles to enhance the attachment of PC3 cells to PEG-DA, which was also observed with 2.5D structures (Figure S5), is not fully understood, but we hypothesize that it arises from the presence of nanotopography, from the increased hydrophobicity of the CNCs, and from the higher local stiffness introduced by the rigid nanoparticles. The coverage of the hydrogel surface with CNCs may mask the protein-repelling properties of PEG-DA and in turn allow adhesion proteins, which are present in media and on the cellular surface, to attach to the scaffold. This effect may be complemented by the chemical properties of the CNC surface, which presents both hydrophobic and hydrophilic facets that potentially act as adhesion sites for the cells.[46,47] Additionally, nanotopography and the increase in surface roughness introduced by the CNCs, which have been previously shown to significantly enhance cellular adhesion, may provide more features for the cells to interact with and adhere to.[48−50] The possibility of PAH being responsible for the enhanced cellular adhesion was ruled out with a control experiment on 2.5D PEG-DA structures coated only with PAH, where cells could not bind to the hydrogel (Figure S5). The concentration of PAH also remained constant when the woodpiles were coated with 30 or 3000 ppm CNCs, while the observed cellular adhesion was dependent on the concentration of the CNC coating. Thus, it can be concluded that the enhanced adhesion was a direct result of the presence of CNCs.

Similar enhancements in cell binding were not observed for DS3000 scaffolds coated with CNCs (Figure 6). This material is designed to be biocompatible and supported culturing of PC3 prostate cancer cells without any coatings. However, coating 2.5D DS3000 scaffolds with CNCs altered the morphology of PC3 cells. In uncoated scaffolds, PC3 cells appeared to organize in clusters and lay flat on the surface while adopting epithelial-like, polygon-shaped morphologies. Upon sparsely coating the scaffold with CNCs (30 ppm), the cells were more uniformly distributed along the scaffold and adopted elongated, multipolar configurations that are reminiscent of fibroblasts and similar to those adopted by PC3 cells cultured on control glass surfaces (Figure S6). When the scaffolds were densely coated with CNCs (3000 ppm), most of the cells were spherical and exhibited little to no cellular extensions. Similar trends in morphology were observed with PC3 cells cultured on 3D PEG-DA scaffolds densely coated with CNCs (Figures 5 and S5). However, it is difficult to make a comparison to pristine PEG-DA as little to no cells adhered. Given the propensity of PC3 cells to adhere to CNCs, as seen with coated PEG-DA, their morphology appeared to be dictated by the amount of CNCs present within their surroundings. With a moderate CNC density, the cells extended filipodia to sites where CNCs are present, giving rise to their elongated morphology. When the scaffold surface was densely covered with CNCs, the cells did not extend to other areas and retained a circular morphology. This could be the result of excessive nanotopography, resulting in a poor cell condition (despite the fact that they did not stain red with ethidium bromide homodimer), which highlights the importance of nanotopography not only on adhesion but also on cell phenotype. Thus, by tuning the density of CNCs present on the

https://doi.org/10.1021/acsabm.1c00970
ACS Appl. Bio Mater. XXXX, XXX, XXX−XXX

scaffold surface, it was possible to alter the adhesion and phenotype adopted by PC3 prostate cancer cells when cultured on DS300 and PEG-DA. In future work, this can be complemented with metabolic assays and biochemical functionalization of the scaffolds to assess cellular fitness and further recapitulate real cell microenvironments to guide the differentiation of cells to specific lineages. On the other hand, the control offered by CNC coatings on the adhesion of PC3 cells to PEG-DA scaffolds can be used for the development of medical devices that isolate rare circulating tumor cells from the blood.

3. CONCLUSIONS

The process of additive manufacturing through single- and two-photon polymerization 3D printing systems allowed the fabrication of PEG-DA and DS3000 scaffolds with precise control on their size, hierarchy, and geometric complexity. We have extended the method of layer-by-layer polyelectrolyte dip coating with CNCs to introduce nanostructured topography and chemical functionality onto the surface of 3D printed structures in a tunable and versatile fashion. Coating the scaffolds with various densities of CNCs enabled control on the adherence of GFP-PC3 prostate cancer cells to PEG-DA surfaces and altered the phenotype of the cells when cultured on both PEG-DA and DS3000 structures. The mechanism by which CNCs influence the attachment and morphology of these cells remains unclear as it is challenging to decouple the effects of surface nanoroughness and surface chemistry that are simultaneously introduced by the CNCs. The versatility offered by biotin-CNCs in functionalizing scaffolds with streptavidin-conjugated molecules allows future exploration on using biochemical factors to further mimic real cellular microenvironments. Fabricating realistic cellular scaffolds would promote the desirable cellular behavior that is necessary to study fundamental biological concepts and create artificial tissues, organoid models, and medical devices.

4. EXPERIMENTAL SECTION

4.1. Materials. 3-(Trimethoxysilyl)propyl methacrylate (98%, TPM), poly(ethylene glycol)diacrylate (PEG-DA, M_n = 700 Da, n = 1.47), diphenyl(2,4,6-trimethylbenzoyl)phosphine oxide (Irgacure 819), Triton X-100, 10% formalin, 4% glutaraldehyde, 99% acetic acid, poly(ethylene glycol) (PEG, M_w = 1050 Da), triethylamine (Et_3N), 4-dimethylaminopyridine (DMAP), *p*-toluene sulfonylchloride, sodium sulfate (NA_2SO_4), copper sulfate pentahydrate ($CuSO_4 \cdot 5H_2O$), ascorbic acid, cyanuric chloride, propargylamine, sodium hydroxide (NaOH), potassium carbonate (K_2CO_3), *N*-hydroxysuccinimide, dicyclohexylcarbodiimide (DCC), and biotinyl-*N*-hydroxysuccinimide were purchased from Sigma-Aldrich (Oakville, Ontario, Canada). The DS3000 negative tone resist was purchased from DWS Systems (Italy). Poly(allylamine hydrochloride) (PAH, M_w = 120 000−200 000 Da) was purchased from Polysciences (Warrington, PA) and stored at −20 °C. Sulfo-Cyanine5 azide was purchased from Lumiprobe Corp. (Hunt Valley, MD). Poly(ethylene glycol) monoallyl ether (M_w = 388 Da) was a gift from EnRoute Interfaces, Inc. (Hamilton, ON, Canada). Cellulose nanocrystals (CNCs, spray-dried), were kindly donated by CelluForce Inc. (Montreal, QC, Canada) and were previously characterized by dynamic light scattering, atomic force microscopy, and X-ray diffraction to have an average hydrodynamic radius of 70 ± 3 nm, a ζ-potential of −39 ± 1 mV, length of 180 ± 90 nm, cross section of 6 ± 2, and crystallinity of 90%, respectively.[51] All mentions of water refer to double-distilled 18.2 MΩ water (ddH_2O, ultrapure, type I), generated from a Milli-Q direct purifier system (Millipore Sigma). Cy5-conjugated streptavidin (0.1 mg/mL in phosphate-buffered saline, PBS with 4 mg/mL bovine serum albumin, BSA), Gibco Dulbecco's modified Eagle medium (DMEM) (high glucose, GlutaMAX supplement, pyruvate), Gibco penicillin−streptomycin, Gibco fetal bovine serum, and Gibco geneticin were purchased from Thermo Fisher Scientific (Mississauga, Ontario, Canada). Human prostate cancer cells (PC3), which were transformed to constitutively express the green fluorescent protein in their cytoplasm (PC3-GFP), were kindly provided by the Cuvillier Laboratory at the Institute of Pharmacology and Structural Biology (IPBS, Toulouse, France).

4.2. Functionalization of CNCs with Cy5 and Biotin. CNCs were functionalized with Cy5 or biotin using triazine click-chemistry using methods adapted from our previous work.[33,52] Since trichlorotriazine presents a substitution site at each chlorine, grafting this molecule onto the CNC surface hydroxyl groups allows it to be used as a linker when other sites are reacted with the functionality of interest. A general implementation of this involved appending, to the triazine linker, a group that can participate in a click-reaction with a molecule of interest that presents a complementary chemical handle. Many widely used functionalities, such as dyes and ligands, are commercially available with chemical handles that are compatible with click-reactions. CNCs were grafted with: (i) dichlorotriazine propargylamine, which was then reacted with sulfo-Cy5 azide, or (ii) chlorotriazine azido-PEG-allyl-PEG, to which alkyne-biotin was then conjugated (Scheme S1). The second linker also possesses an alkene group, which could be used to functionalize the CNCs with molecules bearing a thiol moiety. The synthesis of the triazine linkers and alkyne-biotin (Scheme S2), and their subsequent grafting onto CNCs are outlined in the Supporting Information.

4.3. Silanization of Glass Coverslips and Indium-Tin-Oxide (ITO)-Coated Slides. Glass substrates were silanized with a methacrylate group to ensure the proper adhesion of spin-coated thin films. Circular glass coverslips (No. 1.5, 18 mm diameter, 170 μm nominal thickness, VWR, Mississauga, Ontario, Canada) or indium-tin-oxide (ITO)-coated glass slides (25 mm × 25 mm, 0.7 mm thickness, Nanoscribe GMBH, Karlsruhe, Germany) were sequentially cleaned with acetone, ethanol, and water and then dried with an air gun. The glass or ITO surface was activated with a Diener Electronic air plasma machine (5 min, 0.6 mbar, 30 W) immediately before drop-casting TPM (2% v/v in water with 0.1% v/v of acetic acid) over the substrates. The droplets of the TPM solution were kept for 2 h before rinsing the substrates with ethanol and water and then drying with an air gun.

4.4. Spin-Coating Thin Films of PEG-DA and DS3000 on Circular Glass Substrates. DS3000 was spin-coated onto silanized 18 mm glass slides (5000 rpm, 60 s, 1000 rpm/s) using a Suss MicroTec spin-coater (Karl Suss, Garching, Germany) and cured immediately with a flood exposure of 405 nm light (60 s, 30 mW/cm^2) using a Suss MicroTec MA/BA6 mask aligner (Karl Suss, Garching, Germany). The samples were rinsed in ethanol for 10 s and then dried with an air gun. PEG-DA thin films were prepared the same way but on DS3000-coated glass coverslips to improve adhesion.

4.5. 3D Printing DS3000 Using Single-Photon Polymerization. DS3000 structures were fabricated using laser-assisted stereolithography; a DWS 029J+ 3D-printer from DWS Systems equipped with a 405 nm laser (86 mW, Solid State BluEdge BE-1800C) and a galvanometric mirror that can achieve a maximum scanning speed of 6000 mm/s. To ensure proper adhesion of the samples to the printer platform, the first four layers were overexposed by reducing the scanning speed to 200 mm/s, whereas the rest of the structures were printed at 3000 mm/s. The hatching and slicing distances were set to 40 μm and 50 μm, respectively. The 2.5D pyramids, which consisted of three, 50 μm high steps with side lengths of 700, 500, and 300 μm, were printed as an array on a circular base with a diameter of 20 and 2 mm thickness. The 3D bone scaffold was printed from a digital reconstruction model that was generated using propagation phase-contrast synchrotron microtomography of a trabecular bone within a horse femoral epiphysis, as described in previous work.[39] 3D printed samples were then developed in an ethanol bath under sonication for 15 min to remove the nonpolymerized material. Afterward, the samples were air-dried and flood exposed to UV light to ensure complete cross-linking of the resin.

4.6. 3D Printing PEG-DA Using Two-Photon Polymerization Direct Laser Writing. PEG-DA structures were 3D printed by two-photon polymerization (2PP) direct laser writing using a Nanoscribe

https://doi.org/10.1021/acsabm.1c00970
ACS Appl. Bio Mater. XXXX, XXX, XXX−XXX

Photonic Professional GT2 (Karlsruhe, Germany) system similar to previous work.[42] Briefly, PEG-DA 700 was thawed (from −20 °C) for an hour at room temperature (rt), combined with the photoinitiator Irgacure 819 to a concentration of 0.5% w/w and stirred for 3 h in the dark. Water was added to make a 3:1 PEG-DA/water solution and stirred overnight at rt in the dark. Silanized ITO glass slides were coated with DS3000, using the same procedure as above, to improve the adhesion of PEG-DA to the substrate and allow the microscope to find the substrate interface. The substrate was fixed onto a dip-in laser lithography holder and a droplet of the PEG-DA solution was placed in the center. The holder was inverted and mounted onto the stage of the Nanoscribe. In such a configuration, the employed 2PP objective is directly immersed in the photosensitive liquid. The 2PP setup system consisted of an inverted two-photon Carl Zeiss microscope, coupled to a 780 nm femtosecond pulsed fiber laser (100 fs, 50 mW, FemtoFiber Pro, Toptica Photonics), with a resonating scanner and a galvanometric mirror system allowing a moving-beam fixed-sample configuration. The sample was approached with a 25× (NA 0.8) water-immersion objective, with the collar set a quarter way from the glycerol mark to the watermark, until the lens was in immersion with the resin, and the interface between the substrate and the photosensitive PEG-DA interface was found. The structures of interest were designed beforehand using CAD software Autodesk Fusion 360 and imported as a work file into Nanoscribe with both the hatching and slicing distance writing parameters equal to 400 nm. The 2.5D pillar array design, which consisted of a 300 μm × 300 μm × 15 μm base, half-covered with 5 μm diameter pillars, 10 μm apart, was printed with a writing speed of 25 mm/s and a nominal laser power of 70%. The 3D woodpile design (270 μm × 270 μm × 280 μm) consisted of perpendicularly stacked layers, each composed of 20 μm diameter cylinders interspaced 50 μm apart. This structure was printed three times on each sample with a writing speed of 50 mm/s and different laser powers (78, 79, and 80%) to produce scaffolds with various structural integrities, stiffness, and adhesion to the substrate (Figure S1B). The 3D printed structures were developed in two water baths for 30 min each. No differences in the coating were observed between the samples fabricated using different laser powers.

4.7. Dip-Coating Thin Films and 3D Printed Structures with CNCs. Spray-dried CNCs were dissolved in water to make a 3 wt % (30 000 ppm) suspension through repeated cycles of vortex mixing and dispersion with a VC334 Vibracell point probe sonicator (100 W, 2 s pulses, 6 min with a 3 mm tapered microtip) until it was clear. Through serial dilutions of this solution, 3000−3 ppm CNC suspensions were prepared and dispersed with point probe sonication after each dilution. To dip-coat structures with CNCs, it was first necessary to coat them with PAH, which was prepared from powder form to make a 1 wt % solution. The PAH solution was used within 2 weeks, while all of the CNC solutions with a concentration lower than 3000 ppm were prepared fresh each time as they could be significantly depleted with each coating.

To ensure adequate wettability, 3D printed DS300 structures were first activated with air plasma (30 s, 0.6 mbar, 30 W). 3D printed PEG-DA structures were not plasma-activated as they were stored in water after printing to avoid collapse of the hydrogel. The samples were then "dipped", or placed, into a plastic petri dish containing 20 mL of PAH for 15 min. To wash off excess PAH, the samples were washed in two steps by placing them in a water dish for 10 min, air drying, and then washing in another water dish for 10 min. Samples that were washed in one step only involved submersion in a water dish for 10 min and then air drying. The structures were then dipped into a 20 mL solution of CNCs for 15 min, washed in a water dish for 10 min, and air-dried. Thin films and 3D printed DS3000 samples could be dried using an air gun, while PEG-DA structures were left to gradually dry at rt as they could easily detach from the substrate in the presence of strong airflow.

4.8. Functionalization of 3D Scaffolds. Three-dimensional (3D) structures were coated using the dip-coating method with a layer of CNCs, 10% of which were functionalized with either Cy5 or biotin. For postcoating functionalization, the PEG-DA woodpile scaffold was incubated with 100 μL of 0.01 mg/mL Cy5-streptavidin in PBS for 30 min within a Pyrex cloning cylinder and then washed for 30 min in PBS.

4.9. Culture of PC3-GFP Prostate Cancer Cells. A 1.5 cm × 1.5 cm frame cut from double-sided adhesive tape (0.25 mm thick, Thermo Fisher) was placed on the center of a glass substrate containing 3D printed PEG-DA structures. The samples were placed in a Petri dish and sterilized with 70% ethanol for 30 min, rinsed with PBS, and 300 μL of PC3-GFP cells were seeded within the frame (to confine the seeding area and minimize the number of cells used during the inoculation step) at a density of 10 000 cells/cm^2 and incubated for 1 h (37 °C, 5% CO_2). The cells were supplemented with media (2 mL of DMEM with 10% FBS, 1% penicillin/streptomycin, and 1% geneticin) and cultured for 1 or 2 days on the 2.5D or 3D structures, respectively. DS3000 2.5D structures were cultured with PC3-GFP cells in a similar fashion, but an additional washing step of 2 days in PBS was done before dip coating and cell culture. The structures, without a frame, were placed in a 6-well cell culture plate (Flat Bottom, Corning Costar), seeded with 15 000 cells/cm^2, and cultured for 3 days.

Cells cultured on 2.5D DS3000 or PEG-DA structures (Figures 6 and S5) were imaged live, without staining or fixation. Cells cultured on 3D PEG-DA woodpile structures (Figure 5a) were fixed with 10% formalin for 30 min, permeabilized with 0.2% Triton X-100 for 3 min, and stained for actin and nuclear DNA with rhodamine−phalloidin (Invitrogen, 16.5 mg/mL, 30 min, rt) and DAPI (Invitrogen, 10 μg/mL, 15 min, rt), respectively. The stained samples were stored in PBS, in the dark at 4 °C until they were imaged. To test for the presence of dead cells, duplicate samples were stained with 4 μM ethidium bromide homodimer (Live/Dead kit for mammalian cells, Invitrogen) for 30 min at 37 °C. After fluorescence imaging, this sample was then fixed with 4% glutaraldehyde (in PBS) for 4 h, washed once with PBS (4 min), three times with water (2 min each), dehydrated with consecutive ethanol baths (50, 70, 90, and 100% in PBS for 4 min per bath), washed with 100% ethanol twice (2 min each) and then gradually air-dried at rt before imaging with SEM (Figure 5c).

4.10. Characterization of the Surface Roughness and CNC Coating Density with AFM. The nanostructure and roughness arising from the CNC coating process and its response to variations in CNC concentrations were assessed using a Bruker ICON AFM. All images were acquired in tapping mode with a Bruker FESP cantilever of a spring constant of 1−5 N/m and a resonating frequency of 72 kHz. Areas of 2.5 μm × 2.5 μm were scanned at three or more random locations on each thin film, the flat side of the PEG-DA 2.5D pillar arrays, or the top of the DS3000 pyramids, with 256 lines at a rate of 0.5 lines/s. Image correction, including plane leveling and row alignment, and analysis were performed with Gwydion 2.47. RMS roughness, S_q, was calculated by this software using the following formula, where z_n and $\bar{z}$ represent the height and mean height, respectively

$$S_q = \sqrt{\frac{1}{N}\sum_{n=1}^{N}(z_n - \bar{z})^2}$$

4.11. Laser Scanning Confocal Microscopy Imaging of Scaffolds Coated with Functionalized CNCs. The functionalization of 3D printed structures with Cy5 was characterized in terms of coverage and density using a Leica SP8 DM6000CS laser scanning confocal microscope. All samples were excited with a 638 nm, 30 mW, diode laser (LASOS, Jena, Germany), and fluorescence was collected with a spectral photomultiplier tube detector (Hamamatsu R6357, Hamamatsu City, Shizuoka, Japan) set to an emission band of 730−800 nm. Images of PEG-DA woodpile structures were acquired using LAS X software with a 20×/NA 0.7 water-immersion objective using *xy*- and *z*-steps of 0.45 and 1.2 μm, respectively. Laser power compensation, where higher laser intensities were used at deeper sections, was employed in an attempt to completely visualize the structure. DS3000 bone scaffolds were imaged similarly, however, given their centimeter sizes, it was not possible to image them in their entirety. To this end, images of the control and coated samples were all acquired using the same conditions, where 1.5 mm × 1.5 mm × 0.75 mm sections were captured using a 10×/NA 0.3 air objective, 10% laser power, and *xyz*-steps of 3 μm. Orthogonal projections and 3D renders were produced with ImageJ software.

https://doi.org/10.1021/acsabm.1c00970
ACS Appl. Bio Mater. XXXX, XXX, XXX−XXX

4.12. Spinning-Disk Confocal Imaging of PC3 Cancer Cells on PEG-DA 3D Woodpiles. Cells cultured on 3D scaffolds were imaged using a Leica DMI8 inverted microscope controlled using imaging software ImageJ MicroManager and equipped with Yokogawa CSU-X1 spinning-disk confocal, 405 nm and 488 nm diode, 100 mW lasers, and a 561 nm, diode-pumped solid-state 100 mW laser. Emitted light was collected with a 50 μm Nipkow disk spinning at 5000 rpm before being filtered with a 450/50 nm, 525/50 nm, or 595/50 nm bandpass filter and captured with a Flash4.0 v3 Hamamatsu camera. The samples were inverted and mounted onto a No. 1.5 glass coverslip with a 0.25 mm thick double-sided sticky frame to create an aqueous chamber of cell medium and allow imaging with the inverted microscope. Images were captured using a 10×/NA 0.45 water-immersion objective using an exposure of 200 ms and 2 μm z-steps. Cell counting was done manually using the multipoint tool in ImageJ.

4.13. Epifluorescence Imaging of PC3s on 2.5D DS3000 and PEG-DA Structures. PC3-GFP cells were imaged with an Olympus BX51 upright epifluorescence microscope using a 10× NA 0.3 objective and an X-Cite 120 lamp. Emitted light was filtered through a 545/55 nm bandpass filter and captured with a Hamamatsu C13440 ORCA-Flash4.0 CMOS digital camera controlled by imaging software ImageJ MicroManager.

4.14. SEM Characterization of 3D Printed Structures. Three-dimensional (3D) printed samples were imaged through secondary electron emission with a Hitachi S-4800 system set to a working accelerating voltage and a current of 0.7 kV and 10 μA, respectively, at a distance of 12.8 mm.

■ ASSOCIATED CONTENT

Supporting Information

The Supporting Information is available free of charge at https://pubs.acs.org/doi/10.1021/acsabm.1c00970.

List of synthetic procedures and schemes of linkers and their grafting onto cellulose nanocrystals; AFM, SEM, and fluorescence results of various control experiments regarding the impact of PAH coating and its washing on CNC coating and cell adherence; and thorough topographical and roughness analysis of CNC coatings and 3D rendered confocal fluorescence images (PDF)

■ AUTHOR INFORMATION

Corresponding Author

Jose Moran-Mirabal − *Department of Chemistry and Chemical Biology, Centre for Advanced Light Microscopy, and Brockhouse Institute for Materials Research, McMaster University, Hamilton, Ontario L8S 4M1, Canada;* orcid.org/0000-0002-4811-3085; Email: mirabj@mcmaster.ca

Authors

Mouhanad Babi − *Department of Chemistry and Chemical Biology, McMaster University, Hamilton, Ontario L8S 4M1, Canada*

Roberto Riesco − *LAAS-CNRS, Université Toulouse III—Paul Sabatier, 31400 Toulouse, France*

Louisa Boyer − *LAAS-CNRS, Université Toulouse III—Paul Sabatier, 31400 Toulouse, France*

Ayodele Fatona − *Department of Chemistry and Chemical Biology, McMaster University, Hamilton, Ontario L8S 4M1, Canada*

Angelo Accardo − *Department of Precision and Microsystems Engineering, Delft University of Technology, 2628 CD Delft, Netherlands;* orcid.org/0000-0003-0442-3652

Laurent Malaquin − *LAAS-CNRS, Université Toulouse III—Paul Sabatier, 31400 Toulouse, France;* orcid.org/0000-0003-4791-3352

Complete contact information is available at: https://pubs.acs.org/10.1021/acsabm.1c00970

Author Contributions

The manuscript was written through contributions of all authors. All authors have given approval to the final version of the manuscript.

Notes

The authors declare no competing financial interest.

■ ACKNOWLEDGMENTS

M.B. was supported through the Natural Sciences and Engineering Research Council (NSERC) of Canada Graduate Scholarship—Doctoral Award. J.M.-M. is the Tier 2 Canada Research Chair in Micro and Nanostructured Materials and the recipient of an Early Researcher Award from the Ontario Ministry of Research and Innovation. This work was supported by funding through a Discovery Grant from NSERC to JMM (RGPIN-2019-06433) and by the French RENATECH network. This research was partly supported as part of the MultiFAB project funded by FEDER European Regional Funds and French Région Occitanie (grant agreement number 16007407/MP0011594) and by the HoliFAB project funded by the European Union's Horizon 2020 Research and Innovation Program (grant agreement No. 760927). This research made use of instrumentation within McMaster's Centre for Advanced Light Microscopy.

■ ABBREVIATIONS

CNCs, cellulose nanocrystals; AFM, atomic force microscopy; ECM, extracellular matrix; PEG-DA, poly(ethylene glycol)-diacrylate; NPs, nanoparticles; LbL, layer-by-layer; PAH, poly(allylamine hydrochloride); PC3, human prostate cancer cells; GFP, green fluorescence protein; ITO, indium-tin-oxide; 2PP, two-photon polymerization; EthD-1, ethidium bromide homodimer; TPM, 3-(trimethoxysilyl)propyl methacrylate; Irgacure 819, diphenyl(2,4,6-trimethylbenzoyl)phosphine oxide; DMAP, 4-dimethylaminopyridine; NHS, *N*-hydroxysuccinimide; DCC, dicyclohexylcarbodiimide

■ REFERENCES

(1) Inzana, J. A.; Olvera, D.; Fuller, S. M.; Kelly, J. P.; Graeve, O. A.; Schwarz, E. M.; Kates, S. L.; Awad, H. A. 3D Printing of Composite Calcium Phosphate and Collagen Scaffolds for Bone Regeneration. *Biomaterials* **2014**, *35*, 4026−4034.

(2) Hockaday, L. A.; Kang, K. H.; Colangelo, N. W.; Cheung, P. Y. C.; Duan, B.; Malone, E.; Wu, J.; Girardi, L. N.; Bonassar, L. J.; Lipson, H.; Chu, C. C.; Butcher, J. T. Rapid 3D Printing of Anatomically Accurate and Mechanically Heterogeneous Aortic Valve Hydrogel Scaffolds. *Biofabrication* **2012**, *4*, No. 035005.

(3) Li, K.; Wang, D.; Zhao, K.; Song, K.; Liang, J. Electrohydrodynamic Jet 3D Printing of PCL/PVP Composite Scaffold for Cell Culture. *Talanta* **2020**, *211*, No. 120750.

(4) Yi, T.; Huang, S.; Liu, G.; Li, T.; Kang, Y.; Luo, Y.; Wu, J. Bioreactor Synergy with 3D Scaffolds: New Era for Stem Cells Culture. *ACS Appl. Bio Mater.* **2018**, *1*, 193−209.

(5) Kim, D. H.; Provenzano, P. P.; Smith, C. L.; Levchenko, A. Matrix Nanotopography as a Regulator of Cell Function. *J. Cell Biol.* **2012**, 351−360.

(6) Krishna, L.; Dhamodaran, K.; Jayadev, C.; Chatterjee, K.; Shetty, R.; Khora, S. S.; Das, D. Nanostructured Scaffold as a Determinant of Stem Cell Fate. *Stem Cell Res. Ther.* **2016**, 1−12.
(7) Yim, E. K. F.; Leong, K. W. Significance of Synthetic Nanostructures in Dictating Cellular Response. *Nanomedicine* **2005**, *1*, 10−21.
(8) Canty, E. G.; Lu, Y.; Meadows, R. S.; Shaw, M. K.; Holmes, D. F.; Kadler, K. E. Coalignment of Plasma Membrane Channels and Protrusions (Fibropositors) Specifies the Parallelism of Tendon. *J. Cell Biol.* **2004**, *165*, 553−563.
(9) Baselt, D. R.; Revel, J. P.; Baldeschwieler, J. D. Subfibrillar Structure of Type I Collagen Observed by Atomic Force Microscopy. *Biophys. J.* **1993**, *65*, 2644−2655.
(10) Provenzano, P. P.; Keely, P. J. Mechanical Signaling through the Cytoskeleton Regulates Cell Proliferation by Coordinated Focal Adhesion and Rho GTPase Signaling. *J. Cell Sci.* **2011**, *124*, 1195−1205.
(11) Dickinson, R. B.; Guido, S.; Tranquillo, R. T. Biased Cell Migration of Fibroblasts Exhibiting Contact Guidance in Oriented Collagen Gels. *Ann. Biomed. Eng.* **1994**, *22*, 342−356.
(12) Provenzano, P. P.; Inman, D. R.; Eliceiri, K. W.; Trier, S. M.; Keely, P. J. Contact Guidance Mediated Three-Dimensional Cell Migration Is Regulated by Rho/ROCK-Dependent Matrix Reorganization. *Biophys. J.* **2008**, *95*, 5374−5384.
(13) Wang, W.; Wyckoff, J. B.; Frohlich, V. C.; Oleynikov, Y.; Hüttelmaier, S.; Zavadil, J.; Cermak, L.; Bottinger, E. P.; Singer, R. H.; White, J. G.; Segall, J. E.; Condeelis, J. S. Single Cell Behavior in Metastatic Primary Mammary Tumors Correlated with Gene Expression Patterns Revealed by Molecular Profiling. *Cancer Res.* **2002**, *62*, 6278−6288.
(14) Abrams, G. A.; Goodman, S. L.; Nealey, P. F.; Franco, M.; Murphy, C. J. Nanoscale Topography of the Basement Membrane Underlying the Corneal Epithelium of the Rhesus Macaque. *Cell Tissue Res.* **2000**, *299*, 39−46.
(15) Liliensiek, S. J.; Nealey, P.; Murphy, C. J. Characterization of Endothelial Basement Membrane Nanotopography in Rhesus Macaque as a Guide for Vessel Tissue Engineering. *Tissue Eng., Part A* **2009**, *15*, 2643−2651.
(16) Karuri, N. W.; Liliensiek, S.; Teixeira, A. I.; Abrams, G.; Campbell, S.; Nealey, P. F.; Murphy, C. J. Bilogical Length Scale Topography Enhances Cell-Substratum Adhesion of Human Corneal Epithelial Cells. *J. Cell Sci.* **2004**, *117*, 3153−3164.
(17) Dalby, M. J.; Riehle, M. O.; Sutherland, D. S.; Agheli, H.; Curtis, A. S. G. Changes in Fibroblast Morphology in Response to Nano-Columns Produced by Colloidal Lithography. *Biomaterials* **2004**, *25*, 5415−5422.
(18) Lee, M. R.; Kwon, K. W.; Jung, H.; Kim, H. N.; Suh, K. Y.; Kim, K.; Kim, K. S. Direct Differentiation of Human Embryonic Stem Cells into Selective Neurons on Nanoscale Ridge/Groove Pattern Arrays. *Biomaterials* **2010**, *31*, 4360−4366.
(19) Teixeira, A. I.; Abrams, G. A.; Bertics, P. J.; Murphy, C. J.; Nealey, P. F. Epithelial Contact Guidance on Well-Defined Micro- and Nanostructured Substrates. *J. Cell Sci.* **2003**, *116*, 1881−1892.
(20) Lee, C. H.; Shin, H. J.; Cho, I. H.; Kang, Y. M.; Kim, I. A.; Park, K. D.; Shin, J. W. Nanofiber Alignment and Direction of Mechanical Strain Affect the ECM Production of Human ACL Fibroblast. *Biomaterials* **2005**, *26*, 1261−1270.
(21) Makaremi, S.; Luu, H.; Boyle, J. P.; Zhu, Y.; Cerson, C.; Bowdish, D. M. E.; Moran-Mirabal, J. M. The Topography of Silica Films Modulates Primary Macrophage Morphology and Function. *Adv. Mater. Interfaces* **2019**, *6*, No. 1900677.
(22) Melchels, F. P. W.; Feijen, J.; Grijpma, D. W. A Review on Stereolithography and Its Applications in Biomedical Engineering. *Biomaterials.* **2010**, *31*, 6121−6130.
(23) Zhang, S.; Ou, Q.; Xin, P.; Yuan, Q.; Wang, Y.; Wu, J. Polydopamine/Puerarin Nanoparticle-Incorporated Hybrid Hydrogels for Enhanced Wound Healing. *Biomater. Sci.* **2019**, *7*, 4230−4236.
(24) Guillaume, O.; Geven, M. A.; Sprecher, C. M.; Stadelmann, V. A.; Grijpma, D. W.; Tang, T. T.; Qin, L.; Lai, Y.; Alini, M.; de Bruijn, J. D.; Yuan, H.; Richards, R. G.; Eglin, D. Surface-Enrichment with Hydroxyapatite Nanoparticles in Stereolithography-Fabricated Composite Polymer Scaffolds Promotes Bone Repair. *Acta Biomater.* **2017**, *54*, 386−398.
(25) Tang, Y.; Zhao, Y.; Wang, X.; Lin, T. Layer-by-Layer Assembly of Silica Nanoparticles on 3D Fibrous Scaffolds: Enhancement of Osteoblast Cell Adhesion, Proliferation, and Differentiation. *J. Biomed. Mater. Res., Part A* **2014**, *102*, 3803−3812.
(26) Lee, J. H.; Lee, J. Y.; Yang, S. H.; Lee, E. J.; Kim, H. W. Carbon Nanotube-Collagen Three-Dimensional Culture of Mesenchymal Stem Cells Promotes Expression of Neural Phenotypes and Secretion of Neurotrophic Factors. *Acta Biomater.* **2014**, *10*, 4425−4436.
(27) Hirata, E.; Uo, M.; Takita, H.; Akasaka, T.; Watari, F.; Yokoyama, A. Multiwalled Carbon Nanotube-Coating of 3D Collagen Scaffolds for Bone Tissue Engineering. *Carbon* **2011**, *49*, 3284−3291.
(28) Jung, Y.; Chung, Y. I.; Kim, S. H.; Tae, G.; Kim, Y. H.; Rhie, J. W.; Kim, S. H.; Kim, S. H. In Situ Chondrogenic Differentiation of Human Adipose Tissue-Derived Stem Cells in a TGF-B1 Loaded Fibrin-Poly(Lactide-Caprolactone) Nanoparticulate Complex. *Biomaterials* **2009**, *30*, 4657−4664.
(29) Engler, A. J.; Sen, S.; Sweeney, H. L.; Discher, D. E. Matrix Elasticity Directs Stem Cell Lineage Specification. *Cell* **2006**, *126*, 677−689.
(30) Moon, R. J.; Martini, A.; Nairn, J.; Simonsen, J.; Youngblood, J. Cellulose Nanomaterials Review: Structure, Properties and Nanocomposites. *Chem. Soc. Rev.* **2011**, *40*, 3941−3994.
(31) Habibi, Y.; Lucia, L. A.; Rojas, O. J. Cellulose Nanocrystals: Chemistry, Self-Assembly, and Applications. *Chem. Rev.* **2010**, *110*, 3479−3500.
(32) Gill, U.; Sutherland, T.; Himbert, S.; Zhu, Y.; Rheinstädter, M. C.; Cranston, E. D.; Moran-Mirabal, J. M. Beyond Buckling: Humidity-Independent Measurement of the Mechanical Properties of Green Nanobiocomposite Films. *Nanoscale* **2017**, *9*, 7781−7790.
(33) Fatona, A.; Berry, R. M.; Brook, M. A.; Moran-Mirabal, J. M. Versatile Surface Modification of Cellulose Fibers and Cellulose Nanocrystals through Modular Triazinyl Chemistry. *Chem. Mater.* **2018**, *30*, 2424−2435.
(34) Hu, H.; Yuan, W.; Liu, F.-S.; Cheng, G.; Xu, F.-J.; Ma, J. Redox-Responsive Polycation-Functionalized Cotton Cellulose Nanocrystals for Effective Cancer Treatment. *ACS Appl. Mater. Interfaces* **2015**, *7*, 8942−8951.
(35) Despres, H. W.; Sabra, A.; Anderson, P.; Hemraz, U. D.; Boluk, Y.; Sunasee, R.; Ckless, K. Mechanisms of the Immune Response Cause by Cationic and Anionic Surface Functionalized Cellulose Nanocrystals Using Cell-Based Assays. *Toxicol. In Vitro* **2019**, *55*, 124−133.
(36) Wan, W.; Ouyang, H.; Long, W.; Yan, W.; He, M.; Huang, H.; Yang, S.; Zhang, X.; Feng, Y.; Wei, Y. Direct Surface Functionalization of Cellulose Nanocrystals with Hyperbranched Polymers through the Anionic Polymerization for PH-Responsive Intracellular Drug Delivery. *ACS Sustainable Chem. Eng.* **2019**, *7*, 19202−19212.
(37) Domingues, R. M. A.; Gomes, M. E.; Reis, R. L. The Potential of Cellulose Nanocrystals in Tissue Engineering Strategies. *Biomacromolecules.* **2014**, 2327−2346.
(38) de France, K. J.; Badv, M.; Dorogin, J.; Siebers, E.; Panchal, V.; Babi, M.; Moran-Mirabal, J.; Lawlor, M.; Cranston, E. D.; Hoare, T. Tissue Response and Biodistribution of Injectable Cellulose Nanocrystal Composite Hydrogels. *ACS Biomater. Sci. Eng.* **2019**, *5*, 2235−2246.
(39) Moreau, C.; Beury, N.; Delorme, N.; Cathala, B. Tuning the Architecture of Cellulose Nanocrystal-Poly(Allylamine Hydrochloride) Multilayered Thin Films: Influence of Dipping Parameters. *Langmuir* **2012**, *28*, 10425−10436.
(40) Martin, C.; Jean, B. Nanocellulose/Polymer Multilayered Thin Films: Tunable Architectures towards Tailored Physical Properties. *Nord. Pulp Pap. Res. J.* **2014**, *29*, 19−30.
(41) Mézière, F.; Juskova, P.; Woittequand, J.; Muller, M.; Bossy, E.; Boistel, R.; Malaquin, L.; Derode, A. Experimental Observation of Ultrasound Fast and Slow Waves through Three-Dimensional Printed Trabecular Bone Phantoms. *J. Acoust. Soc. Am.* **2016**, *139*, No. EL13.

https://doi.org/10.1021/acsabm.1c00970
ACS Appl. Bio Mater. XXXX, XXX, XXX−XXX

(42) Accardo, A.; Blatché, M. C.; Courson, R.; Loubinoux, I.; Vieu, C.; Malaquin, L. Two-Photon Lithography and Microscopy of 3D Hydrogel Scaffolds for Neuronal Cell Growth. *Biomed. Phys. Eng. Express* **2018**, *4*, No. 027009.
(43) de Mesquita, J. P.; Patrício, P. S.; Donnici, C. L.; Petri, D. F.; de Oliveira, L. C. A.; Pereira, F. V. Hybrid Layer-by-Layer Assembly Based on Animal and Vegetable Structural Materials: Multilayered Films of Collagen and Cellulose Nanowhiskers. *Soft Matter* **2011**, *7*, 4405−4413.
(44) Huang, C.; Fang, G.; Zhao, Y.; Bhagia, S.; Meng, X.; Yong, Q.; Ragauskas, A. J. Bio-Inspired Nanocomposite by Layer-by-Layer Coating of Chitosan/Hyaluronic Acid Multilayers on a Hard Nanocellulose-Hydroxyapatite Matrix. *Carbohydr. Polym.* **2019**, *222*, No. 115036.
(45) de France, K. J.; Babi, M.; Vapaavuori, J.; Hoare, T.; Moran-Mirabal, J.; Cranston, E. D. 2.5D Hierarchical Structuring of Nanocomposite Hydrogel Films Containing Cellulose Nanocrystals. *ACS Appl. Mater. Interfaces* **2019**, *11*, 6325−6335.
(46) Biermann, O.; Hädicke, E.; Koltzenburg, S.; Müller-Plathe, F.; Müller-Plathe, F.; Biermann, D.-C. O.; Hädicke, E.; Koltzenburg, S. Hydrophilicity and Lipophilicity of Cellulose Crystal Surfaces. *Angew. Chem., Int. Ed.* **2001**, *40*, 3822−3825.
(47) Mazeau, K. On the External Morphology of Native Cellulose Microfibrils. *Carbohydr. Polym.* **2011**, *84*, 524−532.
(48) Or, T.; Saem, S.; Esteve, A.; Osorio, D. A.; de France, K. J.; Vapaavuori, J.; Hoare, T.; Cerf, A.; Cranston, E. D.; Moran-Mirabal, J. M. Patterned Cellulose Nanocrystal Aerogel Films with Tunable Dimensions and Morphologies as Ultra-Porous Scaffolds for Cell Culture. *ACS Appl. Nano Mater.* **2019**, *2*, 4169−4179.
(49) Mo, Y.; Guo, R.; Liu, J.; Lan, Y.; Zhang, Y.; Xue, W.; Zhang, Y. Preparation and Properties of PLGA Nanofiber Membranes Reinforced with Cellulose Nanocrystals. *Colloids Surf., B* **2015**, *132*, 177−184.
(50) Liu, S.; Jin, M.; Chen, Y.; Gao, H.; Shi, X.; Cheng, W.; Ren, L.; Wang, Y. High Internal Phase Emulsions Stabilised by Supramolecular Cellulose Nanocrystals and Their Application as Cell-Adhesive Macroporous Hydrogel Monoliths. *J. Mater. Chem. B* **2017**, *5*, 2671−2678.
(51) Reid, M. S.; Villalobos, M.; Cranston, E. D. Benchmarking Cellulose Nanocrystals: From the Laboratory to Industrial Production. *Langmuir* **2017**, *33*, 1583−1598.
(52) de France, K. J.; Badv, M.; Dorogin, J.; Siebers, E.; Panchal, V.; Babi, M.; Moran-Mirabal, J.; Lawlor, M.; Cranston, E. D.; Hoare, T. Tissue Response and Biodistribution of Injectable Cellulose Nanocrystal Composite Hydrogels. *ACS Biomater. Sci. Eng.* **2019**, *5*, 2235−2246.

https://doi.org/10.1021/acsabm.1c00970
ACS Appl. Bio Mater. XXXX, XXX, XXX−XXX